



International Gemmological Conference

Tokyo - Japan
October 2023



37th International Gemmological Conference

IGC Tokyo, Japan

October 2023

**Dear IGC Participants,
Welcome to Japan!**

It is an incredible opportunity and a great privilege for the IGC Japan organizing committee to host the IGC in Tokyo, Japan. Members of the IGC Japan organizing committee are delighted and pleased that the IGC Delegates, Observers and Special Guests have accepted our invitation to attend to the 37th International Gemmological Conference in Tokyo. In light of the COVID-19 pandemic, it was critical for the Japan organizing committee to postpone and reschedule this conference twice from 2020 to 2023, now, IGC Japan organizing committee is happy that finally it can take on the organizing duty and fulfil it.

Japan was the first Asian country to host the International Gemmological Conference in 1981. Now the IGC 2023 will be the 2nd time for Japan to organize it in Tokyo and it will be the 72nd year for IGC as it first started in 1951. IGC aims to gather all international gemmologists, scholars and researchers to present the specific research topics on natural and synthetic diamonds, colored gemstones, pearls, gem treatments, geological and geographical study of gem mines etc. At this IGC 2023, all the IGC colleagues will gather once again to meet, to discuss and to deliberate on the current and future gemmological issues, as well as to meet some interdisciplinary scientists from earth sciences, gemmologists from local Japanese gemmological laboratories as well as some professional gem traders from Japan at the specially organized events.

It would be wonderful for the IGC attendees to get to know our country, especially Tokyo, which is the capital and most populous, historic city of Japan. It serves as Japan's economic-business center, educational-cultural center, tourism-network center and is the seat of both the Japanese government and the Emperor of Japan. The city is an international research and development hub and likewise represented by several major universities, most notably the University of Tokyo. Tokyo metropolitan city is the third

largest urban jewellery trade industry in the world, there is a public-service association called JJA that represents the Japan jewellery industry, 840 corporate regular companies and 14 organizational regular members engaged in the import, export, manufacture, wholesale and retails of jewellery. There are also jewellery schools, gemmological identification service laboratories and gemmological academic associations.

The IGC conference venue is the prestigious conference hall of the National Museum of Nature and Science. It is a historically important cultural asset of Japan and the official members of the museum are pleased to support a high-quality conference, like IGC that provides state-of-the-art scientific knowledge in the field of gemmology.

The IGC Japan organizing committee has also organized a pre-conference tour called the jade trip and post-conference called the pearl trip for the interested participants who want to get firsthand knowledge about the jade industry and culturing of pearls in Japan. The pre-conference tour will be to see the Itoigawa Jadeite from Niigata prefecture and the post conference tour will be organized to visit a beautiful island-Mikimoto Island in Mie Prefecture to see an Akoya culture pearl farm. Besides this a special tour has been organized to see the Mount Fuji.

Here, we would like to specially thank to the IGC executive committee to supporting and discussing with us to arrange this conference and reviewing the abstracts and preparing the conference proceeding as well.

We hope the IGC participants will have a successful knowledge-rich conference and carry back wonderful memories of Japan and its people!

Best wishes from the IGC Japan Organizing Committee: Dr. Hiroshi Kitawaki, Dr. Ahmadjan Abduriyim, Mr. Masashi Furuya, Mr. Kentaro Emori, Ms. Yoko Okubo



37th International Gemmological Conference IGC 2023 Japan Organizing Committee

Representative of IGC Japan: Hiroshi Kitawaki
International Chairman of IGC Japan: Ahmadjan Abduriyim
Committee Members: Masaki Furuya, Kentaro Emori, Yoko Okubo and
IGC Executive Committee

The head of Program Committees

Pre- and Post-Conference Excursion: Hiroshi Kitawaki and Ahmadjan Abduriyim
Guest programs: Yoko Okubo, Ahmadjan Abduriyim
Events: Organising committee members
Registration and payment: Masaki Furuya

Abstract and Proceedings

Review Board; IGC Executive Committee;
Supported by IGC Japan Organizing Committee;

IGC 2023 Accounting Officer

Japan Germany Gemmological Laboratory
Masaki Furuya
824-5 Furukamijo Kofu Yamanashi 400-0051 JAPAN
TEL +81-55-243-2690 FAX +81-55-243-8377
E-mail: jggl@sapphire.co.jp

Homepage

Laurent Cartier, Ahmadjan Abduriyim, Michael Krzemnicki.

Conference Assistant Committee Members

Prof. Hisao Kanda, Prof. Ritsuro Miyawaki, Akira Ito, Hisao Kato, Hideki Mochizuki, Ken Fujita, Nobuyuki Horiuchi, Yoichi Horikawa, Ikuo Atsumi

Book Layout

Pascaline Minella, Laurent Cartier, Ahmadjan Abduriyim

Review Board

Michael Krzemnicki, Emmanuel Fritsch, Uli Henn, Karl Schmetzer, Hanco Zwaan

Special Advisors

Prof. Hiroyuki Kagi, Tota Koyama, Yasukazu Suwa, Nilam Alawdeen, Yoshi Doi, Michio Iwasaki

Supporting Organization

- National Museum of Nature and Science, Tokyo
- Gemmological Society of Japan
- General Incorporative Foundation; Japan Jewellery Association (JJA)
- General Incorporative Foundation; Japan Gem Society (JGS)
- General Incorporative Foundation; Association of Gemmological Laboratories, Japan (AGL)
- GSTV Co.,Ltd
- Stone Cameo Museum of Furuya Co., Ltd
- Fossa Magna Museum
- Itoigawa City Board of Education
- Mie Pearl Promotion Council
- Mikimoto Pearl Island
- Jadeite Museum-Hisui Gensekikan
- Yamanashi Jewelry Association
- The Kofu Chamber of Commerce & Industry
- Yamanashi Jewelry Museum
- Yamanashi Prefecture
- Kofu City
- Tokyo Diamond Exchange (TDE)
- Japan Gemstone Wholesale Association
- Japan Precious Metal Art & Crafts Cooperative



37th International Gemmological Conference (IGC 2023 Japan)



第37回 国際宝石学会 IGC 2023 日本

Sponsors

GEMMOLOGICAL
SOCIETY OF JAPAN



International Gemmological Conference

History of the IGC

The International Gemmological Conference (IGC) owes much of its origin to BIBOA (Bureau International pour la Bijouterie, Orfèvrerie, Argenterie), the International Jewellery and Gemstone Federation, the first Congress of which in 1926 recommended and defined use of the term cultured pearl.

Experts from various European gem testing laboratories were invited to attend a series of expert meetings that aimed to formulate the policies of BIBOA. In 1936, at the fifth conference of experts, collaboration among laboratories was acclaimed by traders and they encouraged Laboratory Directors to meet each other at a technical conference from which all commercial delegates would be excluded.

Technical meetings were held annually, and in 1951 a Technical Conference was held in Idar Oberstein to prepare for the next London Congress in 1952. Those attending the 1951 conference included Mr B.W. Anderson, Mr G. Göbel, Dr E. Gübelin, Mr F. Wolf, Mr A. Bonebakker, Mr H. Tillander, Mr A. Strondahl, and Mr O. Dragstead. It has been suggested that the future framework of the IGC was established at this meeting in Idar Oberstein.

The London Congress saw the restructuring of BIBOA in which Gemmological Associations were replaced by National Federal Committees, and BIBOA evolved into BIBOAH – the forerunner of CIBJO, now known as The World Jewellery Confederation.

A Technical Conference met at Lugano from 23rd to 25th October 1952 at the initiative of Prof. K. Schlossmacher and Dr. E. Gübelin. Also present at this conference were Messrs B.W. Anderson, A. Bonebakker, O. Dragstead, G. Göbel, K. Siess and H. Tillander. At this historic meeting Dr E. Gübelin proposed creation of a “Committee of an International Gemmological Association” that would consist of

one member per country; this member being the Director of a Gem Testing Laboratory, or a gemmologist of the calibre who could attend that meeting. This was agreed to, and this meeting was later considered to be the inaugural meeting of the IGC.

The first meeting of the IGC in Lugano was followed by subsequent meetings in Amsterdam, The Netherlands (1953), Copenhagen, Denmark (1954), London, UK (1955), Munich, Germany (1956), Oslo, Norway (1957), Paris, France (1958), Milano, Italy (1960), Helsinki, Finland (1962), Vienna, Austria (1964); Barcelona, Spain (1966); Stockholm, Sweden (1968); Brussels, Belgium (1970); Vitznau, Switzerland (1972); Washington D. C., USA (1975), The Hague, The Netherlands (1977), Idar Oberstein, Germany (1979), Kashiko-Jima, Japan (1981), Beruwela, Sri Lanka (1983); Sydney, Australia (1985); Rio de Janeiro, Brazil (1987), Tremezzo, Italy (1989); Stellenbosch (1991), Paris, France (1993); Bangkok, Thailand (1995); Idar Oberstein, Germany (1997); Goa, India (1999); Madrid, Spain (2001), Wuhan, China (2004); Moscow, Russia (2007); Arusha, Tanzania (2009), Interlaken, Switzerland (2011); Hanoi, Vietnam, (2013); Vilnius, Lithuania (2015); Windhoek, Namibia (2017); Nantes, France (2019).

Over the history of the IGC, that now in its fourth decade, it can therefore be seen that the International Gemmological Conference is the longest surviving gemmological conference to remain largely in its original format. Over its history, have been invited to participate in IGC meetings gemmologists from over 40 countries or areas – including Australia, Austria, Bahrain, Belgium, Brazil, Canada, China, Czech Republic, Denmark, Dubai (UAE), England, Finland, France, Greece, Germany, Greenland, Hong-Kong, Israel, India, Italy, Japan, Kenya, Korea, Liechtenstein, Lithuania, Namibia, the Netherlands, Norway, Russia, Singapore,

South Africa, Spain, Sri Lanka, Switzerland, Sweden, Tanzania, Thailand, U.S.A., Vietnam and Zimbabwe.

During the 20th IGC, which was held in Sydney, Australia, the members present elected nine members to Honorary Members status. The first Honorary Members of the IGC were Oliver Chalmers (Australia), Prof. A. Chikayama (Japan), and Mr R. Crowningshield (U.S.A), Mr. O. Dragsted (Sweden), Prof. E. Gübelin (Switzerland), Mr. R. T. Liddicoat (U.S.A), Mr. M. Masso (Spain), Dr. F. H. Pough (U.S. A) and Dr. J. M. Saul (Kenya).

In Italy, the IGC logo was designed by Roberto Sambonet, made in gold by Roberto Cusi, and offered to the conference delegates during the Tremezzo 1989 edition.

In Italy, in 1989, the following rules were agreed for future meetings of the IGC:

1. The prime objective was to be the exchange of gemmological experiences.
2. Gemmology was to be the platform for all topics and was to be regarded as the principal theme.
3. It was decided that attendance at all further Conferences should be by invitation that would be determined where necessary by the Conference Secretary and the Executive Committee.
4. All delegates were to be encouraged to present papers; but this would not be mandatory.
5. All delegates must have a publishing record and all papers at IGC meetings must presented in English, both when written or spoken.
6. The Conference must keep foremost in mind the prime objectives and avoid dilution/confusion of this objective which, if not maintained, could result in a blank organization without true status or credibility.
7. Peripheral commercial activity must be kept to a minimum, and there should be no blatant sponsorship of any kind.

These rules, combined with the original concepts, have been kept as the basis for all conferences since. Any invitation is specific to the person invited and is not transferable. Rules/Standard Operating Procedures of the IGC as of the 2019 revision

Introduction

Over the years, the Rules/Standard Operating Procedures for the IGC have evolved. These were last published in the Proceedings of the 35th IGC 2017 (Windhoek, Namibia). The following Rules and Procedures have been revised in 2018 and 2019 by the Executive Committee of the IGC and agreed for future meetings.

I. General rules

1. The prime objective is the exchange of gemmological experiences. Gemmology is to be regarded as the principal theme.
2. Attendance at the IGC is by invitation only (see Categories of Membership following).
3. All Members (delegates and observers) are encouraged to present a paper or poster. To receive further invitations, it is mandatory for observers to present a paper or poster, at least at their second attendance at the conference.
4. All Members (delegates and observers) must have a publishing record. All papers at IGC meetings must be presented in English, both written and spoken.
5. The Conference must keep foremost in mind the prime objective and avoid dilution or confusion of this objective, which if not maintained could result in the loss of status or credibility.
6. Peripheral commercial activity must be kept to a minimum, and there should be no blatant sponsorship of any kind.

These rules, combined with the original concepts, have been kept as the basis for all conferences since. Any invitation is specific to the person invited and is not transferable.

Membership

Honorary Members are senior members of the IGC who are elected by Delegates at the Business Meeting following each IGC, following nomination by the Executive Committee. Delegates are those who are elected from Observers who have established eligibility by presenting worthwhile presentations (either lectures and/or posters) at three IGC meetings. Following recommendation by the Executive Committee, new Delegates shall be elected by majority vote of Delegates at the Business Meeting following each IGC.

Observers are those who are invited to attend an IGC meeting by majority vote of the Executive Committee. Invitations shall be given only to internationally recognized gemmologists who have published in the gemmological field.

Applications for Observer status, which shall be supported by a pertinent CV and list of publications, should be submitted to the Executive Committee for consideration. An invitation will then be offered by the Secretary of the IGC.

Executive Committee (Execo)

The day-to-day administration and decision making of the IGC shall be overseen by an Executive Committee that meets formally at IGC meetings, and between meetings conducts the routine business of the IGC electronically by email. New members of the Executive Committee are chosen from among IGC Delegates. Following nomination, new members of the Executive Committee shall be elected by majority vote of Delegates at the Business Meeting that follows each IGC.

From time to time, the Executive Committee shall elect a Secretary, who will be responsible for detailed administration, especially activities related to invitations to the conference, and the distribution of decisions of the Executive Committee to Honorary Members and Delegates.

Written minutes shall be kept for all meetings of the Executive Committee and approved by the Executive Committee. After a Conference, written minutes of the General Business Meeting shall be distributed by email to all Members to inform everyone, including those not present, about decisions and further activities.

The Executive Committee elects a Chairman of the Abstract Review Committee, who organizes the handling and review process of the Abstracts. Delegates and Observers shall submit the title and a three-page extended abstract of a paper proposed for presentation at an IGC meeting to the Abstract Review Committee for approval.

II. Meetings of the IGC

IGC meetings should be held every two years in a host country approved by Honorary Members and Delegates.

IGC meetings should be timed so as not to clash with other meetings (e.g. IMA meetings) that Delegates are likely to attend.

A country wishing to host an IGC meeting shall submit a proposal first to the Executive Committee, and then present it formally to Delegates. The decision to accept or reject a proposal to host an IGC meeting will be made by majority vote of Honorary Members and Delegates present at the IGC Business Meeting, or electronically if an IGC meeting is not being held at the time a decision needs to be made.

Countries hosting IGC meetings shall establish their own administrative structures to ensure the efficient planning and operation of the Conference. Costs involved in hosting the Conference shall be met by registration fees paid by Honorary Members, Delegates and Observers attending the meeting, and financial sponsorship from private, institutional and government sources.

Day-to-day administration shall be the responsibility of a Conference Organizer, who is either an Honorary Member or a Delegate. The Conference Organizer is chosen at a Business Meeting following recommendation by the Executive Committee. The Conference Organizer may appoint a Conference Secretary and further members of a Committee as needed.

General responsibilities of the Conference Organizer of each IGC include:

Planning and implementation of

- pre-conference activities
- post-conference activities
- the formal IGC conference
- associated cultural activities and events
- entertainment program for registered Guests of Members
- all finances
- receipt and compilation of abstracts of papers after acceptance by the abstract review committee

- publication of Proceedings of the IGC conference
- implementation of poster presentations
- coordination with the Execo, and updates on progress of arrangements for members

Obtaining the necessary government permissions and other political requirements, including organisation of formalities required for different foreign visitors in the host country, e.g. visas, special permissions etc.

The Conference Organizer is responsible for informing Honorary Members, Delegates and Observers of the prospective dates of the next IGC at least 10 months in advance.

Attendance at IGC meetings of Delegates and Observers from countries other than the host country shall be restricted to a maximum of five registrations per country. This restriction does not include Honorary Members. Local Guests are gemmologists who may be invited by the Conference Organizer to attend an IGC meeting held in the country in which they are resident.

Each IGC shall consist of a minimum of:

1. Two to three day pre- and post-conference study excursions to areas and facilities of gemmological interest.
2. A one-day session, prior to the IGC at which previously nominated Delegates and/or Observers will be invited to give presentations to gemmologist members of the host country
3. A three to five-day professional conference to consist of:
 - Formal papers of 15 minutes duration, followed by 5 minutes of questions and answers; and,
 - Poster presentations that shall be scheduled independently so that adequate time is allowed for each poster to be presented by its authors and then have its content available for discussion.
4. A Business Meeting for Honorary Members, Delegates and Observers that traditionally follows closure of the IGC professional conference to exchange opinions on further directions of IGC, and to decide the location for further IGC meetings. Only Honorary Members and Delegates are allowed to vote at the Business Meeting.

IGC Tokyo 2023

- 20 - 22 October 2023 Pre-conference tour - Itoigawa Jadeite Excursion
- 23 - 27 October 2023 Conference, National Museum of Nature and Science, Tokyo (Japan)
- 29 - 31 October 2023 Post-conference tour - Mikimoto Island Akoya Pearl Excursion
- 27 - 29 October 2023 Mount Fuji and Kofu City Special Tour
- 24 - 27 October 2023 Accompanying Persons Tour

IGC2023 Tokyo, Japan Conference and Event Schedule

		Conference Program			Guest Program		Conference & Guest			Staff				
		8:00	9:00	10:00	11:00	12:00	13:00	14:00	15:00	16:00	17:00	18:00	19:00	20:00
20 (Fri.)	Pre-EX													
21 (Sat.)														
22 (Sun.)														
23 (Mon.)	Conference	Setting	Registration	Opening Ceremony Open Colloquium		Lunch Party		Open Colloquium					Welcome Reception	
24 (Tue.)		Setting	General Session			Lunch	General Session					Dinner at Museum Restrantant		
25 (Wed.)			General Session			Lunch	General Session			Free Evening				
26 (Thu.)			General Session			Lunch	Hisui		National Museum of Nature and Science			GALA dinner		
27 (Fri.)			General Session			Traditional Tea Ceremony, Kimono & Lunch		Genseki-Kan						
27 (Fri.)			Tokyo Bus Tour			Lunch Party		Closing Ceremony		Special Trip to Mt. Fuji				
28 (Sat.)			Special Trip To Mt. Fuji											
29 (Sun.)		Special Trip to Mt. Fuji(Back to Tokyo)												
30 (Mon.)	Post-EX													
31 (Tue.)														

Monday 23rd October

Location: Ueno Seiyoken Hall

9:00 - 10:00	Registration
10:00 - 10:30	IGC Opening words (JJA, JGS, GSJ, IGC Executive Secretary)
10:30 - 17:00	Open Colloquium
10:30 - 11:00	<u>Jayshree Panjekar</u> : Past, present and the future of IGC
11:00 - 11:30	<u>Hanco Zwaan</u> : Diamonds and synthetic diamonds
11:30 - 12:00	<u>Hisao Kanda</u> : A brief history of synthetic diamond researches in Japan
12:20 - 14:00	Lunch party
14:30 - 15:00	<u>Pornsawat Wathanakul</u> : The Importance of Research for Gem & Jewellery Industry
15:00 - 15:30	<u>Yuichi Nakamura</u> : Initiatives for sustainable pearl cultivation in Japan
15:30 - 16:00	<u>Michael Krzemnicki</u> : Colour varieties of gems – where to set the boundary?
16:00 - 16:30	Communication
16:30 - 17:00	Group photo at the front of National Museum of Nature and Science
17:30 - 18:30	IGC Executive Committee Meeting No.1
18:00 - 20:30	Reception & Buffet at the rooftop of National Museum of Nature and Science

Tuesday 24th October

Location: National Museum of Nature and Science, Conference Hall

8:00 - 9:00 Setting and registration

Opening ceremony

9:00 - 9:20 Daily schedule announcement

Session 1: Diamonds, Chairperson: Emmanuel Fritsch

9:20 - 9:40	<u>Robert Coenraads</u> : Mapping underground rivers at the Copeton Diamond Field, New South Wales, Australia Following these 'deep leads' to further riches
9:40 - 10:00	<u>Thomas Hainschwang</u> : Violet Diamonds from Argyle: New Insights into the Cause of their Unique Color
10:00 - 10:20	Suzanne van Leeuwen, <u>J. C. (Hanco) Zwaan</u> : The Banjarmasin Diamond in Amsterdam -War Booty from Borneo
10:20 - 10:50	Coffee break
10:50 - 11:10	<u>Hiroshi Kitawaki</u> , Kentaro Emori, Mio Hisanaga, Masahiro Yamamoto, Makoto Okano, Zhenghao Zhao, Jayam Sonani, Hiroyuki Harada: Gemmological studies of "Hybrid Diamond" (Natural + CVD synthetics)
11:10 - 11:30	Michael Mintrone, Luc Phan, <u>Jean-Pierre Chalain</u> : Ni in type Ia diamonds
11:30 - 11:50	Sergey Sivovolenko, <u>Roman Serov</u> : CVD Rough Diamonds Striae Grading Approach based on Deviated Optical Performance of Polished CVD Diamonds
11:50 - 13:20	Lunch
12:00 - 13:00	IGC Executive Committee Meeting No.2

Session 2: History and Museums, Chairperson: Jayshree Panjekar

- 13:20 - 13:40 Koichi Momma, Ritsuro Miyawaki: Overview of the “GEM” special exhibition at the NMNS
- 13:40 - 14:00 Ahmadjan Abduriyim: A study of Chikayama’s gem and mineral collections and building a gem museum
- 14:00 - 14:20 Stefanos Karampelas, Eloïse Gaillou, Ugo Hennebois, Farida Maouche, Annabelle Herreweghe, Bérengère Meslin Sainte Beuve, Didier Nectoux, Aurélien Delaunay: Study of a historical Alexandrite from Paris school of mines collection
- 14:20 - 14:40 Stephen Kennedy, Mary Montagu-Scott, Susan Tomkins: Snapshot of rubies from 1915
- 14:40 -15:00 Michael Hügi: Quartz crystals from alpine fissures: their formation and the historical significance of alpine quartz as raw material for objets d’art
- 15:00 - 15:30 Coffee break

Session 3: Gemmology 1, Chairperson: Tay Thye Sun

- 15:30 - 15:50 Maxence Vigier, Emmanuel Fritsch, Theo Cavnignac, Camille Latouche, Stephane Jobic: Blue shortwave luminescence of gems the role of titanate groups
- 15:50 - 16:10 Miro Ng: Proposed New Filler Type for Emerald Fracture Filling: Design, Detection, Differentiation, Disclosure
- 16:10 - 16:30 Javier Garcia-Toloza, Holman Alvarado, Carlos Julio Cedeño, Camilo Betancourt: Fingerprint differences between Emeralds from two main zones of production in Colombia in response to input from their host rock
- 16:30 - 17:00 Coffee break

Session 4: Gemmology 2, Chairperson: Wilawan Atichat

- 17:00 - 17:20 Lore Kiefert, Michael Krzemnicki, Jeanette Fiedler, T. Sintayehu, Masaki Furuya: Purple to bluish grey chalcedony from Ethiopia
- 17:20 - 17:40 Karen Fox, Andrew McDonald: Rose Quartz: Journey Into the Nano-Jungle
- 17:40 - 18:00 Boris Chauviré, Jean-Yves Mevellec, Jacques Ferreire, Paul Thomas, Emmanuel Fritsch: Opal stability: a step toward detection
- 18:30 - 20:30 Dinner at Museum Restaurant

Wednesday 25th October

Location: National Museum of Nature and Science, Conference Hall

Session 5: Colored stones 1, Chairperson: Ahmadjan Abduriyim

- 9:00 - 9:20 Nathan Renfro: Microfeatures of Beryl Group Gems including the Newest Mineral Variety, Johnkoivulaite
- 9:20 - 9:40 Gagan Choudhary: New yellow to grey-brown opals from Australia
- 9:40 - 10:00 Anette Juul-Nielsen, Arent Heilmann: A nuummite occurrence from kangerluarsuk in the Maniitsoq Region, West Greenland
- 10:00 -10:20 Claudio Milisenda, Stefan Müller: Colour change Paraiba tourmaline from Brazil
- 10:20 - 10:50 Coffee break

Session 6: Colored stones 2, Chairperson: Shane McClure

- 10:50 - 11:10** Seung Kwon Lee, Dongwook Shin: Sulfur-based species induced photochromism in sodalite
- 11:10 - 11:30** Jayshree Panjekar, Aatish Panjekar: Study and investigation of garnet from Balangir in Odisha, India
- 11:30 - 11:50** Bihan Lin, Xingtong Li, Longbo Zhang, Xiaojing Lai, Qian Zhang: Gemological and Luminescence Characteristics of Taaffeites from Mogok, Myanmar
- 11:50 - 12:10** Bahareh Shirdam, Yang Mingxing, Andy Shen, Nader Taghipour, Soheila Aslani: Investigating the Provenance signature of Tourmaline-Bearing Turquoise in the Kuh Zar Gold Deposit, Semnan Province, Iran
- 12:10 - 13:40** Lunch

Session 7: Colored stones 3, Chairperson: Stefanos Karampelas

- 13:40 - 14:00** Masaki Furuya: Cobalt spinel from Bai Buoi mine, Yen Bai, Vietnam
- 14:00 - 14:20** Chengsi Wang, Jiling Zhou, Andy Shen: Quantitative estimation of spinel's thermal and geothermal history by photoluminescence spectroscopy and its application in spinel origin determination
- 14:20 - 14:40** Qingchao Zhou, Chengsi Wang, Andy Shen: Mechanism and Application of High-Temperature Copper Diffusion in Surface Recoloring of Labradorites
- 14:40 - 15:00** Brendan Laurs: A Review and Synthesis of the Geology and Gem Resources of Granitic Pegmatites in Southern California, USA
- 15:00 - 15:30** Coffee break

Session 8: Technology & Techniques, Chairperson: Brendan Laurs

- 15:30 - 15:50** Michael Krzemnicki, Pierre Lefèvre, Wei Zhou: Phase transformations as important markers for heat treatment detection in corundum and other gemstones
- 15:50 - 16:10** Tasnara Sripoonjan, Bhuwadol Wanthanachaisaeng: Applications of Python for Spectroscopic Data Processing, Analysis and Machine Learning Modeling in Gemmology
- 16:10 - 16:30** Hao Wang, Dirk Weltz, Michael S. Krzemnicki, Andreas Mack, Markus Wälle: Effects of Gamma Irradiation on Ruby and Pink Sapphire and Potential Detection. Methods in Gem Labs
- 16:30 - 16:50** Tom Stephan, Vladimir Hutanu, Xiaosong Li, Thomas Lind, Stefan Müller: Irradiation treatment and gamma-spectroscopy of morganite
- 16:50 - 17:10** Montira Seneewong-Na-Ayutthaya, Bhuwadol Wanthanachaisaeng, Waratchanok Suwanmanee, Thanapong Lhuaamporn, Pimlapat Kamkeaw, Sarun Phibanchon Tasnara Sripoonjan, and Thanong Leelawatanasuk: An implementation of machine learning in ruby and sapphire origin determination

FREE EVENING

Thursday 26th October

Location: National Museum of Nature and Science, Conference Hall

Session 9: Corundum 1, Chairperson: Claudio Milisenda

- 9:00 - 9:20** U. Atikarnsakul, W. Soonthorntantikul, Sudarat Saeseaw: Color enhancement in yellow sapphire
- 9:20 - 9:40** Aaron Palke, Shane McClure, Nathan Renfro: Unstable Color in Padparadscha
- 9:40 - 10:00** Seika Oto, Akira Miyake, Yohei Igami, Kentaro Emori, Hiroshi Kitawaki:
Crystal structure of nano inclusions in blue sapphire from Diego Suarez, Northern Madagascar
- 10:00 - 10:20** Waratchanok Suwanmanee, Chotika Kittikunlayaworakun, Thanapong Lhuaamporn, Chanenkant Jakkawanvibul, Thanong Leelawatanasuk, Wilawan Atichat,
Visut Pisutha-Arnond, Nongnuch Jangsawang, Kanwalee Pangza: Influence of Irradiation on Colour Modification and Colour Stability of Rubies: A Preliminary Study
- 10:20 - 10:50** Coffee break

Session 10: Corundum 2, Chairperson: Michael Krzemnicki

- 10:50 - 11:10** E. Billie Hughes, Wim Verriest: Low Temperature Heat Treatment of Burmese Ruby
- 11:10 - 11:30** Bovon Ubolchay, Chakkaphan Sutthirat, Bhuwadol Wanthanachaisaeng, Gamini Zoysa, Waratchanok Suwanmanee, Arūnas Kleišmantas: Milky appearance of Geuda sapphire from Sri Lanka
- 11:30 - 11:50** Wiwat Wongkokua, Thanapong Lhuaamporn, Natthapong Monarumit, Phongsakorn Kajornboonsook, Pornsawat Wathanakul: Explanation on Yellow, Green and Brown Coloration Series of Basalt Related Bangkok Sapphires
- 11:50 - 12:10** Walter Balmer: FTIR Fingerprinting: a case study on mineral inclusion identification by FTIR applied on rubies from marble-hosted deposits
- 12:10 - 13:00** Lunch
- 12:10 - 13:00** IGC Executive Committee Meeting No.3
move to Jadeite Museum
- 13:00 - 15:00** Visit of Hisui Genseki-Kan (Jadeite Museum)
move to National Museum of Nature and Science
- 15:30 - 18:00** Visit of Tokyo National Museum of Nature and Science
- 18:00 - 18:40** Move to Symphony Cruise Terminal
- 19:00 - 21:00** Gala Dinner

Friday 27th October

Location: National Museum of Nature and Science, Conference Hall

Session 11: Pearls and amber, Chairperson: Pornsawat Wathanakul

- 9:00 - 9:20** Tay Thye Sun, Michael Krzemnicki, Gina Brombach, Thet Tin Nyunt, Myo Lwin, Tay Zar Linn, Loke Hui Ying: Analysis of Myanmar golden-lipped cultured pearls using X-ray radiography, EDXRF, UV-Vis-NIR and Raman spectroscopy
- 9:20 - 9:40** Laurent Cartier, Michael Krzemnicki, Bertalan Lendvay, Nadja Morf, Joana B. Meyer: DNA Fingerprinting and age dating of historic natural pearls: a combined approach
- 9:40 - 10:00** Sutas Singbamroong, Mohamed Karam, Nazar Ahmed, Nahla AlMuheiri, Thanong Leelawattanasuk, Bhuwadol Wanthanachaisaeng, Jirapit Jakkawanvibul: Nacreous Blister Pearl Discovered in Edible Oyster (*Crassostrea gigas*)
- 10:00 - 10:20** A. Costanzo, B. Bojarski, M. Kosior, A. Klikowicz-Kosior: Baltic amber and its inclusions: an insight into the origin and nature of the trapped material
- 10:20 - 10:40** Yan Li, Minghan Peng, Yamei Wang: Effects of weathering on FTIR spectra and origin traceability of archaeological amber: The case of the Han Tomb of Haihun Marquis, China
- 10:40 - 11:10** Coffee break

Session 12: Jade, Chairperson: Andy Hsitién Shen

- 11:10 - 11:30** Supparat Promwongnan, Wilawan Atichat, Kannatee Fueangaksorn, Visut Pisutha-Arnon, Thanong Leelawattanasuk: Treated jadeite-jade: Unusually bright fancy colours
- 11:30 - 11:50** Elizabeth Su: Origin Identification Characteristics of High-quality Green Jadeite
- 11:50 - 12:10** Shang-I (Edward) Liu, Ka-Yi (Angela) Man, Montira Seneewong-Na-Ayutthaya, Chanenkant Jakkawanvibul: Geographic Origin Determination of Fei Cui: A comparison of high-quality green Fei Cui from Myanmar, Guatemala, and Italy
- 12:10 - 13:30** Lunch
- 13:30 - 14:00** IGC Business Meeting

Closing ceremony

- 14:00 - 15:30** IGC plenary meeting & closing ceremony
- 16:00 - 19:00** Move to Xiv Lake Yamanaka, Mount Fuji area



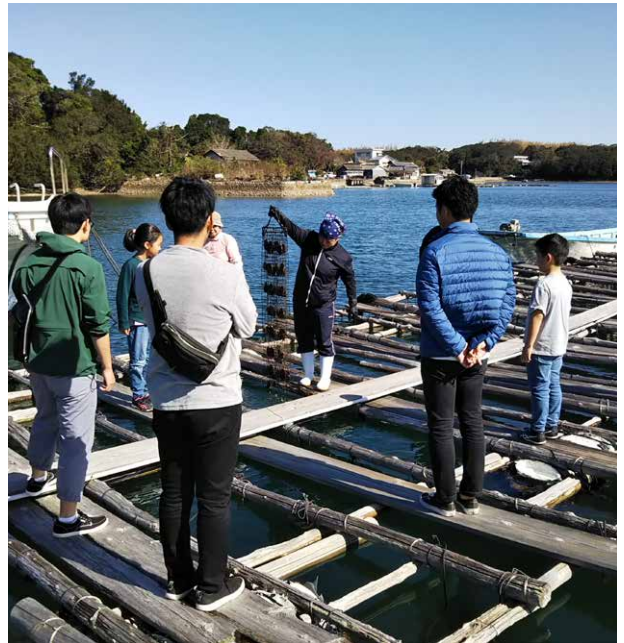
Pre-conference excursion: 20-22 October 2023

Itoigawa Jadeite Excursion

Pre-conference excursion:



Post-conference excursion: 29-31 October 2023 - Pearl Excursion



Past, Present and the Future of IGC



Jayshree Panjkar

Executive Secretary
International Gemmological Conference

Exactly, seventy-one years ago, in the month of October, to be precise from the 23rd to the 25th of October 1952 in Lugano, Switzerland, the inaugural meeting of the International Gemmological Conference (IGC) was held. It is a wonderful coincidence that this year the 37th IGC Japan is also taking place from the 23rd to the 27th October 2023 in Tokyo, Japan. I am sure it will be a great success.

The Past: Formation of IGC

Many of the gemmologists and researchers may be knowing that the International Gemmological Conference (IGC) owes much of its origin to BIBOA (Bureau International pour la Bijouterie, Orfevrene, Argentierie), the International Jewellery and Gemstone Federation.

In fact, it may be interesting to know that although Kokiichi Mikimoto of Japan had already started culturing pearls in the year 1893, it was only in the year 1926 in the first Congress of the BIBOA, that the use of the term “cultured pearl” was recommended and precisely defined. At the various subsequent meetings of experts and commercial traders that the policies of BIBOA were formulated. Later in 1936 at the fifth BIBOA conference of experts, collaboration among laboratories was acclaimed by traders and they encouraged Laboratory Directors to meet each other at a technical conference from which all commercial delegates would be excluded.

Finally in 1951 a technical committee meeting was held in Idar Oberstein to prepare for the next Conference in 1952. Those attending the 1951 meeting included Mr B.W.

Anderson, Mr G. Gobel, Dr E. Gübelin, Mr F. Wolf, Mr A. Bonebakker, Mr H. Tillander, Mr A. Strondahl, and Mr O. Dragstead. It is said that the future framework of the IGC was established at this meeting in Idar Oberstein.

Accordingly, a Technical Conference was organised at Lugano from 23rd to 25th October 1952 at the initiative of Prof. K. Schlossmacher and Dr. E. Gübelin. Also present at this conference were Messrs B.W. Anderson, A. Bonebakker, O. Dragstead, G. Göbel, K. Siess and H. Tillander. At this historic meeting Dr E. Gübelin proposed creation of a “Committee for an International Gemmological Conference” that would consist of one member per country; this member being the Director of a Gem Testing Laboratory, or a gemmologist of the calibre who could attend that meeting. This was agreed to, and this meeting was later considered to be the inaugural meeting of the IGC.

The first meeting of the IGC in Lugano was followed by subsequent meetings in Amsterdam, the Netherlands (1953), Copenhagen, Denmark (1954), London, United Kingdom (1955), Munich, Germany (1956), Oslo, Norway (1957), Paris, France (1958), Milano, Italy (1960), Helsinki, Finland (1962), Vienna, Austria (1964); Barcelona, Spain (1966); Stockholm, Sweden (1968); Brussels, Belgium (1970); Vitznau, Switzerland (1972); Washington D. C., USA (1975), The Hague, the Netherlands (1977), Idar Oberstein, Germany (1979), Kashiko-Jima, Japan (1981), Beruwela, Sri Lanka (1983); Sydney, Australia (1985); Rio de Janeiro, Brazil (1987), Tremezzo, Italy (1989); Stellenbosch, South Africa (1991), Paris, France (1993); Bangkok, Thai-

land (1995); Idar Oberstein, Germany (1997); Goa, India (1999); Madrid, Spain (2001), Wuhan, China (2004); Moscow, Russia (2007); Arusha, Tanzania (2009), Interlaken, Switzerland (2011); Hanoi, Vietnam, (2013); Vilnius, Lithuania (2015), Windhoek, Namibia (2017), and in 2019 the IGC was held in Nantes, France. During the pandemic of the Covid19 the International Gemmological Conference was conducted on line in the year 2021. So, this year 2023, after four years the IGC Delegates and Observers are meeting in person in Tokyo, Japan.

One can see that the existence of the IGC, now is in its seventh decade, since 1952, it can therefore be said that the International Gemmological Conference is the longest surviving gemmological conference to remain largely in its original format. Considering that the science of gemstones or gemmology is a very recent science in that sense, it is indeed spectacular to observe that the invited delegates represent more than 33 countries, which include Australia, Austria, Belgium, Brazil, Canada, China, Czech Republic, Denmark, England, Finland, France, Greece, Germany, Hong Kong, Israel, India, Italy, Japan, Kenya, Korea, Netherlands, Norway, Russia, Singapore, South Africa, Spain, Sri Lanka, Switzerland, Sweden, Thailand, U.S.A. and Zimbabwe – have been invited to participate in IGC meetings.

Present: Ever increasing need

Over the years gemmological science has developed in leaps and bounds. The delegates of the IGC in 1952, may not have imagined the technological advances that would take place in every aspect of the gemmological science, and how useful the presentations made at the subsequent International Gemmological Conference would be for the delegates and observers to keep abreast with latest developments in the gem industry. There was a time when we had synthetic gemstones made by the flame fusion method, synthetic emeralds made by the hydrothermal method or flux method and the gem testing laboratories were efficient enough to detect the synthetics. In the present day, the techniques for syntheses of gems have been such that they are almost similar to the conditions and the processes taking place in nature, resulting in synthetic gems having almost similar looking inclusions seen in natural gemstones. With the advent of techniques like High Pressure High Temperature (HPHT) and Chemical Vapour Deposition (CVD) have made an impact on the synthetic diamonds manufacturing. Japanese companies like Sumitomo, Kyocera, Tomei etc are well known world. In the area of cultured pearls, Japan has been the fore runner, be it Akoya cultured pearls, be it fresh

water Biwa co pearls... Japan has led the way. All these innovations, syntheses, culturing requires proper identification. Added to this are the treatments and enhancements done on gemstones which are becoming rampant in the trade. Then there are also variety of glasses and imitation gems, new artificial gemstones, meaning those not having natural counterparts like Cubic Stabilised Zirconia, YAG, Moissanite etc. which need to be addressed by a gem testing laboratory. New gem bearing mines are discovered, new gem enhancement techniques with less visual impact on the inclusions are being invented, new gemstone minerals are constantly being discovered or one can say minerals which were hitherto known as opaque and unattractive, if one finds a transparent variety of the same, it becomes no doubt a rare gem material. Then we have organic gem materials like the pearls, corals, amber, ivory etc. each in their own respective trade need verification and certification of authenticity.

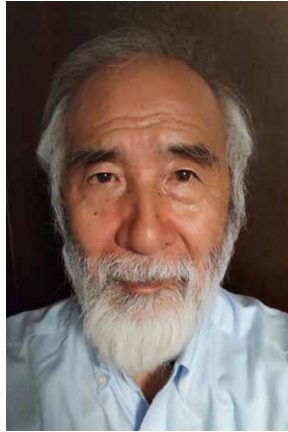
Today, it is impossible to imagine a gem testing laboratory, without the latest sophisticated instrumentation. Gone are the days where only a refractometer and a good microscope were sufficient to a large extent to run a gem testing laboratory. Ultraviolet- Visible range spectrometer, FTIR, Ramon Spectroscope, LIBS, Xray Fluorescence Spectrometer etc are required for the proper identification for the certification of gemstones, for detection of treatments done on natural and synthetic gemstones, for the determination of their geographical origin etc. Therefore, ethical gem testing laboratories with technical staff having the latest state-of-the-art knowledge are the need of the hour. Gemmological Conferences are one of the best sources to get a mine of information and knowledge for the gem technocrats.

Future of IGC

In 2052, when International Gemmological Conference will be completing 100 years of its existence, I do not know how many of the existing delegates and observers will be physically present to celebrate the same. Nevertheless, by that time the gemmological science would have advanced to another niveau. The general public, the consumer, the gem buyer will be more knowledgeable due to the social media and other means, therefore precise disclosure of the gemstone would be expected from the seller and from the gemmologists in gem testing laboratories.

Then, Conferences like the IGC will be still one of the major sources of the latest technical knowhow about gemmological sciences.

A brief history of synthetic diamond researches in Japan



Prof. Hisao Kanda

National Institute for Materials Science, Japan

Research on diamond synthesis started in early 1960s in Japan, following GE's success in 1955. The research was most active between 1980 and 2000 in Japan, triggered by success in CVD diamond synthesis in NIRIM in 1982. A research society named "Japan New Diamond Forum" was established in 1985, and national projects were also implemented. The Japanese research activity spread to Western countries, inducing publication of an international journal, "Diamond Related Materials" in 1991 and regularly held

international conferences all over the world. In the active years, interesting results were achieved. For example, several methods were invented to synthesize diamond films from carbon containing gas. High quality HPHT diamond crystals were commercialized. Non-metallic catalysts similar to materials in the earth's interior were found to convert graphite to diamond. It could be said that the technology has led to a huge production of synthetic diamond in China and India since 2000.



Diamonds and synthetic diamonds



Hanco Zwaan

Netherlands Gem Laboratory / Naturalis Biodiversity Center
Leiden, the Netherlands

Diamond is historically one of the most important gemstones, in terms of value, use and general appreciation. Diamonds were generally formed relatively early in the Earth's History, deep down in the Earth's mantle, where pressures were high enough to force carbon atoms in the dense diamond crystal structure. This created the hardest, but also one of the most beautiful minerals around. During a long geological history, a fascinating succession of geologic events eventually led to the concentration of diamonds at or near the Earth's surface, where they could be discovered. For a long time we know diamond as a natural mineral, being a treasure from nature, beautiful, durable and rare. However, since the 1950's scientists first synthesised diamonds and especially from the 1990's and the start of the new millennium, more and more companies started to produce synthetic diamonds for use in the jewellery industry, in ever increasing quantities and sizes.

Synthetic diamond is a diamond that has been crystallised artificially in a laboratory or factory. Synthetic diamond has the same physical and chemical properties as natural diamond, but has different growth structures and impurities. Synonyms of synthetic diamond are laboratory-grown diamond and laboratory-created diamond. More and more the abbreviation LGD is being used as well, which, depending on the context in which it is used, may be confusing or even misleading, and is not consistent with the ISO standard (ISO 18323), which sets the nomenclature for diamonds, synthetic diamonds and diamond simulants.

This presentation will focus on differences between natural diamond and synthetic diamond mainly in terms of growth history and conditions, and properties. It will also discuss specific equipment that will enable rapid distinction and identification.

Initiatives for sustainable pearl cultivation in Japan



Mr. Yuichi Nakamura

Mie Prefecture Pearl Promotion Council Vice Chairman
PJ Nakamura International CEO

Natural pearls are a gift from nature. On the other hand, cultured pearls are a symbol of humanity and nature. Skilful pearl smiths and rich nature are needed to cultivate beautiful pearls. Traditionally, farmers in Japan strived to maintain the beauty of the sea and the circulation of nutrients between the sea and the land. But these activities were not much revealed. This would be the best time to introduce such activities. And also, the new initiative, PEARL COM-POST is conducted these years in Mie prefecture, the birthplace of the cultured pearl industry. This time, the status quo of the Akoya pearl industry and initiatives for sustainable pearl cultivation in Japan will be introduced.



The Importance of Research for Gem & Jewellery Industry



Pornsawat Wathanakul

Gem and Mineral Science Special Research Unit, Department of Physics and Department of Earth Sciences, Faculty of Science, Kasetsart University, Bangkok, Thailand

Research has always been an essential tool for business leaders who always realise that the consuming public is active, and hence, research investment could help lead their business to the goal. The talk covers how research is important along the supply chain of gem & jewellery industry, i.e., from gemstone occurrences to the markets and the final consumers. The examples of in-depth research & advanced technology with new results are given and discussed for better knowledge in gem science and its applications such as the new explanation on causes of colour in sapphires and treatment detections. Some problems during in the past two decades are used as case examples to remind the audiences of how the research has helped protect and sustain the gem & jewellery industry.



Colour varieties of gems – where to set the boundary?



Michael S. Krzemnicki

Swiss Gemmological Institute SSEF
Basel, Switzerland

In theory it is simple: a gemstone is a mineral formed in nature by geological processes and, as such, it has a mineralogical name that is scientifically defined and accepted by the International Mineralogical Association (IMA) and its Commission of New Minerals, Nomenclature and Classification (CNMNC). In some cases, this mineral name is known and valued by the trade and consumers (e.g. diamond) and does not need further classification. However, for most coloured gemstones, things are much more complex, as most of them are known to consumers and the trade only by their variety names.

Generally, variety names are related to variations in chemical composition and colour of a mineral. Some variety names are well-known in literature since the advent of modern mineralogy in the 18th century (e.g. ruby, sapphire, emerald), whereas others have been introduced in the last few decades with the aim of making a new gem material more

appealing in the market (e.g. tanzanite for vanadium-bearing variety of zoisite, tsavorite for vanadium-bearing variety of grossular garnet). In some cases, such variety names are also linked to external appearance, such as for example single crystalline quartz (e.g. rock crystal) and polycrystalline chalcedony. Although the classification of variety names often seems straightforward (e.g. emerald for the chromium-bearing green variety of beryl and aquamarine for the iron-bearing light blue variety of beryl), we need to remember that they are generally rather vaguely defined, especially when it comes down to separating different varieties of the same mineral from each other (Hughes 1994).

In this presentation, we would like to provide insight into the issue of classifying coloured gems into their respective varieties and present a number of case studies to illustrate the topic from a gemmological laboratory perspective.

Mapping underground rivers at the Copeton Diamond Field, New South Wales, Australia. Following these ‘deep leads’ to further riches

Robert R. Coenraads

Gemmological Association of Australia
NSW Division 128 Terry Street, Rozelle, NSW 2039, Australia.
author@robertcoenraads.com.au

Keywords: Alluvial diamond, basalt, Bingara, Copeton, deep lead, Delungra volcano, Gwydir River, New England Gemfields, palaeochannel, palaeodrainage, palaeotopography.

Background

In Australia’s ‘New England’, early gold and tin explorers discovered diamonds in their sluice boxes without realising their significance, but by the 1890s the Copeton-Bingara area had grown into New South Wales’ premier diamond area with a total reported production of 202,000 carats, although actual production probably far exceeded this amount (MacNevin, 1977). Most of the diamonds were mined via shafts and drives between 1873 and 1922, with minor production continuing until 1960. Today the diamond field lays abandoned.

The glossy, rounded Copeton diamond crystals (Figure 1 inset) were known in Antwerp’s diamond cutting circles as ‘can-ni-faire’ or ‘impossible to cut’ (Curran, 1897; Idriess, 1948).

Their resorbed crystal forms are discussed by Hollis (2003) and their enigmatic origins remained a mystery for many decades. Barron et al. (1996) proposed that they formed when cold slabs of oceanic crust and their overlying carbon-rich sediments were subducted beneath the Australian continent and pushed down into the correct depth/pressure range for diamond crystal growth.

MacNevin (1977) reports the presence of fragile polycrystalline boart up to 12 carats in size from the Copeton Field suggesting local sources for the diamonds because such material cannot withstand transport in a river.

The Copeton deep lead alluvial deposits have long been recognised as river channel deposits that were buried by basalt lava flows with the richest grades of diamonds and other heavy minerals found along the channel axes. Idriess (1948) in his book, ‘Stone of Destiny’ poetically describes how the diamond-bearing deep leads in the Copeton area formed following eruption of the Delungra Volcano:

“Millions of years ago this lost river had come roaring from the mountain tops to sing its song of freedom under sunlight, down to the distant plains, flowing on placidly to the far away ocean. Then a black day came when the volcanoes erupted in a sea of fiery lava, which for all time drowned the river. What a sight for the gods! The river in unbridled triumph, plunging along its mountain course in foamy cascades of all powerful water; then the mountain tops catching fire, belching lava in molten fury down into the river; steam clouds hissing skyward against the volcanoes’ fiery smoke. A titanic battle, that between fire and water, a terrifying holocaust as the tortured river was slowly overwhelmed. And in its silenced bed now lay the diamonds.”

In the quest for these diamonds many attempts were made to map the course of the buried Copeton palaeochannels (Anderson, 1888; Stonier, 1895; Curran 1897; Pittman 1897; Cotton 1914; Gibbons and Pogson, 1963; Fried 1988; Smith 1988; Coenraads, 1990). The palaeotopographic analysis carried out by Coenraads (1990) covered most of the New England at 1:25,000 scale producing a more widespread and detailed study than previously possible.

The Coenraads (1990) maps were updated over the Copeton Diamond Field as part of the Ancient River Diamonds Pty Ltd work programme for Exploration Licence EL 7688 (Coenraads, 2015). The reinterpretation used the Fugro air-

borne geophysical maps (Brown 2006). The magnetic data, radiometric data and total count data show a remarkable contrast between the basalt lava flows and underlying basement rocks allowing extremely accurate mapping of their geological contact.

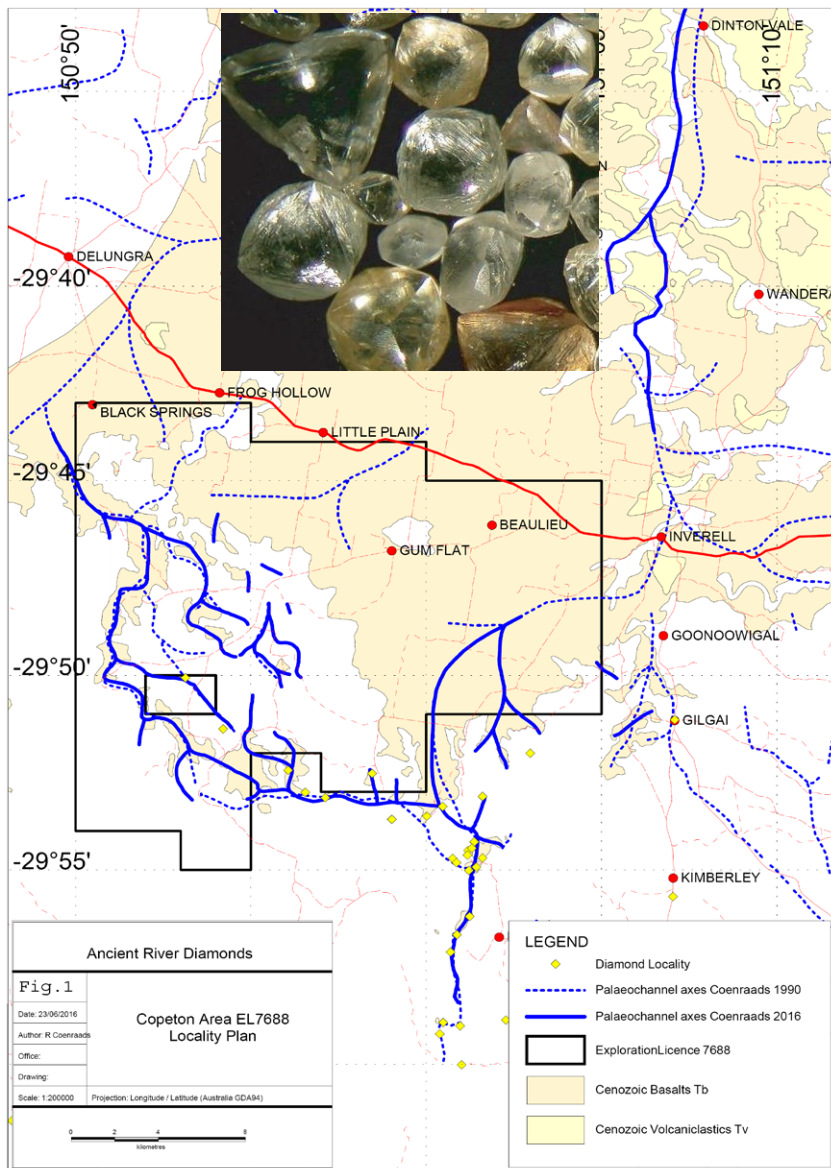


Figure 1: Diamond-bearing deep-leads associated with the palaeo-Gwydir River buried beneath basalts of the Delungra Volcanic Suite in the vicinity of Copeton Dam west of Inverell, NSW. Inset photo shows typical resorbed Copeton 'can-ni-faire' diamond crystals.

The Gwydir River appears to have been progressively diverted from its original northerly course, through a series of at least four westerly-stepping increments to its present course. The drivers for this diversion are the 19-24Ma volcanic activity centred on Mt Russell, near Little Plain, to the northwest of Inverell.

The resultant “treasure map” presented here (Figure 1) connects the known and historically mined-out deposits to as-yet-undiscovered targets hidden beneath the basalt flows that filled these ancient palaeochannels.

Conclusions

The Gwydir River in the Copeton-Bingara area was forced to change course at least four times in the last 20 million years due to uplift and faulting associated with the growing Delungra Volcano. Originally flowing north, the Gwydir was turned gradually westwards and, with each diversion, its payload of alluvial diamonds was carried off into a different area. The older diamond-bearing channels were

progressively filled and ‘fossilized’ into ‘deep leads’ by the volcano’s advancing basalt lava flows. Over the intervening years to the present day, erosion and down-cutting by modern streams has inverted the landscape by wearing down the surrounding hills and leaving proud the ancient diamond-bearing channels as isolated caps or shoestring ridges of hard basalt. Today, portions of the palaeo-Gwydir River and its diamond-bearing gravels lie, as-yet, undiscovered beneath their protective basalt capping to the north and west of Copeton. Furthermore, potential still remains for the discovery of primary diamond sources, possibly dykes, within the catchment of the Gwydir palaeodrainage system as indicated by north-south trending linear features visible in the Fugro airborne magnetic data (Brown 2006). Exploration licence EL8640 (formerly EL7688 in Figure 1) is currently held by Copeton Diamond Mines Pty Ltd with an aim to mine the basalt-covered channels and explore for potential diamond sources.

References:

- Anderson, W. 1888. Appendix No. 8 in Report in progress for 1887 by the Geological Surveyor in Charge. Report, Department of Mines NSW for 1887 155-156.
- Barron, L.M., Lishmund SR, Oakes GM, Barron BJ and Sutherland FL 1996. Subduction model for the origin of some diamonds in the Phanerozoic of eastern New South Wales. *Australian Journal of Earth Sciences* 43, 257-267.
- Brown, R.E., 2006. Inverell Exploration NSW geophysics — new data for exploration and geological investigations in the northern New England area of New South Wales, *Quarterly Notes* July 2006 No 121, Geological Survey of New South Wales, NSW Department of Primary Industries.
- Coenraads, R.R., 2015. Final annual report for EL7688 for the period ended 19/01/2015. Ancient River Diamond Project, Unpub report Ancient River Diamonds Pty Ltd, 6th February 2015.
- Coenraads, R.R., 1990. Key Areas for Alluvial Diamond and Sapphire Exploration in the New England Gem Fields, New South Wales, Australia. *Economic Geology* 85, 1186-1207.
- Cotton, L.A., 1914. The diamond deposits of Copeton, New South Wales, *Proceeding of the Linnean Society of New South Wales* 39, 803-838.
- Curran, J.M., 1897. On the occurrence of precious stones in New South Wales and the deposits in which they are formed. *Journal of the Proceedings of the Royal Society of New South Wales*, 30, 228-237.
- Fried, A.W., 1988. Equilibrium landscapes and drainage evolution in the Glen Innes/Inverell region. Unpublished Honours Thesis, University of Sydney, 64pp.
- Hollis, J.D., 2003. Morphology of diamond crystals from the Bingara Range, Northern New South Wales, Australia: Volume 21, Number 9, January-March 2003, 350-359.
- Gibbons, G.S., and Pogson, D.J., 1963. Diamond Deposits at Mt Ross. Unpublished report, Geological Survey of New South Wales GS1963/002.
- Idriess, I.L., 1948. *Stone of Destiny*. Angus & Robertson, Sydney & London 344pp.
- MacNevin, A.A., 1977. *Diamonds in New South Wales*. Geological Survey of New South Wales, Mineral Resources 42, 125pp.
- Pittman, E.F., 1897. Report on the Boggy Camo diamond fields. Annual Report Department of Mines NSW for 1896, 98-99.
- Smith, N.M., 1988. Reconstruction of the Tertiary drainage systems in the Inverell Region. Unpublished Honours Thesis, University of Sydney.
- Stonier, G.A., 1895. Report on the Bingara diamond fields. Ann. Report Dept of Mines NSW for 1894, 131-136.

Violet Diamonds from Argyle: New Insights into the Cause of their Unique Color

Thomas Hainschwang

GGTL Liechtenstein, Balzers, Liechtenstein.

thomas.hainschwang@ggtl-lab.org

Until its recent closure, the Argyle mine in Australia has been the only source of uniquely colored violet diamonds produced during the 35 years of its operation. These diamonds that are mostly of small sizes – the largest ever recovered weighed 2.83 ct after cutting - are of rather low saturation appear generally grayish and only the best qualities face up truly violet. Caused by the low saturation, to many observers, these diamonds look gray or blue face up, but when comparing them to type IIb blue diamonds, then it becomes obvious, that practically all these Argyle diamonds are violet and not blue. The violet color is unknown for any diamonds from any other deposit, with exception of

some ultra rare type IIb blue diamonds that show a violet appearance because of an unusually strong red phosphorescence that is even triggered by daylight.

The color of the Argyle violets is the result of a very complex UV-Vis-NIR absorption spectrum as shown in Figure 1. Since these diamonds are always rich to extremely rich in hydrogen, the color has traditionally been associated with hydrogen defects, without providing any actual evidence for this claim. While nickel has been detected in earlier works (Van der Bogert et al., 2009), a deeper look into the role of nickel in these diamonds has not been realized prior to this present study.

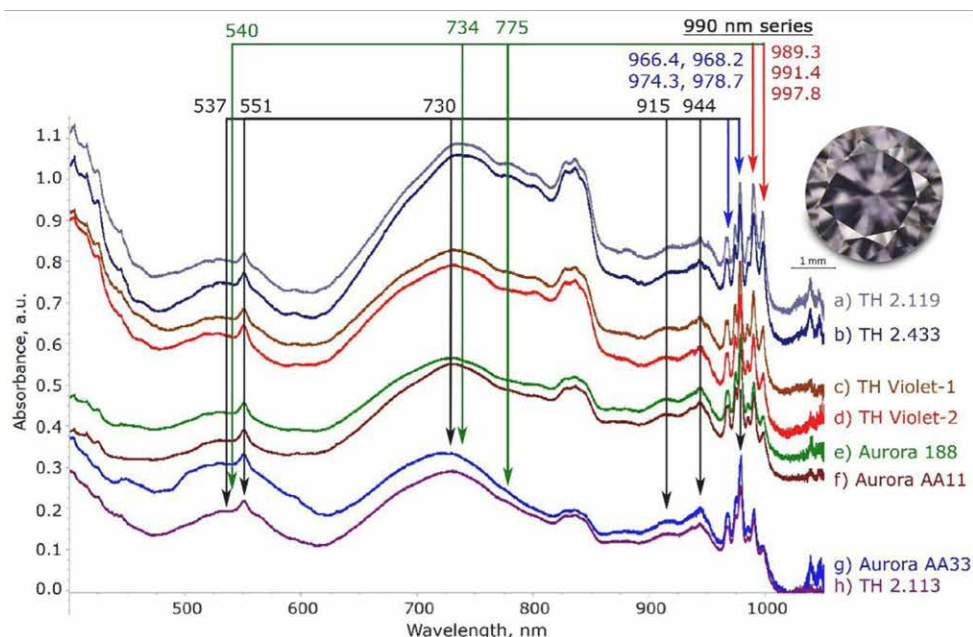


Figure 1: The complex UV-Vis-NIR spectra of a series of violet diamonds from Argyle, recorded at 77K

The structure of the 1330 nm center

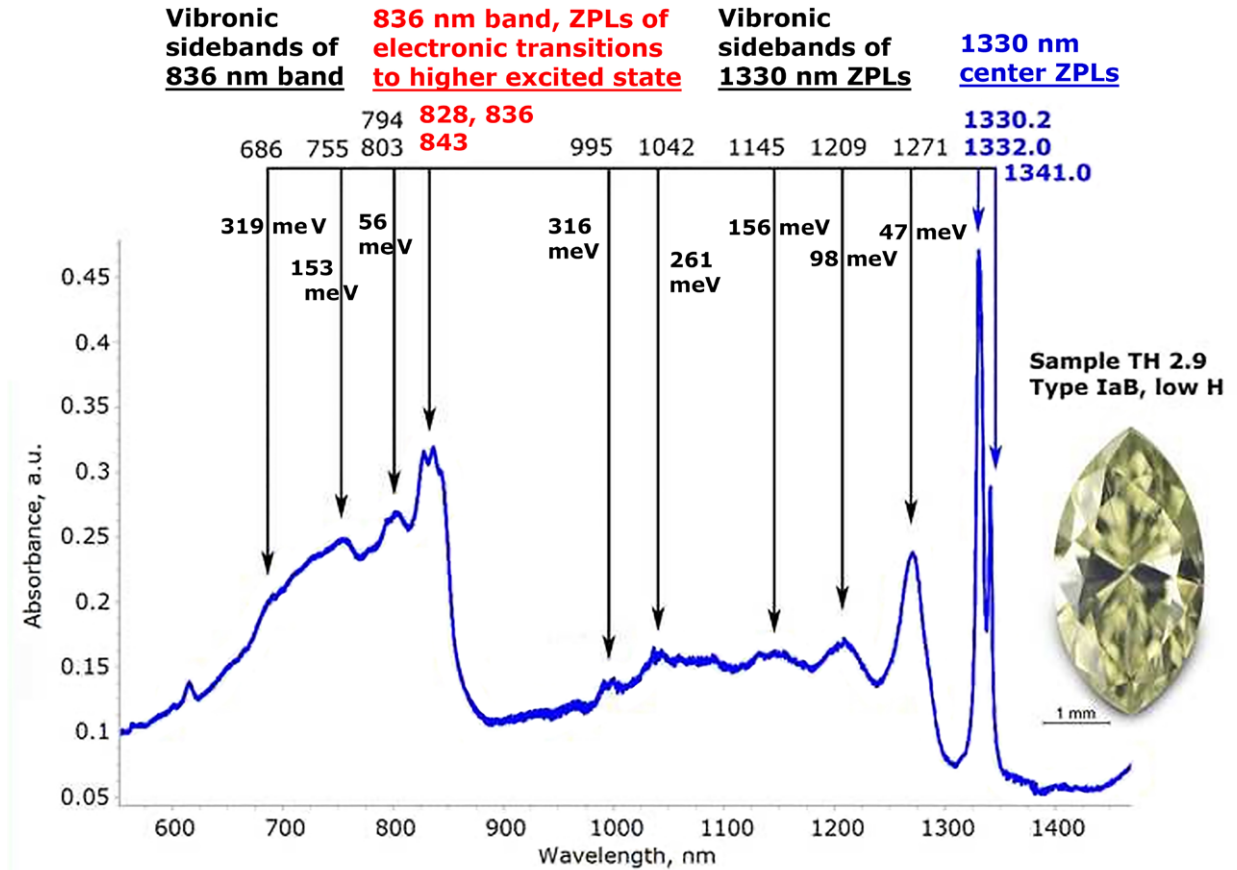


Figure 2: The structure of the 1330 nm center, recorded at 77K, as seen in a green yellow diamond nearly free of IR active hydrogen.

For this study we tested not only violet diamonds but also otherwise colored diamonds that exhibit related absorption characteristics to find an explanation of the unusual UV-Vis-NIR spectra. Specifically for this study we have developed technology to acquire extended UV-Vis-NIR spectra at 77K, from 240 nm all the way to 2500 nm, as the true shape and structure of absorption bands in the NIR know from FTIR spectra of all violet diamonds appeared to be of particular interest.

The data acquired permitted us to define a series of defects responsible for the violet color of these diamonds:

The 1330 nm center – a very distinct defect with strong ZPLs at 1330.2, 1332.0 and 1341.0 nm and associated absorptions that range all the way to the visible spectral domain (Figure 2).

The 990 nm series – up to 17 ZPLs in the range from 966 to 1001 nm that can be correlated with many of the broad absorptions seen in the UV-Vis-NIR absorption spectra of such violet diamonds. Of these, the ZPLs between 976 and 979 nm were found to correlate with the broad band absorptions at 550 and 735 nm.

As the most intense 1330 nm center has been found in diamonds that were practically free of any IR active hydrogen and as its intensity did in no way correlate with the hydrogen absorptions, it was safe to conclude that the defect was not associated with hydrogen. In contrast, the 990 nm series could only be found in diamonds with significant hydrogen, which could mean that hydrogen plays a role in these defects. The common property of all diamonds colored by any of the above-mentioned centers is their richness in nickel: in every diamond that showed any of these absorptions, the PL was dominated by nickel and nickel-nitrogen defects such as S2, S3, NE3 etc.

All data acquired during this study suggests that the color of Argyle violet diamonds is caused by nickel-nitrogen defects, some of which – the 990 nm series – possibly involve hydrogen. Compared to diamonds of olive to brown-yellow to greenish yellow color that exhibit similar UV-Vis-NIR absorption spectra (Hainschwang et al. 2020), the violet diamonds are pure type IaB diamonds, lack N3 center absorption and exhibit stronger ZPLs between 976 to 979 nm – and in consequence stronger broad band absorption at 550 and 735 nm. The combination of these characteristics results in violet color, which may appear gray when the tone is very light.

References:

- Hainschwang, T., Notari, F., Pamies, G., 2020. An in-depth study and classification of brown diamonds, Part II: Brown diamonds with non-deformation-related colour. *Minerals*, 10(10), 914.
- Van der Bogert, C.H., Smith, C.P., Hainschwang, T., McClure, S., 2009. Gray-to-Grayish Blue and Gray-to-Grayish Violet Hydrogen-Rich Diamonds from the Argyle Mine, Australia. *Gems & Gemology*, 45(1), pp. 20 - 37.

The Banjarmasin Diamond in Amsterdam - War Booty from Borneo

Suzanne van Leeuwen¹, J. C. (Hanco) Zwaan²

¹ Rijksmuseum, Amsterdam, the Netherlands, hanco.zwaan@naturalis.nl

² Netherlands Gem Laboratory – Naturalis Biodiversity Center, Leiden, the Netherlands

The Banjarmasin diamond in the collection of the Rijksmuseum in Amsterdam plays a questionable role in the history of the Dutch occupation of Southern Borneo. Confiscated from the Sultan of Banjarmasin, the 70 carat rough diamond arrived in the Netherlands in 1862. This marked the beginning of a forty-year-long political debate on the fate of this former piece of state regalia and whether or not to cut and sell it. In 1902 the Banjarmasin was finally transferred to the Rijksmuseum in Amsterdam as a permanent loan from the then called 'Ministry of Colonies'. This work not

only focused on the colonial history of the diamond, but also on the material properties, which were never studied in detail before. The rough diamond was cut into a 38.23 carats cushion modified brilliant cut and is now graded to have an exceptional white (E) colour and a SI2 clarity. It is a type Ia diamond, containing forsterite inclusions. As one of the few large diamonds found in the alluvial deposits of Kalimantan the results of this study contribute to the acknowledgement of Kalimantan as a historically small but important source of diamonds.



The Banjarmasin diamond, one of the few large diamonds found in Kalimantan. Photo by Hanco Zwaan.

Gemmological studies of “Hybrid Diamond” (Natural + CVD synthetics)

Hirohi Kitawaki¹, Kentaro Emori¹, Mio Hisanaga¹, Masahiro Yamamoto¹, Makoto Okano¹,
Zhenghao Zhao¹, Jayam Sonani², Hiroyuki Harada²

¹ Central Gem Laboratory (Miyagi Bldg. 6th Fl. 5-15-14, Ueno Tito-ku, Tokyo, Japan)

² Diamond Elements, Pvt. Ltd. (India)

kitawaki@cgl.co.jp

Introduction

Size and quality of CVD synthetic diamonds for jewelry market have been improved over the years, and various fancy colour CVD diamonds have also been produced. In addition, overgrowth of type IIb blue CVD synthetic diamond on colourless natural diamond has been made, aiming at fancy colouration (Moe et al., 2017, Ardon et al., 2019), and colourless natural diamond on which CVD diamond layer has been overgrown with the aim of increasing its weight has been reported (Serov et al., 2017., Tan et al., 2018). Appearance of these natural diamonds with CVD overgrowth layer, so called “hybrid diamonds” constitute a new challenge for diamond identification. For this report, we have overgrown a CVD diamond layer on a natural diamond substrate with a target thickness of 2000 μm , and performed gemmological observations after cutting and polishing in order to investigate possibilities of commercial benefits and gemmological detection of such “hybrid” diamonds.

2. Materials and Methods

The CVD overgrowth and cutting/polishing process were performed at Diamond Elements Pvt. Ltd. India, and gemmological observations were performed at Central Gem Laboratory (CGL), Japan. Two apparently colourless octahedral type Ia natural rough diamonds (1.570ct and 1.049ct) were divided by center sawing to obtain four substrates. The CVD overgrowth was performed using a MP-CVD system (Seki Technotron Corp., SDS6K) at temperatures of 1050-1100 $^{\circ}\text{C}$, a pressure of 150 Torr, and a growth rate of 12 $\mu\text{m}/\text{hour}$. In order to grow the colourless layer so that the layer is not discerned from the natural diamond substrates, strict temperature control around the substrates was required. A special holder was designed to grow the diamond layer with the same quality on each of the four substrates in a single step. After growing the layer of a target thickness of 2000 μm , 3 of the 4 grown stones were cut and polished to

square modified brilliant cut (Fig.1). These faceted stones were subjected to standard gemmological examinations: UV-Vis Absorption Spectroscopy, FTIR Spectroscopy, DiamondViewTM observation, Photoluminescence Spectroscopy and SYNTHdetect.

3. Results

Sample 1 was 0.494 ct, G colour, SI1 clarity, and the CVD layer thickness was 1100-1200 μm . Sample 2 was 0.391 ct, H colour, I2 clarity, and the CVD layer thickness was 660-910 μm . The natural parts of Sample 1 and Sample 2 are cut from the same rough crystal. Sample 3 was 0.329 ct, H colour, I2 clarity, and the CVD layer thickness was 880-940 μm .

Standard Gemmological Observation

Observation using a gemmological microscope showed black inclusions in all three samples, and these were the main sources affecting clarity grade. It was confirmed that these black inclusions are located near the boundary between the CVD growth layer and the natural seed crystal used as the substrate. In addition, pinpoint-like inclusions were distributed at the boundary. Under cross-polarized light, strain birefringence parallel to the octahedral plane was observed in the natural seed crystal, and brush-like strain birefringence was observed in the CVD growth layer. In samples 1 and 2, a boundary between the seed crystal and the CVD growth layer was observed on the girdle (Fig.2).



Figure 1: "hybrid diamonds" (from left 0.494ct, 0.391ct, 0.607ct (as grown), 0.329ct)



Figure 2: A boundary between natural seed crystal and the CVD growth layer was seen on the girdle.

UV-Vis Absorption Spectra

The N3 absorption system (415.2, 403.2, 394.4, 384 nm), N4 (344.2 nm), N5 (329.6 nm) and N6 (315 nm) were detected in all three samples in the ultraviolet-visible absorption spectrum at a liquid nitrogen temperature. All of these absorption peaks are all believed to be located in the natural diamond substrates. The Si-V (737 nm doublet) peak shown by Tang et al. (2018) was not detected.

FTIR Spectra

Absorption spectra from a whole body were measured by bringing the table facet into contact with the diffuse reflector. All three samples showed a type Ia character consisting of A center, B center, platelet and hydrogen-related peaks.

DiamondView™

When observed from the table side, the samples 1 and 2 showed dark blue and reddish fluorescence, which probably originate from band A and NV center, respectively. Dark blue with yellow-green fluorescence was observed from sample 3. The yellow-green fluorescence is thought to be due to the H3 from the natural site protruded to the crown region. Observation from the pavilion side showed blue fluorescence, which is thought to be due to N3, in all three samples. When observed from the girdle direction, it was difficult to find a difference in fluorescence colour between the natural crystal substrate and the CVD layer, but a clear bluish-white phosphorescence was observed at the boundary between the CVD layer and the natural diamond substrate.

Photoluminescence Spectra

Photoluminescence measurement was performed at a liquid nitrogen temperature using 457, 488, 514, 633 and 830 nm lasers. The measurements were performed at a number of points on the table side (CVD layer) and the pavilion side (natural substrate) as well, but no clear difference was observed in the spectra. They exhibited the same peaks with the same intensity at each point. The peaks were N3 (415 nm), H4 (496 nm), H3 (503 nm), Si-V (737 nm doublet), 596 nm, 597 nm doublets, NV0 (575 nm) and NV- (637 nm). The former three peaks may be from the natural substrate and the latter from the CVD growth layer.

SYNTHdetect

The table side (CVD layer), the pavilion side (natural substrate) were inspected with SYNTHdetect. All three samples were judged as "refer" from the table side, but sample 1 was "natural" from the pavilion side although the others were "refer".

4. Conclusions

CVD synthetic diamonds were overgrown on type Ia natural diamond. In order to grow CVD synthetic diamonds with the same colour as natural diamonds, growth temperature was precisely controlled around the natural diamonds used as substrates.

In general, overgrowth on small stones would have little commercial benefit, but large crystals may give some profit. Since the diamonds contain type Ia natural diamonds, they may be misidentified as natural by rough sorting methods such as UV transparency, N3 defect detection, and bulk FTIR measurement. But SYNTHdetect judges as refer, when inspected from the table side (CVD part). The presence of black inclusions and minute inclusions distributed on the plane and characteristic strain birefringence are clues for detecting the CVD overgrowth. Concludingly, our study shows that it is possible to identify “hybrid diamonds” by combining data obtained from advanced identification techniques such as DiamondView and PL spectroscopy as well as standard methods.

References:

- Ardon T. and McElhenny G., 2019. Lab Notes: CVD layer grown on natural diamond. *Gems & Gemology*, 55(1), 97-99.
- Moe K.S., Johnson P., D'Gaenens-Johansson U. and Wang W., 2017. Lab Notes: A synthetic diamond overgrowth on a natural diamond. *Gems & Gemology*, 53(2), 237-239.
- Serov R., Shelementiev Y. and Serova A., 2017. Hybrid diamonds: Natural diamonds overgrowth with CVD synthetic. 35th International Gemmological Conference, Windhoek, Namibia 11-15 October, 51-53.
- Tan S., Su J., Lu T., Ma Yongwang., Ke J., Song Z., Zhang J. and Liu H., 2018. A thick overgrowth of CVD synthetic diamond on a natural diamond. *The Journal of Gemmology*, 36(2), 134-141.

A study of nickel-bearing type Ia diamonds

M. Mintrone, L. Phan and J-P. Chalain

Swiss Gemmological Institute – SSEF, Basel, Switzerland.

michael.mintrone@ssef.ch

We present a detailed FTIR and PL spectroscopic study (i.e. at 298 and 77°K) of a large number of colorless (i.e. color D to G) type Ia diamonds (i.e. >200), showing the presence of the 787 nm peak (1.575 eV). We detected this center in at least ca. 40% of more than 8000 analyzed diamonds. All these diamonds are type Ia, as previously described by Vohra et al., (1989). This peak is always associated with Ni-related centers (e.g. 496.7 nm center (S3)), and hence thought to be related to nickel-nitrogen defects (Dobrinets et al., 2013 and reference therein).

Our preliminary results show that most of these diamonds are type IaAB showing no to strong blue fluorescence, while a non-negligible proportion of nearly pure type IaA diamonds (i.e. 5-10 %) show no to strong yellow fluorescence (Fig. 1a, b). Moreover, at least ca. 90% of these diamonds (i.e. type IaA and IaAB) show the characteristic infrared absorption peak at 3107 cm^{-1} (VN_3H) (see Fig. 2), corresponding to a well-known hydrogen center in natural type Ia diamond (e.g. Fritsch and Scarratt, 1989; Goss et al., 2014). Photoluminescence spectra in the visible and near-infrared regions always show the 787 nm center associated with nickel-nitrogen defects (see Fig. 3). The 694, 701, and 794 nm centers were described in untreated natural and synthetic diamonds and are thought to be related to the presence of nickel (Chalain 2003; Dobrinets et al., 2013 and reference therein). The 709 nm center may correspond to the 711 nm Ni-related center observed by Yelissev and Kanda (2007), which coupled with the presence of the 787 and 794 nm centers constitutes a reliable indicator of untreated natural diamonds (Dobrinets et al., 2013).

The presence of nickel in diamonds is thought to facilitate the aggregation of nitrogen, which leads to the combination of single dispersed nitrogen atoms to more complex aggregates such as A and B centers. The catalytic role of nickel may be due to the higher mobility of nickel-nitrogen complexes compared to the “pure” nitrogen defects (Dobrinets et al., 2013). Hence, most of the natural nickel-containing diamonds formed and stored at the Earth’s mantle temperature during geological timescales (i.e. at $T > \text{ca. } 1000^\circ\text{C}$ for $10^3\text{-}10^9$ years, e.g. Stachel and Harris, 2009) should easily reach the formation of B center. Indeed, only ca. 5-10% of our studied diamonds containing nickel are nearly pure nitrogen-rich (i.e. > ca. 500 ppm of N) type IaA diamonds (i.e. with no or only a few ppm of B center, and no platelets) with no detectable N3 defect. Nevertheless, these diamonds show a VN_3H center, testifying of an advanced nitrogen-hydrogen aggregation state (e.g. Goss et al., 2014). This result may be consistent with recent studies suggesting that hydrogen can potentially modify the nitrogen aggregation route (e.g. Wood 2021 and reference therein). However, it is important to note that the formation of the VN_3H center and its influence on other aggregated defects is still poorly constrained and requires more study. As a consequence, our study aims at better understanding the role of hydrogen and nickel in natural diamonds and their influence on the aggregation process of nitrogen.

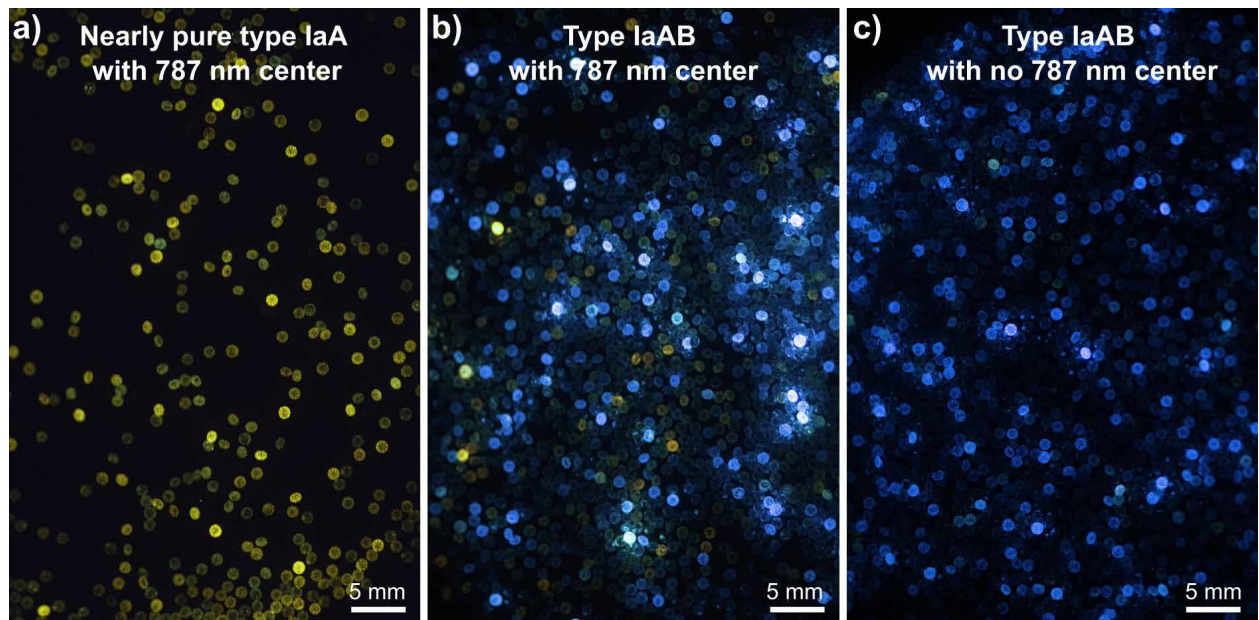


Figure 1: Visible luminescence of the studied natural diamonds, obtained under U.V excitation (365 nm). (a) Nearly pure type IaA diamonds having the 787 nm center show no to strong yellow fluorescence, (b) Type IaAB having the 787 nm center mostly show blue fluorescence and more rarely a yellow fluorescence, and (c) Type IaAB with no 787 nm center detected showing only blue fluorescence (i.e. representing ca. 60% of the 8000 analyzed diamonds, this fraction is not the purpose of this study). Note that the blue fluorescence is described as a result of N3 luminescence at 415 nm.

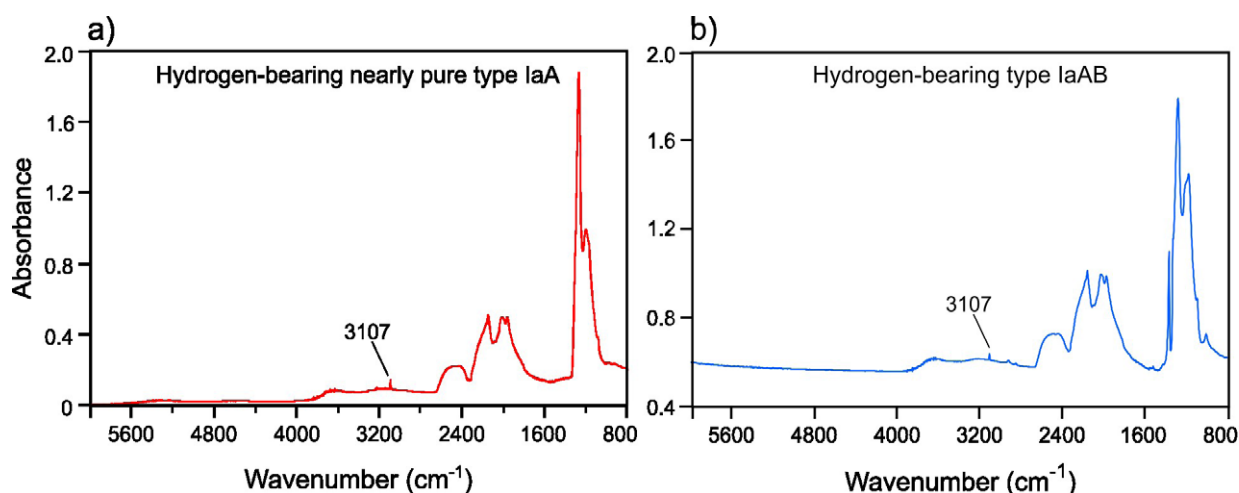


Figure 2: Infrared spectra of hydrogen-bearing diamonds. (a) and (b) are nearly pure type IaA and type IaAB diamonds respectively. The infrared spectra were collected with a resolution of 4 cm⁻¹.

References:

- Chalain J. P. (2003) A natural yellow diamond with nickel-related optical centers. *G&G* 39, 325-356.
- Dobrinets I.A., Vins V.G., Zaitsev A.M. (2013) *HPHT-Treated Diamonds: Diamonds Forever*. Springer, Heidelberg, Germany.
- Fritsch E. and Scarratt K. V. G. (1989) Optical Properties of Some Natural Diamonds with High Hydrogen Content, *Proc. SPIE 1146, Diamond Optics*, <https://doi.org/10.1117/12.962079>.
- Goss J.P., Briddon P.R., Hill V., Jones R., Rayson M.J. (2014) Identification of the structure of the 3107 cm⁻¹ H-related defect in diamond. *J. Phys.: Condens. Matter* 26 145801.
- Stachel T. and Harris J. W. (2009) Formation of diamond in the Earth's Mantle. *J. Phys.: Condens. Matter* 21 364206. DOI 10.1088/0953-8984/21/36/364206
- Vohra Y. K., Vanderborgh C. A., Desgreniers S., Ruoff A.L. (1989) Near-infrared photoluminescence bands in diamond. *Phys. Rev. B*, 39 5464-5467.
- Wood J. O. (2021) An elusive impurity: studying hydrogen in natural diamonds. Ph.D. thesis, University of Bristol. 218 pages.
- Yelissev A. P. and Kanda H. (2007) Optical centers related to 3D transitional metals in diamond. *New Diam. Front. Carbon Technol.* 17(3), 127-178.

CVD Rough Diamonds Striae Grading Approach based on Deviated Optical Performance of Polished CVD Diamonds

Sergey Sivovolenko¹, Roman Serov²

¹ Octonus Finland Oy, Tampere, Finland, ² Octonus Software, Moscow, Russia
potom_skajy@mail.ru

Keywords: Optical Performance, Diamond, LGD, Cut Grading, Striae, Birefringence

Introduction

Diamond's optical performance cognition and scientific descriptions are based on the three key attributes: brilliance, fire and scintillation.

- Brilliance is an illusion caused by the fact that the perceived brightness (subjective) of the diamond significantly exceeds its actual (objective) brightness.
- Fire is the simultaneous (local) contrast of color that is observed in a diamond.
- Scintillation is observed as quick bright flashes that appear and disappear when a diamond is moved and illumination originates from bright light sources of small size.

There are two fundamentally different approaches to grading diamond performance:

- Cut Grade: assessment of the diamond cut is based on the diamond 3D model or the average parameters of the diamond 3D model.
- Diamond Grade: assessment of optical characteristics of diamond visually by experts or with the help of specialized computer-aided systems (Octonus DiBox2, Sarine Light).

The fundamental difference between these two approaches and their corresponding results is that in the Cut Grade approach, the properties of the material, the facet polishing smoothness, and the quality of diamond cleaning are not taken into account. However, material properties such as transparency, absorption, anisotropy, inclusions, and fluorescence can strongly influence the final optical properties of the diamond.

To describe some of the material effects of natural stones, the diamond industry historically used the terms "milky" and "graining". With the emergence of CVD LGD

(CVD laboratory-grown diamond), the term "oily" diamonds became widely used to describe the optical effect caused by the anisotropy of the refractive index (RI).

Variations in the growth conditions of CVD diamonds during the increase in the height of the diamond crystal lead to changes in its composition, which, in turn, are the cause of changes in RI and the source of RI anisotropy. The external manifestations and physical reasons for this RI anisotropy are the same as for striae in a glass. The term striae itself originated from amorphous glass studies. We propose to use the term striae to describe RI anisotropy in CVD diamonds.

The objective of this study is to evaluate the influence of striae on diamond optical properties, such as Brilliance, Fire, and Scintillation. In the future, this approach may allow for the development of a striae grading methodology based on the extent of influence on diamond optical performance.

Striae shadowgraphy in CVD diamonds

Striae identification and grading in glass is a common practice that can be accomplished using a number of methods, including shadowgraphy, interferogram analysis, and wavefront phase measurements.

In CVD diamonds, striae can be easily seen in collimated light and in crossed-polarisers due to amplitude modulation caused by interference in areas with different RI, as shown in Figure 1. This feature is widely used for striae identification in glass, but the amplitude modulation itself is not the main reason for striae influence on the diamond optical performance.

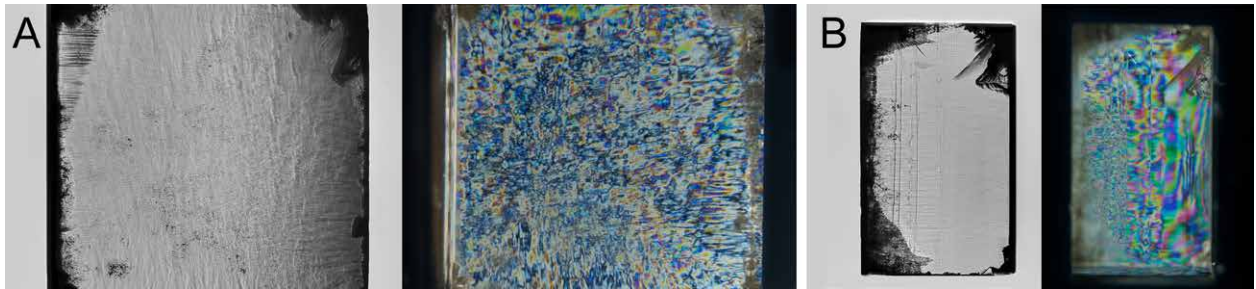


Figure 1: CVD plate perpendicular (A) and parallel (B) to the growth axis in collimated light (DiBox360) and in crossed polarisers (DAL5 ++ Stereo), FOV 8 mm

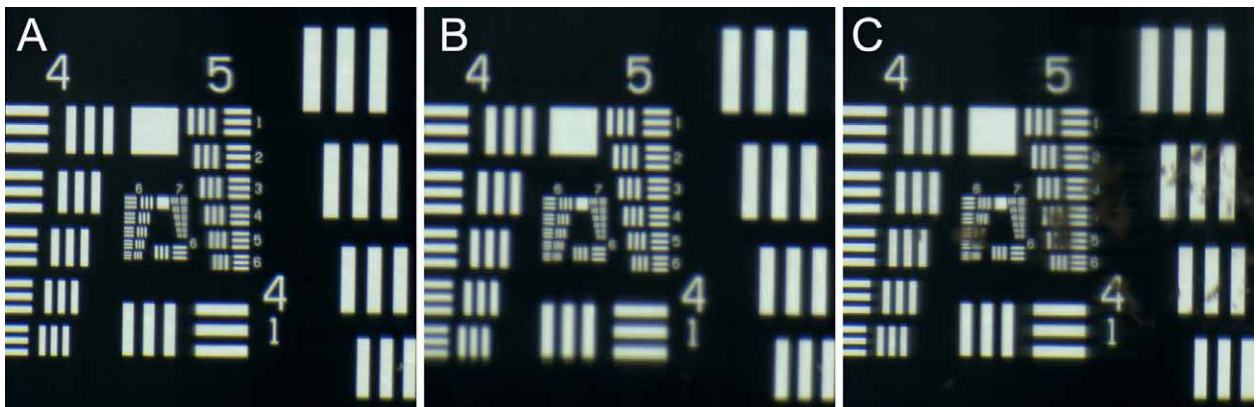


Figure 2: 1951 USAF Resolution Target, FOV 0.8 mm
A - Resolution target, B - CVD sample perpendicular to the Growth sectors, C - CVD sample parallel to the Growth sectors.

Striae impact at the Diamond Modulation Transfer Function

The presence of striae can affect the Modulation Transfer Function (MTF) curve of diamonds. This is due to the wave-front phase aberrations caused by striae, which result in a decrease in MTF at higher spatial frequencies, as shown in Figure 2.

Striae influence on MTF directly affects Diamond Optical Performance. Polished diamond is a combination of virtual facets (VF) that is created when we look through crown facets and see various pavilion facets and internal reflections. Diamond VF reflects the light sources to the human eye retina. In the ideal case, the point light source is projected to the point on the retina, so the observer perceives intensive flash. In the case of a diamond with striae - the point light

source projection on the retina becomes blurred. Thus the flash contrast decreases. MTF can be greatly reduced if the ray passes the same striae multiple times. That is why striae have a higher impact on diamonds with long ray paths. The observer perceives such flashes as blurred and low contrast that generate an "oily" effect in the diamond.

MTF curve decreases at higher spatial frequencies and affects Diamond performance attributes in different degrees:

- Brilliance is affected less, because it is defined mainly by large VF with a short ray path.
- Fire is based on Medium to Large coloured VF and is affected more.
- Scintillation is caused by small/medium VF with a long ray path. It is affected the most.

Striae influence at polished CVD Diamonds Optical Properties

Modern technologies allow for diamonds to be cut according to a predetermined plan. Thus, pairs of diamonds with identical cutting (RMS error for main facets below 0.1 degrees), but made of different materials, can be created and compared for the impact of the material on Diamond optical performance attributes. Several pairs of natural diamonds and CVD diamonds with similar parameters were cut.

One of the cushion pairs is shown on Figure 3A. The stone on the left is natural, and the one on the right is CVD. We can see that performance evaluation based on the diamonds themselves differs. Brilliance for the stones are close, with a difference of 1%. Natural cushion has a 15% higher Fire metric than the CVD.

If performance evaluations are based on 3D models of these diamonds' data (Figure 3 B), they are equivalent because the cutting parameters of these cushions are very close. At the same time, the performance calculated from virtual data is slightly higher than the data for real diamonds (due to the influence of polishing smoothness and diamond material).

Conclusions and suggestions

In summary, striae have a significant impact on diamond optical performance, particularly on fire and scintillation attributes. Striae influence for specific stones is recommended to be determined at the rough stage through MTF measurements on a resolution target. Based on these data, diamonds can be planned for cutting to achieve the desired brilliance/fire/scintillation performance attributes with either a short or long ray path depending on the level of striae present in the CVD rough material.

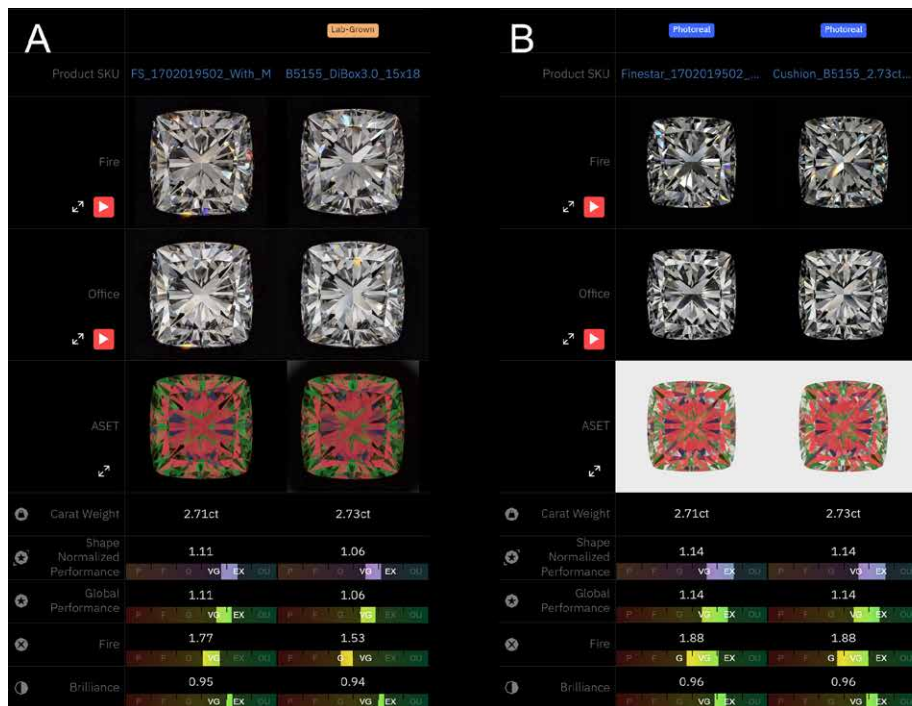


Figure 3. A. DiBox2 Data set for Natural Cushion 2.71 ct and CVD LGD Cushion 2.73 ct with similar proportions. A QR code to the collection is shown on the image.

B. Photoreal data set based on 3D models for Natural Cushion 2.71 ct and CVD LGD Cushion 2.73 ct. A QR code to the collection is shown on the image.

Collection A



Collection B



Acknowledgements

We want to thank Janak Mistry and Lexus Softmac staff for their contributions, discussions and data collection.

Overview of the “GEM” special exhibition at the NMNS

Koichi Momma¹, Ritsuro Miyawaki¹

¹National Museum of Nature and Science, Tokyo, Japan

k-momma@kahaku.go.jp

A special exhibition “GEM” was held at the National Museum of Nature and Science (NMNS), Tokyo, from February 19th to June 19th, 2022. The exhibition covered all aspects of gems, from their origin on the Earth, the science behind the beauty of gems, varieties of gems, history

of cutting and setting techniques, to historic masterpieces. 1000 m² of exhibition hall was filled with about 200 varieties of thousands of pieces of gems. The exhibition attracted over 300,000 visitors.



Figure 1: A pair of amethyst geodes from Uruguay.

The display was composed of 5 chapters. The first chapter, “The Birth of a Gem” told a story of where and how gem minerals occur. Among a number of large specimens showing gem minerals on top of host rocks, a pair of gigantic amethyst geodes each 2.5 m tall and ~2.5 t in weight especially caught visitors’ eyes (Figure 1). The second chapter, “From Gem to Jewel” explains mining and cutting processes, shapes and styles of cutting. In the third chapter, “The Essence and Diversity of Gems”, combinations of rough and loose gems were displayed for each of about 200 varieties of gems. They were grouped by several topics explaining important nature for gems, i.e., brilliance, color, hardness and toughness, dispersion, and other optical effects. As an example, a color circle made of 365 stones demonstrated rich color variation and tones of gems (Figure 2).

A lot of rare gem minerals such as pezzottaite, afghanite, magnesiotaaffeite-6N'3S (musgravite), and also fluorescent gem minerals were displayed. Jumbo gems, such as 21,290 ct of rock crystals and 7,626 ct of topaz, loaned from GIA were also displayed here. The fourth chapter “How a Gem becomes Jewelry” illustrates how important it is to set a qualified loose gem with precious metals in its proper placement to tailor a beautiful piece of jewelry. It was exemplified in the beautiful world of Gimel Trading and Van Cleef & Arpels' creations. The last chapter, “Ultimate of Gems” presented historic masterpieces from collection of Albion Art Jewellery Institute. The collection ranged from Mesopotamian carvings of c.a. 3000 B.C. to royal jewelry pieces of the Middle Ages to modern ages. These pieces of jewelry, which once existed only for a limited number of people, are now inherited as historical arts and cultural assets that transcend the realm of ornaments.

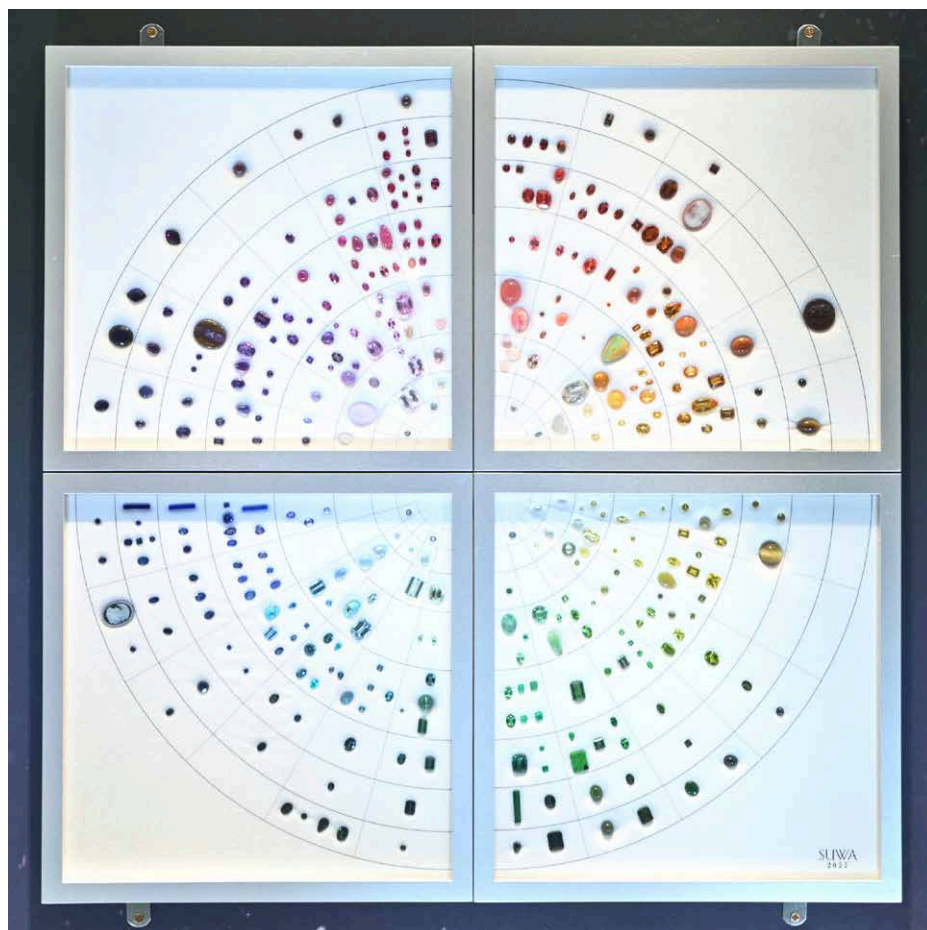


Figure 2: Color circle made of 365 stones, showing rich color variation and tones of gems.

A study of Chikayama's gem and mineral collections and building a gem museum

Ahmadjan Abduriyim^{1,2}

¹ Tokyo Gem Science LLC; tgs@gemscience.tokyo

² GSTV Gemological Laboratory

Abstract

Based on the belief that “a gemstone is art and science,” Mr. Akira Chikayama devoted his life to gemological research and study for the benefit of people involved in gemstones and dedicated himself to the promotion of gemological education in Japan. The author by chance came across his vast collection comprising more than 30,000 precious rough gemstones, crystals, minerals, rocks, fossils and meteorites from all over the world. In 2022, “The Chikayama's Collection, GSTV Gem Museum” was established to make gem researchers, gemmologists and connoisseurs aware of this fascinating outstanding collection. We will continue to introduce the findings and insights gained from the collection both nationally and internationally.

Introduction of Akira Chikayama

With the aim to exchange research and studies in gemology, the first International Gemmological Conference IGC was held in 1952 in Switzerland. Mr. Chikayama participated at this biennial conference since 1966 and by this laid the foundation of gemological education in Japan. By that time, he was teaching at the Faculty of Engineering, University of Yamanashi, and the Yamanashi prefectural Jewelry Art College as well as giving instruction in fashioning hard and brittle gem materials at the Yamanashi prefectural Institute of Polishing Industry.

In 1960s he started visiting gem mines all over the world to get the authentic impression of local gem deposits and collect rough stones directly at the sites. He also visited many international jewelry and mineral shows annually to collect and bring fine specimens and the latest information back to Japan for gemological education and research purposes. The number of the specimens that had been collected over a period of more than forty years reaches over 30,000, which is comparable to the samples collected by the renowned gemologist Dr. Edward J. Gübelin for gemstone research. As more than 20,000 students have studied these samples

and graduated from Chikayama's gemological education courses, he is also known as the ‘pioneer of gemology’ in Japan. He wrote numerous articles, books and dictionaries with great detail – mostly in Japanese, providing us until today with valuable resources and knowledge (Chikayama, 1969-78, 1973, 1979-91, 2005, 2013).

Akira Chikayama, one of the world's leading gemology educators, who devoted his entire life to the education and research in gemology, died in 2007, and his countless precious specimens had been left in his study room since then. In 2016, the author had a chance to visit the Chikayama's Gem Laboratory for the first time. Having felt strongly about the fascination, rarity, and research value of the specimens, the author had a desire to re-collect, organize, and conserve them to play an important role in delivering the wealth, preciousness and attractiveness of these precious specimens to the public through these actual items.

In March 2022, all the collection was moved to the GSTV Gemological Laboratory to establish The Chikayama's Collection, GSTV Gem Museum. Since then, findings and insights from the collection are regularly presented in articles to gemstone connoisseurs and researchers. In addition, selected specimens are now used for display, education, and research purposes.

Studying the Chikayama's collection and building a gem museum

The Chikayama's Collection comprises specimens and samples such as about 600 rocks, 2,000 minerals, 25'000 gems and rough stones with matrix, 500 transparent gem crystals with distinct crystal forms, 2500 faceted stones, 300 synthetics and imitations, 50 fossils, and 10 meteorites, as well as hundreds of books and magazines and photos. These samples were neatly separated into categories such as the country of origin, rock minerals, excellent gemstone crystals, faceted stones, synthetic stones with each man-

ufacturer, specimens to be used in practical courses for students, and master stones, and the information such as mineral names, gem names and country of origin are described both in English and Japanese.

A project to establish the Museum was initiated in March 2022. All items in the collection were cleaned, numbered, and grouped into mineral names, gem varieties and any other classification required. The country, state or region from where Mr. Chikayama collected the specimen and which was recorded by himself, and the geographical information reported for each mine name were re-organized to be recorded.

The specimens were divided into two parts: a) for study and b) for display, with the latter being classified and displayed in three separate Museum sections: “Earth Miracles”, “Crystals World” and “Education of Gemology”.

Minerals and rough gemstones placed in the “Earth Miracles” section are classified into five major categories related to their formation process: related to igneous rocks, pegmatites, hydrothermal formations-gas, regional-contact metamorphic rocks, and sedimentary rocks, and specimens with matrix are displayed as their examples.

In the “Crystals World” section, single crystals of colored gemstones with beautiful crystal forms from each different country are displayed based on the seven crystal systems as shown below:

Cubic: diamond, garnet group, spinel, fluorite, hematite and pyrite.

Hexagonal: beryl group, apatite, calcite/aragonite, phenakite and benitoite.

Trigonal: corundum group, variously colored tourmalines, quartz (amethyst-citrine), agate, rhodochrosite and smithsonite.

Tetragonal: zircon, rutile, vesuvianite (idocrase), scapolite, anatase and apophyllite.

Orthorhombic: topaz, chrysoberyl group, cordierite, peridot, zoisite (tanzanite), celestite, sillimanite, sinhalite, kornerupine, andalusite, prehnite and thomsonite.

Monoclinic: spodumene (kunzite/hiddenite), orthoclase/moonstone, titanite, diopside, euclase, mica, gypsum, and brazilianite.

Triclinic: amazonite/sunstone/andesine/labradorite, kyanite and amblygonite.

Among these exhibition specimens particularly, a suite of three types of Japanese law quartz twins is extremely rare and enthralling.

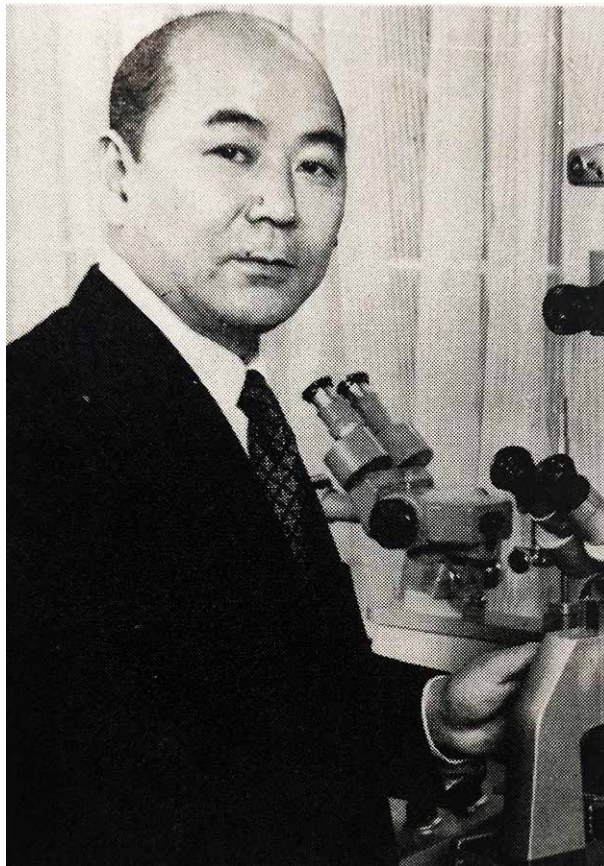


Figure 1: One of the world pioneer gemologist, Akira Chikayama (1921-2007).



Figure 2: Numerous gemstone collections were used for gemological education for several decades in the Akira Chikayama Gem Laboratory (ACGL) since 1979.

The “Education of Gemology” section displays more than 2,000 inorganic or organic, faceted or polished (cabochon) natural gemstones and synthetic stones, either of transparent, translucent or opaque appearance. These specimens had long been used for gemological education purposes. With the basic gemological information attached to each specimen, they are quite suitable for measurement of gemological properties. Gemstones with a wide variety of inclusions are also displayed. This area also includes different types of master stones, various portable/handheld gem testing devices and books, and is designed so that visitors can browse and understand easily.

Planning of future research

In addition to the three sections mentioned above, storage shelves are installed in the museum and thousands of rough gemstones (such as ruby, sapphire, emerald, spinel, alexandrite, chrysoberyl, peridot, aquamarine, and Paraiba tourmaline) and hundreds of minerals and rocks collected from primary and the secondary gem deposits all over the world are stored, separated by country.

The historical collection created by Prof. Chikayama is of great importance and is expected to be used for studies about country-of-origin determination of gems. To begin with, we will gather data from these specimens using advanced scientific analyses (such as inclusion identification, spectral analyses using FTIR, UV-Vis, Raman or Photoluminescence, quantitative analysis for chemical composition, trace element analysis and isotope analysis) and add to our current database, and we will start expanding the education project with our collaborative research partners.

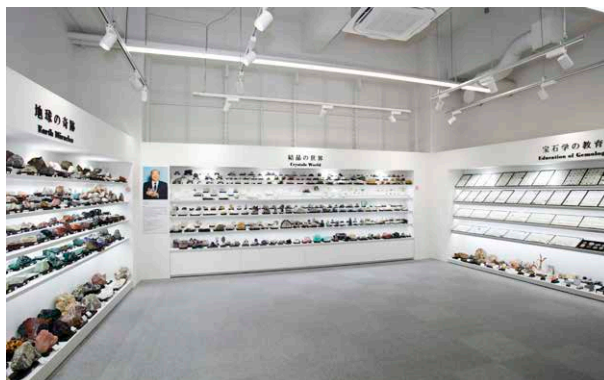


Figure 3: More than 30,000 of rough gemstones, crystals, minerals, rocks, fossils and meteorites from all over the world are displaying in the newly opened “The Chikayama's Collection, GSTV Gem Museum” from May of 2022.



Figure 4: Collection of various lower grade gemstones and minerals in a wooden and steel box stock separated by their country origin

References:

- Chikayama A., 1969-78. Gemmology. Monthly journal, in Japanese. No.1-98.
- Chikayama A., 1973. Gem Identification by their inclusions, in Japanese, pp. 246.
- Chikayama A., 1979-91. The Gemmological Review. Monthly journal, in Japanese, No.1-12 for per year.
- Chikayama A., 1982. Gemstones – their beauty & science, in Japanese, pp. 263.
- Chikayama A., 2005. The wonder of minerals & gemstones, in Japanese, pp. 218.
- Chikayama A., 2013. Dictionary of gemstones & jewelry, 1st edition, translated by Stephen H. Gill, pp. 652.

Study of a historical Alexandrite from Paris school of mines collection

Stefanos Karamelas^{1*}, Eloïse Gaillou², Ugo Hennebois¹, Farida Maouche²,
Annabelle Herreweghe¹, Bérengère Meslin Sainte Beuve¹, Didier Nectoux², Aurélien Delaunay¹

¹ LFG (Laboratoire Français de Gemmologie), 30 rue de la Victoire, 75009, Paris, France

² Mines Paris – PSL, PSL Research University, Musée de Minéralogie, 60 boulevard Saint-Michel, 75006 Paris, France
s.karamelas@lfg.paris

Keywords: historical alexandrite, non-destructive analysis, geographic origin determination

Rare are the scientific studies on exceptional gemstones belonging to museum collections. This investigation is part of an ongoing project, on the study of historic gems, of the Mineralogy Museum of Mines Paris - PSL in partnership with the French Gemological Laboratory (LFG) on a 42.54 ct alexandrite (Fig. 1). This exceptional gem was kept in the

vault since its donation to the museum in 1882 but will be exhibited later this year as part of a temporary exhibit at the Mineralogy Museum. It was exhibited at the World Fair in Paris in 1878 by its lapidary and owner, M. Henri Garreaud, who eventually donated it to the museum four years later; no provenance was indicated at the time of the donation.

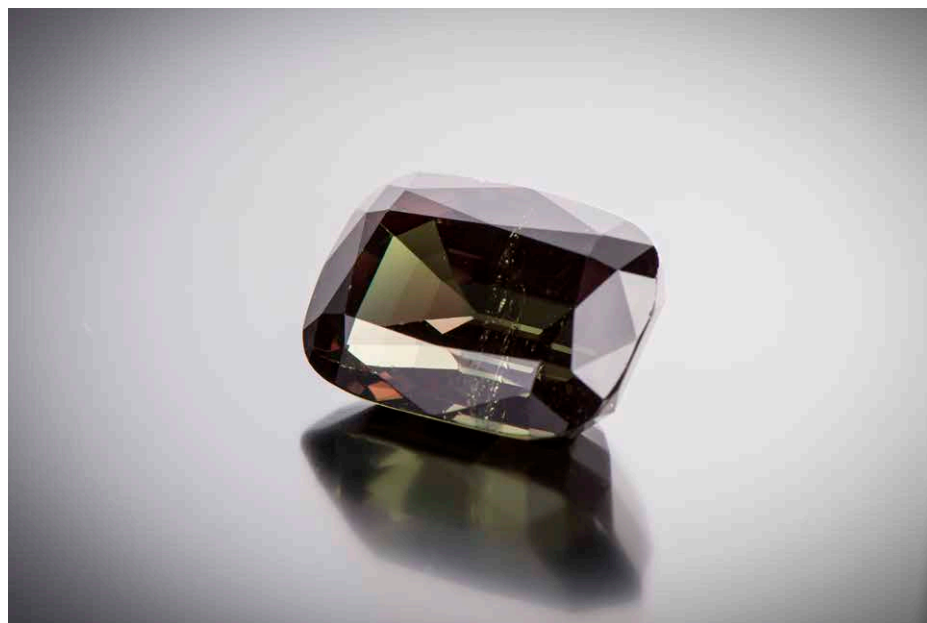


Figure 1: The 42.54 carat – alexandrite was donated in 1882 by M. Henri Garreaud to the Mineralogy Museum of Mines Paris – PSL (ENSMP 69873). Copyright: Musée de Minéralogie Mines Paris - PSL / Andreas Stanger.

The classical gem characterization (using refractometer, specific gravity kit, a 3 Watt SW- and LW-UV lamps) was conducted at the Mineralogy Museum. The microscopic, chemical and spectroscopic analyses were done the LFG in Paris over a single day, the stone having to find its way back to the museum on the same evening. Raman and PL spectra were carried out using a mobile Raman spectrometer with a 532 nm excitation wavelength and a Raman spectrometer with a microscope with a 514 nm excitation wavelength, UV-Vis-NIR spectra were acquired from 365 to 1000 nm using a mobile instrument with an integrating sphere, FTIR spectra from 400 to 8000 cm^{-1} in transmission mode, using a beam condenser and EDXRF using a set of parameters (combining various filters and voltage) to optimize the analysis.

The gem has a cushion shape, sized 23.15 x 15.95 x 12.31 mm, with specific gravity of 3.72, refractive index 1.74-1.75 and inert under UV lamps. It presented strong pleochroism and the colour changes from brownish green under daylight to purplish red under incandescent light. Under microscope a twin plane (confirmed under polarizing filter) at the center of the stone was observed along with short needles,

some geometric polyphase inclusions and some irregularly shaped crystals (one identified with micro-Raman spectroscopy as assemblage of carbonates). About 0.95 wt % of iron and 900 ppmw of gallium were measured with EDXRF. The combination of the above mentioned inclusions and chemical results acquired on the historical alexandrite is consistent with those mined in Sri Lanka (Gunawardene et al., 1986; Sun et al., 2019).

It has been believed that alexandrites from Sri Lanka entered in the market at the beginning of 1920s and in the 19th century these gems were coming from Russia (Sun et al., 2019). However, references can be found that alexandrites from Sri Lanka were in the market since the last quarter of 19th century on at least (Schmetzer, 2010).

References:

- RGunawardene, M., Rupasinghe, M.S., 1986. The Elahera gem field in centra Sri Lanka. *Gems & Gemology*, 22(2), 80-95.
- Schmetzer, K., 2010. *Russian Alexandrites*. Schweizerbart Science Publishers, Stuttgart, Germany, 141 pp.
- Sun, Z., Palke, A.C., Muyal, J., DeGhionno, D., McClure S.F. 2019. Geographic origin determination of alexandrite. *Gems & Gemology*, 55(4), 80-95.

Snapshot of rubies from 1915

Stephen Kennedy¹, Mary Montagu-Scott², Susan Tomkins³

¹ The Gem & Pearl Laboratory Ltd, Unit 23, Arundel House,
43 Kirby Street, London EC1N 8TE; info@thegemlab.co.uk

² Director of Buckler's Hard Village & Maritime Museum, New Forest, SO42 7XB

³ Archivist of the Beaulieu Estate and Buckler's Hard, New Forest, SO42 7XB,



Figure 1: SS Persia © Buckler's Hard – Beaulieu Enterprises Ltd



Figure 2: Buckler's Hard Village © Buckler's Hard – Beaulieu Enterprises Ltd

Keywords: Beaulieu, SS Persia, Natural ruby, Verneuil

In 2008 the Honourable Mary Montagu Scott oversaw the opening of a permanent exhibition at Buckler's Hard Maritime Museum on the Beaulieu Estate about the steamship SS Persia (Figure 1).

SS Persia, owned by Peninsular & Oriental (P&O) Steam Navigation Company, left Tilbury, London on the 18th December 1915, sailing via Gibraltar, Marseille, and Malta and heading for Alexandria and the Suez Canal on its way to India. On the 30th December 1915 it was torpedoed by a German U-boat south-east of Crete. The torpedo caused an explosion in the steam boiler, which meant it sank quickly. Only four lifeboats launched. Of the 500-507 people on board 156 were rescued by HMS Mallow and 11 by SS Ning Chow (Wren, 2020).

Deep Tek Ltd, run by Alec and Moya Crawford located the wreck in 2001 at a depth of 2800 metres and in 2003 they set about salvaging the contents of the ship's strong room. They designed equipment including a fibre hoist rope with their patented winding drum and also a heavily engineered grab doubling as a cutting tool. The salvage exercise in itself enhanced Deep Tek's commercial reputation but an added motivation was the rumour that the strong room

contained gold and silver bars, Egyptian coins and precious gemstones belonging to Maharajah Sir Jagatjit Singh of Kapurthala. The bullion room was situated five decks down through 11mm steel plate and 60mm concrete. Many personal artefacts were recovered, and on the last grab of their charter period brought up gemstones – over 300 natural and synthetic rubies, as well as 44 moonstones, five amethysts, and one garnet. No other sign of the Maharajah's 'treasure' was found.

It is known that the Maharajah and his wife and most of his entourage did not join the ship at Marseille as planned. His wife travelled on a Dutch ship instead. However, members of his staff did travel on SS Persia, which allowed the rumours to persist that treasures might still be onboard.

Deep Tek Ltd wished to find a home for all the artefacts they had recovered. John Douglas-Scott-Montagu, 2nd Baron Montagu of Beaulieu had boarded SS Persia in Marseille with his private secretary Eleanor Velasco Thornton (at some stage she modelled for the sculptor Charles Sykes and is believed to be the inspiration for Sykes' Spirit of Ecstasy bonnet ornament for Rolls-Royce cars). Baron Montagu was returning to India after lobbying Par-

liament and the House of Lords on behalf of the Viceroy of India, Lord Hardinge, to provide vehicles and airplanes for the Indian Army. Baron Montagu survived the sinking, in part due to wearing a Gieve inflatable waistcoat. Eleanor Thornton did not survive.

The Beaulieu estate, centred around the village of Beaulieu, is situated to the west of Southampton on the south coast of England. On the estate is Palace House, home of the Montagu family, a Motor Museum and Buckler's Hard. The latter (Figure 2) was a shipbuilding village, where from 1744 until 1814 the carcasses of wooden naval ships were built on launchways sloping down into the Beaulieu River. They were then towed to Portsmouth to be fully fitted out. The facilities were once again used in the Second World War but it was the 19th/20th Century past-times of tourism and sailing that revitalised the village in the area (Buckler's Hard catalogue). The personal connections of the Montagu family and the existing Museum of Maritime History, which was opened in 1963, provided a logical destination for the artefacts and gemstones, and for the telling of the SS Persia's story.

The first author visited the Museum on several occasions and his interest was particularly piqued by the synthetic rubies, but also on the origins of the natural rubies recovered.

All of us when identifying synthetic rubies wonder if inclusions of tight curved lines and heavy clouds of bubbles are examples of early synthetics (Figure 3). This year the first author was kindly offered the chance to re-examine the rubies recovered. I say re-examined since after the recovery of all the gemstones in 2003 they were tested by Alan Hodgkinson and Brian Jackson, well known Scottish gemmologists, towards the provision of a valuation prepared by Adrian Smith for Moya Crawford of Deep Tek Ltd.

The aim of the examination by the first author was to confirm the limited number of countries from which natural rubies were sourced at the time. With regard to the synthetic rubies can we learn anything about early historical production?

The red gemstones were tested by hand spectroscope, ultra-violet light and microscope. The screening under short-wave ultraviolet light allowed a quick separation of iron-rich rubies from iron-poor and chromium-rich natural rubies and synthetic rubies. The rubies inert to SW UV were checked with a hand spectroscope - one was found to be a garnet.

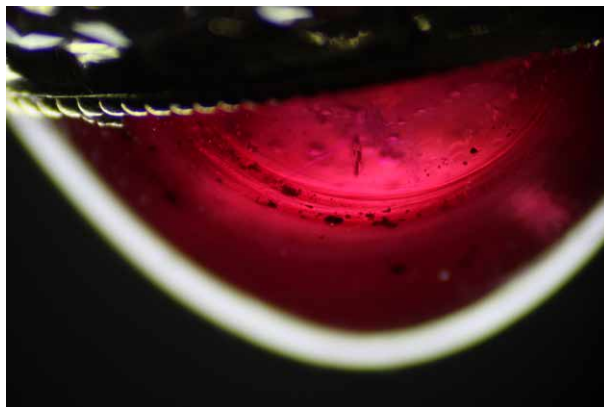


Figure 3: Curved swaths in a synthetic ruby cabochon set on a ring submitted to the Lab

Weight ranges (ct)	Number of synthetic rubies (162 total)	Weight ranges (ct)	Number of natural rubies (166 total)
0.02 – 0.3	68	0.04 – 0.1	43
0.3 – 0.5	41	0.1 – 0.2	63
0.5 – 1	30	0.2 – 0.3	30
1 – 2	18	0.3 – 0.5	23
2 – 3	5	0.5 – 1	7

Table 1: Weights and numbers of natural and synthetic rubies

All the natural rubies were small in size (Table 1). Those inert under SW UV were likely to be of a magmatic origin. Some were quite clean but many showed inclusions of laths (boehmite crystallisation along overlapping twin planes), feathers, and poached eggs (feather/fingerprint surrounds to crystals/negative crystals), which accords with those expected in Siam or Thai rubies, which was historically the main source at the time for these types of rubies. The brighter SW & LW UV fluorescing natural rubies displayed needle silk clusters, crystals and roiling typical for a Burma origin. Some pinker stones could be interpreted as being of Sri Lankan origin. This superficial study seems to confirm Thailand, Burma and Sri Lanka as known origins for ruby and pink sapphire at that time.

Turning to the synthetic rubies, a consideration of early history is needed. Auguste Victor Louis Verneuil worked at the Paris Natural History Museum under the directorship of Edmund Frémy (Evans, 2020). The Geneva rubies and Frémy's experiments were superseded in 1891 by Verneuil's approach of dropping powdered feed down the central tube of the blow pipe. This was revealed retrospectively in two sealed memoirs at the Academy of Sciences from 1904 and 1910. It is stated that Verneuil could produce boules of 6mm diameter in a period of two hours (Evans, 2020, p 40). It would seem that between 1904 to 1910 some commercial production takes place – maybe to take advantage of the situation before his techniques were published. No clear figures are obtainable.

An unattributed quote (<https://www.youtube.com/watch?v=cDH3upLgc7A>) mentions 1000kg production of boules in 1907 and rising to 3200kg in 1912. In the same quote by 1910 there is an estimate of 30 furnaces being operated. By 1914 Hrand Djevahirdjian had started his factory in Monthey Switzerland, but had experimented himself before this as he watched the synthesizers in Paris. Instinctively one feels that Djeva synthetic rubies would have needed more time for commercial quantities to be dissipated into the trade channels of the time and hence Verneuil is the likeliest commercial manufacturer. Verneuil noted that there were fewer bubbles by slowing the growth process but more curved striations occurred when the growth was speeded up.

The larger five synthetic rubies all showed bubble inclusions. Were larger stones rarely clean of bubbles at that time? In the smaller stones 0.02 – 0.50 ct few were inclusion free. The interesting ones showed tightly curved bubble clouds following the growth structures covering most of the stone areas, typical of stones cut from small boules. Unusual in such small stones were the circular growth patterns, indicating it had been cut across the centre of the flame fusion boule (Figure 3). Early on Verneuil discovered that splitting the boules lengthways released the tension build up within its structure and forestalled random fracturing. It seems fair that the circular growth lines are an indication of smaller early boules, where splitting was not carried out. The presence of cracks in many of the synthetics reflects that the issue of random fracturing was still being addressed. The fact that the majority of the synthetics are small in size, possibly reflects the prevailing need to recover as much as possible from the limited production. Many

stones show curved swathes of growth structure rather than the more common less discernible tightly formed growth lines resembling the grooves on a vinyl record, which we mainly see today. Does this point towards a manufacturer battling against fast growth times?

In the absence of historical records these synthetics do provide us with an indication that the structures reflect smaller sizes and coarser growth. Earlier finds and in similar large numbers would be of interest towards building a better picture.

The recovery of the synthetic rubies provides their provenance but only as the result of a tragic episode of war. The loss of life has been remembered firstly by a memorial at sea in 1966 and then another in 2016 at the Buckler's Hard Maritime Museum, marked by a permanent wall-mounted sundial. Descendants of SS Persia passengers and other visitors can purchase items of specially designed synthetic ruby mounted jewellery as a memento – proceeds going to charity.

We conclude on the question of ownership of the gemstones. It is not known to whom they belonged. Understandably the rumours associated with the Maharajah of Kapurthala means he is strong candidate for being the owner. Is it more likely that he would have had items of mounted jewellery amongst his belongings as well as loose gemstones? Any number of people may have been taking the gemstones for mounting to India. Then of course the gemstones may have simply been contained in an item of mail bound for India.

References:

- Buckler's Hard. Published by Beaulieu Enterprises Limited, www.bucklershard.co.uk
- Evans, James, 2020. The History of Synthetic Ruby. ISBN 978-1-91616-52-0-5
- Wren, Alan, 2020. The Ambush of SS Persia (Voices from a Lost Liner) ISBN 978-1-8380408-0-2 (Paperback)

Quartz crystals from alpine fissures: their formation and the historical significance of alpine quartz as raw material for objets d'art

Michael F. Hügi

Swiss Gemmological Society, Bern, Switzerland
michael.huegi@gemmologie.ch

Quartz in alpine fissures

The central Alps, especially the central granite massifs (Aar Massif, Gotthard Massif, Mont Blanc Massif) in Switzerland and adjacent France are known since ancient times for their rich deposits of mainly rock crystal and smoky quartz. The formation of quartz and other minerals took place in extensional fissures (clefs), which were formed by tectonic processes during the Alpine orogeny resulting from the collision of the African plate with the European plate. (Gnos et al. 2021). This orogeny caused regional stress, strain and faulting in rocks during the peak of Alpine metamorphism about 20 million years ago. Quartz crystal formation occurred in granitic rock units located at about 13 to 18 km depth at that time at pressures between 0.3 to 0.45 GPa and temperatures of 450 to 550 °C (Mullis 1996). The tectonic stress led to the formation of fissures in the rock (clefs), which could form caverns up to several meters in size depending on the lithologies. Especially the southern margin of the Aar Massif in Switzerland was strongly tectonically affected, and most important historical quartz discoveries in the Swiss Alps are restricted to this area. These caverns (large clefs) were filled by hydrothermal fluids of metamorphic origin, which due to their supercritical state were able to dissolve locally minerals (mainly quartz) from the surrounding rocks. Due to the mountain-building processes of the Alps, which are still ongoing today, the buried rock formations were slowly uplifted and by this experienced a continuous decrease in pressure and temperature. This led to a supersaturation of the dissolved substances in the hydrothermal solutions circulating in these fissures and to the crystallization of mainly quartz crystals (Fig. 1). This growth process lasted for about 5 to 7 million years until the temperature in the fissures dropped to about 200 °C and the growth of quartz stopped. The P-T ratios prevailing

during formation as well as the chemistry of the hydrothermal solution in the fissures determined the habit of the quartz crystals, so that an approximate regional assignment of alpine quartz crystals is possible (Gnos et al. 2021).



Fig. 1: Rock crystal (approx. 20 cm length) with pink fluorite, in-situ situation in an unexploited and protected crystal cavity in the access tunnel to the Gersteneegg power plant, Grimsel region, Switzerland

Due to the low cooling rate of the rocks by the slow uplift of the Alps, the formation of alpine quartz crystals took much longer compared to the formation of quartz in pegmatites. The rate of cooling of pegmatite bodies was controlled primarily by the temperature difference from the adjacent rock into which the pegmatitic magma intruded. Calculations indicated that quartz and other typical pegmatite minerals could form large crystals in druses in pegmatites within a few days to weeks in extreme cases (Webber et al. 1999 and Phelps et al. 2020).

The importance of alpine quartz in history

Alpine quartz was already used in prehistoric times as cutting tools due to its hardness and sharp chipping. The Roman natural scientist Pliny the Elder (AD 23-79) reports that already in his time rock crystals were specifically searched for in the Alps. Since that time, but especially starting from the Middle Ages, alpine rock crystals and smoky quartz were primarily used as raw material for objets d'art with a religious context (e.g. monstrances, reliquaries) and for ornamental objects (Fig. 2). The latter served less as objects of daily use, but rather as symbol of status due to the limited availability of the raw material in sufficient quality and size, as well as the great craftsmanship and artistic effort required to carve such an objet d'art from quartz. Consequently, only mighty rulers could afford them because of their high value which was far above that of fine arts (e.g. paintings) (Distelberger 2002).

The availability of sufficiently large quartz crystals with good purity for the production of objets d'art is very limited. In the European historic context, it depended very much on finds of large quartz crystals in very large hydrothermal clefts, as they occur primarily in the Aar Massif. Such large clefts with well-formed quartz crystals are found only every few decades to centuries. Historically, the trade of quartz crystals developed into an important economic activity of the mountain population in Switzerland. These quartz crystals were carried along several trade routes to the lapidary workshops, mainly in Milan and Venice (Italy), Prague (Czech Rep.) and in the area of the Upper Rhine, especially Freiburg (Southern Germany). In 1719, a large cavern with exceptional quartz crystals was found in the area of the Grimsel Pass (Aar Massif, Switzerland). This find is a good example to document the economic and cultural importance of this quartz trade in historic times in Europe. The cavern, forgotten for centuries after its excavation, was finally rediscovered only very recently in 2020 (Arlt and Bolliger 2020).

With the development of natural sciences in modern times, quartz from alpine deposits became increasingly important as objects of scientific study and collection, while their use as raw material for works of art decreased.

The presentation also includes the description of the latest discovery of a huge crystal cavern at Planggenstock in the Swiss Alps, which yields rock crystals weighing up to 300 kg as well as pink fluorite in very high (gem) quality. Due to the sufficient availability of material in cutting quality, the historical tradition of producing art works from Alpine quartz has been resumed by the well-known gemstone designers Bernd and Tom Munsteiner (Germany).



Fig. 2: The so-called pyramid, by Dionysio Miseroni, 1653.

This 145 cm tall masterpiece was cut from a single rock crystal, possibly from Switzerland.

Collection Kunsthistorisches Museum, Vienna

Photo: ©KMH-Museumsverband

References:

- Arlt, T., und Bolliger, M., 2020: Die Kristallhöhle von 1719 am Zinggenstock. Mitt. Naturforsch. Ges. Bern NF, 77, pp. 70-89
- Distelberger, R. 2002: Die Kunst des Steinschnitts. Ausstellungskatalog des Kunsthistorischen Museums Wien. 365 pp.
- Gnos, E., Mullis, J., Ricchi, E. et al., 2021: Episodes of fissure formation in the Alps: connecting quartz fluid inclusion, fissure monazite age, and fissure orientation data. Swiss Jour. Geosciences, 114, 14. <https://doi.org/10.1186/s00015-021-00391-9>
- Mullis, J., 1996: P-T-t path of quartz formation in extensional veins of the Central Alps. Schweiz. Min. Petrogr. Mitt., 76, 159–164
- Phelps, P.R., Lee, C.T.A. & Morton, D.M, 2020: Episodes of fast crystal growth in pegmatites. Nature Commun., 11, 4986. <https://doi.org/10.1038/s41467-020-18806-w>
- Webber, K.L., Simmons, Wm B., Falster, A.U., Foord, E.E, 1999: Cooling rates and crystallization dynamics of shallow level pegmatite-aplite dikes, San Diego County, California. American Mineralogist, 84, 708 – 717

Blue shortwave luminescence of gems: the role of titanate groups

Maxence Vigier, Emmanuel Fritsch, Theo Cavignac, Camille Latouche, Stephane Jobic

IMN, Institut des Matériaux de Nantes Jean Rouxel, Centre National de la Recherche Scientifique,
Nantes Université, F-44000 Nantes, France
emmanuel.fritsch@cncrs-imn.fr

The purpose of this study is to describe Blue Shortwave-UV excited Luminescence (BSL) in gems and related materials, and demonstrate the role of titanate groups in a number of gems (Vigier et al., 2023). These titanate groups with the formula $(\text{TiO}_6)^{8-}$ contain a central Ti^{4+} cation surrounded by six oxygen atoms at the corners of an octahedron.

Blue shortwave-UV luminescence is considered unusual in gems, as fluorescence generally is stronger in longwave than shortwave ultraviolet. However, there are well documented cases of BSL in gems, such as for example scheelite and benitoite. In scheelite it is due to the tungstate group of this calcium tungstate (Theisen & al, 1988). In benitoite, it is the titanate group which is the activator and thus respon-

sible for the emission (Gaft & al, 2004). Surprisingly, the reason for BSL of sapphire is still under discussion, i.e. whether it is related to titanium (titanate groups or Ti^{3+}) or color centers (oxygen vacancies). For our study we chose to use sapphire as a reference material, as most articles agree that the well-known sapphire BSL is attributed to titanate groups. To bring further proofs of the role of titanate, theoretical calculations are starting to weigh in on the interpretation. For example in synthetic baddeleyite ZrO_2 , it has been demonstrated through density functional theory (DFT) simulations that BSL is due to titanate groups, and not to Ti^{3+} transitions or oxygen vacancies related defects (Lafargue-Dit-Hauret et al., 2021)



Figure 1: The ten samples investigated for BSL in daylight (top row) and shortwave ultraviolet light (bottom row). Synthetic corundum, benitoite and synthetic spinel are used as reference materials.

We studied in detail the emission of seven minerals and gems displaying BSL, as well as three references in which BSL is caused by titanate groups (TiO_6): benitoite, Ti-doped flame fusion synthetic sapphire and spinel (Figure 1). Emission (under 254 nm shortwave excitation) and excitation spectra were recorded and fluorescence decay times were measured. It is proposed that BSL in beryl (morganite), dumortierite, hydrozincite, pezzotaite, tourmaline (elbaite), some silicates glasses and synthetic opals is due to titanate groups, present at a concentration of 20 ppmw Ti or above. They all share a broad emission with a maximum between 420 and 480 nm (2.95 to 2.58 eV) (thus perceived as blue), and an excitation spectrum peaking in the short-wave range, between 230 and 290 nm (5.39 to 4.27 eV). Furthermore, their luminescence decay time is about 20 microseconds (from 2 to 40). These three parameters are consistent with a titanate emission, and to our knowledge, no other activator.

References

- Lafargue-Dit-Hauret, W., Schira, R., Latouche, C., & Jobic, S. (2021). Theoretical calculations meet experiment to explain the luminescence properties and the presence of defects in *m*-ZrO₂. *Chemistry of Materials*, vol. 33, n° 8, pp. 2984-2992.
- Vigier, M., Fritsch, E., Cavignac, T., Latouche, C., Jobic, S. (2023) Shortwave UV Blue Luminescence of Some Minerals and Gems Due to Titanate Groups. *Minerals*, Vol. 13, pp. 104-121. <https://doi.org/10.3390/min13010104>
- Theisen, A.F., Hemphill, W.R (1988) Effect of the W:Mo ratio on the shift of excitation and emission spectra in the scheelite-powellite series. *American Mineralogist*, vol. 73, no 9-10, p. 1145-1154.
- Gaft, M., Nagli, I., Waychunas, G. (2004) The nature of blue luminescence from natural benitoite BaTiSi₃O₉. *Physics and Chemistry of Minerals*, vol. 31, no 6, p. 365-373.

Causes of color in brown mammoth ivory

Tao Chen, Zhaoying Huang, Duo Wang, Xing Xu

Gemmological Institute, China University of Geosciences, Wuhan, China
chentao@cug.edu.cn

The mammoth species were once the largest terrestrial mammals in the world during the late Pleistocene (approximately 350,000 to 10,000 years ago), inhabiting the northern hemisphere, starting in Europe and extending as far east as North America (Lister & Sher, 2001; Nogués-Bravo et al., 2008). Mammoth ivory has a long history of use in jewelry and artworks because of its beauty and pleasing texture (Saunders et al., 1989; Pitulko et al., 2015). Similar to elephant ivory, mammoth ivory exhibits fascinating colors and patterns and can take on a smoother polish than other organic raw materials. Due to various international

bans on the sale of elephant ivory, mammoth ivory has gradually replaced it as an organic gemstone (Martin, 2006; Yin et al., 2013). To date, gemmological studies of mammoth ivory have focused mainly on the material's composition, the crystallographic characteristics of inorganic minerals within, and the means of separating it from elephant ivory (Qi et al., 2010; Wu et al., 2013; Ngatia et al., 2019; Sun et al., 2022). The surface of mammoth ivory usually has a brown color (Figure 1) but is occasionally blue to dark blue or even black. Research on the causes of this surface color is scarce, however.

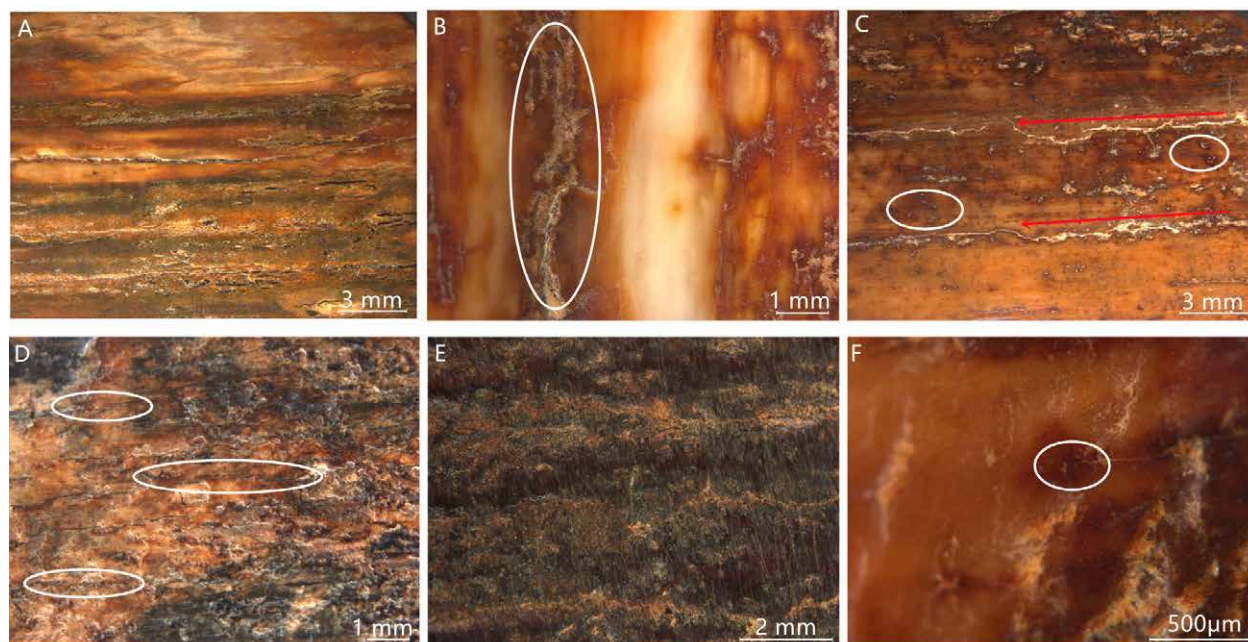


Figure 1. Microscopic images of the surface of mammoth ivory samples. A: Uneven color distribution on the surface. B: Large crack (in the white circle). C: Two parallel cracks consistent with the direction of the blue arrows and tan dots in the white circles. D: Irregular color distribution and darker brown cracks (in the white circle). E: Brown and darker brown interspersed on the surface. F: Tan dots (in the white circle) on the surface.

D: Irregular color distribution and darker brown cracks (in the white circle). E: Brown and darker brown interspersed on the surface. F: Tan dots (in the white circle) on the surface.

In order to investigate the causes of this color, Fourier-transform infrared spectroscopy (FTIR), Powder X-ray diffraction (XRD), and scanning electron microscopy with energy-dispersive X-ray spectroscopy (SEM EDX) were used to study the samples' spectroscopic and mineralogical characteristics, surface morphology, and chemical composition. Brown mammoth ivory is composed mainly of hydroxyapatite, carbonate hydroxyapatite, and collagen (Figure 2). With the dissolution and loss of organic matter and phosphate ions (PO_4^{3-}), fissures and cracks formed. Hematite, pyrite, pyrolusite, and manganite crystallized on the mammoth ivory's surface and concentrated in the cracks of the cementum layer. The phase transformation processes during the burial time promoted the formation of iron oxides, manganese oxides and hydroxides, and iron sulfide, which caused the brown surface color.

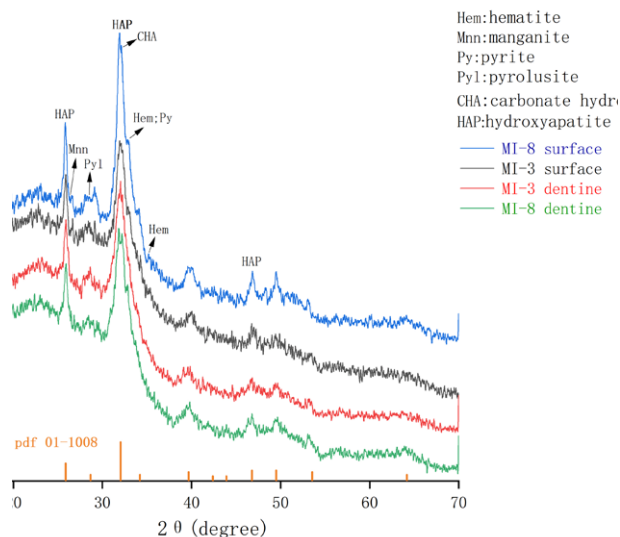


Figure 2. Powder XRD patterns of mammoth ivory samples. Characteristic peaks of hydroxyapatite (ICDD pdf 01-1008), hematite (ICDD pdf 72-0469), manganite (ICDD pdf 74-1631), pyrite (ICDD pdf 71-2219), pyrolusite (ICDD pdf 72-1984), and carbonate hydroxyapatite (ICDD pdf 19-0272) can be distinguished in the XRD pattern.

References:

- Gates-Rector S., Blanton T. 2019. The Powder Diffraction File: A quality materials characterization database. *Powder Diffraction*, 34(4), 352-360.
- Lister A.M., Sher A.V. 2001. The origin and evolution of the woolly mammoth. *Science*, 294, (5544), 1094–1097.
- Martin E. 2006 Are we winning the case for ivory substitutes in China? *Pachyderm*, 40, 89–101.
- Ngatia J.N., Lan T.M., Ma Y., Dinh T.D., Wang, Z., Dahmer T.D., Xu Y.C. 2019. Distinguishing extant elephants ivory from mammoth ivory using a short sequence of cytochrome b gene. *Scientific Reports*, 9, No. 18863,
- Rodríguez J., Hortal J., Batra P., Araújo M.B. 2008. Climate change, humans, and the extinction of the woolly mammoth. *PLoS Biology*, 6(4), 685–692.
- Pitulko V.V., Pavlova E.Y., Nikolskiy P.A. 2015. Mammoth ivory technologies in the Upper Palaeolithic: A case study based on the materials from Yana RHS, Northern Yana-Indighirka lowland, Arctic Siberia. *World Archaeology*, 47(3), 333–389.
- Qi L.J., Zhou Z.Y., Liao G.L., Lin S.S. 2010. Differences on growth microstructure and FTIR absorption spectra between mammoth teeth and ivory. *Journal of Gems and Gemmology*, 12(3), 1–4.
- Saunders J.J., Jr. Haynes C.V., Stanford D., Agogino G.A. 1989. A mammoth-ivory semifabricate from Blackwater Locality No. 1, New Mexico. *American Antiquity*, 55(1), 112–119.
- Sun X., He M., Wu J. 2022. Crystallographic characteristics of inorganic mineral in mammoth ivory and ivory. *Minerals*, 12(2), 117.
- Wu X., Zhang J., Lu X.H. 2013. Study on ivory and mammoth teeth. 2013 China Gems & Jewelry Academic Conference, 143–146.
- Yin Z.W., Zhang P.F., Chen Q.L., Luo, Q.F., Zheng C., Li Y.L. 2013. A comparison of modern and fossil ivories using multiple techniques. *Gems & Gemology*, 49(1), 16–27.

Proposed New Filler Type for Emerald Fracture Filling: Design, Detection, Differentiation, Disclosure

Miro Fei Yeung Ng

Centre for Gemmological Research, Hong Kong & Shenzhen, China
 miro.ng@ctrgemresearch.com

Introduction

Fracture filling is common in gem trading to enhance gemstones' beauty and / or durability. Common textbook examples are (lead) glass filling of rubies and diamonds, polymer/resin type filler impregnation of aquamarine, quartz, tourmaline, opal, turquoise, etc. Undoubtedly, the most common practice will be fracture filling of emeralds (Hänni, 1993) which involves the introduction of filler material to decrease the visibility of surface-reaching fractures so as to enhance the overall apparent clarity. In certain scenarios, the filler may also aid in increasing the stability of emeralds during the cutting process.

Common fillers used in the trade for emeralds can be classified into oils, resins, polymers/prepolymers, and wax (Johnson et al., 1999). These fillers are usually organic in nature. In this work certain new fillers are being proposed. The properties, method of introduction, detection and disclosure (qualitative and quantitative) will be discussed.

The RI matching, volatility and acceptability issue

Traditionally the lower RI Colombian emeralds are better matched with oil-type fillers. However, with the introduction of higher RI emeralds like Pakistani emeralds, resin-type fillers will be a better alternative, (Figure 1). In terms of evaporative stability, resin-type fillers are much more stable than oils thus no “re-oiling” is required after months. However, for end users resins are synonyms for “artificial glues” and consider less acceptable. Therefore, there is a need for a search of “all-round” filler.



Figure 1: Pakistani emerald cabochons before (left) and after fracture filling with Johnson baby oil. Notice the fractures are not well hidden due to the difference in RI between the filler and the emerald.

The ideal filler

- For a filler suitable for commercial manipulation, it should possess the followings:
- RI compatibility: the closer the RI between the filler and the gemstones to be treated, the lesser the fractures visibility. For emeralds, this is origin dependent (Figure 2).
- Stability: fillers should be stable towards light, moisture, temperature and various chemicals. The colour should not change over time. (Bergman, web resource)
- Viscosity: preferably free-flowing during treatment for better penetration but become more viscous and stay inside the fissures.
- Additional optional properties include:
 - Occurrence: end users usually prefer natural over synthetic or artificial substances.
 - Removability: some traders prefer emerald filler to be removed from stones for extra manipulation.

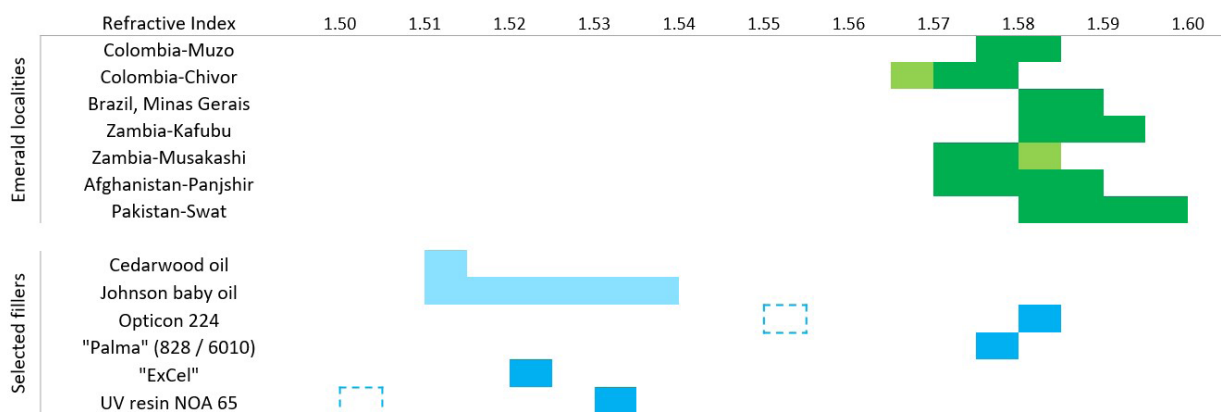


Figure 2: Refractive index ranges of emeralds from commercially available origins and selected common emerald fracture fillers. Oil type (light blue), uncured/unhardened resin (blue dotted) and cured/hardened resins (blue).

New filler type in this work

There are two new directions proposed in this work: 1. Liquid with tuneable RI (TRI) and 2. Inorganic filler (IF).

1. Liquid mixture comprising a “base oil” and a high RI liquid.

In this work different combinations of high RI liquid such as diiodomethane (RI 1.74), bromonaphthalenes (RI 1.64-1.66) is mixed with “base oil” such as baby oil (RI 1.52), paraffin oil (RI 1.44-1.45), Glycerin (RI 1.47), ethylene glycol (RI 1.43). The base oil serves the purpose of: a. adjusting the RI suitable for the emerald of interest, b. provide vis-

cosity, c. provide certain functional groups for subsequent sealing purposes (see below). In this work mixtures with RI range of 1.56-1.61 have been prepared for fitting different emeralds. (Figure 3).

2. Inorganic filler material

In this work sodium silicate solution (RI 1.51-1.52) was used as the first suitable candidate for its low toxicity and availability. Since water tension is an issue for fracture filling, a surfactant such as sodium dodecyl sulfate (SDS) was incorporated into the solution.

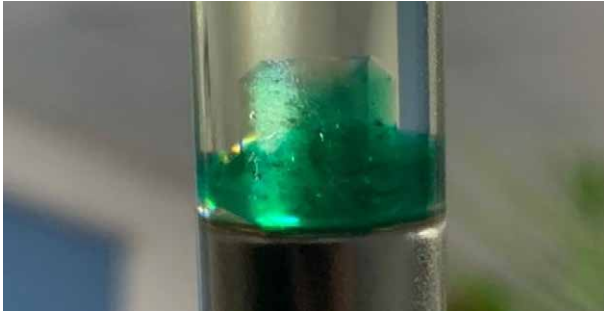


Figure 3: Several Pakistani emeralds with RI 1.595-1.598 (Guo et al., 2020) were immersed under a vacuum in a mixture of liquids attaining a RI of 1.596. Notice the facet edges appear to vanish due to a very close match in RI matching.

The fracture filling process with sealing

As both the aforesaid TRI and IF fillers are susceptible to evaporation, a sealing process is introduced to complete the filling process. In a routine approach, the emeralds follow the reported processes of acid cleaning followed by vacuum pumping. After the introduction of the filler material with or without pressure the filled emeralds are taken out from filler solution and subject to a sealing chemical

reaction. For TRI liquid mixtures with ethylene glycol base oil, attempts have been made by esterification with organic acids (acetic acid, amino acid) of the surface filler to form a solid (Figure 4). For IF attempts have been made by using citric acid or oxalic to produce silica gel as a fracture opening sealer. With this process, the overall filler may be classified as a “composite” filler type.

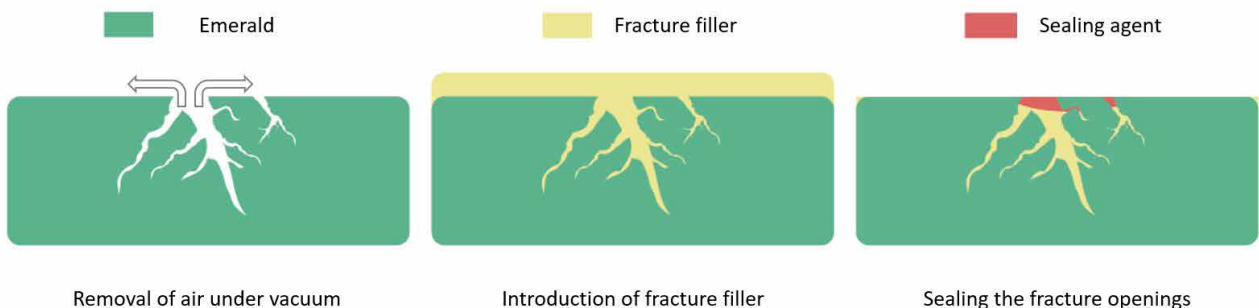


Figure 4: Schematic diagram for the fracture filling process in this work.

Detection of treatment

Detection of TRI filler is straightforward and follows the protocol for normal oil-type fillers: aliphatic C-H stretching related FTIR peaks, colour flashes etc. (Kiefert et al., 1999) For IF, however, only the luster difference at fracture openings is observed with no classic “organic materials’ FTIR peaks nor fluorescence, Careful inspections are required for proper qualitative and quantitative detection of such treatment.

Conclusion

A novel approach using tuneable RI filler and inorganic filler with sealing provides a new way for emerald fracture filling. The process provides a better way to conceal eye-visible fractures for emeralds from different geographic origins while maintaining evaporative stability. This also fulfils certain end consumers’ wish for using non-resin type emerald fillers. However, it is noteworthy that the proposed fillers may not be able to fall into the previous classification in literature. Also, the detection of inorganic filler may require a less straightforward approach and may pose a challenge to certain qualitative and quantitative determinations. Further work has to be done for identifying better filler candidates and to fine-tune optimal reaction parameters.

Remark

The use of IF in emeralds may impose unintended weight to the stones. Further investigations are required to address the issue.

References:

- Bergman, J., Emerald Enhancements: A Consumer and Trade Guide, <https://eighthdimensiongems.com/emerald-enhancements-a-consumer-and-trade-guide>, accessed 1 May 2023
- Guo, H. S., Yu, X. Y., Zheng, Y. Y., Sun, Z. L. and Ng M. F. Y., 2020, Inclusion and Trace Element Characteristics of Emeralds from Swat Valley, Pakistan, *Gems & Gemology*, Fall 2020, Vol. 56, No. 3
- Hänni, H. A., 1993, Filled emeralds: please face reality, *Jewellery News Asia*, June, 76-80
- Johnson, Mary L., Elen, S., Muhlmeister, S., 1999, On the Identification of Various Emerald Filling Substances, *Gems & Gemology*, Summer, 82-107
- Kiefert L., Hanni, H. A., Chalain J-P., Weber W., 1999, Identification of filler substances - in emeralds by infrared and Raman spectroscopy, *The Journal of Gemmology*, 26, 8, 501-20

Fingerprint differences between Emeralds from two main zones of production in Colombia in response to input from their host rock

Garcia-Tolosa Javier^{1,2}, Alvarado Holman¹, Cedeño Carlos Julio¹, Betancourt Camilo^{1,2}

¹ Technological Development center for the Colombian Emerald CDTEC, Bogota, Colombia

² National University of Colombia, Bogota, Colombia

ceo@gemlabcdtec.co jagarciato@unal.edu.co

Keywords: Emeralds, fingerprint, geochemistry, gemology.

Although there is information about techniques to separate Colombian emerald material from that of other countries, not much information is available on how to differentiate Colombian emeralds from the Western Belt (COC), and those from the Eastern Belt (COR). The two main producing zones in Colombia are Muzo and Chivor respectively (Fig.1). The authors try to set a baseline using some tech-

niques to separate emeralds within Colombia, understanding a fingerprint inputted by the rocks that host them.

In the COR, the emerald-bearing veins are hosted in a stratiform brecciated level predominantly composed of gray albitites. Mineralization was controlled by an extensional structural style. In contrast, mineralized veins and breccias in the COC are hosted by organic-rich black shales and were emplaced in a compressional tectonic regime. (Cheilletz et al. 1994; Mantilla et al 2008).

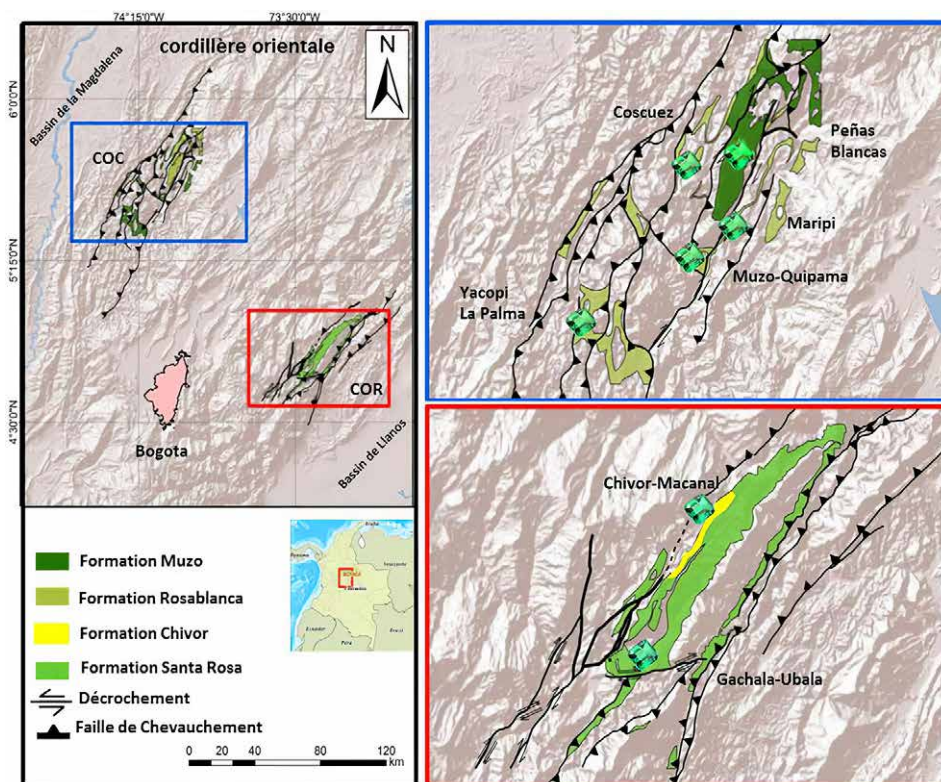


Figure 1: Western (COC) and Eastern (COR) emerald belts of Colombia and the lithostratigraphic units of the host rocks of the deposits. Modified from Terraza et al. (2008) and Reyes et al. (2006).

From the gemmological point of view differences in the fluorescence behaviour, higher for the COR, combined with some other features like chemical aspects (Cr, V, Fe ratios), photoluminescence (R2 and R1 emission).

A total of 694 rough emerald samples were used in this study. Emeralds from COC and COR have, on average, dif-

ferent concentrations of Cr³⁺ therefore their reaction to UV light excitation differs. Emeralds from COR almost always display higher intensities whereas samples from the COC display a wide range of intensities ranging from very high to inert, being the most common reactions those who fall in the lower intensities.

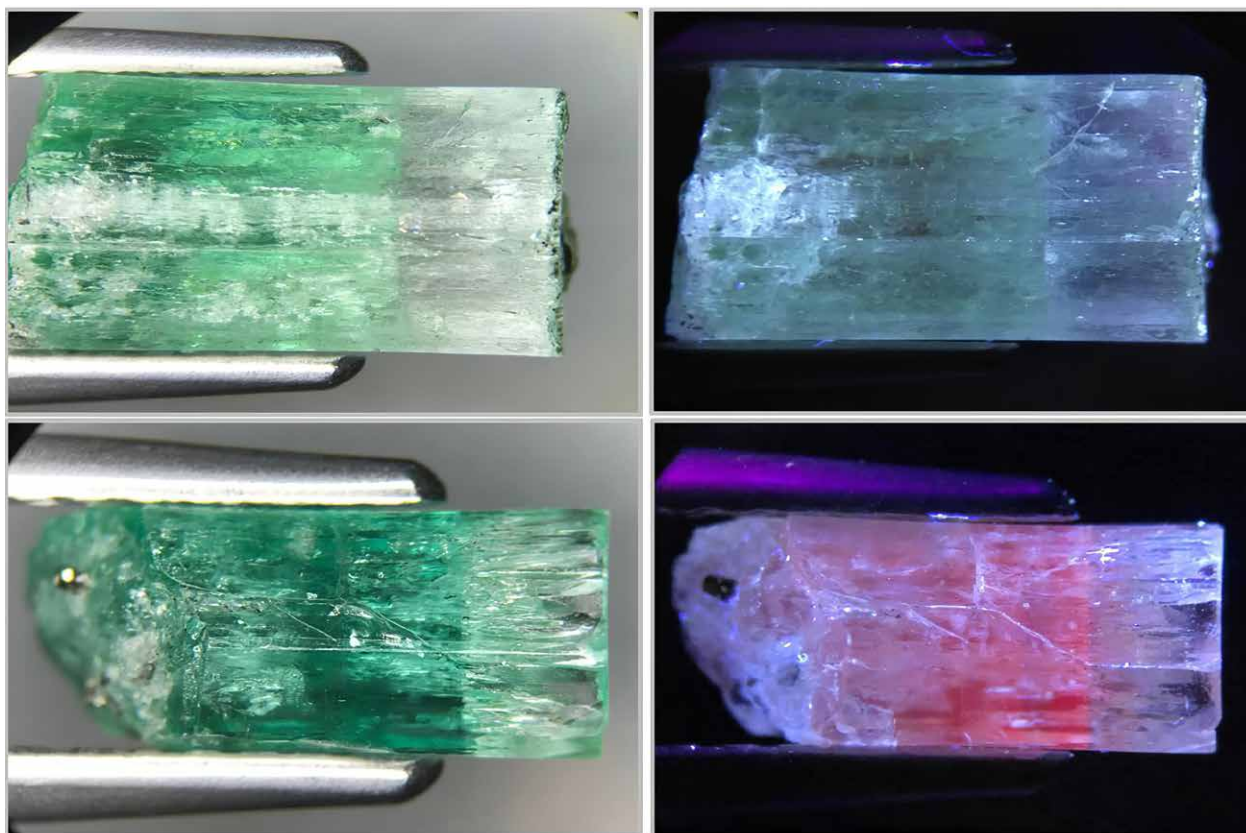


Figure 2: Emeralds in natural light (left) and in UV light (right). A) Sample of the western belt. B) Sample of the eastern belt.

Low Cr-V values (less than 100 ppm per element) are not uncommon in certain localities, especially in the COC, accounting for populations of weakly colored stones. These samples can even display a Fe major than Cr-V behaviour. On the other hand, high concentrations of Cr and V (above

4000 ppm) are typically found in the finest emeralds occurring in the COC. In the COR, highly colored emeralds can contain major than ~4000 ppm of Cr but no more than ~2200 of V. That high Cr/V ratio is responsible for the typical bluish hue displayed by emeralds from the COR.

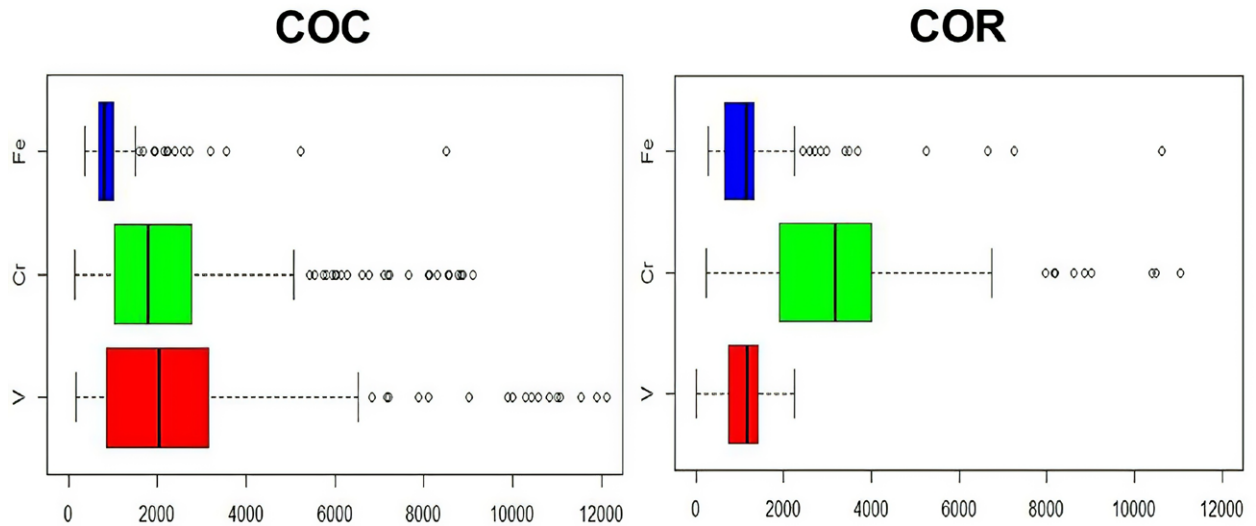


Figure 3: Diagram showing the concentration of chromophore elements of emeralds in the two eastern and western belts (values in ppm).

The average of the position of the R1 and R2 peaks shows ranges that can help to distinguish between the two emerald belts. The CEOR emeralds show an average R1 peak of 683.603nm, those of COC 683.735 nm. Also, the high

intensity of the spectra in the R1 peak in the CEOR emeralds reached almost 15,000 cps contrasts with the COC emeralds are close to 5,000 cps.

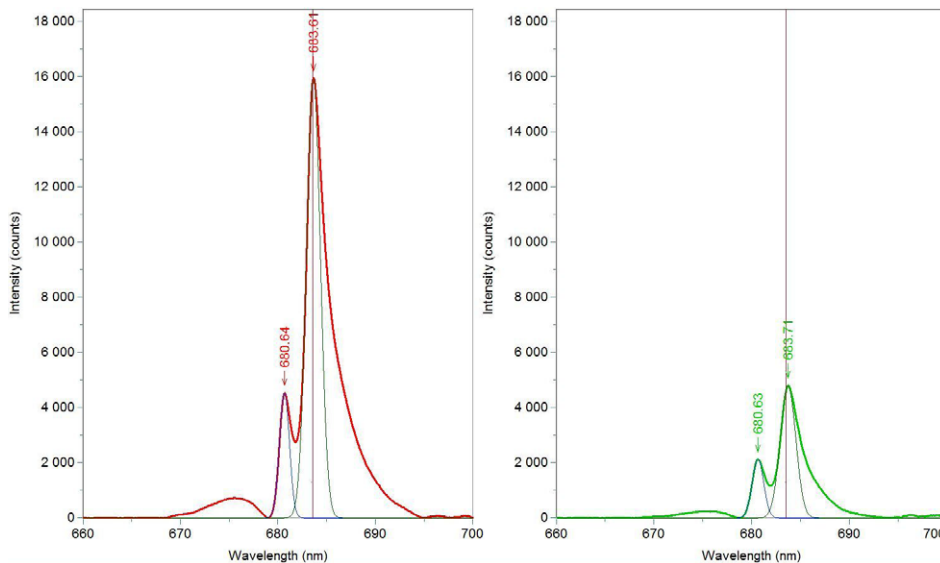


Figure 4: Spectra photoluminescence from the two Colombian emeralds belts, Western emerald belt (left). Eastern emerald belt (right)

It is evident that the geological environment is the main factor controlling the emerald chemistry. In view of the differences between the two emerald belts, the variations and trends in the Cr-V-Fe ratios of emeralds are not unexpected. For instance, in the COC most of the host rocks are organic-rich shales with Cr/V ~0.25 (Campos & Roser, 2007); whereas in the COR, the host rocks are dominated by black shales, evaporitic levels and albitites from the Chivor formation (formerly known as the Guavio limestones) (Terraza et al., 2008). A higher V supply might imply a higher V incorporation in the emeralds from the COC. The occurrence of V-dominated emeralds, associated with organic-rich sedimentary and metasedimentary rocks, have been documented in distinct locations (Lake et al., 2017 and references therein). Thus, indicating that the Cr-V-Fe ratios are rock-controlled and reliant on the lithostratigraphy column of the geologic formations.

References

- Campos, N.O., Roser, B.P. (2007) Geochemistry of black shales from the Lower Cretaceous Paja Formation, Eastern Cordillera, Colombia: Source weathering, provenance, and tectonic setting. *Journal of South American Earth Sciences*, 23(4), pp. 271-289.
- Cheilletz, A., Feraud, G., Giuliani, G., Rodriguez, C.T. (1994) Time-pressure and temperature constraints on the formation of Colombian emeralds: an ⁴⁰Ar/³⁹Ar laser microprobe and fluid inclusion study. *Economic Geology*, 89(2), pp. 361-380.
- Lake, D.J., Groat, L.A., Falck, H., Mulja, T., Cempírek, J., Kontak, D., Marshall, D., Giuliani, G., Fayek, M. (2017). Genesis of Emerald-Bearing Quartz Veins Associated with the Lened W-Skarn Mineralization, Northwest Territories, Canada. *Canadian Mineralogist*, 55(4), pp. 561–593. <https://doi.org/10.3749/canmin.1700025>
- Mantilla, L.C, Arias, S. A., Serrano, J. J., Conde, G. J., Gomez, D. C., Ramirez, J. C.,..., Pena, N. (2007) Investigación petrográfica y geoquímica de las sedimentitas del Cretácico Inferior (K1) y sus manifestaciones hidrotermales asociadas; planchas 169, 170, 189, 190 (cordillera oriental): Ingeominas-UIS, Colombia
- Terraza, R., Montoya, D., Reyes, G., Moreno, G., Fuquen, J. (2008) Geología del cinturón esmeraldífero oriental, planchas 210, 228 y 229 (informe). Bogotá: Ingeominas, Colombia.

Acknowledgements

The authors would like to thank all the organizations and institutions that made this work possible. This research project has received financial support from the National Emerald Fund (FNE) and the agreement of the Ministry of Mines, the professional organizations Aprecol, Asocoesmeral and Acodes, and finally the Colombian Emerald Federation FEDESMERALDAS.

Purple to bluish grey chalcedony from Ethiopia

Lore Kiefert¹, Michael S. Krzemnicki², J. Fiedler³, T. Sintayehu⁴, M. Furuya⁵

¹ Gemmology Consulting, Heidelberg, Germany, info@gemlabhelp.com

² Swiss Gemmological Institute SSEF, Basel, Switzerland

³ DDI German Diamond Institute, Pforzheim, Germany ⁴ Orbit Ltd., Addis Ababa, Ethiopia

⁵ Japan Germany Gemmological Laboratory JGGL, Kofu, Japan

Introduction

In the past 15 years, Ethiopia has repeatedly gained attention for a variety of new gem finds. In 2008, a large deposit of white play-of-colour opal was found (Rondeau et al., 2010), followed by black opal with play-of-colour in 2013 (Kiefert et al., 2014). Both deposits were located in the north of the country near the town of Lalibela. In 2016, high-quality emeralds were recovered from southern Ethiopia (Renfro et al., 2017; Schollenbruch et al., 2017). In the same year, significant deposits of basaltic blue sapphires were discovered in the country's north (Bruce-Lockhart, 2017). Besides these, other gem deposits, such as sunstone, have been discovered in the Afar region in north-Eastern Ethiopia (Kiefert et al., 2019).

In 2019, yet another gemstone deposit was discovered in Ethiopia, this time blue to purple chalcedony partly with an extraordinary saturated colour (Figure 1), which was introduced at the Tucson Gem show in 2022 (see also Furuya, 2022).



Figure 1: Purple to bluish grey chalcedony from Ethiopia. ring submitted to the Lab

The deposit is located approximately 550 km southwest of Addis Ababa in the southwestern part of Ethiopia. The mining site is situated in the area between the provincial towns of Garda Marta, Kamba, and Gerese. The chalcedonies are found either loose as rough fragments and pebbles in sediment or at the flanks of hills.

When the material was introduced in Tucson in 2022, it immediately caught attention by many gem dealers, but questions also arose about colour authenticity and colour stability. We then decided to study the material in detail and performed all the necessary analyses.

Materials and methods

Figure 1 shows the samples collected in Tucson in 2022. Additional samples were acquired at the Tucson Show in February 2023. One of the authors had a dyed chalcedony of unknown origin showing nearly the same colour which was included in this study for comparison.

All samples were studied with the microscope. On two of the samples we performed a colour stability test by wrapping half of the chalcedony in aluminium foil and exposing the stone to LW UV light for 5 hours. Two more samples were placed in sunlight for 3 days. In addition, we analysed selected samples by UV-Vis absorption spectroscopy, infrared spectroscopy (FTIR), Raman spectroscopy, and for chemical data by EDXRF.

Preliminary results and discussion

These new chalcedonies from Ethiopia range in colour from pale blue to saturated purple. As rough fragments, these chalcedonies often show white banding (agate), partly also in globular circles, and often also Fe-rich brownish specks and patches. By careful cutting, it is possible to produce either cabochons of very homogeneous colour (pale blue to deep purple) or polished stones with attractive banded and globular patterns (see Figure 1). Careful examination

of the samples under the microscope revealed a closed surface with no colour concentrations in grooves and cracks. In comparison, the dyed chalcedony of unknown origin showed evident colour concentrations along cracks and grain boundaries. Under high magnification (200-500x), the surface of the purple chalcedony showed a slight granular “orange peel” effect, whereas the bluish grey chalcedony from the same source was perfectly polished and shiny. Inside the purple chalcedony, we observed clouds of tiny dark particles and small spherical orange spots (probably Fe-hydroxide).

The samples that were placed in the UV light as well as the samples that were placed in sunlight did not show any change in colour. This confirmed the colour of the samples to be natural and stable under normal conditions.

UV-Vis spectra of selected samples showed a uniform broad absorption band at about 540 nm for the purple samples, with the height of this band being correlated to the purple colour saturation. In contrast to this, the bluish grey sample was characterized by a broad flat shoulder extending from about 590 nm towards UV, with a small band at about 380 nm. This additional shoulder was not observed in the absorption edge of our purple samples (Figure 2).

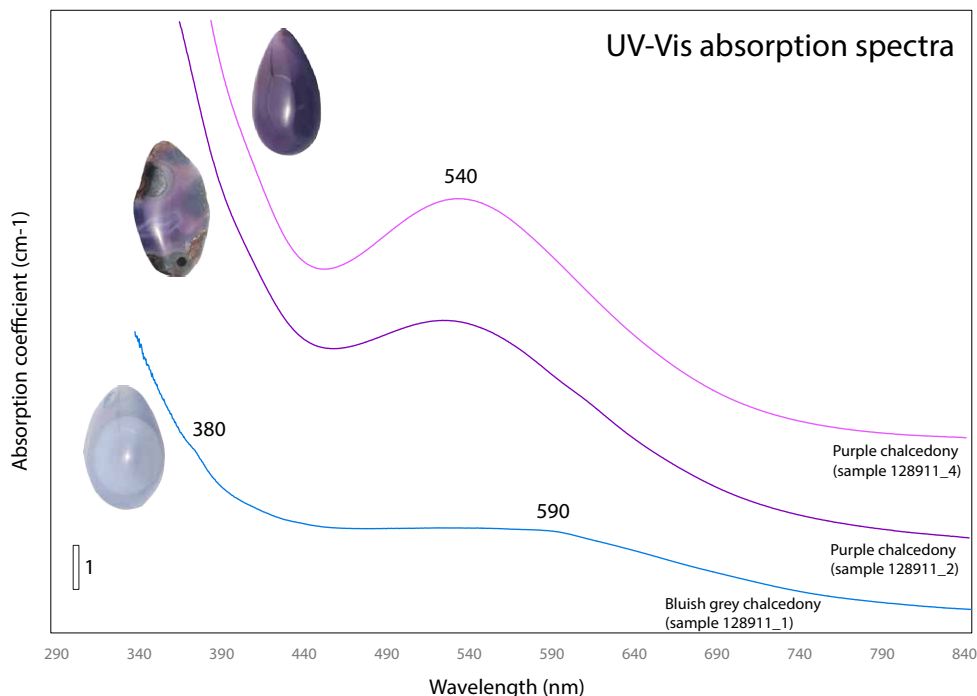


Figure 2: UV-Vis absorption spectra of three selected chalcedony samples of different colour.

The spectra are normalized (absorption coefficient) and stacked vertically for clarity.

Raman analyses reveal that our samples consist mainly of chalcedony, with minor amounts of moganite (main peak at 501 cm⁻¹), a monoclinic silica polymorph commonly associated with chalcedony and chert (Kingma & Hemley,

1994). Interestingly, the bluish grey chalcedony from Ethiopia contains distinctly higher amount of moganite (approx. 30-40%, see Schmidt et al. 2013) than the purple chalcedony from the same deposit (see Figure 3).

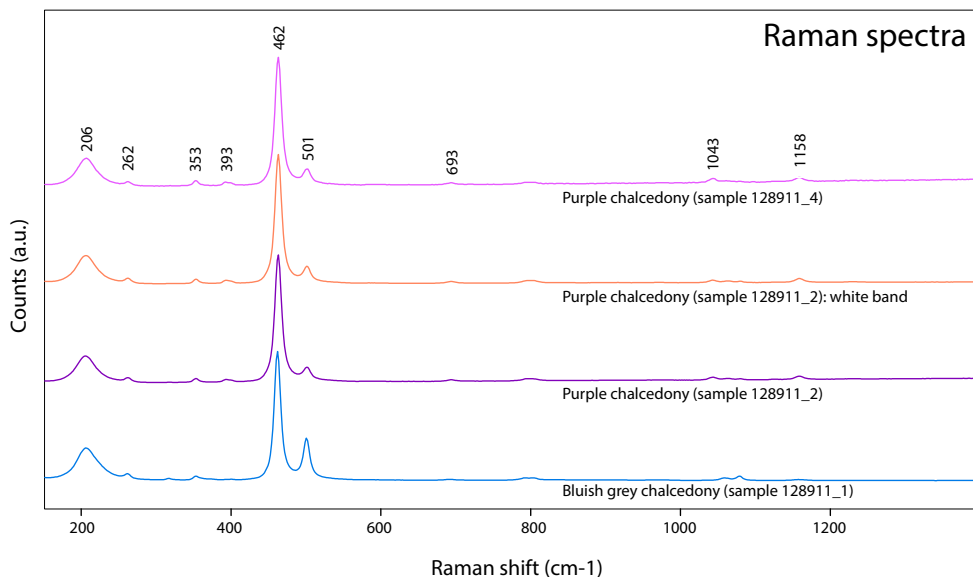


Figure 3: Raman spectra of selected chalcedony samples from Ethiopia. The main peak of moganite (quartz polymorph) is at 501 cm^{-1} Raman shift.

Chemical analyses using EDXRF of a homogenous purple chalcedony showed mainly SiO_2 , with low concentrations of Fe (0.20 wt% Fe_2O_3). Since these chalcedonies occasionally contain small orange inclusions, it is assumed that this iron concentration is representing iron hydroxides rather than substitution for Si in the quartz crystallites of the chalcedony.

Conclusions

Pale bluish grey to saturated purple chalcedony from Ethio-

pia is yet another sign of the wealth of gems in this country. Various tests led to the conclusion that the colour is natural and stable. No specific trace element was found to explain the saturated purple colour in these samples (see also Renfro & Challener 2019). Based on the close similarity of the absorption spectrum of amethyst and our purple chalcedony samples, we assume that the colour is due to natural irradiation and activation of similar colour centres as in amethyst and thus related to iron impurities in their crystal structure (Shigley & Koivula, 1985; Henn & Schultz-Güttler, 2012).

References:

- Bruce-Lockhart, S., 2017. The Forbidden Road to Chila. *Gems & Jewellery*, 26 (3), 10-12.
- Furuya, M., 2022. Purple Chalcedony from Ethiopia. *Japan Germany Gemmological Laboratory Gem Information*, 49, 1-2.
- Henn, U. & Schultz-Güttler, R.A., 2012. Review of some current coloured quartz varieties. *J. Gemm.*, 33 (1-4), 29-43.
- Kiefert, L., Hardy, P., Sintayehu, T., Abate, B. & Woldetinsae, G., 2014. New deposit of black opal from Ethiopia. *Gems & Gemology*, 50 (4), 303-305.
- Kiefert, L., Wang, C., Sintayehu, T. & Link, K., 2019. Sunstone Labradorite-Bytownite from Ethiopia. - *J. Gemm., Gem Notes*, 36 (8), 694-696.
- Kingma, K.J. & Hemley, R.J., 1994. Raman spectroscopic study of microcrystalline silica. *American Mineralogist*, 79, 269-273.
- Renfro, N. & Challener, S., 2019. Native copper inclusions in Indonesian purple chalcedony. *Gems & Gemology*, 55 (1), 111.
- Renfro, N., Sun, Z., Nemeth, M., Verriest, W., Raynaud, V. & Weeramonkhonlert, V., 2017. A new discovery of emeralds from Ethiopia. *Gems & Gemology*, 53 (1), 114-116.
- Rondeau, B., Fritsch, E., Mazzero, F., Gauthier, J.-P., Cenki-Tok, B., Bekele, E. & Gaillou, E., 2010. Play-of-Color Opal from Wegel Tena, Wollo Province, Ethiopia. *Gems & Gemology*, 46 (2), 90-105.
- Schmidt, P., Bellot-Gurlet, L., Léa, V., & Sciau, P., 2013. Moganite detection in silica rocks using Raman and infrared spectroscopy. *European Journal of Mineralogy*, 25 (5), 797-805.
- Schollenbruch, K., Link, K. & Sintayehu, T., 2017. Gem Quality Emeralds from Southern Ethiopia. *InColor*, Issue 35, 48-50.
- Shigley, J.E. & Koivula, J.I., 1985. Amethystine Chalcedony. *Gems & Gemology* 21 (4), 219-223.

Rose Quartz: Journey Into the Nano-Jungle

Karen E. Fox¹, Andrew M. McDonald²

¹ Earth Sciences Museum, University of Waterloo, Waterloo, Canada

² Harquail School of Earth Sciences, Laurentian University, Sudbury, Canada
kefox.ca@gmail.com

Keywords: rose quartz, dumortierite, fibre, fiber, boron, colour, color, stability, fading, nano, asterism

Introduction

Massive rose quartz is a readily available mineral ranging in colour from pink to salmon- or lavender-pink (Figure 1). Given its popularity in the market, it might be assumed that most aspects of its formation and the mechanism producing its colour would be well understood. Nevertheless, as is shown in the following review of prior work by other investigators, outstanding questions remain. These serve to guide our planned further studies into the nature, cause, long-term permanence and geological implications of the rose colour in quartz.



Figure 1: The colour of massive quartz commonly ranges from subtle salmon pink (top left) through blue-tinged pinks to violet-grey (right hand side). Sources: Top left – Brazil; bottom left – Namibia; centre – Quadville, Canada; right – presumed Madagascar. Scale: 1 cm/division. This type of quartz is the focus of the current discussion. Photo: K.E. Fox

Definition of pink-coloured quartz types

Part of the confusion with rose quartz lies in the tendency to apply this name to any pink-coloured quartz, regardless of the cause of colour, crystal habit, or other differences. The most common type is massive rose quartz that displays no external crystal morphology and always shows a turbid translucent to milky transparency. Several investigators found that dissolution of this material in hydrofluoric acid left a fibrous residue that matched the original colour of the samples. Analysis of the fibres using high-resolution transmission electron microscopy and spectroscopic and diffraction techniques subsequently identified the cause of colour in massive rose quartz to be a nano-scale fibrous dumortierite-like material (DLM) (Applin & Hicks, 1987; Goreva et al., 2001; Ma et al., 2002). This rose quartz is the focus of the current discussion. It is distinct from similarly coloured small turbidity-free euhedral crystals that form in more evolved pegmatites, and owes its (unstable) colour to irradiation-induced colour centres associated with phosphorus and Al replacing silicon in the quartz lattice (Maschmeyer & Lehmann, 1983). Hori (2001) has suggested that this latter material should be known simply as “pink quartz”. Additional occurrences of pink-hued quartz owe their colour to inclusions, coatings or other mechanisms.

Colour and the role of fibres of a dumortierite-like material Rose quartz is expected to be pink, but quite pale material still displays a translucency that suggests the presence of inclusions that scatter light. Kunz (1968) recorded localities in Maine that graded in colour from an imperfection-free, opalescent, hyaline-like white to a rich rose colour. Similarly “white rose quartz” is currently offered on the market. Large regions of white quartz, potentially with a different crystallization history, are often intermixed with the rose in the core of a pegmatite, just as white quartz makes up

part of the pieces shown in Figure 2. Reduced colour intensity could indicate any of the following conditions: (1) the quartz contains no, or a very low concentration, of DLM fibres; (2) the fibre size or orientation impacts colour; (3) dense fracturing or a high concentration of microscopic fluid inclusions masks colour; (4) the DLM fibres might be present, but colourless themselves. Dumortierite is commonly blue, but pink, violet and even colourless forms also occur. The colour of dumortierite has been attributed to heteronuclear intervalence charge transfer (IVCT) between Fe^{2+} and Ti^{4+} that substitute for Al in face-sharing octahedral sites in the straight chains of the structure (Platonov, 2000). The possible contribution of an Fe^{2+} to Fe^{3+} IVCT has also been discussed by Alexander et al. (1986). Assuming similarity between the DLM and its namesake, the quartz colour may be dictated by the concentration of Fe and Ti in the DLM fibres.

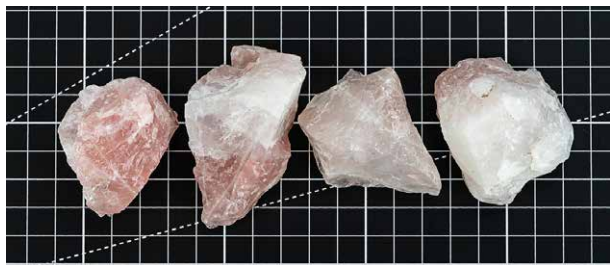


Figure 2: Do the white regions of these specimens from Brazil also enclose dumortierite-like fibres? Scale: 1 cm/division. Photo: K.E. Fox.

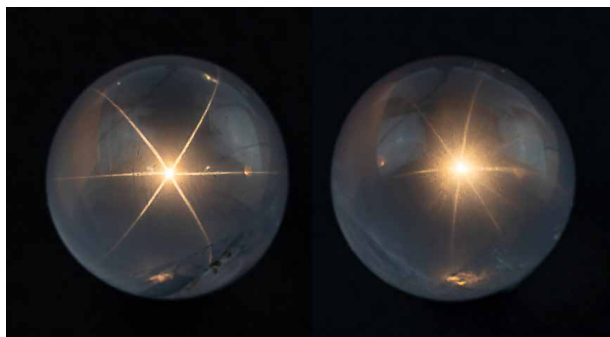


Figure 3: A 1.5 cm diameter sphere showing diasterism with a clear 6-rayed star and a less common multi-arm star. Origin unknown. Photo: K.E. Fox.

Asterism in rose quartz

The reported presence of oriented rutile needles in rose and blue quartz (von Vultée, 1956) has contributed to their acceptance as a cause of colour and asterism. The presence, however, of oriented DLM nano-fibres seems a more probable explanation of the majority of cases, considering that Ma et al. (2002) found no evidence of rutile in any of the 29 samples examined. Asterism is not uncommon in rose quartz, but also not ubiquitous. Diasterism (with illumination from behind) with six-rayed stars or more is most prevalent (Figure 3) while epiasterism is often visible in more opaque spheres. It is interesting to ask why all rose quartz is not asteriated if the DLM fibres are always present. This could simply be the result of inclusions masking the effect, or it could be related to a crystallographically controlled versus random orientation of the DLM fibres, which in turn could be related to the cooling history experienced by a given sample of rose quartz.

Stability of the pink colour in rose quartz

There are conflicting reports as to whether the colour in rose quartz is permanent or prone to fading upon exposure to sunlight or normal ambient heating. Although it is unlikely that an intervalence charge transfer such as that exhibited by dumortierite or blue sapphire will fade, the lore of fading is so oft-repeated that claims should be tracked down where possible, and scientifically evaluated to identify possible alternative mechanisms behind the colour.

Boron and the nature of the dumortierite-like material

Boron is an incompatible element that, along with Li, Be, P, F, water and other species, becomes progressively enriched by fractionation in the melt. Importantly, B can behave as a fluxing agent that modifies the melt structure and depresses the temperature of crystallization. Given the seemingly ubiquitous presence of a B-containing dumortierite-like mineral, it might be expected that crystallization of rose quartz would take place at lower temperatures than for other types of quartz (e.g. milky quartz), implying that its presence could significantly impact the crystallization history of the rocks in which it is found. Furthermore, the fibres themselves bear further inspection to understand why they have developed a superstructure of

regular dumortierite where the a and b parameters are twice the norm. Applin and Hicks (1987) were among the first to isolate these fibres from rose quartz and identify them. They reported similar fibres in a couple of examples of pegmatitic non-rose quartz and suggested that DLM fibres in quartz may be more prevalent than previously thought.

Further investigation

Research is being undertaken that will seek to address: (1) the likelihood that a DLM is present in most, if not all, rose quartz; (2) the mineralogical nature of the specific DLM present (chemistry, crystal structure); (3) whether certain varieties of rose quartz demonstrably fade upon exposure to sunlight; (4) the nature of the exsolution of a DLM as the cause of asterism in rose quartz and (5) the geological impact and significance of rose quartz in select pegmatite systems. It will employ samples obtained from several Canadian and international localities that are well-known for their occurrences of rose quartz.

References:

- Alexander, V.D., Griffen, D.T., Martin, T.J., 1986. Crystal chemistry of some Fe- and Ti-poor dumortierites. *American Mineralogist*, 71, 786 – 794.
- Applin, K.R. and Hicks, B.D., 1987. Fibers of dumortierite in quartz. *American Mineralogist*, 72, 170 – 172.
- Goreva, J.S., Ma, C., Rossman, G.R., 2001. Fibrous nanoinclusions in massive rose quartz: The origin of rose coloration. *American Mineralogist*, 86, 466 – 472.
- Hori, H., 2001. Nomenclature of quartz color variations – pink and rose. *The Mineralogical Record*, 32, 42.
- Kunz, G.F., 1968. *Gems & Precious Stones of North-America*. Dover Publications, Inc., New York, 367 pp.
- Ma, C., Goreva, J.S., Rossman, G.R., 2002. Fibrous nanoinclusions in massive rose quartz: HRTEM and AEM investigations. *American Mineralogist*, 87, 269 – 276.
- Maschmeyer, D. and Lehman, G., 1983. A trapped-hole center causing rose coloration of natural quartz. *Zeitschrift für Kristallographie – Crystalline Materials*, 163(3), 181 – 196.
- Platonov, A.N., Langer, K., Chopin, C., Andrut, M., Taran, M., 2000. Fe²⁺ - Ti⁴⁺ charge-transfer in dumortierite. *European Journal of Mineralogy*, 12, 521 – 528.
- Von Vultée, J., 1956. Die Verwachsungsgesetze der orientierten Einlagerungen von Rutil in Quarz. *Zeitschrift für Kristallographie*, 107(1 – 2), 1 – 17.

Opal stability: a step toward detection

Boris Chauviré¹, Jean-Yves Mevellec², Jacques Ferreire³, Paul. S. Thomas⁴, Emmanuel Fritsch²

¹GeoGems, Guérande, France ; boris.chauvire@geogems.fr

²Institut des Matériaux de Nantes Jean Rouxel, Nantes Université, CNRS, IMN, 44000 Nantes, France

³Centre de Recherche Gemmologique, Nantes, France

School of Civil and Environmental Engineering, University of Technology, Sydney, NSW 2007, Australia

Opal is a gem of captivating beauty that stems from its complex microscopic structure composed mainly of silica. In the most striking specimens, the light diffraction from a three-dimensional mosaic of spheres offers a unique play-of-color pattern, different from one opal to another. Nevertheless, the esteemed status of gem-quality opals is marred by their susceptibility to destabilize. Gem materials are deemed unstable if certain physical properties, notably color, transparency, and cohesion, are prone to altering over time. Opal's instability manifests in two distinct manners: a loss of transparency ("whitening") and the development of fractures (Rondeau et al., 2011). Naturally, the induced changes significantly affect the value of the specimen.

Opal refers to a wide range of natural hydrated varieties of non- to nano-crystalline silica. Occasionally, monodispersed hundred-nanometer-sized particles can arrange themselves into organized patterns, giving rise to the mesmerizing play-of-colors by the diffraction of visible light. Opal may possess a porous framework capable of containing water, either in the form of molecular water (H₂O) or as silanol (SiOH). In a recent study, we compiled over 200 measurements from the literature (Chauviré et al., 2023), and by adding some measurements not included previously (Villie, 2003), we estimate that opal typically contains 7.07±3.28wt% of water (including both molecular water and silanol).

Both whitening and cracking have been described in the literature, and initial empirical studies on opal destabilization point to the crucial influence of drying as a fundamental factor (e.g., Pearson, 1985; Smith, 1988). Whitening is thought to arise from the porosity that scatters light. Chauviré et al. (2023) highlight that cracking in ambient conditions stems from a desiccation mechanism, where capillary pressure induces stress leading to fracture. The pores size is a critical factor in both light scattering and desiccation.

In the last few years, low-temperature infrared spectroscopy has been used to estimate the pore size using the freezing temperature of water (Chauviré and Thomas, 2020; Thomas et al., 2020). It has been established that the freezing temperature varies according to the size of the containing pores (the smaller the pore is, lower the freezing temperature is), and infrared spectroscopy is sensitive to the phase of water (liquid or ice). By monitoring the changes in the hydration bands in opals during low-temperature experiments, we may assess the pore size. We analyzed a set of hydrophane opal (defined as opal that become transparent when plunged in water, and return back to opaque during drying, Figure 1) by low-temperature infrared spectroscopy before and after hydration (respectively opaque and transparent). We observed that most hydrophane opal exhibit almost no freezing water when dry (a regular band shift during the experiment), and a significant amount when hydrated (sudden shift toward higher frequencies when ice melts; Figure 2). The maximum shift rate in analyzed samples was observed between -12 and -16°C. With the calibration established in Thomas et al. (2020), we calculated that hydrophane opal contains pores of 2.5 to 3 nm, consistent with a light scattering. These pores are all connected to each other and to the atmosphere, allowing them to be filled and emptied from the exterior.

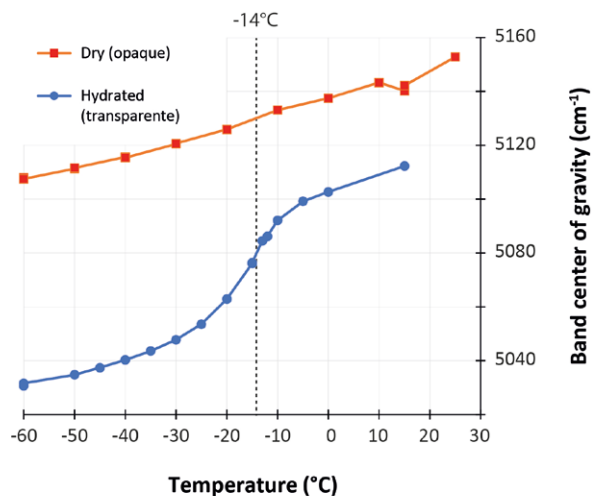


Figure 1 : Position of the center of gravity of the near infrared band of water in opal at low temperature.

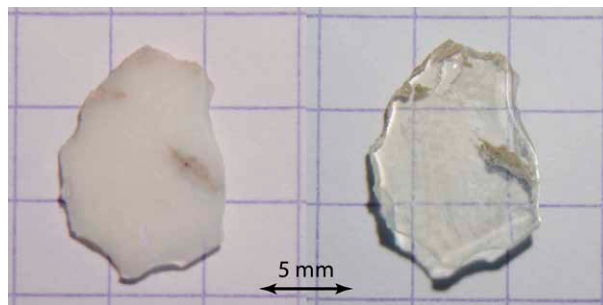


Figure 2 : Example of hydrophane opal before and after hydration

Through the analysis of hydrophane opal, we have estimated the pore size involved in the light scattering causing the whitening. Several parameters must be assessed in order to efficiently model the scattering in opal, but this method could lead to predicting the effect of whitening before the opal is drying. By combining measurements of pore size with the present method and a precise model for both light scattering and capillary pressure, we may be able to develop an analytical procedure to identify unstable opal in the future.

References:

- Aguilar-Reyes, B., 2004. Etude microstructurale des opales : application à la déstabilisation par blanchissement. PhD thesis, Université de Nantes.
- Chauviré, B., Mollé, V., Guichard, F., Rondeau, B., Thomas, P.S., Fritsch, E., 2023. Cracking of Gem Opals. *Minerals* 13, 356.
- Chauviré, B., Thomas, P.S., 2020. DSC of natural opal: insights into the incorporation of crystallisable water in the opal microstructure. *J. Therm. Anal. Calorim.* 140, 2077–2085.
- Jones, J.B., Segnit, E.R., 1971. Nature of Opal Part I : Nomenclature and constituent phases. *J. Geol. Soc. Aust.* 18, 57–68.
- Paris, M., Fritsch, E., Aguilar-Reyes, B., 2007. ¹H, ²⁹Si and ²⁷Al NMR study of the destabilization process of a paracrystalline opal from Mexico. *J. Non. Cryst. Solids* 353, 1650–1656.
- Pearson, G., 1985. Role of Water in Cracking of Opal. *Aust. Gemol.* 15, 435–445.
- Rondeau, B., Fritsch, E., Mazzero, F., Gauthier, J., 2011. Opal – The Craze for Stability. *InColor* 4, 2–5.
- Smith, K.L., 1988. Opals from Opal Butte, Oregon. *Gems Gemol.* 24, 229–236.
- Thomas, P., Chauviré, B., Flower-Donaldson, K., Aldridge, L., Smallwood, A., Liu, B., 2020. FT-NIR and DSC characterisation of water in opal. *Ceram. Int.* 46, 29443–29450.
- Villie, F., 2003. Déstabilisation des opales d’Ethiopie. DUG thesis. Université de Nantes.

Microfeatures of Beryl Group Gems including the Newest Mineral Variety, Johnkoivulaite

Nathan Renfro

Gemological Institute of America, Carlsbad California, USA
nrenfro@gia.edu

Beryl group minerals often provide clues to their pegmatitic origin in the suite of inclusions contained within such gems. They regularly showcase examples of pegmatitic minerals such as albite, muscovite, spessartine, quartz and other minerals that form in those environments or environments where pegmatitic interactions played a role in their formation, such as contact metamorphism with ultramafic rocks which may result in emerald formation (Figure 1) (London, 2008). They also regularly contain complex fluid inclusions, which can result when gems crystallize in fluid rich pegmatites (Figure 2). While the inclusions found in

beryl are generally not diagnostic of a particular origin, they do provide a wonderful view into the types of geologic interactions that are responsible for producing beryl gems. This presentation will focus on a wide cross section of unique inclusions seen in beryl gems from a number of deposits.

Recently a new gem mineral was added to the beryl group. A cesium, boron and magnesium rich beryl from Mogok, Myanmar, Johnkoivulaite was named after gemologist John Koivula (Palke et al, 2021). The inclusions in the type specimen of Johnkoivulaite were primarily etch tubes with limonitic epigenetic residue (Figure 3).

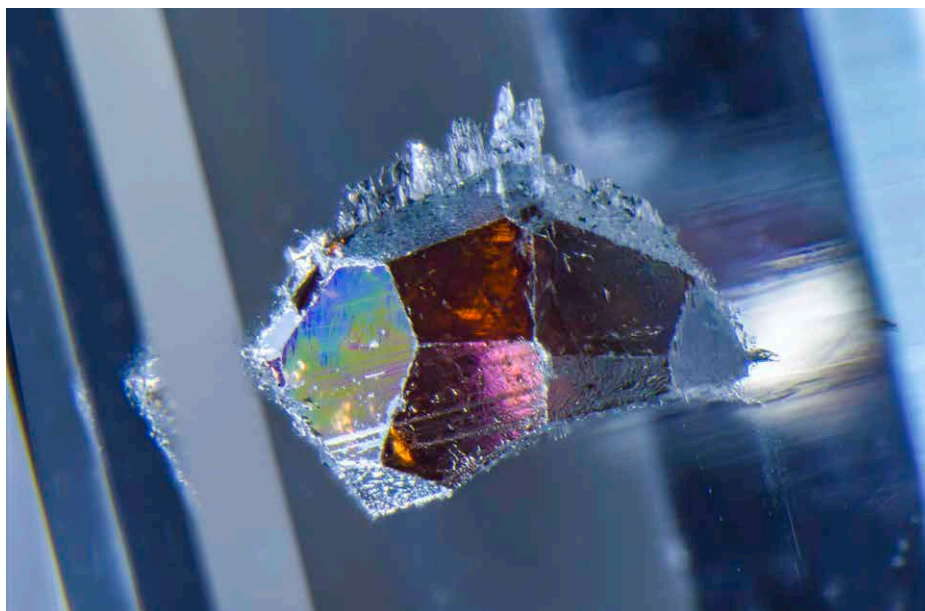


Figure 1: This aquamarine from Pakistan contains a beautiful spessartine garnet. Both minerals provide clues to their pegmatitic origin. Field of View: 5.63mm Stone Courtesy of the John Koivula Inclusion Collection.

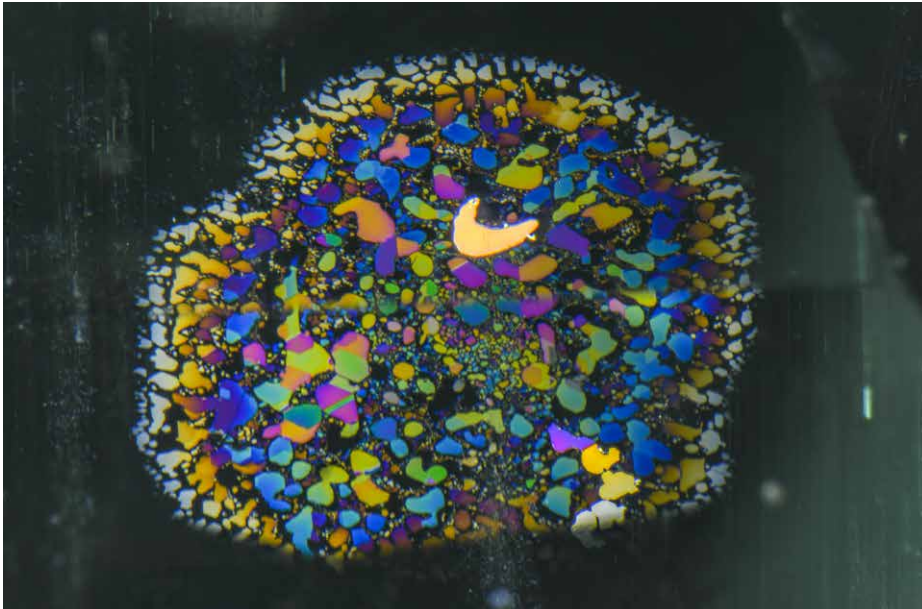


Figure 2: This iridescent thin film fluid inclusions in this beryl provides proof of fluids present in the growth environment. These fluid inclusions are trapped along the basal plan of the beryl and often have a hexagonal shape consistent with crystallographic alignment of the host beryl. Field of view j5.63mm. Stone Courtesy of the John Koivula Inclusion Collection.

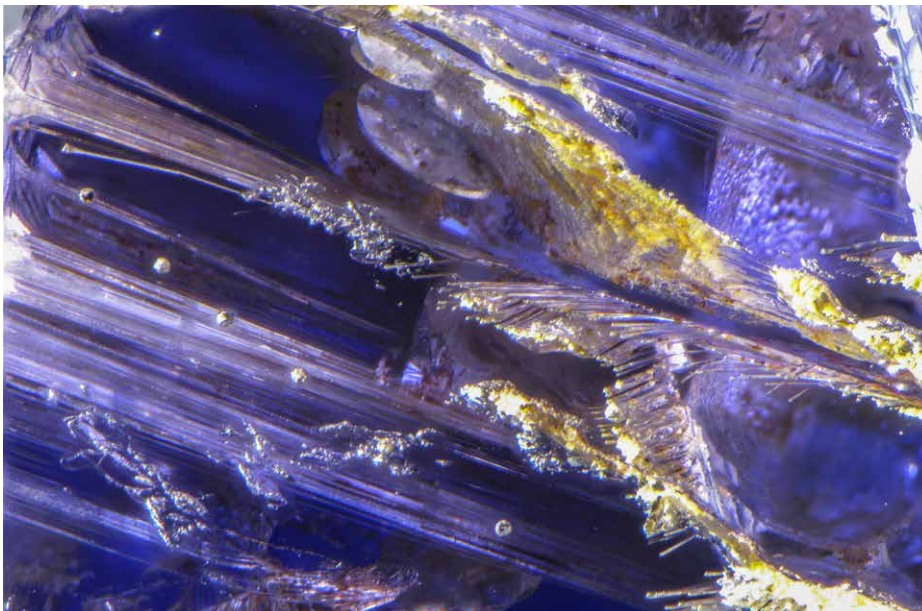


Figure 3: Etch tubes were present in the type specimen of johnkoivulaite, a new Cesium, Boron and Magnesium rich mineral variety of the beryl group. Field of view 4.01mm

References:

- London, D. 2008. Pegmatites. Mineralogical Association of Canada, 347pp.
- Palke, A. C., Henling, L. M., Ma, C., Rossman, G. R., Sun, Z., Renfro, N., Kampf, A.R., Thu, Kyaw., Myo, Nay.,

Weeramonkhonlert, V. 2021. Johnkoivulaite, Cs (Be₂B) Mg₂Si₆O₁₈, a new mineral of the beryl group from the gem deposits of Mogok, Myanmar. *American Mineralogist: Journal of Earth and Planetary Materials*, 106(11), 1844-1851.

New yellow to grey-brown opals from Australia

Gagan Choudhary

IIGJ-Research & Laboratories Centre, Jaipur, India;
gagan.choudhary@iigjrlc.org

Keywords: opal, Australia, properties

Introduction

With the mining activity for over 170 years (Hsu et al., 2015), Australia has been a premium source for precious opal in white to black body colours with vibrant ‘play-of-colour’ effect. In early 2023 Mr. Sharad Garg of Sevenstones Gemfields Private Limited, Jaipur, India showed us a few specimens of transparent to translucent specimens of opal ranging in colours from near colourless to greyish brown and brownish grey. According to Mr. Garg these opals are a new discovery in Australia and he himself is involved in mining activities with local miner in Australia. In the author’s experience, such opals were not seen earlier at the laboratory, although, colourless to near-colourless ‘hyalite’ opal do exist in the trade along with crystal opal. However, these new varieties of opals were distinct from the existing hyalite opal. Mr. Garg also informed that these opals are not yet released in the trade and is planning to release only when significant supply is ensured.

According to Mr. Garg, these new opals are recovered from opal fields around Lightning Ridge in New South Wales, Australia (The exact mine location was not revealed); this region is known for producing exceptional qualities of precious black opal (Hsu et al., 2015). He further informed us that the tunnel for mining was originally dug up in search of black opals, however, this new type yellow to grey-brown opals were discovered after cleaning the nodules. Like any other black or crystal opal in this area, these yellow to greyish brown-brownish grey opals are found in seams between sandstone layers.

Results and Discussion

Visual appearance

13 faceted samples were selected from a larger packet for study. They weighed from 0.05 to 5.80 ct. These new opal specimens ranged in colour from near colourless to light

yellow to brownish-grey and greyish brown (Figure 1); some samples displayed brown-yellow patchy, banded, or zonal colouration. Grey to brown samples as well as the brown/grey areas in colour zoned/banded samples appeared translucent while yellow to near colourless areas appeared transparent with good polish quality. Play-of-colour was missing in the majority of samples under standard room lighting, however, brown to grey samples displayed a weak play-of-colour when illuminated with strong fibre-optic light (Figure 2). Further, this play-of-colour was visible only in small areas and restricted to grey-brown colour zones. Yellow samples displayed very weak opalescence.

These opals may further be related to precious black opal from Lightning Ridge due to their brown-grey zones or areas and subtle play-of-colour. Purer and deeper body colour and stronger play-of-colour could have qualified these opals as precious black opal.



Figure 1: Range of colours seen in this new yellow to grey-brown opals from Australia. Some of these display a patchy and zonal colouration. Photo by G. Choudhary



Figure 2: Weak play-of-colour effect was visible as small spots confining to grey-brown areas when illuminated with strong fibre-optic light. Photo by G. Choudhary

Property	Description
Colour Range	Near colourless, yellow, brownish grey to greyish brown; yellow body colour: evenly coloured; brownish grey to greyish brown body colours: patchy to banded colouration with yellow and brown/grey areas
Diaphaneity	Transparent to translucent
RI	1.45
SG (hydrostatic)	2.10-2.13
Porosity	None
UV Fluorescence	Yellow samples / areas: Chalky greenish blue (long wave stronger than short wave) Brown / grey samples or areas: Inert
FTIR Spectra	Absorption bands from 5400-4750 cm^{-1} and 4500-4250 cm^{-1} ; complete absorption of wavelengths from 4100-500 cm^{-1}
Raman Spectra	Broad band at $\sim 420 \text{ cm}^{-1}$, associated with type-A opal

Table 1: Properties of yellow-brown-grey opals from Australia

Properties

Gemmological properties of the studied samples of opals are summarized in Table 1.

During hydrostatic specific gravity measurements, none of the opal sample displayed signs of porosity, suggesting that these opals are quite stable. Further, during storage of these samples in standard package in a locker safe for approximately three months, no signs of crazing were observed, again suggesting high stability.

Raman spectroscopy using 532 nm excitation, in the range 200-2000 cm^{-1} displayed a rising signal from 200 to 2000 cm^{-1} , related to fluorescence; in the experience of the author, such Raman spectra are usually seen in type-A opals. Raman spectra collected with 785 nm laser revealed a broad band centred at $\sim 410 \text{ cm}^{-1}$, which suggested type-A opals (e.g., Rondeau et al., 2010).

Microscopic examination

The most important features observed in grey to brown opals was their colour distribution, which appeared to follow a cellular or web-like pattern or flow pattern (Figure 3). Such patterns have been reported earlier in Ethiopian opals (e.g., Johnson et al., 1996; Rondeau et al., 2013). These dark bands or zones of colour appeared cloudy and translucent in fibre optic lighting (Figure 4). Raman spectra of these cloudy areas did not reveal any additional features. Further, these grey-brown zones also displayed subtle play-of-colour effect, which was otherwise missing in transparent yellow areas.

In addition, some scattered dendritic clouds were also present in few samples (Figure 5). Such inclusions are previously seen and reported in many opals including Mexican fire opals (e.g., Gübelin & Koivula, 2005).

Conclusion

These new type of opals from Lightning Ridge, in the colour range from near colourless to yellow to greyish brown and brownish grey, including the banded varieties are an interesting find due to their unusual colours and patterns. Black opals from Lightning Ridge are coloured by black pigment composed of fine-grained sulfides, Ti-oxides, and assorted minor minerals, and their organic matter, which may represent a mixture of fossilised sulfate reducing bacteria (SRB) and their organic food source (Hermann et al., 2019). Detailed chemical study is in progress to determine this elemental correlation. Black opals from Ethiopia also exist in the trade; Raman spectroscopy of black Ethiopian

opals revealed presence of carbon as major colouring agent (Kiefert, et al., 2014), which was absent in these studied opals from Australia. Further, their high durability (no crazing or porosity) makes them an interesting gem for fashion jewellery.

References:

- Gübelin E.J., and Koivula J.I., 2005. Photoatlas of Inclusions in Gemstones, Vol. 2. Opinio Publishers, Basel, Switzerland, 491, 493, 495
- Herrmann J.R., Maas R., Rey P.F. & S. P. Best S.P., 2019. The nature and origin of pigments in black opal from Lightning Ridge, New South Wales, Australia, Australian Journal of Earth Sciences, DOI: 10.1080/08120099.2019.1587643
- Hsu T., Lucas A., and Pardieu V., 2015. Splendor in the Outback: A Visit to Australia's Opal Fields, *Gems & Gemology*, 51(4), 418-427
- Johnson M.L., Kammerling R.C., DeGhionno D.G., and Koivula J.I., 1996. Opal From Shewa Province, Ethiopia, *Gems & Gemology*, 32(2), 112-120
- Kiefert L., Hardy P., Sintayehu T., Abate B., and Woldetinsae G., 2014. Gem News International: New Deposit of Black Opal from Ethiopia, *Gems & Gemology*, 50(4), 303-305
- Rondeau B., Fritsch E., Mazzero F., Gauthier J-P., Cenki-Tok B., Bekele E., and Gaillou E., 2010. Play-Of-Color Opal from Wegel Tena, Wollo Province, Ethiopia, *Gems & Gemology*, 46(2), 90–105
- Rondeau B., Gauthier J-P., Mazzero F., Fritsch E., Bodeur Y., and Chauviré B., 2013. On the Origin of Digit Patterns in Gem Opal, *Gems & Gemology*, 49(3), 138-46

Acknowledgement

Mr. Sharad Garg of Sevenstones Gemfields Private Limited, Jaipur, India for providing information on new deposit and sharing samples for study.

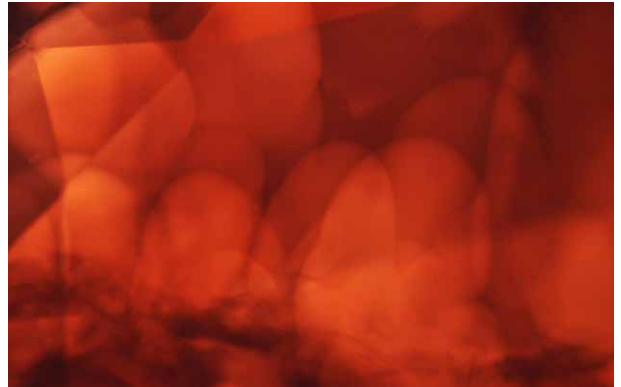


Figure 3: Growth pattern in grey-brown opals appeared as elongated cellular / flow pattern. Photomicrograph by G. Choudhary; image width 5.08mm



Figure 4: Grey-brown zones or areas appeared cloudy and translucent in fibre-optic lighting. Photomicrograph by G. Choudhary; image width 5.08mm

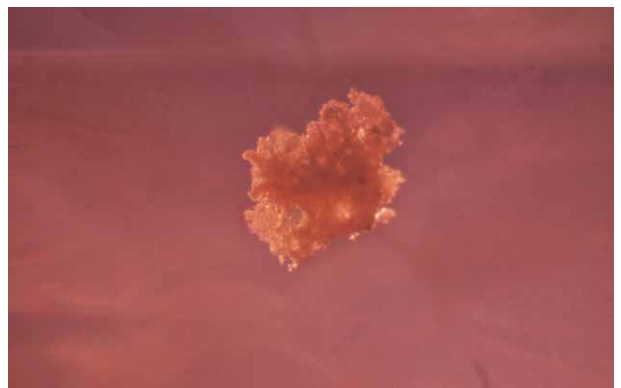


Figure 5: Dendritic clouds or crystals were commonly present in few samples. Exact nature of these inclusions could not be determined by Raman spectroscopy. Photomicrograph by G. Choudhary; image width 5.08mm

A nuummite occurrence from kangerluarsuk in the Maniitsoq Region, West Greenland

Anette Juul-Nielsen, Arent Heilmann

Department of Geology, Ministry of Mineral Resources and Justice,
 Government of Greenland, Imaneq 4, 3900 Nuuk, Greenland
 anjn@nano.gl

Keywords: Nuummite, Iridescent amphibole, gemstone formation, Greenland

K. I. Giesecke was the first to recognize the beauty of the iridescent amphibolitic gemstone Nuummite in 1810 when he collected samples from the island Simiuttat in the Nuuk area, West Greenland (Figure 1), for further investigation (Johnstrup, 1878). The trade name ‘Nuummite’ was introduced in the early 1980s after the rediscovery of the gemstone at eight localities in the Nuuk area (Appel & Jensen, 1987). Nuummite consists mainly of the amphibole minerals anthophyllite $(Mg, Fe^{2+})_7[Si_8O_{22}](OH)_2$ and gedrite $(Mg, Fe^{2+})_5Al_2[Al_2Si_6O_{22}](OH)_2$ with accessory minerals such as cordierite, chalcopyrite and pyrite (Appel & Jensen, 1987). While Simiuttat has been subject to detailed investigations by Rodgers et al. (1996), Champness & Rodgers (2000) and Franz et al. (2018) among others, only limited descriptions of nuummite occurrences occur from other parts of Greenland. We describe a new nuummite occurrence at Kangerluarsuk, East of Maniitsoq (Figure 2), far from the original find. It is compared to the Simiuttat occurrence to better understand the formation of nuummite deposits and the potential of finding new deposits.

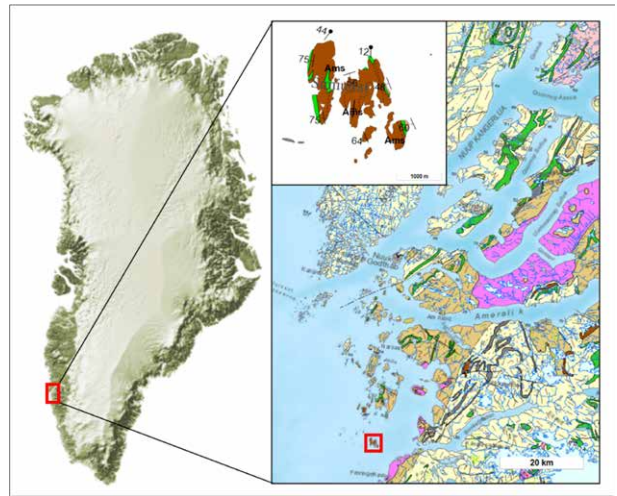


Figure 1: Geological map of Nuup Kangerlua with the location of Simiuttat, 13 km Southeast of Nuuk. Pale yellow: orthogneiss, green: amphibolite, dark brown: supracrustal rocks, light brown: tonalitic to granodioritic gneiss, purple: Qooqut granite, light pink: granodiorite and grey: leucogabbro and anorthosite. (Map modified after Govmin.gl).



Figure 2: Geological map of the Maniitsoq area with the location of Kangerluarsuk, 18 km East of Maniitsoq. See Figure 1 for legend. (Map modified after Govmin.gl).

The nuummite at Kangerluarsuk occurs in a 2 meter wide and 15 meter long lens within a garnet-gneiss ridge with thin garnet-, gedrite- and mica-rich layers (Figure 3). The ridge is open along strike and flanked by gneisses to the West and garnet-gedrite-mica-kyanite-schist and amphibolites to the East. The nuummite consist of anthophyllite, gedrite and minor biotite and pyrite, and the grain size is 0.1-1 cm. It has a brownish gray body colour and is highly weathered. Iridescence is blue and displayed as <1 mm thin elongate iridescent grains. At Simiuttat, the nuummite has grain sizes of 0.1-5 cm resulting in larger iridescent grains compared to Kangerluarsuk. The mineral assemblage of the Simiuttat nuummite is anthophyllite, gedrite, biotite, cordierite, chalcopyrite and pyrite. The nuummite has a dark grey body colour with a weathered rusty surface and golden or blue iridescence (Figure 3). The nuummite was difficult to recognize in the field at the inland locality of Kangerluarsuk. By contrast, iridescent grains of the Simiuttat nuummite were easily recognized in the field at the seashore where the nuummite is polished by nature itself through wave actions (Figure 3). The Simiuttat nuummite has been dated to 2732 ± 10 Ma (zircon) - 2707 ± 12 Ma (monazite) (Rodgers et al., 1996). Calculations made by Franz et al. (2018) suggests formation at low-to-moderate pressures with minimum temperatures of 590-600°C corresponding to upper greenschist to amphibolite facies.

Most of the Greenlandic Archean rocks have been subject to intense ductile deformation resulting in the discontinuation of amphibolitic units, transformed into thin layers, lenses or boudinage structures. This is the case at Simiuttat where the nuummite occur as small centimeter-thick veins and in lenses up to one meter in width within a 3-meter-thick section between a garnet-gneiss and orthogneiss. Similarly, the Kangerluarsuk occurrence is a discontinuous lens. While the nuummite occurrences in the Nuuk area can be traced for several hundred meters, it will need to be investigated whether the Kangerluarsuk nuummite similarly can be traced along strike. Appel & Jensen (1987) suggested that nuummite occurrences in the Nuuk area are related to the Malene Supracrustal Belt, that primarily encompasses amphibolitic rocks and metasediments enclosed by gneiss. However, investigations carried out in the past 30 years by the Government of Greenland and the National Geological Survey of Denmark and Greenland have yet to yield new nuummite occurrences. The authors suggest that this might be due to a focus on ore deposits rather than gemstones in combination with the difficulties of recognizing nuummite in the field. That nuummite occurrences occur as mafic enclaves or bands at the boundary of metasedimentary units and amphibolites in shear zones is a hypothesis that need to be investigated further. This may help locating new nuummite occurrences – a gemstone that is not easily recognized in the field.

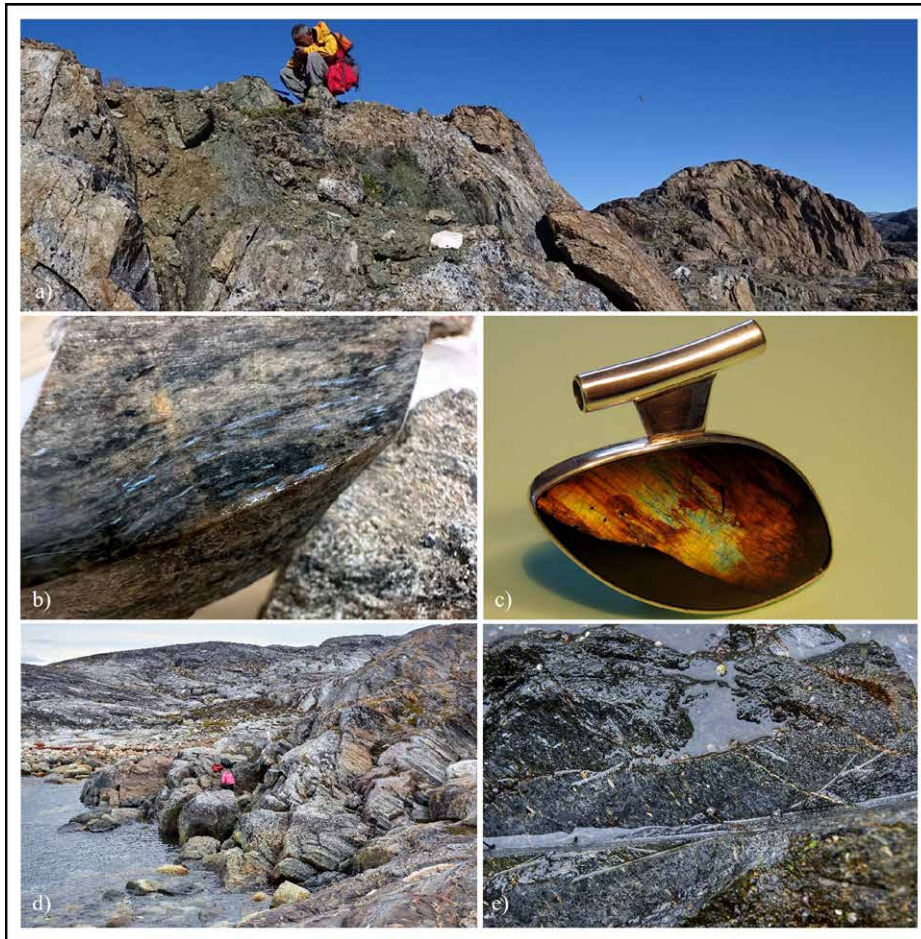


Figure 3. a) Kangerluarsuk ridge; b) Kangerluarsuk nuummite; c) Nuummite pendant from Nuuk, courtesy of P. Møller; d) Simiuttat; e) Simiuttat nuummite. (Photos: MMR/VHDesign).

References:

- Appel, P. W. E. & Jensen, A., 1987. A new gem material from Greenland: iridescent orthoamphibole. *Gems & Gemology*, 23(1), pp. 36-42.
- Champness, P. E. & Rodgers, K. A., 2000. The origin of iridescence in anthophyllite-gedrite from Simiuttat, Nuuk district, southern West Greenland. *Mineralogical Magazine*, 64(5), pp. 885-889.
- Franz, L., Sun, T. T., Wirth, R., de Capitani, C. & Ying, L. H., 2018. Violet-to-Blue 'Nuummite' from Simiuttat, Greenland: Origin of Colour Appearance and Conditions of Formation. *The Journal of Gemmology*, 35(4), pp. 330-338.

- Johnstrup, F., 1878. Gieseckes mineralogiske rejse i Grønland. Bianco Lunos Bogtrykkeri, p. 149.
- Rodgers, K. A., Kinny, P. D., McGregor, V. R., Clark, G. R. & Henderson, G. S., 1996. Iridescent anthophyllite-gedrite from Simiuttat, Nuuk district, southern West Greenland: composition, exsolution, age. *Mineralogical Magazine*, 60, pp. 937-947.

Acknowledgements

The authors thank Clark R. L. Friend for pointing out the approximate location of the Kangerluarsuk nuummite occurrence.

Colour change Paraiba tourmaline from Brazil

Claudio C. Milisenda¹, Stefan Müller¹

¹ DSEF German Gem Lab, Prof.-Schlossmacher-Str. 1, D-55743 Idar-Oberstein
ccm@dgemg.com, s.mueller@dgemg.com

Keywords: Paraiba tourmaline, Brazil, colour change

In just a few decades Paraiba tourmalines have developed into one of the most valuable and sought-after gems in the world. Of particular interest are specimens from the legendary Batalha mine near Sao Jose de Batalha in the Brazilian state Paraiba where these gemstones were first mined. However, fine specimens from Batalha are rare and production in Brazil is sporadic and focused on melée and matrix stones obtained from the overburden.

Peak production with about ninety percent of the tourmalines recovered from the site occurred between 1989 and 1992 (Cook, 1993). Recently a number of Paraiba tourmalines ranging between 0.75 ct and 1.75 ct. were submitted to the DSEF German Gem Lab. According to the owners they were kept on stock and originally purchased in the early 1990ies.

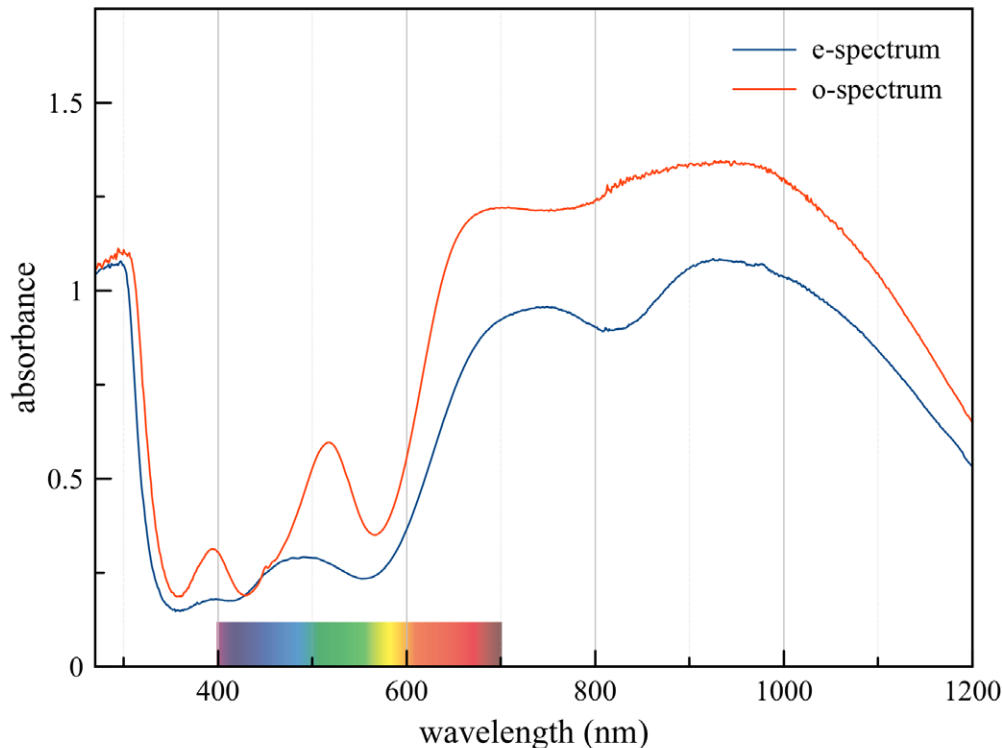
When viewed table up some of these stones showed a colour change from violetish-blue to blue-violet in daylight to a greyish-green-blue to greyish blue-green in incandescent light, respectively. A 0.81 ct. specimen is shown in Figure 1. It measures approx. 7.30 x 5.24 x 3.31 mm and changes from blue-violet to green blue.

Colour change in cuprian elbaite tourmaline has been reported for a small number of samples from Nigeria (Smith et al., 2001) and Mozambique (Wentzell 2004, Wentzell et al. 2005, Laurs et al. 2008). However, to our best knowledge this is the first report on colour change Paraiba tourmalines from Brazil. Chemical analyses were consistent with elbaite tourmaline. The elevated copper concentrations are comparable to those found in Brazilian specimens and the low Ga contents are typical for samples from the Batalha mine. Most cuprian tourmalines from Rio Grande do Norte show higher Ga contents.

Polarized absorption spectra of the sample shown in Figure 1 showed broad absorption bands at around 395 nm, 520 nm as well as at 690 and 910 nm in the o spectrum and at 395 nm, 485 nm and 730 and 940 nm in the e spectrum (Figure 2). The distinct bands at 395 and 520 nm can be attributed to trivalent manganese typically found in unheated Paraiba tourmalines and the two bands in the red and infrared part of the electromagnetic spectrum are due to divalent copper. The absorption band of Mn³⁺ at 520 nm forms two transmission windows, one in the blue-violet and one in the yellow-green part of the visible spectrum, which are responsible for the color change.



Figure 1: Paraiba tourmaline from the Batalha Mine in Paraiba, Brazil with a colour change from day light (left) to incandescent light (right).



The question arises as to why no colour change Paraiba tourmalines from Brazil have been observed so far. The colour of natural coloured, unheated tourmalines is far less attractive than the coveted “neon colors” that made these tourmalines so well known. From the absorption spectra it is obvious that the stones examined are all suitable for heat treatment and therefore it is very likely that in the past most of the stones had been heat treated before they were released on the market.

Figure 2: Polarized absorption spectra of the Paraiba tourmaline shown in Figure 1.

References:

- Cook, B., 2013. The Paraiba promise. Rapaport Magazine 36(10), 130.
- Laurs, B.M. et al, 2008. Copper-bearing (Paraiba-type) tourmaline from Mozambique. *Gems & Gemology* 44(1), 4-30.
- Smith, C.P., Bosshart, G., Schwarz, D., 2001. Nigeria as a new source of copper-manganese-bearing tourmaline. *Gems & Gemology* 37(3), 239-240.
- Wentzell, C., 2004. Copper-bearing color change tourmaline from Mozambique. *Gems & Gemology* 40(3) 250-251.
- Wentzell, C., Fritz, E., Muhlmeister, S., 2005. More on copper-bearing color change tourmaline from Mozambique. *Gems & Gemology* 41(2), 173-175.

Sulfur-based species induced photochromism in sodalite

Seung Kwon Lee^{1,2}, Dongwook Shin²

¹ Wooshin Gemological Institute of Korea, 06022, Seoul, South Korea; sklee1201@hanyang.ac.kr

² Division of Materials Science and Engineering, Hanyang University, 04763, South Korea

Keywords: Hackmanite, Tenebrescence, Photochromism

Sodalite $\text{Na}_4(\text{Al}_3\text{Si}_3\text{O}_{12})\text{Cl}$ is a natural aluminosilicate mineral that contains sulfur or sulfur-related defects, known as chromophores (Reinen et al. 1999; Fleet et al. 2010). Hackmanite, a variety of sodalite, exhibits unusual optical properties such as photoluminescence, tenebrescence, or photochromism upon absorption of UV light, causing a change in color that can be reversed (see Fig. 1) (Williams et al. 2010). Since Kirk's research on the photochromism of sodalite in 1955, the cause of the photochromism of hackmanite has been studied. It has been attributed to a sulfur-related defect and, more recently, an interaction between disulfide ions and chloride vacancies (Kirk 1955, Agamah 2020). However, the exact mechanism is still under investigation (Blumentritt 2021). The objective of this study is to examine the role of sulfur-related defects on the photochromism of hackmanite by investigating the spectroscopic properties of sodalite and hackmanite.

Thirteen stones used in this study were cabochon-cut from Myanmar, comprising eight hackmanites with color ranges of very pale yellow, light gray, and red hues, and five sodalites with blue hues. The stones weighed between 0.45 and 1.67 carats and ranged in transparency from translucent to semi-opaque (see Fig. 2).

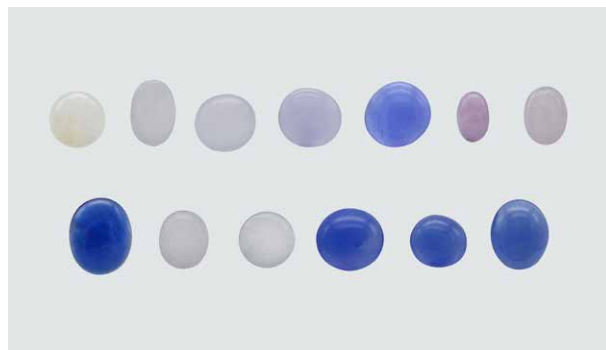


Figure 2: Thirteen samples from Myanmar (cabochons weighing 0.45–1.67 ct) under this study.

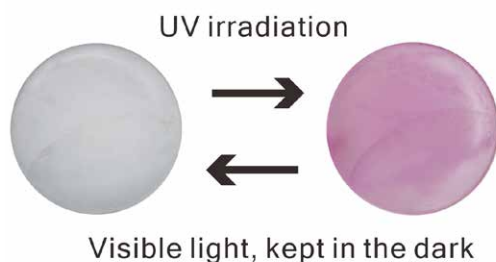


Figure 1: Tenebrescence or reversible photochromism of hackmanite before and after UV (365 nm) irradiation after one hundred seconds.

UV-Vis spectra were obtained using a JASCO UV-Vis spectrometer (V-660, Japan) with a bandwidth of 2 nm. The transmission mode spectrum was measured in the range of 200 to 800 nm at a scan rate of 400 nm per minute. Chemical analyses were performed using Energy-Dispersive X-ray Fluorescence spectroscopy (EDX-8000, Shimadzu, Japan) with an acceleration voltage of 50 kV and a beam current of 1000 μA measured by irradiating the sample using a 1000 μm collimator. Additionally, X-ray photoelectron spectroscopy (XPS) was used to determine the oxidation state of sulfur, using a Nexsa instrument from ThermoFisherScientific.

Table 1 displays the results of the chemical analysis conducted on the 13 stones. The weight percentages of SiO₂ and Al₂O₃, which form the basic framework of both sodalite and hackmanite, were found to be similar, as expected. As per Jackson's definition, hackmanite is identified as a sulfur-bearing sodalite that exhibits fluorescence (Jackson

1997). The photochromism of hackmanite is believed to be associated with the presence of sulfur (Agamah 2020, Carvalho 2018). However, sulfur was detected in all samples at levels lower than approximately 0.4 wt.%, with the highest concentration being found in the sodalite sample. XPS analysis revealed that SO₄²⁻ ions were present in all samples, while mono-/polysulfur species were not detected.

	SiO ₂	Al ₂ O ₃	Na ₂ O	Cl	CaO	SO ₃	K ₂ O	Br	Ga ₂ O ₃	Fe ₂ O ₃
Sodalites	36.253-37.130	32.115-32.623	22.901-24.110	6.442-6.792	0.253-0.789	0.070-0.344	0.128-0.307	0.008-0.024	0.003-0.004	0.004-0.008
Hackmanites	36.317-38.298	32.062-32.867	21.840-24.151	6.247-6.880	0.184-0.551	0.028-0.204	0.144-0.189	0.009-0.015	0.002	0.004-0.008

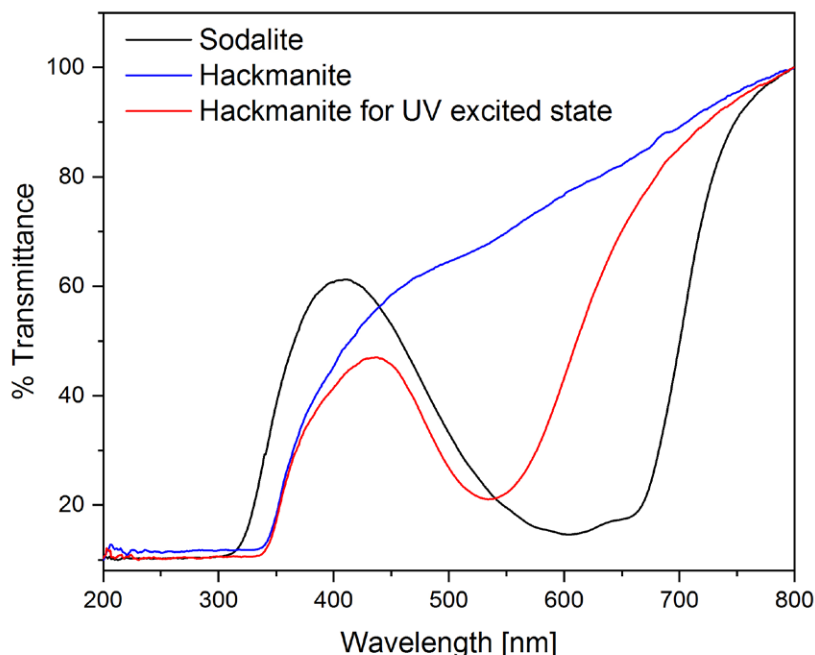


Figure 3: UV-Vis spectra for representative hackmanite show an increase in absorption at ~530 nm for the UV excited state (in red) compared to the desaturated color state (in blue). However, spectrum of representative sodalite shows two broad band absorptions at ~600 nm and 660 nm (in black).

The optical properties of sodalite and hackmanite are clearly shown in the UV-Vis spectra (Fig. 3). In previous studies (Williams et al. 2010; Stoliaroff et al. 2021), the origin of color in hackmanite is that one of electrons of the disulfide ion is captured at a chlorine vacancy and acts as a color center (F-center). Such charge transfer requires energy corresponding to the ultraviolet region (Medved 1953).

A blue spectrum was measured before hackmanite was exposed to UV light, and a red spectrum was measured after exposure (using a Fabel FUV-R2 lamp with a wavelength of 365 nm) in Figure 3. An absorption band due to the chlorine vacancy is observed over a broad range centered at 530 nm. This absorption decreases with time, which can take from minutes to hours depending on the stone, in a dark room or under visible light and returns to the pre-UV irradiation state (as shown in Fig. 2).

The UV-Vis spectrum of blue sodalite (Figure 3) was found to be identical before and after UV irradiation, indicating the absence of photochromism. The blue color of sodalite is known to be caused by tri-sulfur radical ions substituted for the chlorine site, resulting in an absorption band at 595 nm (Reinen et al., 1999). However, in this study, the blue sodalite sample showed a combined spectrum of two absorption bands centered at 600 nm and 660 nm, suggesting the existence of different cage environments containing trisulfide or other types of sulfides.

Based on these measurements, it can be summarized that the manifestation of photochromism is not proportional to the concentration of sulfur and is likely due to the presence of trace sulfur-related defects that meet certain conditions, such as disulfide ions and chloride vacancies.

References:

- Agamah, C., et al., 2020. Hackmanite—The Natural Glow-in-the-Dark Material, *Chemistry of Materials*, 32, 8895-8905.
- Blumentritt, F., Fritsch, E., 2021. Photochromism and Photochromic Gems: A Review and Some New Data (Part 1), *The Journal of Gemmology*, 37(8), 780–800.
- Carvalho, J.M., Norrbo, I., Ando, R.A., Brito, H.F., Fantini, M.C.A. & Lastusaari, M., 2018. Fast, low-cost preparation of hackmanite minerals with reversible photochromic behavior using a microwave-assisted structure conversion method. *Chemical Communications*, 54(53), 7326–7329.
- Fleet, M.E., Liu, X., 2010. X-Ray Absorption Spectroscopy of Ultramarine Pigments: A New Analytical Method for the Polysulfide Radical Anion S₃- Chromophore, *Spectrochimica Acta, Part B*, 65 (1), 75-79.
- Jackson, J., 1997. *Glossary of Geology*, 4th ed., American Geological Institute, Alexandria, VA, 288.
- Kirk, R.D., 1955. The luminescence and tenebrescence of natural and synthetic sodalite, *American Mineralogist*, 40 (1-2), 22-31.
- Kondo, D., Beaton, D., 2009. Hackmanite/Sodalite from Myanmar and Afghanistan, *Gems & gemology*, 45 (1), 38-43.
- Medved, D.B., 1953. The Optical Properties of Natural and Synthetic Hackmanite, *Journal of Chemical Physics*, 21 (7), 1309-1310.
- Reinen, D., Lindner, G.-G., 1999. The nature of the chalcogen colour centres in ultramarine-type solids. *Chemical Society Reviews*, 28 (2), 75-84.
- Stoliaroff, A., Schira, R., Blumentritt, F., Fritsch, E., Jobic, S., Latouche, C., 2021. Point Defects Modeling Explains Multiple Sulfur Species in Sulfur-Doped Na₄(Al₃Si₃O₁₂)Cl Sodalite, *The Journal of Physical Chemistry C*, 125 (30), 16674-16680.
- Williams, E., Simmonds, A., Armstrong, J., Weller, M., 2010. Compositional and structural control of tenebrescence, *Journal of Materials Chemistry*, 20, 10883-10887.

Study and investigation of garnet from Balangir in Odisha, India

Jayshree Panjekar^{1,2} and Aatish Panjekar^{1,2}

¹Pangem Testing Laboratory, Pune, India

²PANGEMTECH – Panjekar Gem Research & Tech Institute, Pune, India

jayshreepanjekar@gmail.com

Keywords: almandine-pyrope garnet, inclusions, spectroscopic analyses, Balangir, Odisha

Introduction

In the present study investigation of almandine-pyrope garnet, found in the Khaliapali village (20.8639° N, 83.4708° E) located in Balangir Tehsil of Balangir district of Odisha state, was carried out. In Khaliapali the area constitutes a part of the Precambrian khondalite-charnockite-granite gneiss in which broken garnet crystals are found. Gemmological properties, values for refractive indices, specific gravity, as well as UV-VIS and FTIR data have been determined. Semi-quantitative analyses carried out using EDXRF show presence of titanium and chromium. Inclusions studies along with Raman spectroscopy identified mineral inclusions as rutile, sillimanite, ilmenite, apatite and zircon.

Materials and methods:

From numerous garnet cabochon pieces polished from the broken garnet crystals, ten garnet specimen with prominent inclusions were selected. Using gemmological methods their optical properties, refractive index, specific gravity, UV fluorescence etc. were determined. In depth study of the internal features was done using gemmological microscopes. Laser Raman Spectroscopy was used to determine the identity of the microscopic inclusions crystallizing near the surface. Non-polarized UV-VIS spectra for all samples were collected using JASCO F660 spectrophotometer over the 350nm - 700nm range. Mid Infrared spectra of 4 samples were collected in transmission mode by JASCO FT/IR-6600 with a resolution of 4cm⁻¹. Semi-quantitative analyses were carried out using EDXRF and electron microprobe.

Results

Visual Appearance:

The garnet cabochons from Khaliapali village of Balangir District of Odisha were found to be transparent and have a combination of purplish red to maroon red color. Balangir garnet appear to be a member of the pyrope-almandine solid solution series, their coloration is due to high Fe content and show presence of various inclusions.

Gemmological Properties:

Specific Gravity was found to be in the range of 3.84 to 3.87, determined by spot method refractive indices fell in the range of 1.77 but most of the specimen had refractive indices above the range of the refractometer. All samples showed no fluorescence under LWUV as well as under SWUV.

Microscopic Observations:

Surface reaching inclusions were identified using laser Raman spectroscopy. Balangir garnet has small elongated crystals of apatite (Figure 1). Black colored crystals of ilmenite and rutile (Figure 2) were observed in many of the specimen. Rutile needles (Figure 3) were found to be prominent in most of the samples and appear to be oriented. In many samples there were crystals of zircon surrounded by haloes (Figure 4). Among the other commonly found inclusions was those of quartz crystals (Figure 5). Fibrous crystals of sillimanite (Figure 6) were seen in four of the specimens.

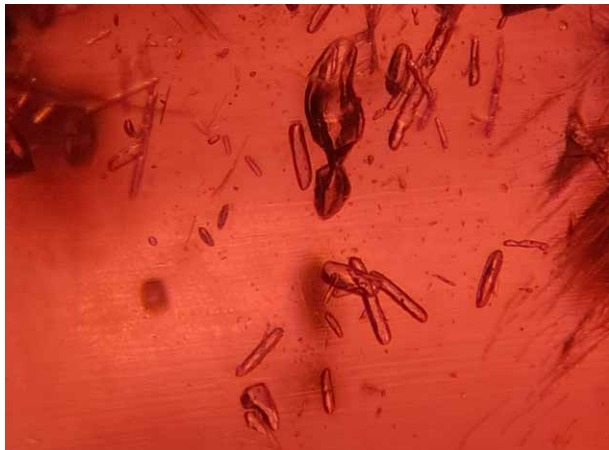


Figure 1: Elongated apatite crystals

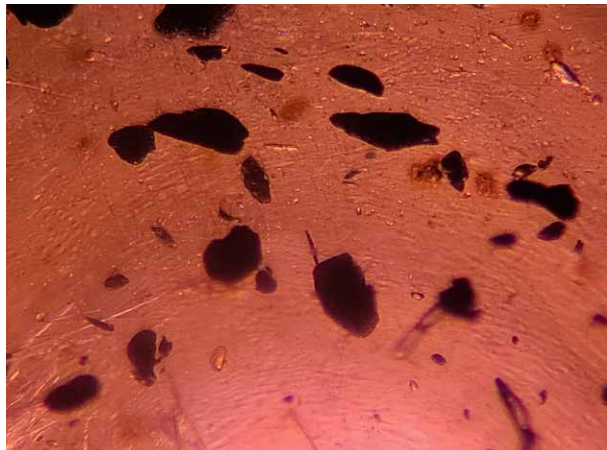


Figure 2: Rutile & ilmenite crystals

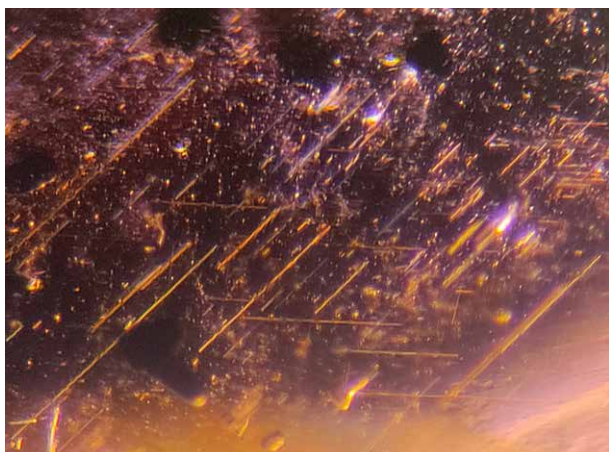


Figure 3: Network of rutile inclusions



Figure 4: Zircon crystal

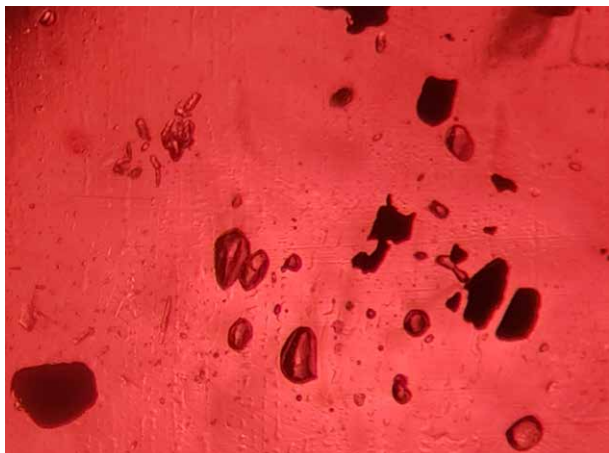


Figure 5: Colourless quartz crystals



Figure 6: Fibrous sillimanite needles

UV-Vis Spectra:

The UV-Vis spectroscopy of Balangir, Odisha garnet revealed the typical almandine pyrope absorption peaks at 505nm, 526nm and 576nm (Figure 7) in the yellow-green region are due to Fe³⁺. In addition, absorption at 369 nm in the purple region, with strong transmission near 655 nm in the red region and a hump near 690nm was observed and this may be the reason why these garnets have a reddish colour. According to Li (2022), this may be attributed to Cr³⁺. In addition to these absorptions and transmissions, the maroon purplish-red garnets also formed narrower but distinct absorptions at 462nm, 427nm, and 401nm in the blue-violet region, particularly in the violet region,

with transmissions near 445 and 385 nm. The purple of the purplish-red garnet is caused by such variation in selective absorption. The colour of a mineral is the result of its selective absorption of visible light, which is often caused by the transitional metal elements contained in the mineral. In this case the additional three absorption lines seen in the spectrum of the purplish red sample at 462nm, 427nm, and 401 nm are due to Mn²⁺, Fe³⁺, and Fe²⁺, respectively. (Stockton & Manson 1985). Whereas Li (2022) attributes these absorption peaks to Mn²⁺ only. The variation in colour shades may be due to the presence of Mn²⁺ in the chemical composition.

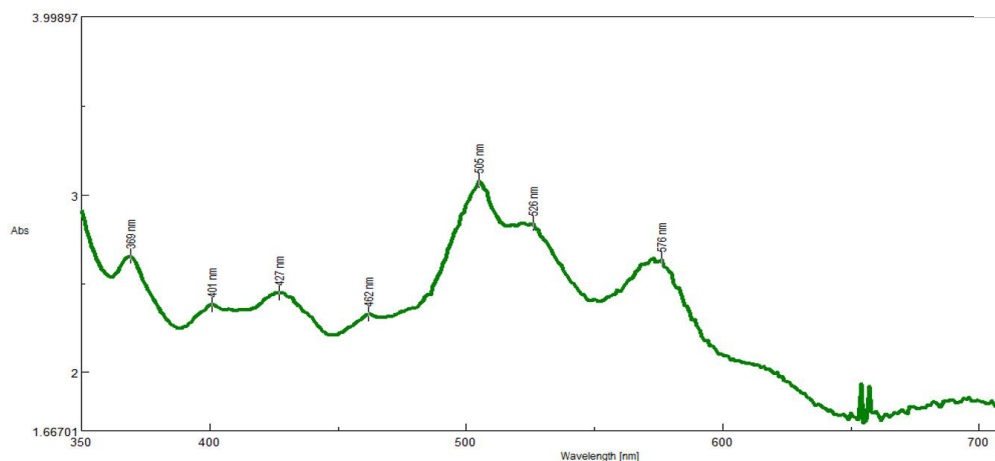


Figure 7: UV-VIS spectrum of garnet from Balangir, Odisha

FTIR Spectra:

The FTIR spectra in the mid infrared region between 400 and 1200cm⁻¹ region for the Balangir garnet showed certain distinct features (Figure 8). According to Sibi & Subodh (2017), who have studied almandine pyrope garnet from Tamil Nadu, the cations in the octahedral site (Al³⁺, Fe³⁺ etc.) result in the bands between 400 and 500 cm⁻¹ appear to be similar to those seen in the Balangir almandine garnet. The peaks around 800–1200 cm⁻¹ can be assigned to Si–O asymmetric stretching vibrations. These bands are independent of multiple cations that might be present in the dodecahedral site. Another group of bands around 500–650 cm⁻¹ could be due to Si–O asymmetric bending vibrations. The presence of band 626cm⁻¹ indicates the garnet to be a combination of almandine-pyrope and this feature has been used to distinguish pyrope from other garnets, in pure pyrope this peak is absent. The FTIR spectrum of

the Balangir garnet contains this peak (626cm⁻¹) and is due to the presence of almandine in the garnet solid solution. Moreover, it is a single peak for pure almandine whereas the splitting of peak in the 600–650 cm⁻¹ in the present IR spectrum indicates the multiple occupancy of cations in the dodecahedral site, and its intensity depends on the pyrope percentage as elaborated by Sibi & Subodh (2017).

Chemical Analyses:

Semi-quantitative chemical analyses by EDXRF for Balangir garnet gave the oxide weight % for SiO₂=37.56 to 38.79, Al₂O₃=21.46–22.75, for FeO=36.92–39.03 for MgO= 2.96–3.27 and for MnO = 1.10-1.30, whereas the oxide weight % for Cr₂O₃ and TiO₂ was determined as 0.07 and 0.06 respectively.

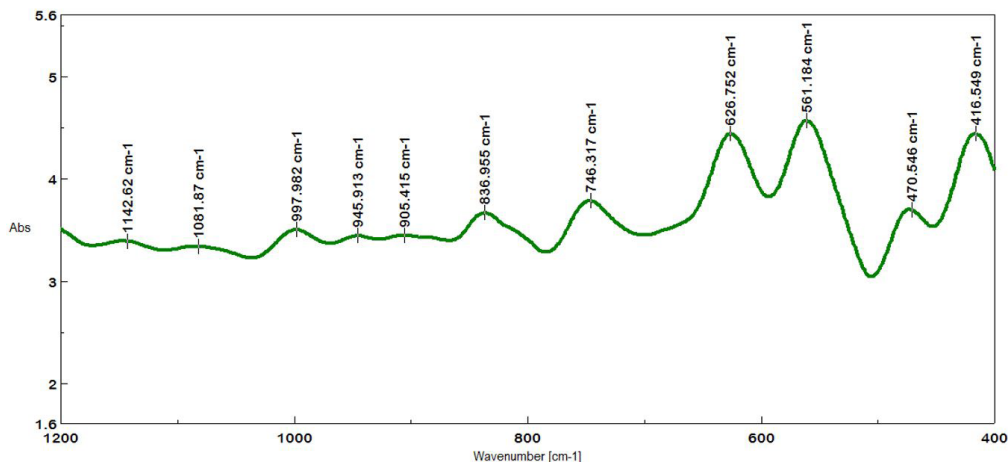


Figure 8: FTIR spectrum of garnet from Balangir, Odisha

Discussion:

Balangir garnet found in the khondalite-charnockite-granite gneiss show a variety of inclusions, which are very similar to the inclusions observed by Schmetzer et al 2017 and Gilg et al 2017, in the garnets from Garibpet and Arikamedu. Axler & Ague (2015) have shown that presence of oriented acicular inclusions indicate that the garnets were crystallised under ultrahigh temperature and pressure. Presence of oriented inclusions like rutile, ilmenite, sillimanite etc reveal the temperature to be above 1000°C and a pressure above 3GPa (Axler & Ague 2015). The variation in colour shades may be due to the presence of Mn²⁺ in the chemical composition Li (2022).

Conclusion:

The Balangir almandine-pyrope garnet has inclusions similar to those studied by Schmetzer et al. (2017), indicating that the emplacements of these garnets may have been in a similar type of metamorphic rock mentioned in that study. The geology of the Indian subcontinent is extremely complicated with numerous metamorphic events, so it is indeed difficult to indicate whether the geological period was also similar to that in the study done by Schmetzer et al. (2017), it could be similar. There are oriented acicular needles of rutile and ilmenite in some of the specimens. Oriented acicular inclusions of the Balangir garnet could be the result of crystallization at ultrahigh temperature of above 1000°C and pressure above 3GPa as stated in Axler & Ague (2015).

Acknowledgements:

Authors thank Dr. Mrs. N. Das for her help to procure the samples. Authors express gratitude to the technical staff of National Chemical Laboratory, Dept. of Geology, University of Pune and Pangemtech for carrying out the analyses.

References

- Axler J.A. and Ague J.J., 2015: Oriented multiphase needles in garnet from ultrahigh-temperature granulites, Connecticut, U.S.A. *American Mineralogist*, Volume 100, pages 2254–2271, 2015
- Gilg H.A., Schmetzer K, And Schüssler U., 2017: An early Byzantine engraved almandine from the Garibpet deposit, Telangana state, India: Evidence for garnet trade along the ancient maritime silk road. *Gems & Gemology*, Vol.54, No.2, pp. 149–165
- Li M., 2022: Spectroscopic Study on the Species and Color Differences of Gem-Quality Red Garnets from Malawi. *Journal of Spectroscopy* Volume 2022, pp1-9
- Schmetzer K., Gilg H.A., Schüssler U., Panjekar J., Calligaro T., Périn P., 2017: The linkage between garnets found in India at the Arikamedu archaeological site and their source at the Garibpet deposit. *Journal of Gemmology*, Vol. 35, No. 7, pp. 598–627
- Sibi N. & Subodh G., 2017: Structural and Microstructural Correlations of Physical Properties in Natural Almandine-Pyrope Solid Solution: Al70Py29. *Journal of Electronic Materials*, Vol. 46, No. 12 pp 6947-6956.
- Stockton C.M., Manson D.V., 1985: A proposed new classification for gem-quality garnets. c, Vol. 21, No. 4, pp. 205-218

Gemological and Luminescence Characteristics of Taaffeites from Mogok, Myanmar

Bihan Lin¹, Xingtong Li¹, Longbo Zhang², Xiaojing Lai¹, Qian Zhang^{1*}

¹ Gemological Institute, China University of Geosciences, Wuhan, China

² National Center for Quality Inspection and Testing of Gem & Gold-Silver Jewelry (Henan), Henan Institute of Product Quality Supervision and Inspection, Zhengzhou 450047, China; * qianzhang@cug.edu.cn

Keywords: taaffeite, Mogok, gemological characteristics, fluorescence spectroscopy

Taaffeite is a rare gem that has been found in different localities such as Tanzania, Sri Lanka, China, and Mogok, Myanmar. Systematic research on the taaffeite from Mogok, Myanmar, is still lacking. In this study, thirty-two taaffeites from Mogok were collected and investigated by conventional gemological testing, laser ablation inductively coupled plasma mass spectrometry (LA-ICP-MS), Raman spectrometry, and fluorescence spectrometry. These samples were observed and photographed under visible light and UV light (Figure 1). According to their fluorescence colors under LWUV light, the samples can be divided into three categories: the pink-red, green, and blue-white fluorescence groups. All of them revealed inert to bright pink fluorescence under SWUV light.

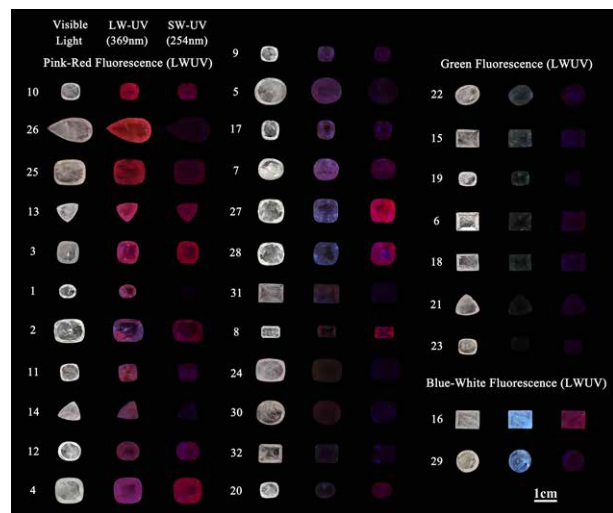


Figure 1: Thirty-two taaffeite samples show different fluorescence under LWUV and SWUV radiation.

Various inclusions were found in these taaffeites. The inclusions can be divided into five types: (1) transparent columnar and irregular inclusions (Figure 2a,b); (2) orange and brown intrusions, mostly filling in the fissures or healed fissures of the host crystal (Figure 2c,d); (3) black punctual and flake inclusions, which occur in large quantities in samples 14 and 16 and are mostly hexagonal plates (Figure 2e,f); (4) fissures and healed fissures (Figure 2g,h); (5) multi-phase inclusions, which are mostly transparent tubes containing black dots or irregular minerals (Figure 2i,j).

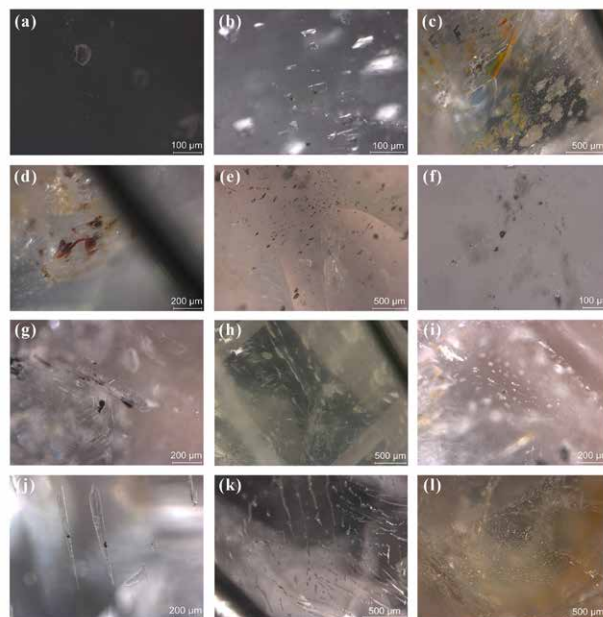


Figure 2. The inclusions in taaffeite samples. (a) and (b) irregular inclusions; (c) and (d) orange and brown intrusions; (e) and (f) black punctual and flake inclusions; (g) and (h) healed fissures; (i) and (j) multi-phase inclusions; (k) and (l) fingerprint-like inclusions (gas-liquid inclusions in healed fissures).

The inclusions of the taaffeite samples were identified by Raman spectroscopy (Figure 3). The mineral inclusions of taaffeites were identified as calcite, forsterite, celestite, dolomite, and graphite. In addition, some transparent tubular or columnar inclusions were filled with CO₂.

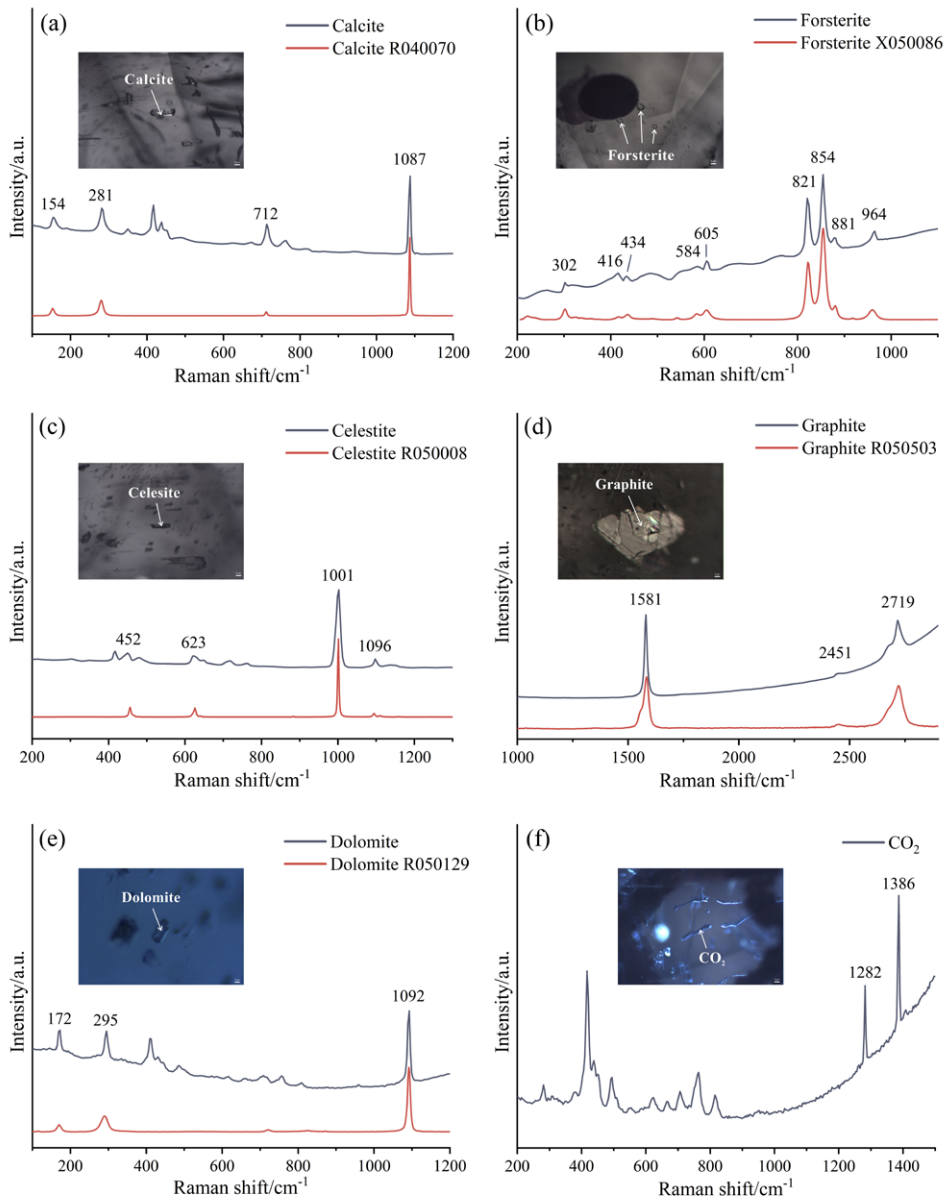


Figure 3: The Raman spectra of inclusions in taaffeite samples. (a) calcite; (b) forsterite; (c) celestite; (d) graphite; (e) dolomite; (f) CO₂.

In general, taaffeite shows inert or chalky fluorescence under long-wave ultraviolet (LWUV) light and inert fluorescence under short-wave ultraviolet (SWUV) light (Malcherek and Schluter, 2016; Schmetzer et al., 2007; Schmetzer et al., 2000; Schmetzer et al., 2005). Using two-dimensional emission spectra, it was found that these samples with pink-red fluorescence had two very strong peaks at 686 nm and 690 nm in the red region. Samples showing green

and blue-white fluorescence had strong peaks at 439 nm and 464 nm in the blue region, a relatively weak peak in the green region, and two very weak peaks at 686 nm and 690 nm in the red region. When combined with the chemical composition data from LA-ICP-MS, this suggests that Cr³⁺ is the activator of the pink-red fluorescence, Mn²⁺ is responsible for the green fluorescence, and Fe inhibits the generation of fluorescence.

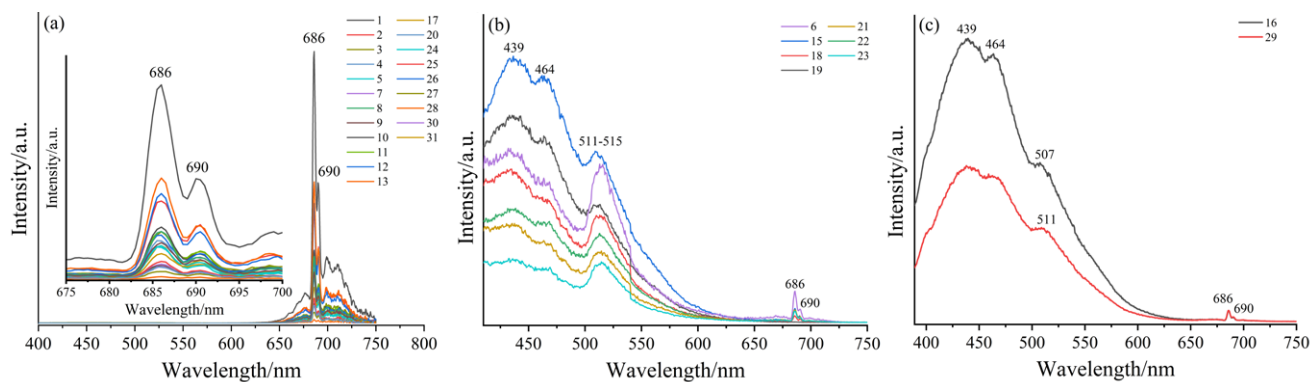


Figure 4. Emission spectra of taaffeites using 369 nm excitation.

(a) Samples with pink-red fluorescence under LWUV. The red region of fluorescence spectra had been enlarged for better analysis, which placed on the left side. (b) Samples with green fluorescence under LWUV. (c) Samples with blue-white fluorescence under LWUV.

References

- Malcherek, T., Schluter, J., 2016. Crystal Structure of Cr-bearing Mg₃BeAl₈O₁₆, a New Polytype of Magnesiotaafeite-2N'2S. *Acta Crystallographica Section E: Crystallographic Communications*, 72, 1060-1063.
- Schmetzer, K., Kiefert, L., Bernhardt, H.-J., 2000. Purple to Purplish Red Chromium-bearing Taaffeites. *Gems & Gemology*, 36(1), 50-58.
- Schmetzer, K., Kiefert, L., Bernhardt, H.-J., Burford, M., 2005. Two Remarkable Taaffeite Crystals from Sri Lanka. *The Journal of Gemmology*, 29(7), 461-466.
- Schmetzer, K., Krzemnicki, M., Hänni, H.A., Bernhardt, H.-J., Pettke, T., 2007. Gem-quality Taaffeites and Musgravites from Africa. *The Journal of Gemmology*, 30(7), 367-382.

Investigating the Provenance signature of Tourmaline-Bearing Turquoise in the Kuh Zar Gold Deposit, Semnan Province, Iran

Bahareh Shirdam¹, Yang Mingxing¹, Andy H. Shen¹, Nader Taghipour², Soheila Aslani³

¹ Gemological Institute, China University of Geosciences, Wuhan, China

² School of Earth Sciences, Damghan University, Damghan, Iran

³ School of Mining Engineering, University of Tehran, Iran; shirdam@gmail.com

Keywords: Baghu Turquoise, Kuh Zar Gold mine, Origin Determination, EPMA, LA ICP MS

The Neyshabur reserve in northeast Iran is renowned for its production of Persian turquoise, yet it is not the sole deposit associated with this valuable gemstone. The Kuh Zar mine, also known as Baghu (Figure 1-A), holds historical significance for its gold deposits (Momenzadeh et al., 2004) and features a cluster of at least four turquoise-bearing tunnels within close proximity. Situated in the Torud-Chahshirin

magmatic arc of Semnan province, central Iran, the studied area encompasses a series of calc-alkaline extrusive igneous rocks intruded by granodioritic stocks and mafic dikes (Figure 1-B) (Niroomand et al., 2018). Notably, turquoise is found within fractures in the Baghu area, specifically within the rhyolites to granodiorites of the First and Ardakani tunnels that have undergone phyllic-argillic alteration (zone I) (Taghipour and Mackizadeh, 2014). Additionally, turquoise is present in the sericitized pyroclastic-volcanic rocks of the Movahed tunnel (zone II).

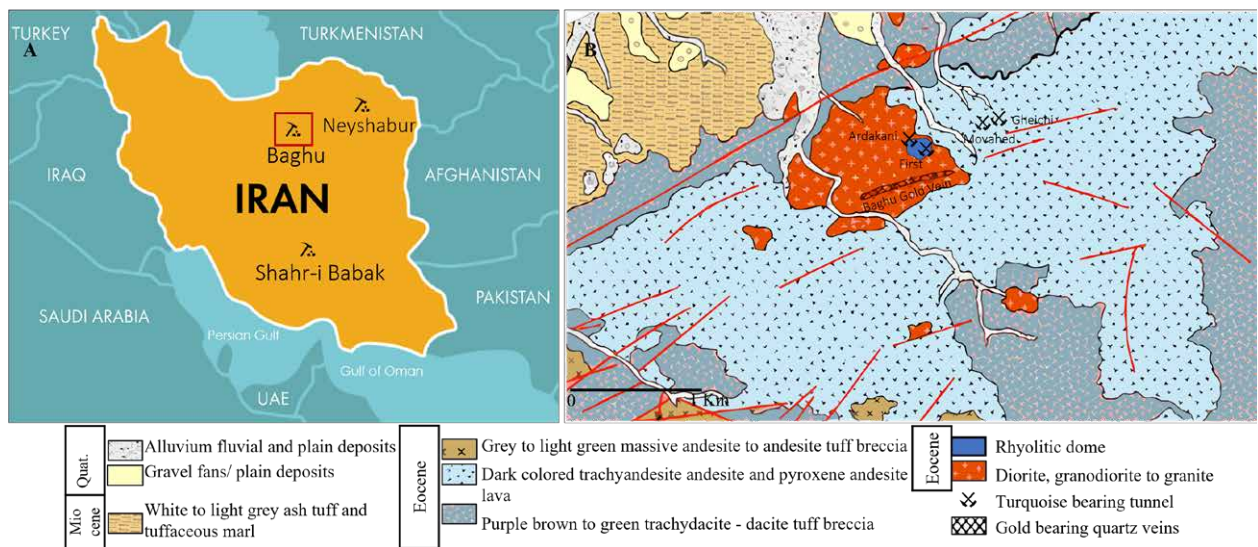


Figure 1: (A) Locations of Iran's main turquoise mines. B: The Geological map of the Kuh Zar mine, Baghu area 1:40000 scale (Niroomand et al., 2018) (Emam Jomeh et al., 2021).

This article focuses on the collection of 49 turquoise samples directly from each zone. Microscopic examination reveals an association of zone I turquoise with tourmaline (Figure 2-A), quartz (Figure 2-B), and pyrite (Figure 2-C), whereas zone II turquoise is associated with iron oxides (Figure 2-D) and sericite, observed as veins, veinlets, and nodules. The Baghu turquoise exhibits a range of colors from pale light to vivid turquoise blue and dark olive-green,

displaying faint to medium blue fluorescence under long UV light. In order to investigate the composition characteristics and rare earth element (REE) patterns of the samples, chemical analysis techniques including Electron Microprobe Analysis (EPMA) and Laser Ablation Inductively Coupled Plasma Mass Spectrometry (LA-ICP-MS) were employed.

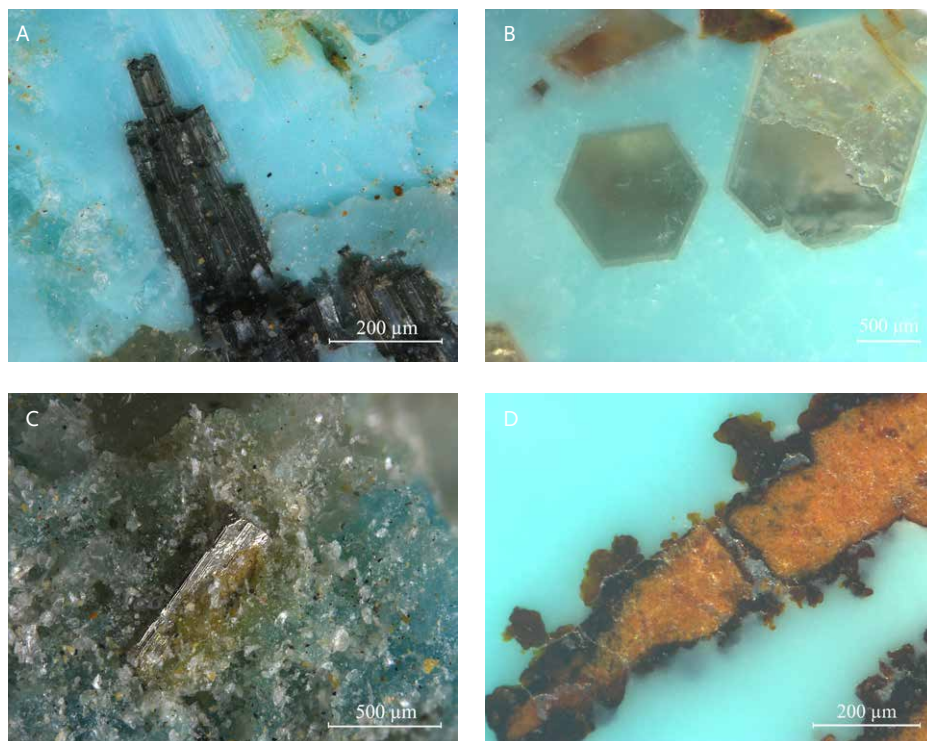


Figure 2: Major inclusions of Baghu turquoise; Tourmaline (A), quartz (B) and pyrite (C) inclusion from zone I and iron oxide (D) inclusion from zone II.

Based on the EPMA results for major elements, zone I turquoise show a higher average content of Fe and Si ($\text{Fe}_2\text{O}_3 = 3.04 \text{ wt\%}$, $\text{SiO}_2 = 2.23 \text{ wt\%}$) in comparison to zone II samples ($\text{Fe}_2\text{O}_3 = 2.18 \text{ wt\%}$, $\text{SiO}_2 = 0.61 \text{ wt\%}$). Conversely, the LA ICP MS data on trace elements revealed that zone II had a higher average concentration of Li, Be, and Sr (Li = 150 ppm, Be = 25 ppm, Sr = 505 ppm) than zone I (Li

= 51ppm, Be = 17ppm, Sr = 224ppm). While both zones demonstrated a notable presence of Ba, zone I (Ba = 662 ppm) showcased a higher concentration than zone II (Ba = 350ppm), thereby serving as a strong marker for Baghu turquoise. These elemental anomalies could be partially attributed to alteration and imposition of zone I with the Oxidation zone of the gold mine.

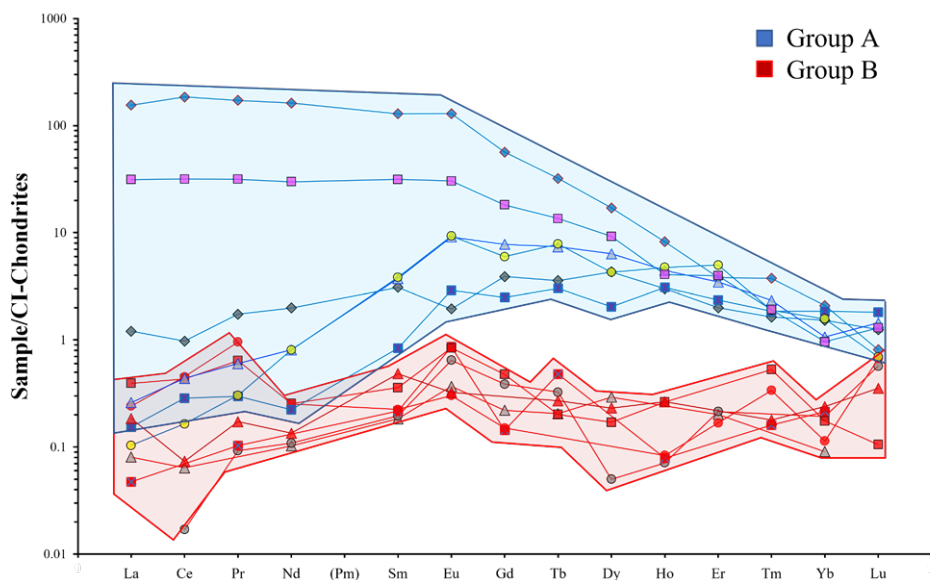


Figure 3: Chondrite-normalized REE patterns for Baghu turquoise

Despite the common use of Rare Earth Element (REE) patterns as a means of determining the origin of gemstones, Baghu turquoise deviates from this conventional pattern. Upon dividing the Chondrite-normalized REE patterns into two distinct groups, it was observed (Figure 3) that all samples with Andesite host rock from the Movahed tunnel in zone II were classified as belonging to group B, which had a noticeably lower concentration of Heavy Rare Earth Elements (HREE) in comparison to group A. However, it should be noted that other samples within group B could not be directly linked to zone II.

It is crucial to recognize that while trace element ratios and REE patterns provide general composition characteristics of a deposit, they should not be solely relied upon for accurate provenancing of turquoise. Turquoise samples within the same deposit can display variations in trace element composition and REE patterns, particularly across different zones. Therefore, consideration of primary gemmological tests, particularly inclusions, becomes essential for determining the origin of turquoise samples.

References

- Momenzadeh, M., Hajisolat, A., Momenzadeh, M., 2004. Metallic mineral resources of Iran, mined in ancient times, A brief review. In T. Stollner, R. Slotta, and A. Vatandoust, Eds., *Persian Antiques Splendor (Mining Crafts and Archaeology in Ancient Iran)*. Deutsches Bergbau-Museum Bochum, Bochum, Germany, 8-21.
- Niroomand, S., Hassanzadeh, J., Tajeddin, H.I., Asadi, S., 2018. Hydrothermal evolution and isotope studies of the Baghu intrusion-related gold deposit, Semnan province, north central Iran. *Ore Geol. Rev.*, 95, 1028-1048.
- Taghipour, B., Mackizadeh, M., 2014. The origin of the tourmaline-turquoise association hosted in hydrothermally altered rocks of the Kuh-Zar Cu-Au-turquoise deposit, Damghan, Iran. *Neues Jahrb. Mineral. Abh.* 272, 61-77.
- Emam Jomeh, A., Jahangiri, A., Moazen, M., 2021. Investigation of the role of fractional crystallization, crustal assimilation and magma mixing in turquoise hosted sub-volcanic intrusion rocks in Damghan gold mine, South of Damghan, Iran. *Iranian Journal of Crystallography and Mineralogy.* 29, 385-402

Cobalt spinel from Bai BUoi mine, Yen Bai, Vietnam

Masaki Furuya

Japan Germany Gemmological Laboratory, Kofu, Japan E-mail: jgg|@sapphire.co.jp

Keywords: Cobalt spinel, Vietnam, Bai Buoi mine, Bãi Bườì, Yen Bai

The cobalt bearing spinel from Lukande, Tanzania, discovered in 2019, has attracted much attention and several papers were published recently (Stephan & Muller., 2022, Krzemnicki et al., 2023, Furuya, 2023). Almost at the same time as the Tanzanian spinel, a new spinel deposit was found at the Bai Buoi (Bãì Bườì) mine near Luc Yen. These two deposits of blue spinel are quite similar in various gemmological characteristics such as colour, fluorescence and chemical composition, except for inclusions.

Location and general properties

The Bai Buoi mine is located 7km northwest of Thac Ba Lake, Yen Bai Province, Vietnam. The mine was reportedly discovered in June 2019 (Blauwet, 2020, Fujita 2022). By 2021, five mining sites around the area were producing spinels. (Fujita, 2022, Tanida 2023). For this study the author examined 37 faceted samples from this new mine in Vietnam.



Figure 1: Samples of blue spinels from Bai Buoi mine, Yen Bai district, Vietnam.

The colour of the samples shows a range of shades of blue. They range from pure blue, deep blue, slightly greyish blue to pale purplish blue. None of them are of electric cobalt-blue colour that is occasionally found in Vietnamese cobalt spinels, but they are sufficiently vivid as are the Tanzanian spinels. The samples ranged in size from 0.12ct to 0.61ct. Most of them are visibly included. Their refractive indices range from 1.714 to 1.718 and their specific gravities from 3.58 to 3.64, which is within the normal range for magnesium spinel. They show weak to moderate green fluorescence under long wavelength UV radiation, but are inert under short wavelength UV radiation.

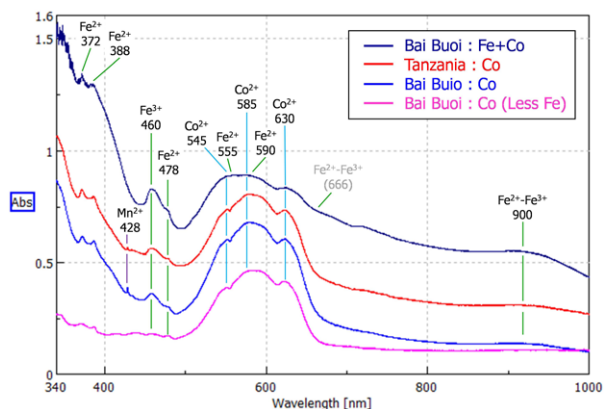


Figure 2. UV-Vis spectra of various type of blue spinels from Bai Buoi mine, Vietnam and a typical one from Tanzania (red trace).

UV-Vis spectra

The most similar property between Bai Buoi and Tanzanian spinel is the UV-Vis absorption. The blue colour of spinel is due to cobalt and iron. The blue trace in Figure 2 represents the pure blue type of Bai Buoi spinel, which is the majority of them. This type shows the strong Co related absorption and also moderate Fe related absorption. It is quite similar to the one of Tanzania (red trace). And whether it is prominent or weak, most of them show the Mn^{2+} related absorption peak at 428nm. Few of the relatively dark blue samples show a strong iron absorption as shown in Figure 2 (dark blue trace). Also, some of the pale blue to violet coloured spinels show quite weak Fe-related absorption features (see pink trace in Figure 2). In this type all Fe-related absorption is weak even at the UV-edge.

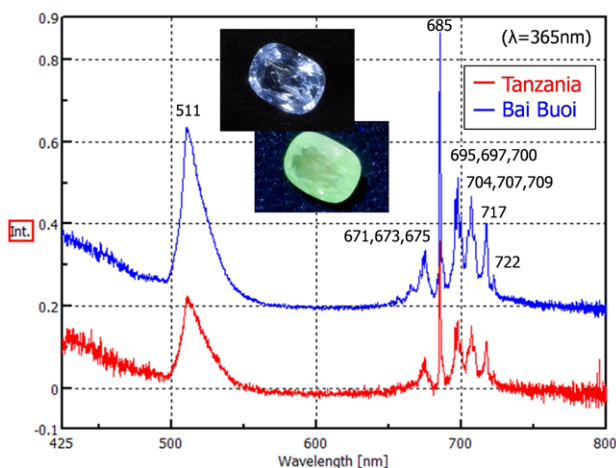


Figure 3: LW UV Fluorescence image and spectra

Fluorescence and photoluminescence

Although the intensity is different, many of the blue spinels from Bai Buoi fluoresce green (511nm centred band) under long-wave UV light. Figure 3 shows the fluorescence spectra of a Vietnamese (Bai Buoi) and Tanzanian cobalt-bearing spinel excited by a 365nm LED. Both show the green broad band emission centred at 511nm. This broad band emission is assumed to be due to Mn^{2+} (Koivula et al., 1991). They also show the emission series related to Cr^{3+} in the red spectral region.

In addition to the UV fluorescence, the photoluminescence shows similar features as mentioned in previous literature by Krzemnicki et al. (2023) about Tanzanian spinels. With 523 nm laser excitation, the Bai Buoi spinels show three types of luminescence (Figure 4). The red trace represents a high-Cr type of blue spinel (spectrum normalized by multiplication of 0.1) which is characterized by the emission series related to Cr^{3+} . The low-Cr type of blue spinel (green trace) shows a broad band emission centred at 655 nm. And the blue trace represents a mixture of these two types. The 655 nm emission is said to be due to Mn^{4+} (Khaidukov et al., 2020), but its intensity is not directly correlated with the Mn content in our samples, but seems negatively correlated with the Cr content.

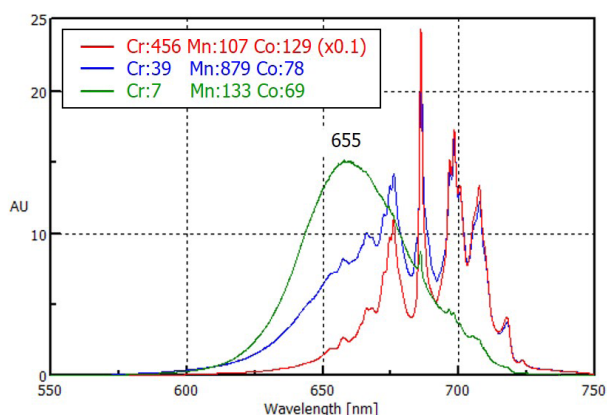


Figure 4: Photoluminescence spectra of various Bai Buoi spinels

Chemical composition

The chemical fingerprint tested by LA-ICP-MS of Bai Buoi spinel and Tanzanian spinel is also similar, especially for the colouring elements of Fe and Co content (Figure 5), as well as the UV-Vis spectra are similar. However, the Zn content tends to be higher in Tanzanian spinels than in Bai Buoi spinels (Figure 6).

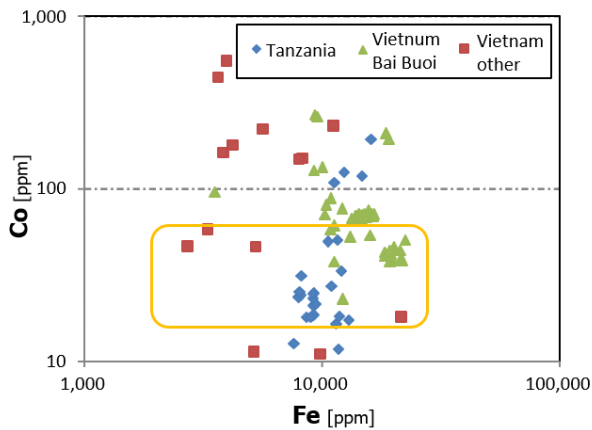


Figure 5: Fe and Co concentration in ppm

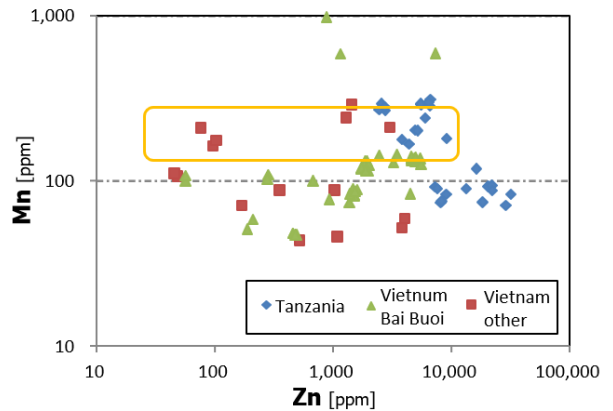


Figure 6: Zn and Mn concentration in ppm

Inclusions and internal features

On the other hand, the inclusions in Bai Buoi spinel are quite different from the Tanzanian ones. In few samples, the dislocation “needle”-like inclusions are seen (Figure 7). And it is common to see flake-like inclusions that are scattered in parallel (Figure 8). Among the crystal inclu-

sions, apatite is the most common (Figure 9). Although it is seen only in one sample, a titanite cluster was identified by Raman spectroscopy (Figure 10). However, none of them have högbomite lamellae that are very abundant in Tanzanian spinels.



Figure 7: Dislocation “needles”

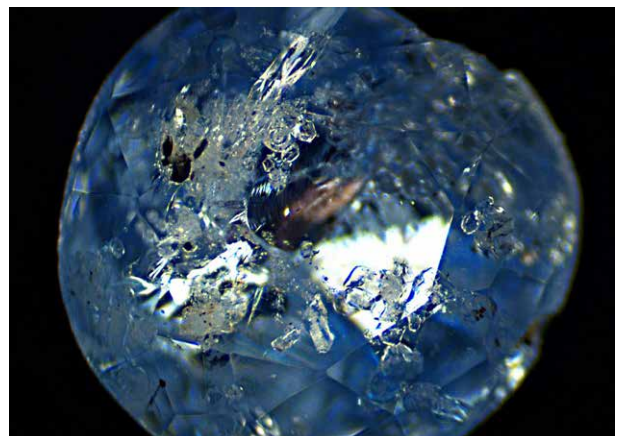


Figure 8: Flake-like inclusions

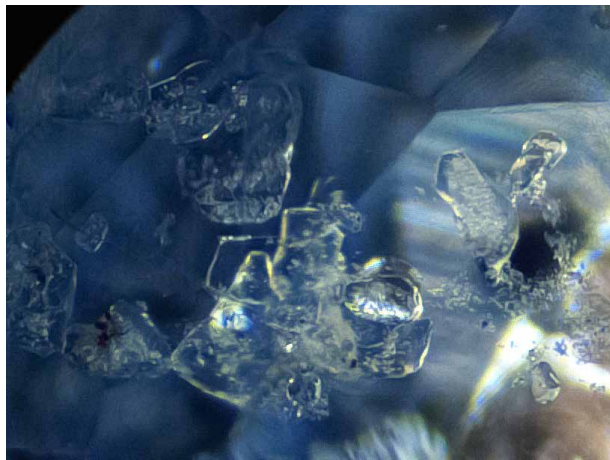


Figure 9. Colourless apatite inclusions

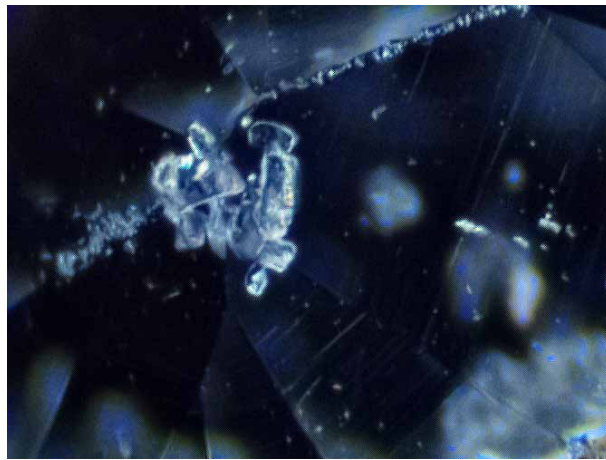


Figure 10. Titanite clusters

Conclusion

The blue cobalt-bearing spinels from the Bai Buoi mine in Vietnam have many similar gemmological characteristics compared to the Tanzanian blue spinels. In particular, the UV-Vis spectra and fluorescence are almost identical. The trace element content is also similar, especially for the colouring elements. However, the inclusions are quite different as Bai Buoi spinels contain some of the typical inclusions known from Vietnamese spinels since many years (Smith et al. 2008).

References:

- Blauwet, D., 2020, Visit to a New Blue Spinel Mining Area in Vietnam, *The Journal of Gemmology*, 37, 2, 142-143
- Furuya, M., 2023, Cobalt spinel from Mahenge, *Gem Information*, 49, 8-9
- Fujita, K. Tanida, T, 2022, The newly found cobalt spinel from Bai Buoi mine in Vietnam and its distribution to the market, personal communication.
- Khaidukov, N.M., Brekhovskikh, M.N., Kirikova, N.Y., Kondratyuk, V.A. & Makhov, V.N., 2020, Luminescence properties of spinels doped with manganese ions. *Russian Journal of Inorganic Chemistry*, 65, 8, 1135–1141
- Koivula, J.I., Kammerling, R.C. & Fritsch, E., 1993, *Gem News: Ruby mining near Mahenge, Tanzania. Gems & Gemology*, 29, 2, 136
- Krzemnicki, M.S., Leuenberger, A., Balmer, W. A., 2023. Cobalt-bearing Blue Spinel from Lukande, near Mahenge, Tanzania, *Journal of Gemmology, The Journal of Gemmology*, 38, 5, 474–493
- Smith C., Beesley C.R., Darenus E.Q., Mayerson W.M., 2008, A closer look at Vietnamese spinel,. *InColor*, Spring, pp. 11-13
- Stephan, T., Henn, U., Muller S., 2022, New finds of cobalt-bearing spinel near Mahenge, Tanzania, *Zeitschrift der Deutschen Gemmologischen Gesellschaft*. 71, 3-4, 57-64

Acknowledgments

- Katsunori Fujita of Tomofin Co. and Takashi Tanida of Gem Eiko Co.
- Yamanashi Prefectural Industrial Technology Center

Quantitative estimation of spinel's thermal and geothermal history by photoluminescence spectroscopy and its application in spinel origin determination

Chengsi Wang¹, Jiling Zhou¹, Andy H. Shen¹

¹ Gemological Institute, China University of Geosciences, Wuhan, China; chance_w@foxmail.com

Keywords: spinel, photoluminescence spectroscopy, thermal history, origin determination

The thermal history of spinel can not only be used to distinguish the natural spinel from heated and synthetic ones, but also to reveal that the spinel underwent different geological processes. It can be estimated by the parameter named degree of disorder, which is the result of order-disorder transition inside the crystal ${}^{IV}[Mg] + {}^{VI}[Al] \xrightarrow{\text{heat}} {}^{IV}[Al] + {}^{VI}[Mg]$. In this case, the temperature where the cations stop exchanging their positions is considered as intracrystalline closure temperature of spinel. Mineralogists studied spinel's degree of disorder by X-ray or neutron diffraction and tried to develop spinel as a geothermometer (Millard

et al. 1992; Uchida et al. 2005; Lenaz et al. 2014), but these methods are destructive and unsuitable for the analysis on gemstones. Photoluminescence (PL) spectroscopy shows considerable potential for nondestructively probing local cation arrangement around the impurities (such as Cr^{3+} and Mn^{2+}) in MgAl_2O_4 spinel. But most gemological research just used it in a non-quantitative comparison to separate natural spinel from heat-treated ones. A quantitative method was established in this work to estimate the thermal history of spinel and was applied to 354 natural samples from 5 countries (Figure 1).

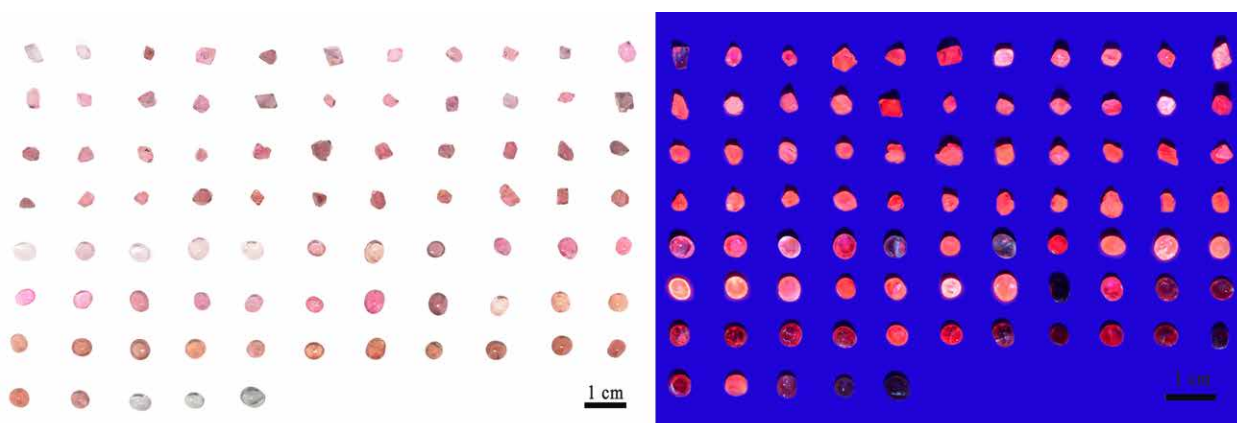


Figure 1. Photo of partial samples under D65 and UV light

The PL spectrum consists of R peaks (emitted by ordered PL centers) and N peaks (emitted by disordered PL centers) (Mikenda and Preisinger 1981) (Figure 2). After obtaining the percent ratio of the integrated area of N peaks to the total integrated area under all peaks, the data were defined as a parameter to monitor the degree of disordering. Spinel from Myanmar was discovered to have a higher disordered degree than spinels from other origins, while those from Morogoro (Tanzania) exhibit the lowest (Figure 3). A thermodynamic model based on this spectroscopic parameter was built, and an equilibrium constant k was established (Wang et al. 2020). The parameter k was quantitatively related to the treatment temperature of spinel crystals (Figure 4), which can be reversely used to estimate the thermal or geothermal history of spinel according to formulas:

$$k = \frac{[N_2]^* [N_1]^* [n_3]^* [N_2]^* [n_5]}{[R]^5}; \ln k = -30605 \frac{1}{T} + 17.681, \text{ in}$$

which $[x]$ indicates the integral area percentage of certain peak. Estimated closure temperature of spinel from different origins located in separate ranges. Furthermore, N peaks of the samples with high Cr content were found to be abnormally strong, which would result in overestimating of thermal history. A relationship between Cr-pair peaks and Cr-content was constructed (Figure 5). By erasing the influence of high Cr content through differential spectrum through differential spectrum method (Figure 6), the estimated results would be more precise and universal. Based on this study, the establishment of an origin determination method and a new geothermometer can be expected.

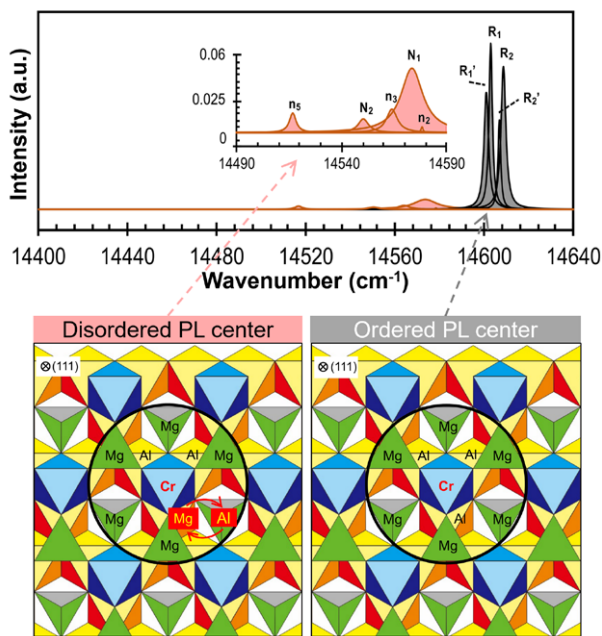


Figure 2. Zero phonon lines of spinel's PL spectrum and their PL centers

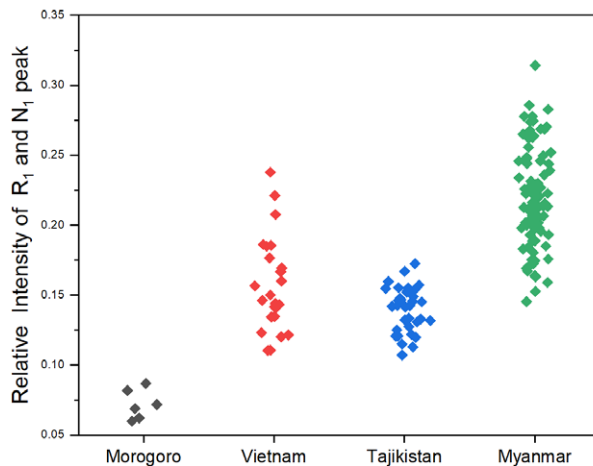


Figure 3. Disordered degree of spinels from 4 origins

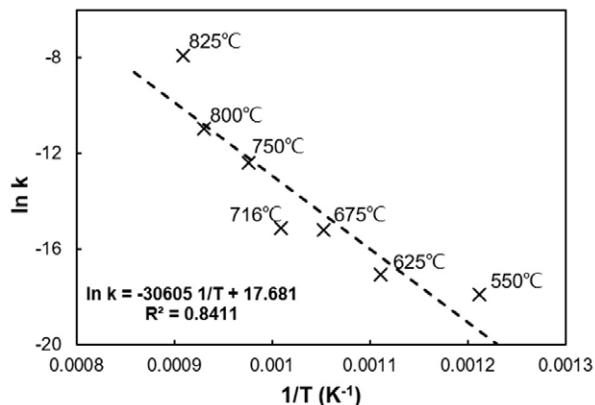


Figure 4. The linear dependence of disorder parameter $\ln k$ with temperature

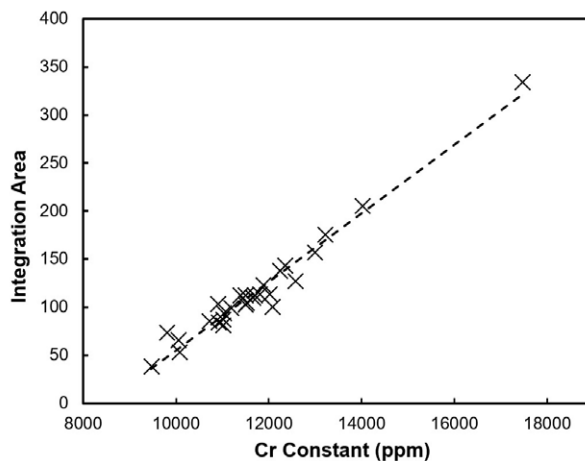


Figure 5. Relationship between integrated area of Cr-pair peak and Cr content

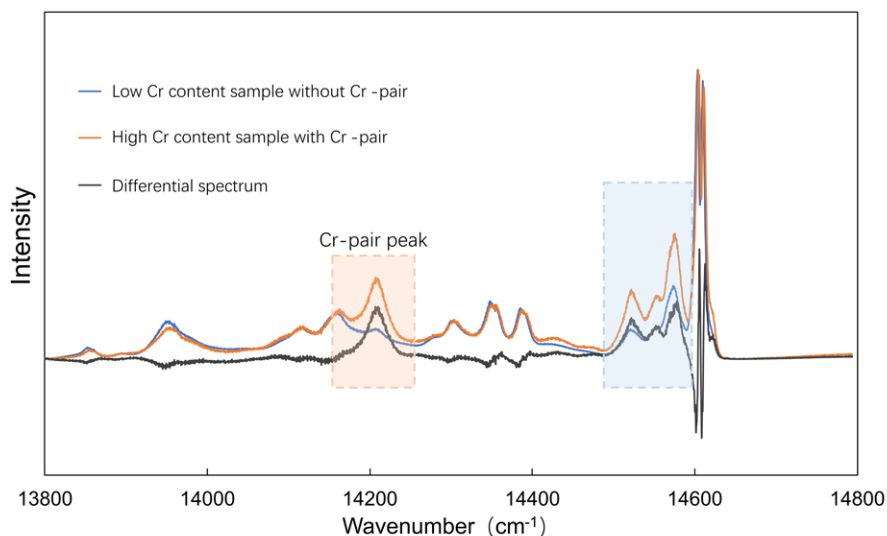


Figure 6. Abstracting Cr-pair peak by differential spectrum method

References

- Lenaz, D., Youbi, N., De Min, A., Boumehdi, M.A., and Abbou, M. Ben (2014) Low intra-crystalline closure temperatures of Cr-bearing spinels from the mantle xenoliths of the Middle Atlas Neogene-Quaternary Volcanic Field (Morocco): Mineralogical evidence of a cooler mantle beneath the West African Craton. *American Mineralogist*, 99, 267–275.
- Mikenda, W., and Preisinger, A. (1981) N-lines in the luminescence spectra of Cr³⁺-doped spinels (I) identification of N-lines. *Journal of Luminescence*, 26, 53–66.
- Millard, R.L., Peterson, R.C., and Hunter, B.K. (1992) Temperature dependence of cation disorder in MgAl₂O₄ spinel using 27Al and 17O magic-angle spinning NMR. *American Mineralogist*, 77, 44–52.
- Uchida, H., Lavina, B., Downs, R.T., and Chesley, J. (2005) Single-crystal X-ray diffraction of spinels from the San Carlos Volcanic Field, Arizona: Spinel as a geothermometer. *American Mineralogist*, 90, 1900–1908.
- Wang, C., Shen, A.H., and Liu, Y. (2020) Characterization of order-disorder transition in MgAl₂O₄:Cr³⁺ spinel using photoluminescence. *Journal of Luminescence*, 227, 117552.

Mechanism and Application of High-Temperature Copper Diffusion in Surface Recoloring of Labradorites

Qingchao Zhou², Chengsi Wang¹, and Andy Hsien Shen^{1*}

¹ Gemmological Institute, China University of Geosciences, Wuhan 430074, China

² School of Jewelry, West Yunnan University of Applied Sciences, Tengchong 679100, China

shenxt@cug.edu.cn

Keywords: Copper diffusion, labradorites, copper nanoparticles

Feldspar, with the chemical formula of $[KAlSi_3O_8]_x[NaAlSi_3O_8]_y[CaAl_2Si_2O_8]_z$ ($x + y + z = 100$), is one of the most important rock-forming minerals in the earth's crust, and those of high quality can be used as gemstones. The main feldspar gems on the market include moonstone, sunstone, amazonite, and iridescent rainbow labradorite. Among them, sunstone exhibits a strong golden and red metallic luster due to microscopic metallic inclusions. But there is a special kind of labradorite sunstone ($[NaAlSi_3O_8]_{30-50}[CaAl_2Si_2O_8]_{50-70}$) that not only shows "schiller", but also presents brilliant red and green bodycolors. Currently, the reported localities of this kind of natural labradorite sunstone are the U.S. state of Oregon and the Afar region of Ethiopia (Johnston et al., 1991; Kiefert et al., 2019; Sun et al., 2020). This material is highly valued and favored by many gem carvers and collectors for its unique optical properties. As for the color origin of labradorite sunstone, authors CW and AHS (Wang et al., 2019) from the present study directly observed the microscopic morphology of Cu nanoparticles (NPs) in natural sunstone by means of Focused Ion Beam - Transmission Electron Microscopy (FIB-TEM).

It is also because of the high price and huge market potential of natural sunstones that an artificially diffused red andesine feldspar was unveiled during the 2006 Tucson gem shows (Rossman, 2011). The diffused red andesine feldspar has the same coloring mechanism (Cu NPs) as natural sunstone. But the treatment methods on the market are not completely understood. Many researchers have tried to generate red and green colors using copper diffusion

experiments, typically by placing colorless or light-yellow feldspar in a zirconia powder containing a small amount of copper and then performing a high-temperature diffusion treatment (Emmett et al., 2009; Thirangoon, 2009). In this abstract, we demonstrated the mechanism and application of high-temperature copper diffusion in surface recoloring of labradorites.

The high-temperature diffusion process was divided into three stages according to the color change of labradorite (Figure 1b). In stage I, the temperature of the tube furnace gradually increased from room temperature to 1050 °C. When the labradorite was taken out from the tube furnace as soon as the temperature reached 1050 °C, the color has not changed. According to experimental results and thermodynamic calculations, when the temperature is lower than 1050 °C in air atmosphere, Cu^{2+} ions with $3d^9$ electronic configuration is more stable (Rakhshani, 1986); when the temperature is higher than 1050 °C, Cu^+ with $3d^{10}$ electronic configuration is more stable. Therefore, the chemical state of the CuO in stage I will remain unchanged within the temperature range of 25~1050 °C. Obviously, it is difficult for Cu^{2+} ions to diffuse into the labradorite.

In stage II, the temperature of the tube furnace is maintained at 1050 °C for 6 h, and the labradorite became light red when they were taken out from the tube furnace. Since the temperature is higher than 1050 °C, the transition of $Cu^{2+} \rightarrow Cu^+$ could occur from the perspective of thermodynamics. Therefore, we inferred here that copper enters the labradorite in the form of Cu^+ ions. The diffusion of Cu^+

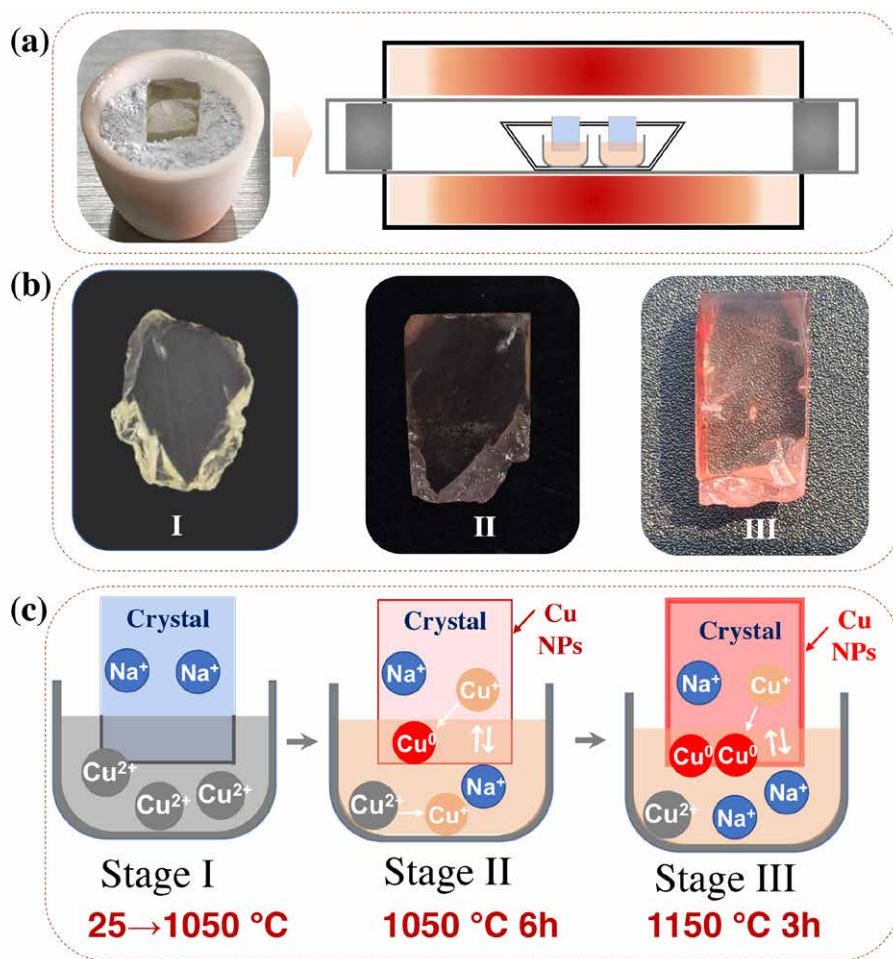


Figure 1. (a) The partly buried labradorite in alumina crucible; (b) The optical images of diffusion-treated labradorite in different stage under ambient daylight; (c) Schematic illustration of the in-situ formation process of Cu nanoparticles in labradorite at different stages.

ions can also be confirmed by the fluorescence spectra. The labradorite after the high-temperature diffusion process have fluorescence peaks at ~394 nm and ~555 nm. According to literature reports, the fluorescence emissions at ~394 nm and ~555 nm are caused by Cu⁺ and Cu⁺-Cu⁺ dimer respectively (Lutz et al., 1997; Puppalar et al., 2011). And the Cu⁺ ions entered in the labradorite could be further reduced to Cu⁰ by capturing hot electrons generated in the labradorite under high temperatures. After holding for 6 h at 1050 °C, with continuous entering and reduction of Cu⁺ ions, the amount of Cu⁰ aggregated on the surface of labradorite reached the critical point, which will lead to the formation of Cu NPs. The LA-ICP-MS data confirm that Cu⁺ ions diffuse into the labradorite through Cu⁺-Na⁺ ions exchange.

In stage III, the temperature of the tube furnace is increased to 1150 °C, then maintained at this temperature for 3 h,

and the labradorite became red when they were taken out from the tube furnace. In this stage, the effect of temperature on the diffusion rate is very important. An increase of 100 °C is beneficial to the formation and growth of Cu NPs, since the temperature rise will accelerate the process of Cu⁺ ions entering the labradorite and being reduced to the form of Cu⁰. The surface plasmon resonance (SPR) absorption peak of the labradorite obtained in stage III is obviously enhanced after holding for 3 h at 1150 °C. The TEM and EELS data revealed that spherical Cu NPs with an average size of 46±5.9 nm were finally produced in the labradorite. The surface of two faceted labradorites were recolored by using a similar high-temperature copper diffusion process. In order to have a more direct comparison with the sample before copper diffusion, the images of the faceted labradorites before and after the high-temperature copper diffusion are presented in Table 1.





Sample number and description	Images before copper diffusion	Images after copper diffusion
CP-1 pear cut, 2.55 ct 11.3×8.2×5.2 mm	 pale yellow	 light red
CP-2 pear cut, 2.77 ct 12.6×7.4×5.7 mm	 pale yellow	 red

Table 1. Properties of faceted labradorites before and after copper diffusion.

References

- Emmett, J., Douthit, T., 2009. Copper diffusion in plagioclase. *GIA News from Research*. Aug. 21
- Johnston, C.L., Gunter, M.E., Knowles C.R., 1991. Sunstone labradorite from the Ponderosa mine, Oregon. *Gems & Gemology*, 27(4), 220–233.
- Kiefert, L., Wang, C., Sintayehu, T., Link, K., 2019. Sunstone labradorite-bytownite from Ethiopia. *Journal of Gemmology*, 36(8), 694–696.
- Lutz, T., Estournes, C., Merle, J. C., Guille, J. L., 1997. Optical Properties of Copper-Doped Silica Gels. *Journal of Alloys and Compounds*, 262, 438–442.
- Puppawar, S. P., Dhoble, S. J., Kumar, A., 2011. Improvement of Photoluminescence of Cu⁺ Ion in Li₂SO₄. *Luminescence*, 26(6), 456–461.
- Rakhshani, A. E., 1986. Preparation, Characteristics and Photovoltaic Properties of Cuprous Oxide—A Review. *Solid-State Electronics*, 29(1), 7–17.
- Rossman, G.R., 2011. The Chinese red feldspar controversy: Chronology of research through July 2009. *Gems & Gemology*, 47(1), 16–30.
- Sun, Z., Renfro, N.D., Palke, A.C., Breitzmann, H., Muyal, J., Hand, D., Hain, M., McClure, S.F., Katsurada, Y., Miura, M., Rossman, G.R., 2020. *Gem News International: Sunstone plagioclase feldspar from Ethiopia*. *Gems & Gemology*, 56(1), 184–188.
- Wang, C., Shen, A.H., Palke, A.C., Heaney, P.J., 2019. Color origin of the Oregon sunstone. In *Proceedings of the 36th International Gemmological Conference IGC, Nantes, France*, August 27–31, pp. 71–74.

A Review and Synthesis of the Geology and Gem Resources of Granitic Pegmatites in Southern California, USA

Brendan M. Laurs¹

¹ Gem-A, Encinitas, California, USA
brendanlaurs@gmail.com

Keywords: Pegmatite, tourmaline, morganite, aquamarine, kunzite, spessartine, San Diego County, California

Introduction

Gem-bearing pegmatites in Southern California are hosted by the Peninsular Ranges batholith, and occur in ten districts in San Diego and Riverside counties (Figure 1a and Table 1). They are important historic sources of high-quality gem rough and world-class mineral specimens of various minerals, including tourmaline (Figure 1b), spodumene (Figure 1c), beryl, topaz and spessartine, and have also been mined for industrial materials (quartz, feldspar and Li minerals).

Most of the mining took place during the first decade of the twentieth century, and subsequently in the 1970s-1980s. Despite some changes in land-use policies, and increasing regulations and costs associated with mining, a few of the mines are still being worked today for gem rough and mineral specimens. Impressive examples of gemstones and crystals are found in numerous museums and important private collections, and also continue to circulate on the market. The tourmaline is revered for its pure vibrant pink and bicolored pink-green appearance, while the kunzite shows an attractive lavender coloration, and the spessartine exhibits a bright orange color even in relatively small sizes.



Figure 1: (a) Map showing main gem pegmatite districts in Southern California (after Shigley & Laurs 2006). (b) Tourmaline from the Himalaya mine, Mesa Grande (21.51 ct gem and 5.0 cm crystal). (c) Kunzite from the Oceanview mine, Pala (40.71 ct gem and 4.7 cm crystal). Stones courtesy of Bill Larson; photos by Robert Weldon.

District	County	Principal gem minerals	Pegmatite age*
Aguanga Mountain	San Diego	Topaz, tourmaline	—
Chihuahua Valley/ Warner Springs	San Diego	Tourmaline, beryl (aquamarine, morganite), quartz	94 Ma (Ar-Ar; M. Taylor, pers. comm.)
Jacumba/ Tule Mountain	San Diego	Beryl (aquamarine), spodumene (kunzite), spessartine	90 Ma (Ar-Ar; M. Taylor, pers. comm.)
Mesa Grande	San Diego	Tourmaline, quartz	95.4 Ma (Ar-Ar; Snee & Foord 1991)
Pala	San Diego	Tourmaline, beryl (morganite), spodumene (kunzite), quartz	99.4 Ma (Ar-Ar; Snee & Foord 1991)
Ramona	San Diego	Spessartine, topaz, tourmaline, beryl (aquamarine, morganite), quartz	97.0–98.7 Ma (Ar-Ar; Snee & Foord 1991)
Red Mountain	Riverside	Tourmaline	—
Rincon	San Diego	Beryl (aquamarine), tourmaline, quartz	
Thomas Mountain/ Cahuilla Mountain	Riverside	Tourmaline, beryl (aquamarine, morganite), quartz	94.4 Ma (U-Pb; M. Taylor, pers. comm.)

Table 1: Gem pegmatite districts in Southern California, their gem minerals, and their ages.

* The argon closure temperature for muscovite is ~350°C. Matthew Taylor is thanked for providing unpublished age data.

Pioneering geological and mineralogical studies of the pegmatites were done by Richard H. Jahns (e.g. Jahns & Wright 1951), John Hanley (1951), Dale R. Simpson (1960), and Eugene E. Foord (1976). More recently, various researchers have focused on the geological setting and petrogenesis of the pegmatites (e.g. Symons et al. 2009; Morton et al. 2018). In addition, summary descriptions of various S. California pegmatite localities were provided by Fisher (2002, 2011).

Geological History of the Peninsular Ranges Batholith and Characteristics of the Pegmatites

Dating by the $^{235}\text{U}/^{207}\text{Pb}$ and $^{40}\text{Ar}/^{39}\text{Ar}$ methods have yielded pegmatite ages ranging from 99.4 to 90 million years (Ma), younging to the east (see Table 1). Nearly all of the pegmatites are hosted by igneous rocks of the Peninsular Ranges Batholith (PRB), which extends from near San Jacinto Mountains in Riverside County southward into Baja California. The PRB has been broadly divided into western and eastern zones according to differences in the physical, compositional

and isotopic properties of its plutons. These two zones are contiguous products of Cretaceous subduction (i.e. of the Farallon plate beneath the North American plate), which transitioned from a Mesozoic oceanic arc setting in the western PRB to a continental-margin arc setting in the eastern PRB (Hildebrand & Whalen 2014; Premo et al. 2014). Rocks of the western zone include weakly to moderately deformed ~128–120 Ma gabbros (and associated volcanics), ~118–115 Ma granodiorite–monzogranite plutons, and ~108–102 Ma quartz diorite–tonalite plutons (which are most abundant). Rocks of the eastern zone consist of large, undeformed, ~99–92 Ma ‘La Posta’-type plutons that are compositionally zoned with a tonalite to granodiorite composition. The youngest of these intrusions (<95 Ma) are small (1–2 km) two-mica granites and associated pegmatites.

The economically important pegmatite districts (Pala, Mesa Grande, and Ramona) are hosted by gabbroic or tonalitic rocks in the western zone of the PRB. The source of these pegmatites has not been identified, while some of those

of the eastern zone (i.e. in the Jacumba/Tule Mountain District) appear to be related to partial melting caused by heat from the La Posta pluton. Geological, geochemical and paleomagnetic evidence indicate that the pegmatites in both zones are broadly cogenetic, but differences in their age, composition and mineralization between the various districts suggests to the present author that they each formed independently from discrete local sources.

The pegmatites occur in groups of subparallel dikes and sills that were emplaced along a well-developed set of fractures (typically in gabbros and norites), which may have been produced by regional contraction during batholithic cooling. Although up to several hundred pegmatite bodies can be present in a particular district, only a few of them are economically important sources of gems and mineral specimens. The pegmatites dip shallowly to moderately (south)west, generally 10°–35°, and are typically several 10s

of meters long and 2–8 m thick (exceptionally up to 30+ m thick). The best-quality minerals and gems occur in specific portions of the pegmatites, where they are concentrated in crystal-lined miarolitic cavities referred to as “pockets” by the miners. The pocket zones are most commonly located near the centerline or just below the quartz core of the pegmatites, and they range from several centimeters across to extensive, multiply-projecting, and branching cavities as much as 3 m or more.

Paleomagnetic data by Symons et al. (2009) indicate that at the time the San Diego Co. pegmatites formed, they were located near what is today the northwestern coastline of mainland Mexico (Sonora State). Rapid exhumation of the PRB, combined with recent uplift and northwest transport of the pegmatite districts along the San Andreas Fault system, are responsible for making these gem and mineral resources accessible to us today in Southern California.

References:

- Fisher, J., 2002. Gem and rare-element pegmatites of Southern California. *Mineralogical Record*, 33(5), 361–407.
- Fisher, J., 2011. Mines and minerals of the Southern California pegmatite province. *Rocks & Minerals*, 86(1), 14–35, <https://doi.org/10.1080/00357529.2011.537167>
- Foord, E.E., 1976. Mineralogy and petrogenesis of layered pegmatite-aplite dikes in the Mesa Grande District, San Diego County, California. PhD thesis, Stanford University, Stanford, California, USA, 326 pp + 2 plates.
- Hanley, J.B., 1951. Economic Geology of the Rincon Pegmatites, San Diego County, California. California Division of Mines Special Report 7-B, 24 pp.
- Jahns, R.H., Wright L.A., 1951. Gem and Lithium-bearing Pegmatites of the Pala District, San Diego County, California. California Division of Mines Special Report 7-A. 72 pp. + 5 plates.
- Hildebrand, R.S., Whalen, J.B., 2014. Arc and slab-failure magmatism in Cordilleran batholiths II – The Cretaceous Peninsular Ranges batholith of southern and Baja California. *Geoscience Canada*, 41(4), 399–458, <https://doi.org/10.12789/geocanj.2014.41.059>.
- Morton, D.M., Sheppard, J.B., Miller, F.K., Lee, C.-T.A., 2018. Petrogenesis of the cogenetic Stewart pegmatite-aplite, Pala, California: Regional implications. *Lithosphere*, 11(1), 91–128, <https://doi.org/10.1130/l1026.1>.
- Premo, W.R., Morton, D.M., Wooden, J.L., Fanning, C.M. 2014. U-Pb zircon geochronology of plutonism in the northern Peninsular Ranges batholith, Southern California: Implications for the Late Cretaceous tectonic evolution of Southern California. In D.M. Morton and F.K. Miller, Eds., *Peninsular Ranges Batholith, Baja California and Southern California*, Geological Society of America Memoir 211, 145–180, [http://dx.doi.org/10.1130/2014.1211\(04\)](http://dx.doi.org/10.1130/2014.1211(04)).
- Shigley, J.E., Laurs, B.M. 2006. Pala Pegmatite District: Stewart, Pala Chief, and Elizabeth R Mines. Field trip guidebook, GIA Gemological Research Conference and the 4th International Gemological Symposium, San Diego, California, USA, 26–29 August, 12 pp.
- Simpson, D.R. 1960. Geology of the Ramona pegmatites, San Diego County, California. PhD thesis, California Institute of Technology, Pasadena, California, USA, 197 pp. + 4 plates.
- Snee, L.W., Foord, E.E., 1991. ⁴⁰Ar/³⁹Ar thermochronology of granitic pegmatites and host rocks, San Diego County, California: Geological Society of America Abstracts with Programs, 23(5), A479.
- Symons, D.T.A., Smith, T.E., Kawasaki, K., Walawender, M.J. 2009. Paleomagnetism of the mid-Cretaceous gem-bearing pegmatite dikes of San Diego County, California, USA. *Canadian Journal of Earth Sciences*, 46(9), 675–687, <https://doi.org/10.1139/e09-035>.

Phase transformations as important markers for heat treatment detection in corundum and other gemstones

Michael S. Krzemnicki^{1,2}, Pierre Lefèvre¹, Wei Zhou¹

¹ Swiss Gemmological Institute SSEF, Aeschengraben 26, CH-4051 Basel, Switzerland

² Department of Environmental Sciences, Bernoullistrasse 36, University Basel, Switzerland

michael.krzemnicki@ssef.ch

Keywords: Heat treatment, diaspore, goethite, dehydration, Raman spectroscopy

Introduction

Detection of heat treatment of ruby and sapphire and other colour varieties of corundum is a major issue for the trade and laboratories alike. Heat treatment of corundum is commonly applied in a large temperature range from about 700 to 1800 °C in both, oxidizing and reducing conditions.

Traditionally, the detection of corundum heat treatment is based mainly on meticulous microscopic observation. As a consequence of the heating process, internal features (e.g. fluid and solid inclusions, zoning features) may be affected and altered (Gübelin & Koivula 2006) and by this provide a straightforward evidence of heat treatment. In general, characteristic heating features (e.g. discoid tension cracks around inclusions, see Figure 1) become more prominently visible with increasing temperature (and heating duration). Far more challenging is the microscopic detection of so-called “low-temperature” heated corundum. In these stones which are heated at about 700 °C to 1100 °C only very minute or even no alterations of inclusions may be observed under the microscope (Hughes & Vertriest 2022). Another classic approach is to check for “chalky” fluorescence reactions under shortwave ultraviolet light. However, such reactions can generally only be expected at higher heating temperatures well beyond 1100 °C.

Heat treatment detection is also very much relying on FTIR and Raman spectroscopy. In FTIR, the focus is very much on the presence and intensity of OH- related absorption peaks. Namely the 3309, 3232 and 3185 cm⁻¹ series in metamorphic corundum is considered a strong indication for artificial heat treatment (Smith 1995; Beran & Rossman 2006; Saeseaw et al. 2020; Pardieu et al. 2015; Krzemnicki 2019). The presence or absence of a Mg-O related band at



Figure 1: Discoid extension features indicating heating (at high temperatures) in this Ti-diffusion treated sapphire. Magn. 50x. Photo: M.S. Krzemnicki, SSEF

3160 cm⁻¹ is another important criterion, as this band is reduced or completely disappears during heating (Smith & van der Bogert 2006). Another approach is to determine the peak width (FWHM) of the main Raman peak of zircon inclusions. This approach has been explored more recently (Wang et al. 2006; Krzemnicki et al. 2021; Karampelas et al. 2021), notably in pink sapphires from Ilakaka (Madagascar) as a way to detect heat treatment. However, this criterion remains to some extent difficult and less conclusive, as the FWHM ranges of unheated and heated corundum show considerable overlap (Krzemnicki et al. 2021).

New research experiments on pink sapphires and rubies

This study presents results of heating experiments on pink sapphires (Ilakaka, Madagascar) and rubies (Montepuez, Mozambique) recently carried out at SSEF. These experiments revealed that mineralogical phase transformations

occurring in-situ in inclusions within corundum may be very promising markers for the detection of heating – or better for evidence of an absence of heat treatment in a corundum

sample. With controlled heating experiments (T, t, oxidizing conditions), two dehydration phase transformations were studied over the past few months.

i.	i)	Diaspore	2 x AlO(OH)	to	Corundum	Al ₂ O ₃ + H ₂ O
i.	ii)	2 Goethite	2 x α-Fe ₃ +O(OH)	to	Hematite	α-Fe ₂ O ₃ + H ₂ O

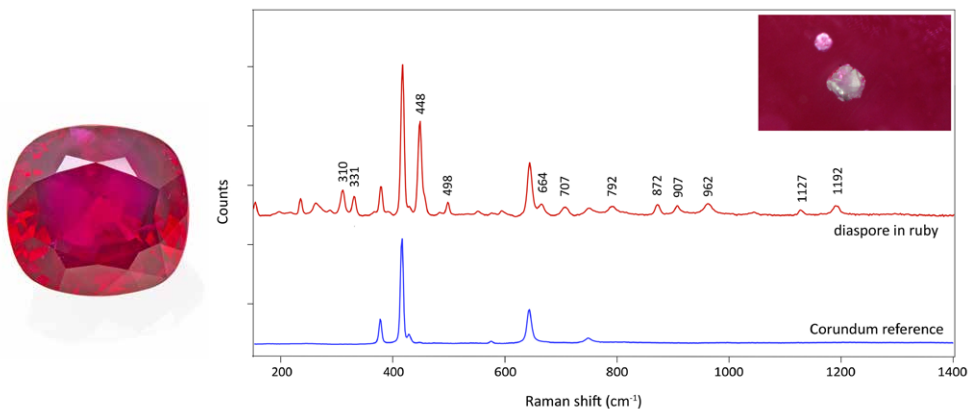
Both phase transformation systems have been studied extensively in the past decades. Both hydrates, diaspore and goethite are known to be thermally stable only up to about 350-500 °C and to transform to their respective Al- and Fe-oxide phases when further heated (Lima-de-Faria 1963; Ervin 1952; Frost et al. 1999; Gialanella et al. 2010). The dehydration of inclusions of goethite to hematite during the heating of corundum was already described by Koivula (2013) and Sripoonjan et al. (2016).

heating step). Our Raman spectroscopic analyses clearly show that both phase transformations mentioned above can be well monitored by Raman spectroscopy even if these phases are present only as tiny inclusions in corundum. Both, diaspore and goethite dehydrated inevitably to their oxides (corundum and hematite) at 350-500° C, thus way below the temperatures at which corundum commonly is heat treated.

In our initial (unheated) samples, diaspore and goethite were common epigenetic inclusions. Diaspore was present as a tiny colourless acicular solid phase in fluid inclusions (e.g. negative crystals), giving it a whitish granular aspect. Goethite, introduced at a late stage through meteoric waters in and on the surface of corundum (pebbles) was present as orange-beige staining in fissures and hollow tubes. Selected inclusions in the studied corundum samples together with goethite and diaspore reference samples were analysed by Raman spectroscopy before heating and after each consecutive step of the heating process (300, 400, 600, 800, 1000 °C, one hour peak temperature per

In summary, the presence of either diaspore or goethite inclusions in corundum can be considered a very strong evidence, that a corundum sample has not been heat treated. It is important to know, however, that the absence of diaspore or the presence of hematite is not necessarily a proof of heating, specifically as hematite precipitations may also occur naturally in corundum. In the past few months, we have applied these phase transformation markers successfully on numerous client stones (Figure 2). By adopting this approach, we were able to conclude a treatment status even in cases where no other feature (microscopically or spectroscopically) was sufficiently conclusive.

Figure 2: The Estrela da Fura Ruby, a 55 ct unheated ruby from Mozambique. This ruby contains small negative inclusions with whitish substance (see inset photo) which was positively identified as diaspore by Raman spectroscopy. Figure: M.S. Krzemnicki, SSEF



References:

- Beran A., Rossman G.R., 2006. OH in naturally occurring corundum. *Eur. J. Mineral.* 2006, 18, pp. 441-447
- Ervin, G., 1952. Structural interpretation of the diaspo-re-corundum and boehmite- Al_2O_3 transitions. *Acta Crystallogr.*, 5, 103-108
- Frost R.L., Klopogge J.T., Russell S.C., and Szetu J., 1999. Dehydroxylation and the vibrational spectroscopy of aluminum (oxo)hydroxides using infrared emission spectroscopy. Part III: diaspo-re. *Applied Spectroscopy*, 53 (7), 829-835
- Gialanella S., Girardi F., Ischia G., Lonardelli I., Mattarelli M., Montagna M., 2010. On the goethite to hematite phase transformation. *Journal Therm. Anal. Calorim.*, 102, 867-873
- Gübelin E.J., Koivula J.I., 2006. Photoatlas of Inclusions in Gemstones, Volume 3. *Opinio*, Basel, 750 pp.
- Hughes E.B., Vertriest W., 2022. A canary in the ruby mine: Low-temperature heat treatment enhancement of Burmese ruby. *Gems & Gemology*, 58 (4), 400-423 <http://dx.doi.org/10.5741/GEMS.58.4.400>
- Karampelas S., Hennebois U., Mevellec J.-Y., Pardieu V., Delaunay A., and Fritsch E., 2021. Identification of heated pink sapphires from Ilakaka (Madagascar). *The 7th International Gem & Jewellery Conference (GIT)*, Chanthaburi, Thailand, Abstract Volume, p. 212
- Koivula J.I., 2013. Useful visual clue indicating corundum heat treatment. *Gems & Gemology*, 49 (3), 160-161. <http://dx.doi.org/10.5741/GEMS.49.3.160>
- Krzemnicki M.S., 2019. Detection of low-temperature heated rubies from Mozambique. *SSEF Facette*, 25, p. 9
- Krzemnicki M.S., Lefèvre P., Zhou W., Wang H.A.O., 2021. Zircon inclusions in unheated pink sapphires from Ilakaka, Madagascar: A Raman spectroscopic study. *IGC 2021 Proceedings*, 21-23
- Lima-de-Faria J., 1963. Dehydration of goethite and diaspo-re. *Zeits. Kristallogr.*, 119, 176-203
- Pardieu V., Saeseaw S., Detroyat S., Raynaud V., Sangsawong S., Bhusrisom T., Engniwat S., Muyal J., 2015. "Low temperature" heat treatment of Mozambique ruby. *GIA Research News*, https://www.gia.edu/doc/Moz_Ruby_LowHT_US.pdf
- Saeseaw S., Khowpong ., and Vertriest W., 2020. Low-temperature heat treatment of pink sapphires from Ilakaka, Madagascar. *Gems & Gemology*, 56 (4), 448-457. <http://dx.doi.org/10.5741/GEMS.56.4.448>
- Smith, C.P., 1995. A contribution to understanding the infrared spectra of rubies from Mong Hsu, Myanmar. *J. Gemmology*, 24, 321-335
- Smith, C.P., van der Bogert, C., 2006. Infrared Spectra of Gem Corundum, *Proceedings of the GIA Gemological Research Conference*, *Gems & Gemology*, 42(3), 92-93
- Sripoonjan T., Wanthanachaisaeng B., Leelawatanasuk T., 2016. Phase transformation of epigenetic iron staining: Indication of low-temperature heat treatment in Mozambique ruby. *Journal of Gemmology*, 35 (2), 156-161
- Wang W., Scarratt K., Emmett J.L., Breeding C.M., Douthit T.R., 2006. The effects of heat treatment on zircon inclusions in Madagascar sapphires. *Gems & Gemology*, 42 (2), 134-150 <http://dx.doi.org/10.5741/GEMS.42.2.134>

Applications of Python for Spectroscopic Data Processing, Analysis and Machine Learning Modeling in Gemmology

Tasnara Sripoonjan¹ and Bhuwadol Wanthachaisaeng²

¹ G-ID Laboratories, Yan Nawa, Bangkok 10120 Thailand; *tasnara@hotmail.com

² The Gem and Jewelry Institute of Thailand (Public Organization), Bangrak, Bangkok 10500 Thailand

Keywords: Python, Machine Learning, ML, algorithms, gemmological analysis

Introduction

Python, a powerful programming tool with extensive scientific computing capabilities, is being increasingly utilized in gemmological science. It is particularly well-suited for processing and analyzing spectroscopic data, which is crucial for various machine learning (ML) applications in gemmology. By leveraging ML algorithms and models, Python can automate time-consuming tasks, reduce human error, and enhance the overall efficiency of gemmological analysis and identification. This article will provide a general overview of how Python processes and analyzes spectroscopic data, highlighting its significance in ML-based gemmological data modeling.

Why Python?

Python is a popular high-level, interpreted programming language known for its strong code abstraction, making it easily understandable for humans. It has gained wide acceptance in various domains, including data science, artificial intelligence, and scientific computing. Python's modularity is a significant advantage, allowing users to import and utilize pre-existing code through packages and libraries designed for specific tasks. Its extensive library ecosystem makes Python suitable for diverse scientific applications, such as analyzing large datasets, creating informative visualizations, and developing advanced models. In scientific disciplines like earth science, geology, and gemmology, Python's versatility shines. Noteworthy libraries that enhance Python's scientific capabilities include:

1. NumPy: Supports large arrays and mathematical functions for efficient spectroscopic data manipulation.
2. SciPy: Provides modules for optimization, signal process-

ing, linear algebra, and spectral deconvolution.

3. Pandas: Simplifies analysis of large datasets with data structures like DataFrames and Series.
4. Matplotlib: A plotting library for creating static, animated, and interactive visualizations, such as line and scatter.
5. Scikit-learn: Tools for predictive modeling, ML algorithms for gemmological determination and classification.

Machine Learning for Gemmological Applications

ML provides an alternative to conventional identification methods that mostly rely on expert knowledge and experience alone. ML algorithms can learn and recognize distinctive properties and characteristic features of gemstones (Wang & Krzemnicki, 2021; Wanthachaisaeng et al., 2022), such as trace element concentrations and spectral data. For example, to determine the country of origin of emeralds, trace element analysis can be employed, focusing on clustering patterns among elements such as K, V, Cr, Fe, Rb, and Cs. Additionally, the analysis of emerald treatment primarily relies on identifying characteristic peaks within the 2700-3200 cm⁻¹ range of FTIR spectra. Support Vector Machines (SVM), Decision Trees & Random Forests, K-Nearest Neighbors (KNN), and Neural Networks & Deep Learning are examples of supervised learning algorithms, where models are trained using labeled data with known outputs to make predictions on new, unseen data. On the other hand, Principal Component Analysis (PCA) is an example of unsupervised learning, where models are trained on unlabeled data to discover hidden patterns, structures, or relationships.

Examples of Gemstone Analysis Process using Python and Machine Learning

This section provides guidance on the typical steps in analyzing and modeling gemmological spectroscopic data using Python. The process involves data collection, pre-processing, cleaning, and feature extraction, followed by

model training, evaluation, and deployment. It is important to note that analyzing and modeling gemmological spectroscopic data can vary depending on the dataset, research question, and intended application. Thus, the examples in this section are a general guide rather than a rigid set of rules. Figure 1 provides an overview of the entire process.

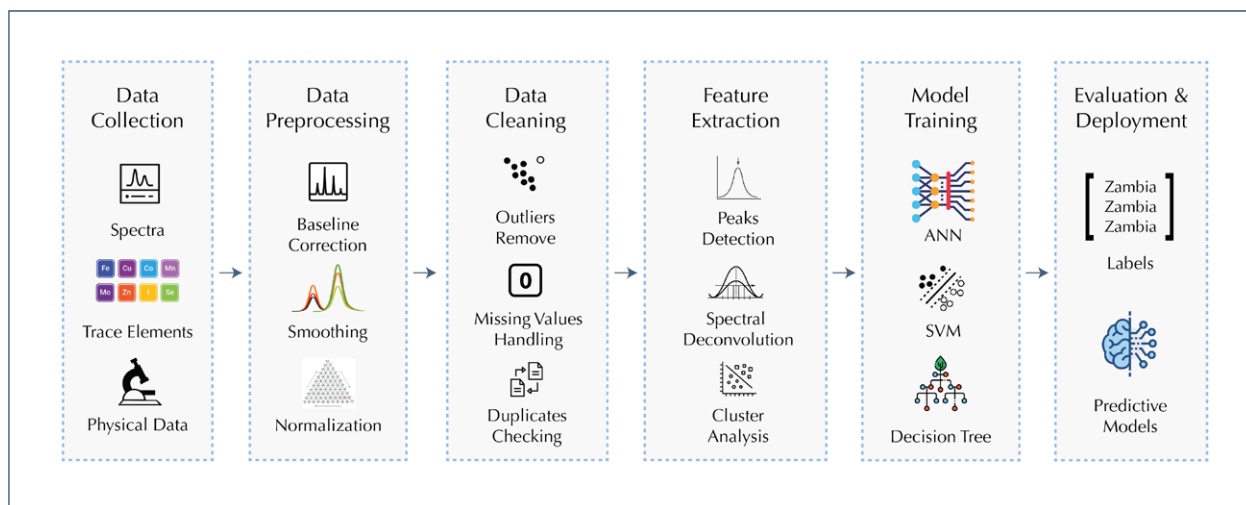


Figure 1. Python and Machine Learning (ML) workflow for gemmological applications.

Let's begin by examining the first step of the process:

(1) Data collection: Digital raw data from techniques like Raman, FTIR, EDXRF, and trace elements are collected and stored in various file formats such as CSV, ASCII, or TXT. Python libraries like Pandas, NumPy, and SciPy, can read, manipulate, and combine these files into the desired format, preparing them for pre-processing and analysis.

(2) Pre-processing: In spectroscopy, specifically Raman spectrum, pre-processing steps like baseline correction, smoothing, and normalization are commonly used to eliminate background fluorescence, instrument noise, and other interferences. The asymmetry least squares (ALS) method is a popular algorithm for baseline correction, implementable in Python using the "als" function from the SciPy library (Figure 2). Applying a Savitzky-Golay filter through the 'savgol_filter' function can effectively denoise and improve the signal-to-noise ratio of a one-dimensional signal. While not demonstrated here, spectrum normalization using SciPy is essential for establishing a consistent metric.

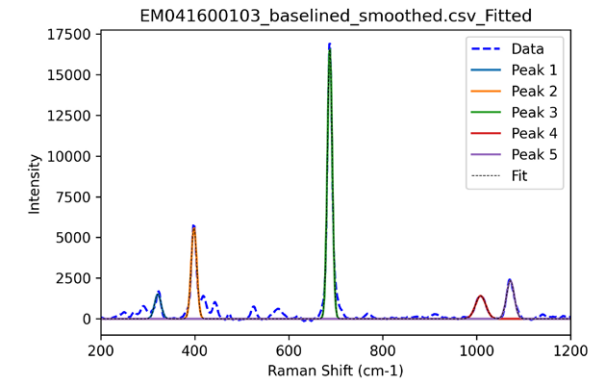
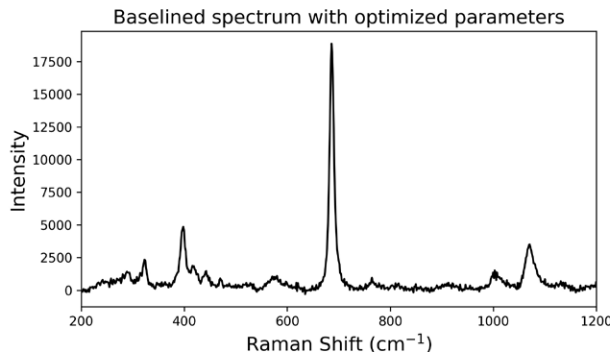
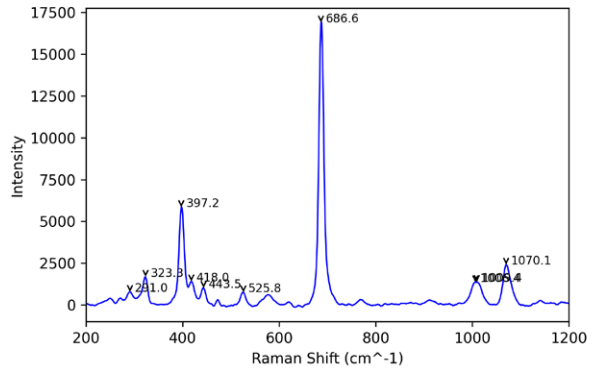
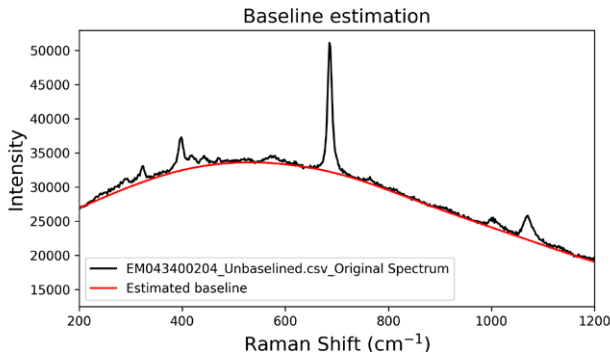


Figure 2. Show here is ALS-based baseline estimation algorithm in SciPy library was used to process a spectrum. The red line represents the baseline estimation of a typical emerald spectrum (left) and result after subtraction (right).

Figure 3. Python offers automation capabilities for extracting spectral features. These include peak detection, which marks the identified peaks as input data for further processing (left). The representative spectrum demonstrates the prominent Raman peaks of emeralds (i.e., 323, 387, 686, 1005, and 1070 cm^{-1}), which are selected for FWHM estimation (right).

(3) Data cleaning: Outliers and artifacts can be problematic in datasets, especially for clustering tasks like gem origin determination based on trace-element concentration patterns. Data cleaning techniques, such as z-score and quantile approaches, help identify and eliminate undesirable outliers and artifacts. By removing data points that deviate significantly from the mean or fall outside the expected range, these methods ensure accurate and reliable results, enhancing the overall data quality.

(4) Feature extraction: In gemmological applications, with spectral data playing a vital role. Manually working with extensive datasets can be time-consuming, particularly

when dealing with relevant features hidden within spectra. The SciPy provides peak detection and curve fitting capabilities (Figure 3), allowing for the peaks fitting and full width at half maximum (FWHM) estimation using mathematical formulas such as Gaussian and Lorentzian functions (Ewusi-Annan and Melikechi, 2021). These methods enable the extraction of FWHM values for multiple peaks in a batch or simultaneous manner, thereby facilitating efficient characterization of spectral features. Python automates selection of all or specific peaks in spectra. FWHM values extracted from multiple peaks support further interpretation and in-depth analysis. Figure 4 demonstrates their application in aiding emerald's origin determination.

country	amp1	xbar1	fwhm1	amp2	xbar2	fwhm2	amp3	xbar3
Ethiopia	1125.045	323.8895	12.92111	1844.477	398.8792	11.74034	7313.884	687.6984
Ethiopia	6955.95	324.1157	9.743058	6493.558	398.6061	11.1174	26254.29	687.6693
Ethiopia	473.0164	320.873	21.3648	2609.593	400.1477	13.79824	9302.993	687.9167
Ethiopia	545.97	319.7164	27.15497	2550.417	399.1955	12.90616	8039.557	687.4567
Ethiopia	1993.27	324.7118	10.37943	2691.164	399.0286	13.41886	11135.49	687.8693
Ethiopia	2132.538	324.0911	10.40488	2709.184	399.0352	10.80796	11787.52	687.5363
Ethiopia	2679.805	324.1559	10.07159	2898.089	398.557	11.69848	12251.13	687.5792
Ethiopia	7088.287	324.316	9.840961	7336.372	398.771	11.05092	28553.14	687.73
Ethiopia	2795.035	323.7875	11.26765	2133.399	398.8458	11.13661	15899.02	687.4856
Ethiopia	2300.196	323.1687	10.15139	976.8378	398.4564	12.95536	15111.73	687.3196
Ethiopia	2273.286	324.239	14.74582	2690.186	399.0625	13.37351	11262.69	687.786
Ethiopia	5263.144	323.8812	10.79853	5032.039	398.439	11.44333	21597.36	687.2896
Ethiopia	3656.603	323.7767	10.14732	4300.458	398.3712	11.76489	16115.35	687.1809
Ethiopia	3474.717	324.1641	10.89909	2409.039	398.6571	13.21645	17280.05	687.6196
Ethiopia	686.1896	322.4724	22.04247	3369.133	399.5133	13.62002	11635.95	687.6109
Ethiopia	655.9182	322.3252	13.49903	3399.879	399.7007	13.36756	11267.61	687.614
Ethiopia	934.7266	324.0766	12.49639	808.9192	399.6733	15.32687	8945.336	687.6966
Ethiopia	667.8871	321.2454	20.06667	2477.28	399.2524	12.98505	8785.506	687.5769
Ethiopia	607.2738	322.8501	14.57039	3040.873	399.1751	11.61113	10124.75	687.6845
Ethiopia	3417.518	323.829	10.71691	1869.096	397.8373	11.73434	17234.7	687.4048
Ethiopia	3069.505	323.7677	9.084293	3264.454	397.915	12.75705	13393.29	686.9
Ethiopia	2932.532	323.749	9.245842	3175.786	397.925	12.2735	13177.5	686.9082

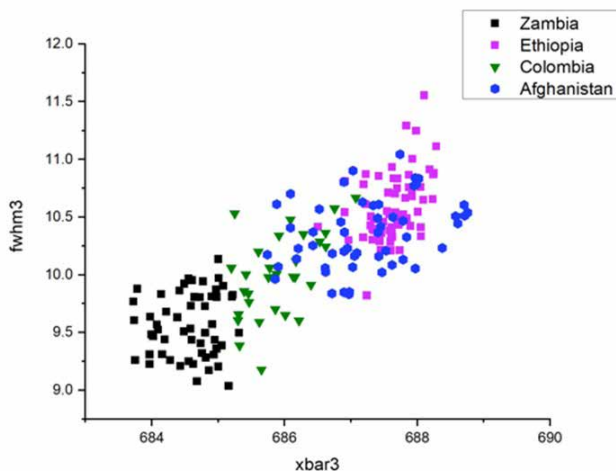


Figure 4. An example of spreadsheet illustrating FWHM values obtained from the selected Raman peaks of emeralds using Python coding techniques. The extracted data can be further utilized for interpretation, clustering visualization, and aiding in the determination of the emerald's origins in the certain case (right).

The processed data, relied on FWHM values of the selected Raman band ($\sim 686 \text{ cm}^{-1}$) in emeralds from different deposits (Zambia, Ethiopia, Colombia, Afghanistan), revealed a spectral feature associated with the difference in peak bandwidth. This feature correlates with the unique crystal structure and also corresponds to varying refractive index of emeralds found from each deposit (Zwaan et al., 2005), making it a potential candidate for ML modeling.

(5) Modeling and evaluation: The processed data is imported for modeling using learning algorithms with the aid of statistical techniques via Python. The choice between supervised or unsupervised learning depends on the data characteristics, and in this study, supervised learning is only employed for demonstration. Model performance is evaluated using metrics such as confusion matrices, accuracy, precision, recall and f1-score. These metrics provide insights into the effectiveness of the model and assist in selecting the appropriate algorithm. The widely recognized Scikit-learn library offers tools for calculating and interpreting these metrics.

In general, precision measures accurate positive predictions, recall measures finding all positive instances, and the

F1 score balances precision and recall. Accuracy evaluates correct class labels. Figure 5 (left) shows the EPA model with ANN using the FWHM feature with 53% accuracy, considered inconsistent. Nevertheless, it may have utility for certain circumstance like distinguishing Zambian from Ethiopian emeralds. In contrast, our research utilized trace-element concentration achieving 94% accuracy (Figure 5, right). However, overfitting can occur when a model performs well on training data but fails to generalize unknown data. Proper feature management and understanding limitations are crucial for ML application. Continuous improvement through model updating and fine-tuning is essential.

Challenges and Future Prospects

As is well-known, certain popular software packages are effective tools for processing, analyzing, and visualizing spectroscopic data. However, these packages may not be able to automate tasks or develop ML models. In contrast, Python provides sophisticated and customizable solutions for complex ML tasks and algorithms. Proficiency in programming is necessary to leverage these capabilities, and the visualization features may be limited compared to the dedicated spectroscopy software.

```
ann: 0.667
```

	precision	recall	f1-score	support
Afghanistan	0.80	0.40	0.53	10
Brazil	0.00	0.00	0.00	5
Colombia	0.17	0.20	0.18	5
Ethiopia	0.50	0.90	0.64	10
Zambia	0.64	0.70	0.67	10
accuracy			0.53	40
macro avg	0.42	0.44	0.40	40
weighted avg	0.50	0.53	0.48	40

```
ann: 0.956
```

	precision	recall	f1-score	support
Afghanistan	1.00	1.00	1.00	10
Brazil	0.80	0.80	0.80	5
Colombia	1.00	1.00	1.00	10
Ethiopia	0.91	1.00	0.95	10
Pakistan	0.67	1.00	0.80	2
Zambia	1.00	0.80	0.89	10
accuracy			0.94	47
macro avg	0.90	0.93	0.91	47
weighted avg	0.95	0.94	0.94	47

Access to high-quality datasets for training ML models in gemmology may be limited, which can hinder their effectiveness and make it challenging to create accurate models and understand the features behind their predictions. These issues are likely to impact gemmologists' trust if wrong results are significantly produced by ML models.

Conclusion

In conclusion, Python can greatly benefit automated tasks and data analysis, but we assume that Machine Learning (ML) algorithms will become more important in gemstone analysis in the future. Python's versatility and scientific computing capabilities are considered suitable for processing and analyzing spectroscopy data, while ML algorithms may enhance the accuracy of gemstone determination.

Figure 5. Data characteristics play a crucial role in accurate predictions during modeling, as shown in the emerald origin determination based on peak FWHM values (left) and trace element concentrations (right) using the same algorithm.

The effectiveness of ML can be hindered by various challenges, including the limited availability of high-quality data, model complexity, and difficulty in understanding algorithms. Nevertheless, we are convinced that improved gemmological analysis with data science may overcome these challenges and eventually lead to more accurate and reliable ML models in the future.

References

- Barton, S. J., Ward, T. E., Hennelly, B. M. 2018. Algorithm for optimal denoising of Raman spectra. *Analytical Methods*, 10, pp. 3759-3769
- Eilers, P. H. C., and Boelens, H. F. M. 2005. Baseline correction with asymmetric least squares smoothing. *Leiden University Medical Centre Report*, 1-22.
- Ewusi-Annan, E., & Melikechi, N. 2021. Unsupervised fitting of emission lines generated from laser-induced breakdown spectroscopy. *Spectrochimica Acta Part B: Atomic Spectroscopy*, 177(50–55): 106109
- GIT. 2021. New Directions: An Announcement from GIT on their work using AI as a New Tool for the Origin Determination of Gemstones. *The Journal of The Gemmological Association of Hong Kong*. 42, pp 5.
- He, S., et al. 2014. Baseline correction for Raman spectra using an improved asymmetric least squares method. *Analytical Methods*, 6(12): 4402-4407.
- Li, Y., Feng, X., Liu, Y., Han, X. 2021. Apple quality identification and classification by image processing based on convolutional neural networks. *Sci Rep* 11, 16618.
- Petrelli, M. 2021. *Introduction to Python in Earth Science Data Analysis: From Descriptive Statistics to Machine Learning*. Springer Textbooks in Earth Sciences, Geography and Environment. Springer Cham, 229p.
- Wanthanachaisaeng, B., et al. 2022. An Artificial Intelligence Approach to Build Smart Databases for Origin Determination of Ruby and Sapphire. *Bangkok Gems and Jewelry Fair*, Bangkok, (Online).
- Zwaan, H., et al. 2005. Emeralds from the Kafubu Area, Zambia. *Gems & Gemology* 41(2): 116-148.

Effects of Gamma Irradiation on Ruby and Pink Sapphire and Potential Detection Methods in Gem Labs

Hao A.O. Wang¹, Dirk Weltz², Michael S. Krzemnicki¹, Andreas Mack², Markus Wälle¹

¹ The Swiss Gemmological Institute SSEF, Basel, Switzerland; hao.wang@ssef.ch

² Swiss Neuro Radiosurgery Center, Zurich, Switzerland.

Keywords: Ruby, Pink sapphire, Gamma irradiation, UV-VIS, Raman, R-Line

Gamma irradiation is a non-destructive and non-invasive treatment method used to enhance the colour and aesthetic appeal of gemstones, such as diamond, topaz, quartz, and sapphire. In this process, high-energy gamma rays emitted - either from radioactive isotopes typically cobalt-60 (⁶⁰Co) or from a linear accelerator (LINAC) - introduce point defects by displacing or ionizing atoms in the crystal structure of a gemstone. The resulting electron movement may create colour centres, inducing a desired colour change that ranges from subtle to dramatic, depending on the chemical composition of the stone and irradiation conditions.

Gamma irradiation has been investigated as a treatment method for corundum for decades (Johnson and Grow 1964, Nassau 1983). Following the initial development of ruby lasers in the 1960s, much research has been dedicated to understanding the influence of gamma radiation on ruby, primarily in relation to alterations in laser properties (Johnson and Grow 1967, Brown and Brown 1981). Within gemmology, the focus has largely been on examining how gamma irradiation can modify the color or hue of yellow or pale-colored corundum to achieve a deeper shade (Nassau and Valente 1987).

Although previously reported (Ashbaugh 1988), more recently, evidence from multiple trustworthy sources has indicated that some rubies and fancy sapphires in pink or purple shades may undergo gamma irradiation before entering the marketplace, which initiate immediate actions in gem labs to detect this treatment (Pardieu et al. 2022, Scarratt - personal communication 2022, Leelawatanasuk – personal communication 2022, Krzemnicki 2022, Krzemnicki 2023). It is believed that this gamma irradiation treatment is carried out in medical facilities, utilizing cancer radiotherapy equipment to enhance the corundum's color.

This practice is driven by the desire to decrease the purple hue in purple sapphires and rubies to reach a better red or pink color, or to increase the yellow hue in pink sapphires, resulting in a pinkish orange colour that is highly coveted in the gemstone industry – the Padparadscha sapphire.

Since more than a year, the Swiss Gemmological Institute SSEF is collaborating with the Swiss Neuro Radiosurgery Center with the aim to better understand the effect of gamma-irradiation on Cr-bearing corundum and to develop subsequently potential methods to detect such irradiated corundum. So far, we have conducted a series of gamma irradiation experiments on corundum samples with colors ranging from light pink to dark red. Some of the samples were annealed (1200°C for 10h) before gamma irradiation to eliminate any potential residual effects from previous treatments on the host gemstone and reset (anneal) the zircon inclusions. The reason for this pre-treatment process was to make the effects of gamma irradiation more pronounced and discernible. A LINAC instrument (ZAP-X, Gyroscopic Radiosurgery platform, USA) was used as the gamma source to irradiate the gemstones. This device features a well-defined 3D radiation profile and offers accurate dose control. The samples were exposed to a total radiation dose of 10,000 Gray in increments of 2,000 Gray. Following the irradiation experiments, immediate visual inspection was conducted. Various analytical methods, such as UV-VIS absorption spectroscopy and ruby R-line fluorescence analysis were applied to compare the results before and after gamma irradiation. In addition to the effects on the host gemstone, the impact on zircon inclusions within the fancy sapphires was assessed using Raman micro-spectroscopy.
















Sample	Original	Heated at 1200°C for 10h	Right after 10k Gy Gamma Irradiation	4 months after Gamma Irradiation
Sample #1 Pink Fancy Sapphire		No heat		
Sample #2 Pink Fancy Sapphire				
Sample #3 Light Pink Fancy Sapphire				
Sample #4 Purplish Pink Fancy Sapphire				

Figure 1: Visual changes of pink sapphires after heat treatment and gamma radiation treatment.



Figure 2: Visual inspection of ruby (six dark red slices, cut from a single stone) after gamma radiation treatment with incremental change in radiation dose.

The study reveals that gamma irradiation has a notable effect on the colour of pink sapphire, causing a shift from pink or purple hues to orange (Figure 1). However, this colour transformation appears to be generally unstable, as most pink sapphires revert to their original colour within a few months. However, in our samples, there was one exception (light pink sapphire Sample #3) which after exposure to gamma irradiation retained its orange hue, albeit with reduced intensity, for more than four months without reverting to its initial color. Even after undergoing a fading test, the orange shade of Sample #3 persists and is deemed stable. Hence, it can be deduced that at least two types of colour centres might be involved in this scenario. One color center might be stable, while the other is unstable. In contrast, the colour of our ruby slices (dark red) did not exhibit any noticeable change after gamma irradiation (Figure 2). These observations on our corundum samples indicate that the effect of gamma irradiation might differ between high Cr and low Cr corundum (Powell 1966).

Furthermore, UV-VIS spectroscopy analysis demonstrates an increase in absorption at around 320 nm and 475nm after gamma irradiation (Figure 3). The absorption band at around 475nm is particularly interesting, since it did not increase after heat treatment, but only after gamma irradiation. A similar absorption band in ruby due to gamma irradiation has been described previously (Maruyama and Matsuda 1964). When a trapped hole (O-1) is formed near Fe³⁺ or Cr³⁺, which replaces Al³⁺ in the crystal lattice, a similar absorption band was reported to cause orange color in corundum (Dubinsky et al. 2020). Gamma irradiation might be responsible for the creation of the trapped holes, as a result showing an increased orange color in Cr-bearing corundum. However, UV-VIS absorption spectra are complex, and a deconvolution of absorption bands to corresponding chromophores is not yet achieved.

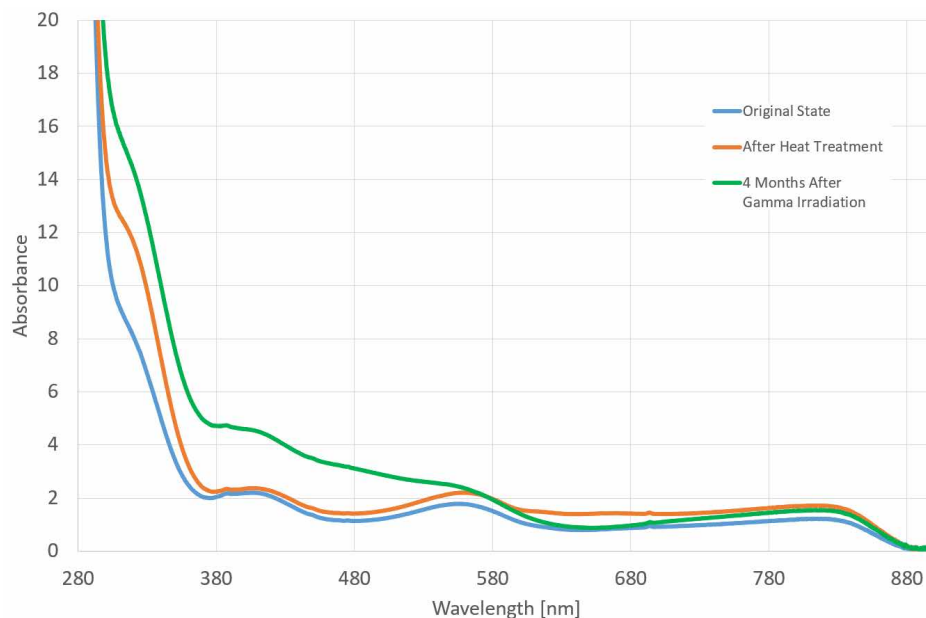


Figure 3: UV-VIS Spectra comparison of Sample #3 in its original state, after heat treatment and four months after gamma irradiation treatment.

Unfortunately, at the time of this abstract submission for IGC 2023, neither colour change nor UV-VIS spectrum can offer conclusive evidence for detecting gamma-irradiated corundum, as the changes induced by gamma irradiation can also be present in natural, untreated stones (Nassau and Valente 1987, Dubinsky et al. 2020). It currently is only possible to detect the treatment when the stone has been analyzed in its pre-treatment state.

The broadening of zircon Raman peaks has been studied in literature (Nasdala et al. 1995; Zhu et al. 2015) and is caused by increased lattice disorder due to gamma radiation. In our experiment, results gathered from over ten zircon inclusions (fixed orientation) in each individual pink sapphire demonstrated no statistically significant indication of Raman peak broadening following gamma radiation. This observation could be attributed to the gamma irradiation dose being insufficient to induce any noticeable change. Conversely, the heat treatment (pre-treatment of

our samples) significantly reduced the FWHM of zircon Raman peaks.

Ruby R-lines are fluorescence emission lines due to Cr^{3+} in the corundum lattice. Prior research has indicated that gamma irradiation may reduce the amount of Cr^{3+} in corundum, leading to the formation of Cr^{2+} and an expected decrease in R-line intensity. The presence of Cr^{2+} has been confirmed through thermal conductivity measurements (De Goer and Dreyfus 1967) and the reduction of Cr^{3+} has been confirmed through electron paramagnetic resonance (EPR) studies (Maruyama and Matsuda 1964). In our R-line experiment, excited by a 514.5 nm laser and analyzed by a Raman system, we observed a reduction in R-line intensity for gamma-irradiated pink sapphires, but not in dark red ruby. After leaving the pink sapphires at room temperature for four months, an increase in R-line intensity was observed, although not fully returning to the original state's level.

Ongoing research is focused on exploring the relationship between R-line intensity and Cr concentration aiming at finding a more conclusive detection method for the gamma-irradiated ruby and pink sapphires. The naturally occurring proportion of Cr³⁺ in the total Cr content of corundum from specific geographic origins and with elemental compositions could potentially be determined and used as a benchmark for identifying gamma-irradiated Cr-bearing corundum, which may contain a disproportionately smaller portion of Cr³⁺. It is essential to note that this proposed detection method should incorporate additional evidence, such as increased absorption around 475nm in the UV-VIS spectrum. It is also crucial to consider that a fancy sapphire may have experienced natural irradiation if exposed to fluids containing radioactive elements. With the current techniques, it remains challenging to differentiate between naturally and artificially irradiated rubies or pink sapphires.

References

- Ashbaugh, C. E., 1988. Gemstone Irradiation and Radioactivity. *Gems & Gemology* 24, no. 4, 196-213.
- Brown, I. J., and M. A. Brown, 1981. Low-Temperature Thermal Expansion of γ -Irradiated Ruby. *Physical Review Letters* 46, no. 13, 835-837.
- De Goer, A. M., and B. Dreyfus, 1967. γ -Irradiation Effect on the Thermal Conductivity of Al₂O₃ with Cr or Mn Impurities at Low Temperature. *Physica Status Solidi* 22, no. 1, 77-82.
- Dubinsky, E. V., J. Stone-Sundberg, and J. L. Emmett, 2020. A Quantitative Description of the Causes of Color in Corundum. *Gems & Gemology* 56, no. 1, 2-28.
- Johnson, V.R., and R.W. Grow, 1964. Gamma Irradiation Effects in Ruby. *Proceedings of the IEEE* 52, no. 2, 185-186.
- Johnson, V. R., and R. W. Grow, 1967. Effects of γ -Irradiation on the Performance of a Ruby Laser. *IEEE Journal of Quantum Electronics* QE-3, no. 1, 858-859.
- Krzemnicki, M. S., 2022. New Additional Test at SSEF for The Colour Stability of Rubies SSEF Newsletter. <https://www.ssef.ch/new-additional-test-at-ssef-for-the-colour-stability-of-rubies/>
- Krzemnicki, M. S., 2023. The Frontier of Research: Irradiation Experiments on Corundum. *Facette* no. 28, 40.
- Maruyama, T., and Y. Matsuda, 1964. Color Centers in γ -Irradiated Ruby. *Journal of the Physical Society of Japan*, no. 7, 1096-1104.
- Nasdala, L., G. Irmer, D. Wolf, 1995. The degree of metamictization in zircon; a Raman spectroscopic study. *European Journal of Mineralogy* 7, no. 3, 471–478.
- Nassau, K., 1983. *The Physics and Chemistry of Color*. John Wiley & Sons Inc, New York.
- Nassau, K., and G. K. Valente, 1987. The Seven Types of Yellow Sapphire and their Stability to Light. *Gems & Gemology* 23, no. 4, 222-231.
- Pardieu, V., K. Scarratt, R. Hughes, 2022. Irradiation of Rubies · A Cautionary Note. dated Feb. 23.
- Powell, R. C., 1966. The Interaction of Chromium Ions in Ruby Crystals. *Physical Sciences Research Papers*, no. 299. Massachusetts: Office of Aerospace Research.
- Zhu, W., L. Fan, and X. Lu, 2015. Structural evolution under gamma ray irradiation of zircon originated from Hainan province, China. In *Proceedings of the 3rd International Conference on Material, Mechanical and Manufacturing Engineering*. Guangzhou, China: Atlantis Press, 1748-1752.

Irradiation treatment and gamma-spectroscopy of morganite

Tom Stephan¹, Vladimir Hutanu², Xiaosong Li², Thomas Lind^{1,3} & Stefan Müller³

¹ German Gemmological Association, Idar-Oberstein; t.stephan@dgemg.com

² FRM II Forschungsneutronenquelle, Technical University, Munich

³ DSEF German Gem Lab, Idar-Oberstein

The pink variety of beryl, morganite, is one of the most popular orangey-pink to pink gemstones. Its colour is attributed to manganese, both Mn²⁺ and Mn³⁺ (Nassau & Wood, 1968, Wood and Nassau, 1968, Schmetzer et al., 1974, Shigley and Ford, 1984, Deer et al., 1992), which produce a series of spin-allowed absorption bands between 450 to 600 nm. Their exact position and quantity depends on the strength and symmetry of the local crystal field, which, among others, also depends on the substitution mechanisms on the Be-position in the crystal lattice (Platonov et al., 1989). By thermal enhancement, the colour of pink morganites is

usually not influenced much (Schmetzer et al., 1975), however, orangey hues can be removed. By artificial irradiation the colour saturation of colourless to pale pink manganese-bearing beryl is strongly intensified, due to an intensification of the manganese-band system (see also Schmetzer et al., 1975). Iron-bearing samples become orangey-pink to brown, due to an additional intensification of the oxygen-metal-charge-transfer-band system (OMCT-band system, Fe³⁺-O²⁻—CT). These samples can be heat treated after irradiation, weakening the OMCT-band system again and resulting in pure pink colours.



Figure 1: Mn- and Fe-bearing beryls from different localities (Braz = Brazil, Mada = Madagascar, Nig = Nigeria, Moz = Mozambique, unk = unknown) before (left) and after (right) irradiation with electrons.

Usually by gamma irradiation, mainly the OMCT-band system of iron-bearing beryl is increased, the pink colour component (Mn) enhances just weakly to not at all. By irradiation with neutrons in nuclear reactors or accelerators also the pink colour component is intensified, however, most morganites, due to their natural caesium contents, become strongly radioactive, mainly by a production of the radioactive isotope Cs-134 from the stable isotope Cs-133 (see e.g. Kitawaki et al., 2012). Therefore, the method-of-choice for the artificial enhancement of the pink hue of morganites by irradiation nowadays is the bombardment with electrons in accelerators. Using this technique only very little Cs is activated to Cs-134, resulting in activities usually far below legal limits.

The most common instrument to detect radioactivity is the Geiger counter, which, however, just indicates if the material is radioactive, but it cannot detect the type or amount of radionuclides causing the radioactivity. Gamma-spectroscopy is used to determine the type of radioactive isotopes and their activity. A detailed description of the technique and the applications in gemmology has been published by Ashbaugh in 1992. In 2012, Kitawaki et al. used gamma-spectroscopy to detect the activation products Cs-134, Mn-54 and Zn-65 in two large morganites irradiated by neutrons. Here we provide for the first time the evidence for usefulness of gamma-spectroscopy to identify also the electron irradiation treatment.

For this study, manganese-bearing morganites from different origins have been targeted irradiated with electrons. Afterwards, the samples were measured by gamma-spectroscopy to identify the kinds and activity of the induced radioactive nuclides, mainly Cs-134, which can be seen as evidence for artificial irradiation. The samples were selected from different localities with various natural Cs-contents. The intent is to prove if there is still enough Cs-134 produced in samples with low Cs-concentration, to clearly identify the treatment. Cs-134 has a half-life time of about 2.1 years only, thus, it could not be found in the natural samples relaxed at the geological time scales and its analytical evidence should be considered as a direct hint to the artificial irradiation treatment. On the other side, because of this relative short half-life time the technique is not expected to be expedient for morganites from old stocks. However, in combination with technologies like e.g. blockchain, it could be possible to separate natural and treated morganites, from recent mining.

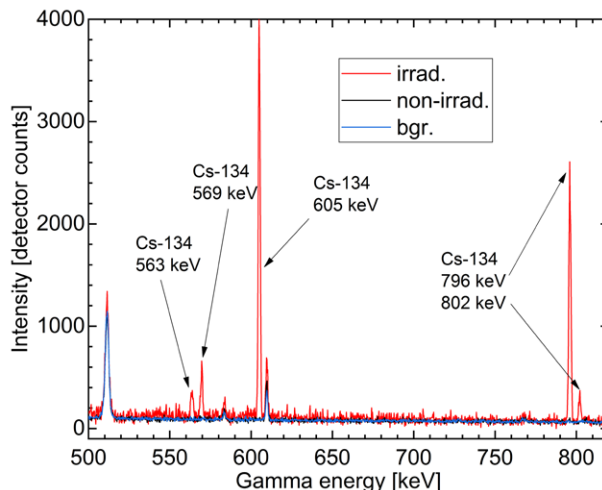


Figure 2: Gamma-spectrum of a non-irradiated and an irradiated morganite from Mozambique. Clear evidence of the characteristic for Cs-134 gamma emission lines observed after few hours of measurement.

Material and methods

For this study, fifteen morganites from the reference collection of the German Gemmological Association were cut into wafers with windows parallel to the c-axis. Different origin locations (Brazil, Madagascar, Mozambique and Nigeria) were covered. Each sample was cut into two halves (Fig. 1). One half remained untreated; the other half has been irradiated with electrons using typical industrial praxis of 10 MeV energy for 6 hours. Depending on their exact position during irradiation process small differences between single samples may occur, but the overall total dose of approximately 250 MGy was reached in all of them. The samples were irradiated together with a big lot of gem-quality morganites in a proprietary irradiation facility.

Polarized optical absorption spectra were measured with a Perkin Elmer Lambda 950S UV/Vis/NIR spectrometer in the range between 200 to 2500 nm with a resolution of 1 nm. Chemical compositions have been determined with an energy dispersive X-ray fluorescence, a Thermo Scientific ARL Quant'X EDXRF. A special beryl programme has been used to calculate the oxide concentrations; BeO was fixed to 14 %, calibration was done with well-analyzed beryl reference samples.

Gamma-spectroscopy was performed at the FRM II Research Neutron Source of the Technical University in Munich using a Canberra/Mirion Technologies coaxial high-purity germanium (HPGe) semi-conductor detector (GX4018) with a relative efficiency of 40 % and an energy resolution of 1.8 keV at 1332 keV connected with a Lynx multichannel analyser. The Genie 2000 software package was used for data analysis.

Results and discussion

Due to the irradiation, all samples became yellowish-brown to orangey-brown in colour, caused by an intensification of both, the OMCT- and the Mn³⁺-absorption bands. Using a Gamma-Scout[®] radiation detector no radiation exposure has been detected. By gamma-spectroscopy, Cs-134 was identified in the irradiated halves, while none was detected in the untreated samples (Fig. 2). Moreover, in the very recently irradiated samples also Cs-132 radioisotope with half-life time of 6.8 days only could be found. It can serve as an additional marker to indicate that irradiation took place within the last 2-3 month. Due to the short half-life time of Cs-134, this technique is effective just for morganites that were recently exposed to artificial radiation. Depending on the caesium concentration of the initial material and the energy it has been exposed to, we expect that identification is possible within few half-life times depending on sample mass, Cs concentration, counting time and gamma-detector efficiency (e.g. up 8-10 years). For samples from old stocks this method may not be appropriate. In combination with techniques tracking the material from mine to market, e.g. blockchain technologies, it can be a powerful tool to separate untreated (or thermally enhanced) material from gems artificially irradiated by high energy electrons. Cs-134 as a product of the neutron capture reaction and is not expected in untreated morganites, since corresponding reactions occur in the nature extremely rarely, combined with the short half-life of Cs-134.

Outlook

We plan more detailed investigations to determine the limits of the proposed method. In a next step, the samples investigated for this report will be heated to remove the yellow colour components and reach the pink hue enhancement. No change in the gamma spectrum is expected by the heating treatment and this will be proved. The samples will be re-measured again at regular intervals over the next few years to determine the threshold Cs-concentration at which the activity of Cs-134 falls below the detection limit, but also to determine the minimal sample size and maximum detection time after irradiation.

References

- Ashbaugh III, C. E., 1992. Gamma-ray Spectroscopy to Measure Radioactivity in Gemstones. *Gems & Gemology* 28 (2), 104-111.
- Deer, W. A., Howie, R. A. and Zussman, J., 1992. The rock forming minerals. Vol. I Longman Group Ltd., England.
- Kitawaki, H., Horikawa, Y., Shozugawa, K. and Nogawa, N., 2012. Radioactive Morganite. *Gems & Gemology* 48 (1) 42-44.
- Nassau, K. and Wood, D. L., 1968. An examination of red beryl from Utah. *Am. Mineral.* 53, 801-806.
- Platonov, A. N., Taran, M. N. and Klyakhin, V. A., 1989. On two colour types of Mn³⁺-bearing beryls. *Z. Dt. Gemmol. Ges.* 38 (4), 147-154.
- Schmetzer, K., Berdesinski, W. and Bank, H., 1974. Über die Mineralart Beryll und Absorptionsspektren. *Z. Dt. Gemmol. Ges.* 23 (1), 5-39.
- Schmetzer, K., Berdesinski, W. and Bank, H., 1975. Farbveränderungen von Edelsteinen der Beryllgruppe. *Z. Dt. Gemmol. Ges.* 24 (2), 81-87.
- Shigley, J. E. and Foord, E. E., 1984. Gem quality red beryl from the Wah-Wah mountains, Utah. *Gems & Gemology* 20 (4), 208-221.
- Wood, D. L. and Nassau, K., 1968. The characterization of beryl by visible and infrared absorption spectroscopy. *Am. Mineral.* 53, 777-800.

An implementation of machine learning in ruby and sapphire origin determination

Montira Seneewong-Na-Ayutthaya¹, Bhuwadol Wanthanachaisaeng¹, Waratchanok Suwanmanee, Thanapong Lhuaamporn¹, Pimlapat Kamkeaw¹, Sarun Phibanchon², Tasnara Sripoonjan³, and Thanong Leelawatanasuk¹

¹The Gem and Jewelry Institute of Thailand (Public Organization), ITF-Tower Building, Silom Road, Suriyawong, Bangrak, Bangkok, 10500 Thailand

²Faculty of Education, Burapha University, Chonburi, 20131 Thailand

³G-ID Laboratories in Yannawa, Bangkok, 10120 Thailand
smontira@git.or.th

Keywords: ruby, sapphire, geographical origin, chemical fingerprinting, artificial intelligence

Introduction

Country-of-origin is one of the most important value factors of corundum (ruby and sapphire) due mainly to its historical or legendary popularity in the trade. Generally, gemological laboratories in the early days determined ruby and sapphire origins simply by relying mostly on diagnostic inclusions scenes because those stones were supplied globally from only a few well-known important sources (Groat et al., 2019). However, as more and more stones have been sourced from many more geographical origins, frontline laboratories have to apply additional scientific approaches, such as spectroscopic and chemical data, to be able to well distinguish the different geological and geographical origins based on such data. (Sutherland et al., 2015; Harlow et al., 2013). Among those approaches, chemical fingerprinting or trace-element data discrimination is the most well-known technique and has become increasingly more reliable for determining the origin of the stones (Guillong & Günther 2001; Abduriyim and Kitawaki, 2006; Karampelas et al. 2019; Palke et al. 2019; Seneewong-Na-Ayutthaya et al., 2021). In addition, machine learning algorithms, a branch of artificial intelligence (AI), have been initially applied to classify the chemical database and assist the country-of-origin determination of stones (Wang & Krzemnicki 2021) For this study, well-documented samples of rubies and sapphires from selected gem-deposits were measured for their trace element contents by both EDXRF and LA-ICP-MS techniques and grouped in the form of a database of each gem deposit. The discrimination of the trace element data to evaluate the country-of-origin was carried out by 3D scatter-

ing plots and our self-developed machine learning program using our preselected samples in this work.

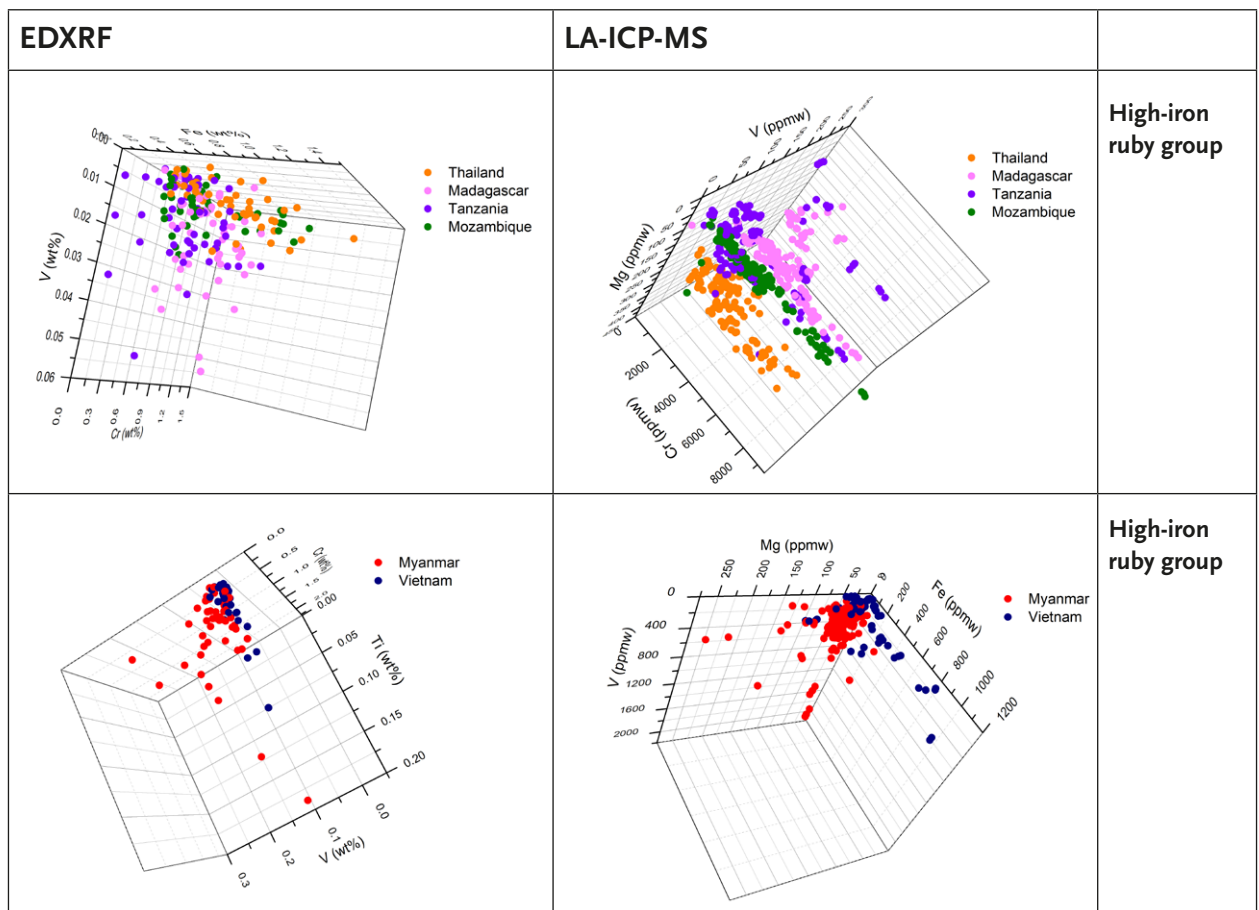
Materials and Methods

The first group of stones consists of 291 ruby samples from Myanmar (50), Vietnam (27), Thailand (50), Mozambique (51), Madagascar (Votomandry) (53), Tanzania (Winza, Mahenge, and Morogoro) (50), and test-samples (10), ranging from 0.11 to 7.21 ct. The second group comprises 290 sapphire samples from Sri Lanka (50), Myanmar (50), Madagascar (54), Thailand (51), Nigeria (50), Australia (25), and test-samples (10), ranging from 0.10 to 4.92 ct. For chemical analyses we used EDXRF (Eagle III XPL model, EDAX) and LA-ICP-MS (ThermoScientific iCAP RQ series ICP-MS coupled with a New Wave NWR-213 Nd:YAG laser) to analyze major, minor, and trace element concentrations. To evaluate the consistency of the data and to manually discriminate the country-of-origin, 3D scattering plots were constructed to depict the clustered concentration of the trace elements. Furthermore, we used a self-developed supervised machine learning program (named “AI for Gem Origin Determination”), which was pioneered and developed by Wanthanachaisaeng et al. (2020) as part of the research mission of the Gem and Jewelry Institute of Thailand (GIT). Learning algorithms consisted of K Nearest Neighbors (KNN), Random Forest (RF), Support Vector Machine (SVM), and Artificial Neuron Networks (ANN) chosen to assess the prediction accuracy of stone’s country-of-origin through the program.

3D scattering plots of trace element contents

For this study, we divided ruby and blue sapphire samples into two groups based on their iron content, i.e., high-iron and low-iron groups (Figure 1). 3D scatter plots allowed us to gain a more detailed insight into data overlapping. For our selected samples, we found that Mg, Cr, Fe, Ga, Ti, and V were good discriminators for distinguishing corundum's

country-of-origin as the selected features. In comparison, however, LA-ICP-MS data enabled a better origin discrimination than by using EDXRF data. We assume that this is due to the difference in the detection limit and quantitative accuracy of these two analytical methods. The manual rotation of plotting axes and the overlapping of some origin-related data groups proved to be a weakness in determining the origin using 3D scatter plots. To address this, machine learning methods were applied in this study.



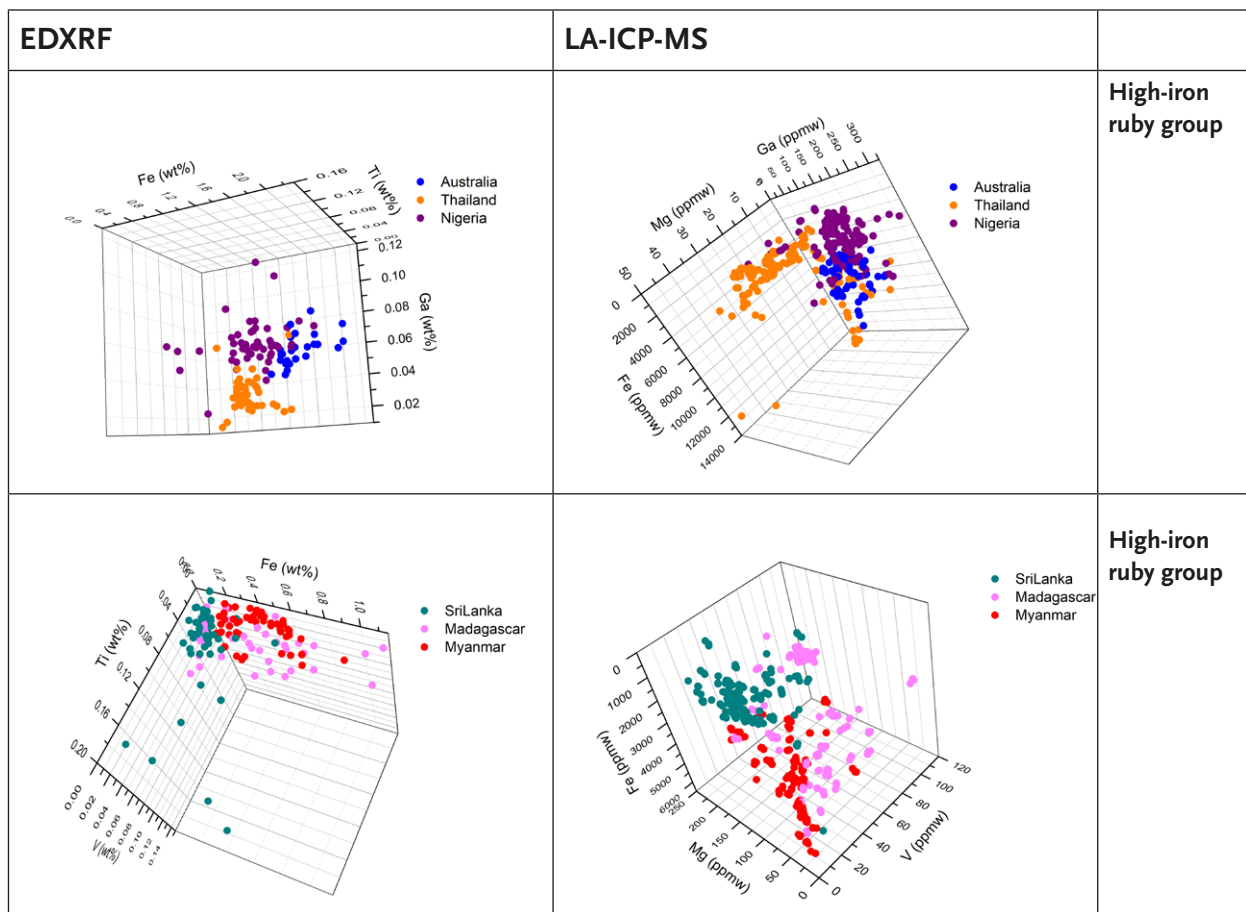


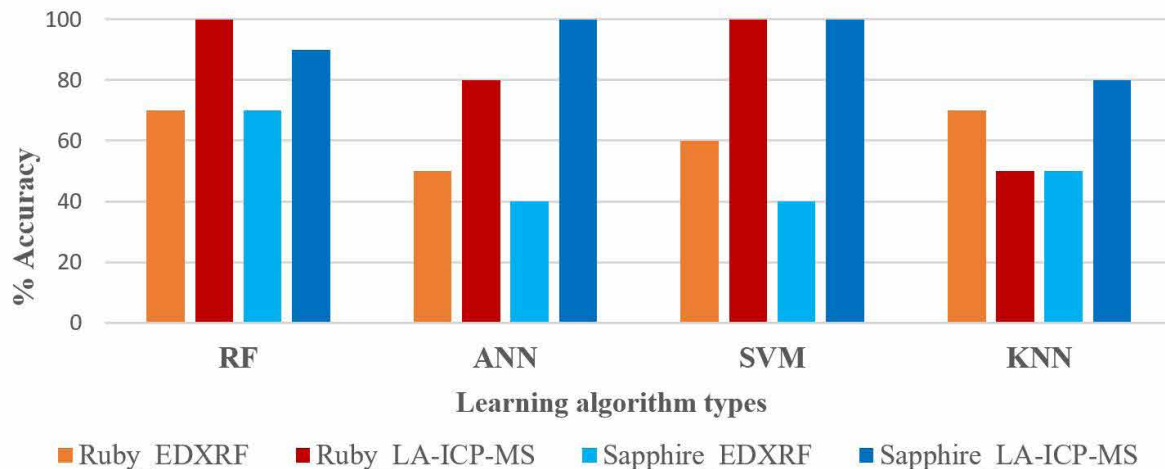
Figure 1: Representative 3D scatter plots of trace elements in ruby and blue sapphires from important sources

Machine learning algorithms for Gem Origin Determination

Machine learning algorithms were used in our study to attribute corundum origins, specifically in cases in which the 3D scatter plots revealed overlapping data groups. We found that our trained model was able to produce a rather high accuracy for origin determination if using LA-ICP-MS data. For example, it was able to achieve an average accuracy of 82.5% for ruby and 92.5% for blue sapphires, whereas the EDXRF only yielded 62.5% and 52.5% for rubies and blue sapphires, respectively (Figure 2). Briefly, the results revealed that the Random Forest Algorithm (RF) demonstrated the best overall learning algorithm for predicting the origin of the selected stones used in the study. The ANN and SVM algorithms, nonetheless, could give reasonable results when the input data were obtained from LA-ICP-MS analyses.

Concluding remarks

Trace element data fingerprinting is an essential method for studying diagnostic chemical features, especially when combined with machine learning methods and suitable algorithms and selected features. They can effectively help to determine the geographical origin of ruby and sapphire data with a low level of error, especially when using LA-ICP-MS data. However, their prediction accuracy and determination success depend on various factors, such as instrumentation performance and limitation, data preparation and processing, model optimization, and validation. Importantly, a sufficient number, reliability, and homogeneity of gemstone samples are the most important key factors to maintaining the accuracy of origin determination by using the chemical database with machine learning methods, consistent application of analytical protocols during sample measure-



ment, and cautious handling of any outliers present in the dataset. Nonetheless, a gemologist is still the one who will decide the final result from considering various analytical data as well, including internal features and others spectral analyses.

Figure 2: The accuracy of origin determination was assessed by applying our program to analyze 20 test-samples of rubies and sapphires.

References

- Abduriyim, A., Kitawaki, H., 2006. Determination of the origin of blue sapphire using Laser Ablation Inductively Coupled Plasma Mass Spectrometry (LA-ICP-MS), *The Journal of Gemmology*, 30(1/2), 23-36
- Groat, L.A., Giuliani, G., Stone-Sundberg, J., Renfro, N.D., Sun, Z., 2019. A review of analytical methods used in geographic origin determination of gemstones, *Gems & Gemology*, 55(4), 512–535.
- Guillion, M. & Detlef, G. 2001. Quasi ‘non-destructive’ laser ablation-inductively coupled plasma-mass spectrometry fingerprinting of sapphires, *Spectrochimica Acta Part B Atomic Spectroscopy*, 56(7), 1219-1231.
- Gubelin Gem Lab. 2020. Gemtelligence. Source: <https://www.gubelingemlab.com/en/news/detail/gemtelligence> [05 January 2021]
- Harlow, G., Bender, W.M., 2013. A study of ruby (corundum) compositions from the Mogok Belt, Myanmar: Searching for chemical fingerprints, *American Mineralogist*, 98(7), 1120-1132
- Karamelas, S., Al-Shaybani, B., Mohamed, F., Sangsawong, S., Al-Alawi, A., 2019. Emeralds from the most important occurrences: chemical and spectroscopic data, *Minerals*, 9(9), 561.
- Palk A.C., Saeseaw S., Renfro N.D., Sun Z., McClure S.F., 2019. Geographic origin determination of ruby, *Gems & Gemology*, 55(4), 580–612.
- Sutherland, F.L., Zaw, K., Meffre, S., Yui, T.F., Thu, K., 2015. Advances in trace element “fingerprinting” of gem corundum, ruby and sapphire, Mogok area, Myanmar, *Minerals*, 5(1), 61-79
- Seneewong-Na-Ayutthaya, M., Chongraktrakul, W., Sripoonjan, T., 2021. Gemological characterization of peridot from Pyaung-Gaung in Mogok, Myanmar, *Gems & Gemology*, 57(4), 318–337
- Wanthanachaisaeng, B., Sripoonjan, T., Rungruengphol, A. 2020. Smart database of world gemstone origins (in Thai). The Gem and Jewelry Institute of Thailand (GIT), Bangkok, 105pp.

Acknowledgements

This research was fully supported by Fundamental Fund, Thailand Science Research and Innovation (TSRI). The authors are grateful to the GIT technical advisors, Dr. Visut Pisutha-Arnond, and Ms. Wilawan Atichat for their valuable comments and kind review of this article.

Color enhancement in yellow sapphire

U. Atikarnsakul, W. Soonthorntantikul, S. Saeseaw

Gemological Institute of America, 944 Rama IV road, Wangmai, Pathumwan, Bangkok 10330
ssaeseaw@gia.edu

Natural yellow sapphire is colored by one or the combination of two different chromophores, Fe^{3+} and the trapped hole- Fe^{3+} ($\text{h}\cdot\text{Fe}^{3+}$) colour center. Fe^{3+} chromophore is typically found in basalt hosted related while the $\text{h}\cdot\text{Fe}^{3+}$ chromophore occurs in yellow sapphire that contains low iron metamorphic sapphire (1).

In this presentation, our aims are 1) to study the effect of annealing on natural yellow sapphires with different chromophores and 2) to study the cause of color enhancement in yellow sapphire that was created by irradiation. All studied samples were fabricated to be optical wafer with a

polished window perpendicular to the crystal's c-axis. For annealing experiments, we studied 15 samples from Sri Lanka, Madagascar and Australia. The samples were heated at varied temperatures from 500°C to 1550°C for fixed durations of 6 hours in air. The color appearance and spectroscopic data were examined before and after each step of heat treatment. FTIR, UV-Vis-NIR spectra and chemical analysis using LA-ICP-MS were collected at the same area. Effect of annealing results showed in table 1.

Chromophores	Before heat	After heat
Only $\text{h}\cdot\text{Fe}^{3+}$	<ul style="list-style-type: none"> • (very) light yellow • medium to strong 3161 cm^{-1} • $\text{h}\cdot\text{Fe}^{3+}$ absorption 	<ul style="list-style-type: none"> • stronger yellow at 900°C and above • 3161 cm^{-1} reduced and may transform to 3000 cm^{-1} series • increase $\text{h}\cdot\text{Fe}^{3+}$ absorption
Only Fe^{3+}	<ul style="list-style-type: none"> • yellow • may show 3000 cm^{-1} series • only Fe^{3+} absorption 	<ul style="list-style-type: none"> • no changed in appearance • 3000 cm^{-1} series disappeared • no changed in UV spectra
$\text{Fe}^{3+} + \text{h}\cdot\text{Fe}^{3+}$	<ul style="list-style-type: none"> • light to medium yellow • weak to medium 3161 cm^{-1} • $\text{Fe}^{3+} + \text{h}\cdot\text{Fe}^{3+}$ absorption 	<ul style="list-style-type: none"> • stronger yellow, may be in unexpected zones • 3161 cm^{-1} reduced • increasing of $\text{h}\cdot\text{Fe}^{3+}$ absorption

Table 1: Effect of annealing on yellow sapphire with different chromophores.

Irradiation is another treatment to create a yellow coloration in corundum. In our preliminary study, we selected 3 samples from Sri Lanka, Burma and Australia. Samples were irradiated using gamma rays (Co-60) at 50 and 500 kGy. The color appearance and spectroscopic data were examined before and after each step of irradiation. Results showed that strong yellow color is induced after irradiation

(figure 1). FTIR spectra displayed no creation nor destruction of FTIR features typically observed in corundum with irradiation, whereas UV-Vis-NIR spectra revealed strong trapped hole feature after irradiation (figure 2).

In our study, sapphire that colored by $\text{h}\cdot\text{Fe}^{3+}$ can create yellow coloration in corundum by either annealing in air or irradiation. In contrast, sapphire that colored by only Fe^{3+} will not affect to color at experimental conditions.



Figure 1: Color-calibrated photo of sapphire from Sri Lanka before and after gamma irradiation. Path length/thickness: 1.404 mm

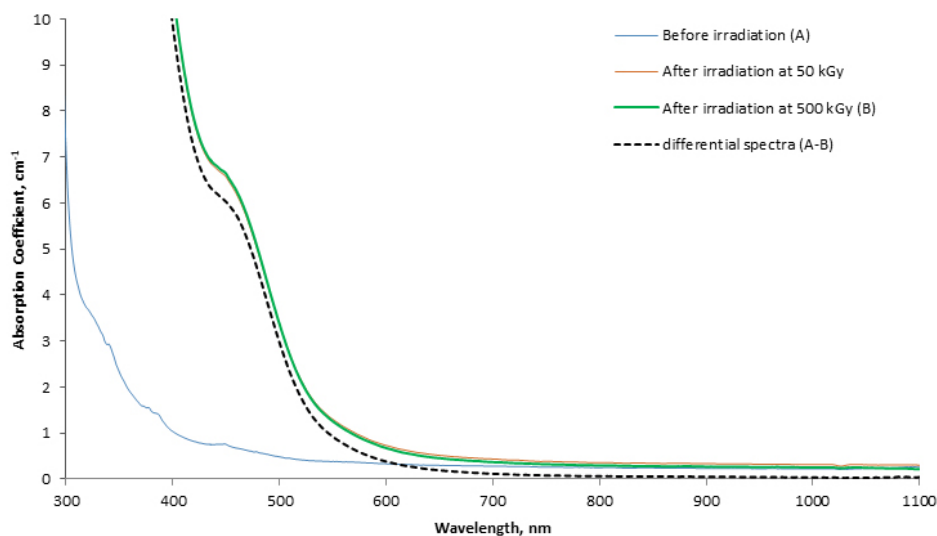


Figure 2. Polarized UV-Vis-NIR spectra comparisons between before and after irradiation with a gamma irradiation dose of 50 and 500 kGy. The difference spectrum revealed a significant increase in trapped hole.

References

Atikarnsakul U., Emmett J. L. 2021. Heat treatment effects on the behavior of the 3161 cm^{-1} feature in low-iron metamorphic yellow sapphire. *Gems & Gemology*, 57(3), 283-288.

Acknowledgements

The authors would like to thank John Emmett and Aaron Palke for their useful advice and support. We also thank Sasithorn Engniwat for photo calibration, Charuwan Khowpong and Suwasan Wongchacree for sample fabrication. Also thanks to Gem Irradiation Center at the Thailand Institute of Nuclear Technology (Public organization) for sample irradiation.

Additional Observations on Unstable Color in Padparadscha Sapphires

By Aaron Palke², Shane McClure¹ and Nathan Renfro²

¹GIA Carlsbad, CA, USA smcclure@gia.edu

²GIA Carlsbad, CA, USA

For the past few years laboratories have been testing the color stability of padparadscha sapphires. It became an issue because we realized that the orange color in some pads was unstable and would fade in light until the stones were just pink. It's not that we were not aware that this was possible in pads – the phenomenon had been reported in the literature years before. What changed was that we seldom saw such stones come through the labs in the past. Then it was reported that some new material was found near Ambatondrazaka, Madagascar which was pad color when it came out of the ground but then over time faded to just pink. Information about these stones and the unstable trapped-hole centers that are responsible for these changes has been covered extensively in several articles (Krzemnicki et al. (2018), Krzemnicki and Cartier (2019), Smith et al. (2019), Hughes (2022)).

It was quickly noticed that exposure to a strong white light source would cause these stones to fade faster, typically in a few hours (Figure 1). The orange color could easily be regained by exposure to ultraviolet light.



Figure 1: This fancy sapphire with unstable color is in its charged state on the left and after stability testing on the right.

These developments made us wonder just how common this phenomenon is. As a quick test we pulled out of our reference collection a large selection of pink sapphires from different locations – Madagascar, Sri Lanka, Burma, Vietnam, Kenya, India, Tajikistan, and others – and put them under a low wattage gemological long wave ultraviolet light for four hours. We also included some yellow sapphires because it is known that some yellow sapphires might also change in a similar way. The color stability of yellow sapphires was studied extensively by Nassau and Valente (1987).

We were quite surprised when after the four hours we found approximately 60% of the samples changed to some degree. Only those deposits with low iron content developed orange or yellow color – anywhere from slightly orangy to pure orange. Most significantly were sapphires from Sri Lanka, Burma and Vietnam. Some but not all of the stones from these sources changed to some degree. Why this only happens to some of these stones is not well understood at this time. Interestingly, almost none of the stones from Ilakaka, Madagascar changed. We did not have any pink sapphires from Ambatondrazaka to test.

All of the affected stones reverted back to pink after exposure to strong incandescent light for about 4 hours. Therefore we instituted a color stability test for padparadscha sapphires submitted to the lab using a 150 watt halogen projector bulb from a fiber optics unit. We made sure the stones were not heated by the light source by keeping them several inches away. Most stones did not change during this test but some did. All the other major laboratories test for color stability using a similar method. We had a similar test in place for years that was used for yellow sapphires, primarily testing for irradiated sapphires which are known to be unstable. However, we almost never saw a yellow sapphire fade to any significant degree.

Several years ago a larger orangy pink sapphire came in that was put under the stability testing protocol. After the requi-

site 4 hours exposure time we found the stone had actually turned more orange. In fact there was now very little pink still visible. This was a completely unexpected result. It was the first time we had seen this happen.

What was going on with this stone? The halogen light source we were using produced the opposite reaction we expected. We exposed the stone to a number of other light sources including LWUV, strong SWUV, daylight and other light sources thinking that maybe we would have an unexpected result with one of these but in none of these cases did the orange component diminish. It occurred to us that heat might affect it but this stone did not belong to GIA so we could not do that. We contacted several outside scientists with significant knowledge of color in gemstones and they also could not initially think of a reason for this unexpected behavior.

Shortly thereafter covid forced our labs to close for three months. Every stone in our possession at that time were locked in our safes. When the labs reopened and this mystery stone was brought out once more it had returned to the orangy pink color it was when we first saw it. We quickly realized that the only thing that had changed was the stone was in the dark for an extended period of time. This is the same type of change we see with chameleon diamonds.

Over the next year or so we encountered several more of these stones – some not treated, some heated and a couple beryllium diffused (Figure 2). We were able to purchase one of the diffused stones so we could perform testing we would not do to a client owned stone. The first such test

was to heat the stone. The stone was heated to 325°C for 2 hours which completely removed the orange color, leaving the stone purplish pink in what might be considered its “ground state”. Again, this is similar to the reaction we would expect from a chameleon diamond. Interestingly, heating the stone to 200°C did not change the color at all.



Figure 2: On the left is a stone as it was submitted to the lab. On the right is after stability testing.

We also exposed this stone to UV light and sunlight from its ground state. As expected the UV light charged the stone more than anything else, but exposing it to direct sunlight for one hour also charged it (Figure 3). The differences in the degree of change between the ground state, after fade testing, exposure to sunlight for one hour and exposure to UV light can be seen in the UV-VIS spectra (Figure 4). The spectra shows a change in the absorption centered at 475nm which has been attributed to trapped-hole centers (Dubinsky et al. 2020).



Figure 3: The sapphire GIA acquired for testing can be seen here in four different states – left to right, ground state after heating at 350°C, after stability testing, after exposure to sunlight for one hour, after UV exposure.

In the interim we had purchased a few LED fiber optics units. After charging this stone back up to its orangy state, performing the stability test using the LED unit once again removed the orange and the stone was once again purplish pink. Obviously there was some difference between the 150 watt halogen light source and the LED light source that was affecting this stone in a different manner. In measuring the output of both of these sources we found that the halogen source did have a very small UV component down to about 360 nm. The LED source however did not have any UV component.

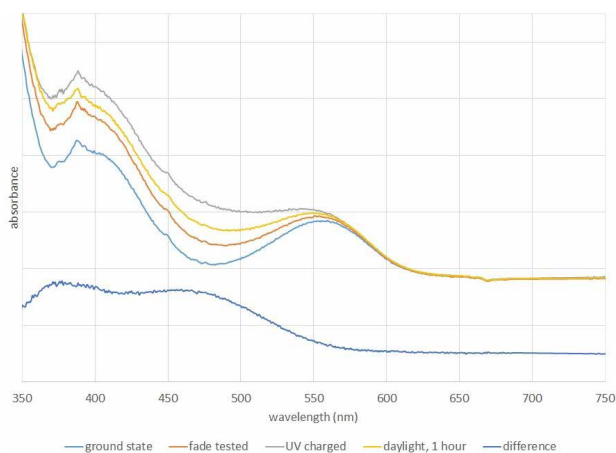


Figure 4: UV-VIS spectra of the stone in figure 3 for each of its four states shows clearly that the changes in color are attributable to the strength of the 475nm trapped-hole center absorption. The difference between the ground state and the UV charged state is also shown.

We can conclude from this information that it is visible light wavelengths that cause the unstable color component to fade. The vast majority of pink sapphires that will develop orange color are sensitive to UV light but not sensitive enough to maintain the unstable color center with the minimal amount of UV produced by a halogen light source. However, a rare few such stones are so sensitive to UV that even that small amount will produce orange. It takes a light source like the LED that is all visible wavelengths with no UV component to eliminate the orange color.

This begs the question – what is the “actual color” of these stones? What color should we call these stones on our gemological reports? To explore this further we mounted the stone we had purchased in a simple solitaire ring in its ground state. One of our wives (AP) then wore the ring

under normal circumstances such as in the home, in an office environment and outdoors for five days. At the end of that time the stone was similar in color to the color that was observed after fade testing the stone. This might be considered the most representative “true color” of the stone as exposure to different light sources during the day and spending the night hours in the dark would all affect the color. In light of these facts we submit that the actual color of these stones is the color they are after normal wear or the color they are after a fade test has been performed. This means that most of the stones that show this behavior will be just pink under those conditions and therefore not properly called padparadscha. This is entirely consistent with the opinion of the labs that belong to the LMHC, which the GIA is one. However, these rare stones that are so sensitive to UV light that they always show an orange component under normal conditions are not the same. These stones can be called padparadscha if they still fall into that range after exposure to normal conditions. Obviously we cannot set client stones in rings and wear them for days at a time. Our testing showed that the color such stones after going through the color stability protocol is similar to the color of the stone after being exposed to noon-time Southern California daylight for one hour. Since sunlight intensity varies depending on where you are in the world, we believe that using the color of the stone after a reproducible stability test is reasonable.

References:

- Dubinsky E.V., Stone-Sundberg J., Emmett J.L. (2020) A Quantitative Description of the Causes of Color in Corundum, *Gems and Gemology*, 56 (1), 1-27
- Hughes, E.B. (2022) Yellow Sapphires with Unstable Color, *Gems and Gemology*, 58 (2), 259-260
- Krzemnicki, M.S., Klumb, A., Braun, J. (2018) Unstable Colouration of Padparadscha-like Sapphires. *The Journal of Gemmology*, 36 (4), 346-354
- Krzemnicki, M.S., Cartier, L.E. (2019) Padparadscha-like Fancy Sapphires with Unstable Colors: Coloration Mechanisms and Disclosure. *InColor*, Issue 41, 92-94
- Nassau, K., Valente, G.K. (1987) The Seven Types of Yellow Sapphires and Their Stability to Light. *Gems and Gemology*, 23 (4), 222-231
- Smith, C.P., Chaipaksa, M., Perlmutter, A., Vasquez, L., Zellagui, R., Che, S. (2019) Heated Sapphires with Unstable Colour Centers. *The Journal of Gemmology*, 36 (7), 602-604

Crystal structure of nano inclusions in blue sapphire from Diego Suarez, Northern Madagascar

Seika Oto^{1,2}, Akira Miyake¹, Yohei Igami¹, Kentaro Emori³, Hiroshi Kitawaki³

¹ Kyoto University (Japan)

² Air Water INC.(Japan)

³ Central Gem Laboratory (Miyagi Bldg. 6th Fl. 5-15-14, Ueno Taito-ku, Tokyo, Japan),
emori@cgl.co.jp

Abstract

Nano inclusions in unheated blue sapphire (Diego Suarez, northern Madagascar) containing naturally occurring beryllium have been studied. Tabular nano inclusions with a diameter of 20 to 30 nm were observed with transmission electron microscope (TEM). Electron diffraction shows that the nano inclusions are possibly a “srilankite”-like mineral phase (srilankite: $ZrTi_2O_6$) which are triple twinned. In addition, the nano inclusions show epitaxial relationship with the corundum matrix. We estimate that the nano inclusions are a product of exsolution.

Introduction

Since September 2001, Be-diffusion treated corundum has been widely seen in gem market across the world. Initially, it was thought that Be did not exist within untreated corundum, but traces of naturally occurring Be have subsequently been confirmed to be present in untreated corundum (e. g. Wathanakul et al. 2004, Krzemnicki 2007, Shen et al. 2012, and Pardieu 2013 and therein).

Shen et al. 2012 found that clouds in samples from Ilakaka, Madagascar, contain Be and the samples contain nano-inclusions 20-40 nm long and 5-10 nm wide which are unnamed high-pressure mineral that has the same composition as rutile, but has the crystal structure of α - PbO_2 . But there was no discussion about Be and nano-inclusions. Emori et al. (2019) showed that nano-inclusions in untreated Be-containing blue sapphire from Diego Suarez, northern Madagascar, contains Ti, Nb and Ta, and that Be is also located in nano-inclusions. Although their crystal structure has not been determined, it may be an unknown mineral which has α - PbO_2 structure (Shen et al. 2012) and has the chemical composition of Be: Ti: Nb: Ta = 3:16:1:4.

In this study, we made more detailed observations of the nano inclusions discovered by Emori et al. 2019, and report the results.

Materials and methods

In this study, we examined an unheated basaltic blue sapphire rough (sample No.10) from Diego Suarez, Madagascar, containing natural Be. This sample was already studied by Emori et al. in 2019. The sample No.10 has a size of 9.10 x 7.58 x 4.02 mm and a weight of 3.89 ct, and has been polished on one side for observation and analysis. Emori et al. (2019) performed LA-ICP-MS analyses of the sample No.10 at points 01-30 and points 31-57 with regular intervals along two lines, respectively. The Be concentrations at the points vary from 0 (below the detection limit) up to 14.16 ppmw, and show a very good correlation with Nb and Ta, but not with Ti. We used Helios G3 CX (acceleration voltage: 30kV, 2kV) for FIB SEM (focused ion beam scanning electron microscopy) and JEOL JED-2100F (acceleration voltage of 200 kV) for TEM (transmission electron microscopy) observation.

Results and Discussion

We prepared a [0001] specimen of corundum for TEM observation using a FIB, choosing an area with maximum concentration of Be. HAADF-STEM images (high-angle annular dark-field imaging scanning-TEM) show circular nano-inclusions with a diameter of 20 to 30 nm.

As a result of STEM-EDS mapping, Ti, Nb, Sn, and Ta were detected only from the nano inclusions but not from the surrounding area (Figure. 1). Although Be is undetectable

by EDS, Be is reasonably presumed to be included in the nano inclusions because Be has been confirmed to coexist with Nb and Ta (Emori et al., 2019). Electron diffraction patterns shown in Figure 2 match structure of only TiO_2

which is an endmember of srilankite ($(\text{Zr}, \text{Ti}) \text{O}_2$), and it is inferred that the nano inclusions have srilankite ($(\text{Zr}, \text{Ti}) \text{O}_2$) like structure. The diffraction mapping also reveals triple twinning (Figure. 2).

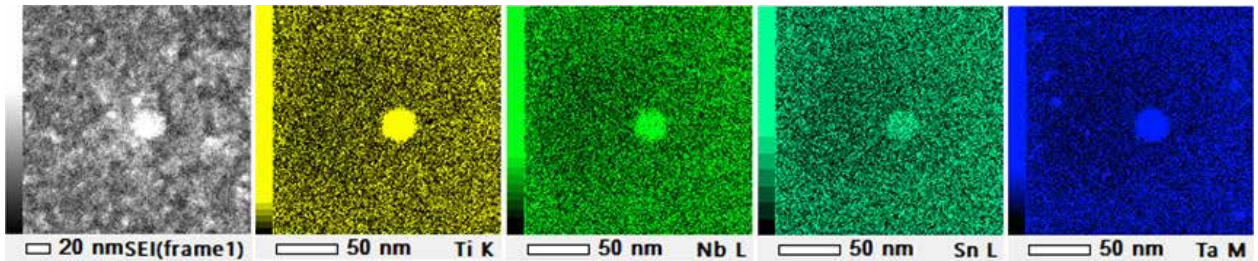


Figure 1: Mapping results by STEM-EDS. Ti, Nb, Sn, and Ta are detected from nano inclusions.

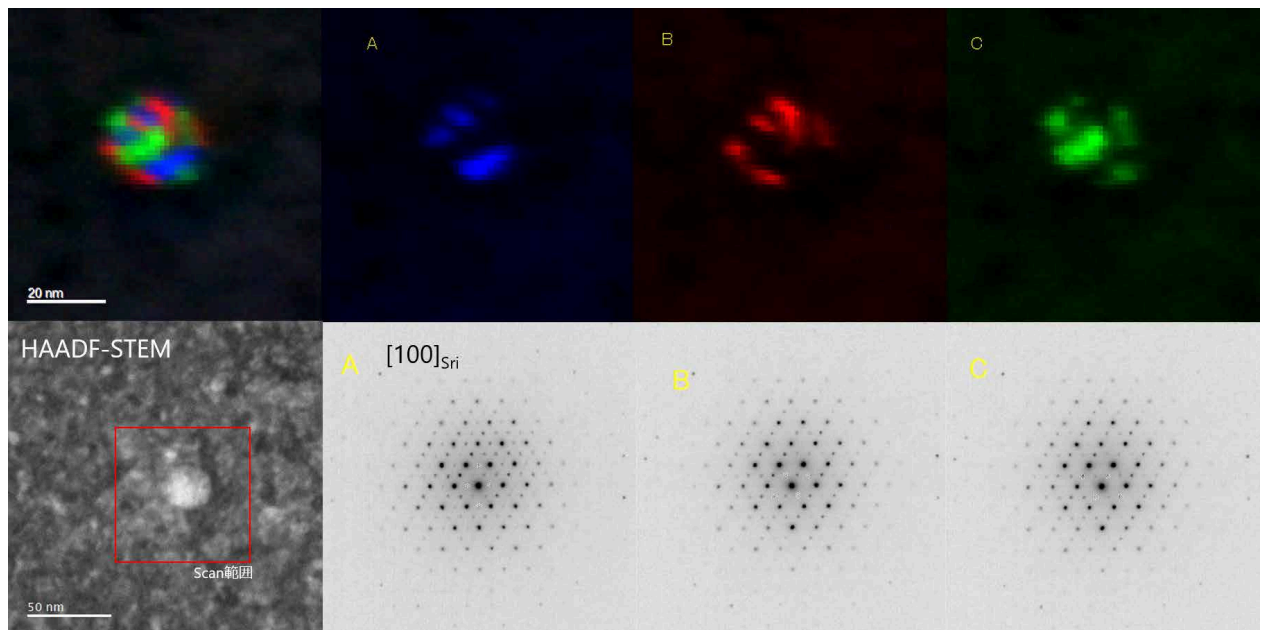


Figure 2: Diffraction mappings and diffraction patterns of the nano-inclusions. Each of A, B and C shows a “srilankite” like phase with different orientations, and the leftmost figure is a superimposed image of A, B and C. It can be seen that the nano inclusions are in the form of triple twin crystals of “srilankite” like phase with three orientations.

All nano inclusions (nano) and the corundum matrix (crn) show the orientation relationship as follows; $\{010\}_{\text{nano}} \parallel \{10\bar{1}0\}_{\text{crn}}$, $\{100\}_{\text{nano}} \parallel \{0001\}_{\text{crn}}$, $\{001\}_{\text{nano}} \parallel \{1\bar{2}10\}_{\text{crn}}$. The relationship indicates that the nano-inclusions and the corundum matrix are in epitaxial correlation, suggesting that the nano-inclusions are exsolution products from the corundum.

In addition, corundum, srilankite and rutile share the same hexagonal close-packed (hcp) oxygen packing. We calculated the lattice misfit values when srilankite and rutile are crystallized in corundum, and found that the misfit values are smaller for srilankite than for rutile in a full temperature range. This indicates that srilankite is easier to nucleate than rutile in corundum. Xiao et al., 1997 reported that srilankite precipitates with cooling from 1300°C for 10 hours after corundum doped with 500-1000 ppm of Ti is held at 1600°C for 24 hours, but the srilankite transforms to rutile with slower cooling for 30 hours from 1300°C. The result indicates rutile is more stable than srilankite. Considering the nucleation and phase stability of srilankite and rutile, we conclude that the nano-inclusions with srilankite structure have precipitated in corundum as metastable phase in the lower crust and have rapidly moved upward to the earth surface (e.g. within an alkali basalt) keeping the metastable phase.

Conclusion

Based on the above results, we assume that the nano-inclusions in the blue basaltic sapphire from Diego Suarez, Madagascar have a triple-twinned “srilankite”-like structure, and that they contain Nb, Sn, and Ta in addition to Ti, and possibly also Be. Since all nano-inclusions were found to be in an epitaxial relationship with the corundum matrix, it is presumed that the nano-inclusions formed by exsolution from corundum and are present at conditions of the earth surface as metastable phase with a “srilankite”-like structure.

References:

- Emori K., Kitawaki H., Miyake A. (2019) Be-containing nano-inclusion in untreated blue sapphire from Diego, Madagascar. International Gemmological Conference Nantes-France Proceedings, 124-126.
- Kremnicki M. S. (2007) LIBS and LA-ICP-MS analysis of gemstones. 30th International Gemmological Conference, Moscow, Russia.
- Pardieu V. (2013) Blue Sapphires And Beryllium ‘An Unfinished World Quest’. InColor 2013, 36-43.
- Shen A., McClure S., Breeding C. M., Scarratt K., Wang W., Smith C., Shigley J. (2007) Beryllium in Corundum: The Consequences for Blue Sapphire. GIA Insider, Vol.9, Issue 2 (January 26, 2007).
- Shen A., Wirth R., (2012) Beryllium-bearing nano inclusions identified in untreated Madagascar sapphire. Gems & Gemology, 48(2), 150-151
- Wathanakul, P., Atichat, W., Pisutha-Arnond, V., Win, T.T., Singbamrung, S. (2004) Evidence of the unusually high Be, Sn, Nb, Ta content in some trapiche like sapphires from basaltic origin. 29th International Gemmological Conference, Wuhan, China.
- Xiao S. Q., Dahmen U. and Heuer A. H. (1997) Phase transformation of TiO₂ precipitates in sapphire (α -Al₂O₃) induced by the loss of coherency. Philosophical Magazine A, 75 (1), 221-238.

Influence of Irradiation on Colour Modification and Colour Stability of Rubies: A Preliminary Study

Waratchanok Suwanmanee¹, Chotika Kittikunlayaworakun¹, Thanapong Lhuaamporn¹, Chanenkant Jakkawanvibul¹, Thanong Leelawatanasuk¹, Wilawan Atichat¹, Visut Pisutha-Arnond¹, Nongnuch Jangsawang², and Kanwalee Pangza²

¹ The Gem and Jewelry Institute of Thailand (Public Organization), Bangrak, Bangkok, 10500, Thailand

² Thailand Institute of Nuclear Technology (Public Organization), Ongkarak, Nakornnayok, 26120, Thailand
swaratchanok@git.or.th

Keywords: Ruby, Treatment, Gamma radiation, Electron radiation, Colour stability test



Figure 1. Gem-quality rubies from three different and important sources (left: Madagascar, 1.02 ct; middle: Myanmar, 1.52 ct; right: Mozambique, 1.18 ct. Photo by W. Suwanmanee.

Introduction

Ruby is the chromium-bearing red colour-variety of corundum Al_2O_3 . Since historic times, ruby is highly popular in the gem and jewellery market because of its highly saturated red colour, high hardness and brilliancy (Figure 1). In recent years, the demand for rubies has continuously increased while production of fine quality stones is getting less. Therefore, some suppliers are preferring to improve rubies of lower quality by various heat treatments to enhance mainly their colour and clarity. In addition to heating, there is also irradiation treatment on corundum. Pough & Rogers (1947) reported that X-rays can produce yellow colour hues in all varieties of corundum but that the extent of colour shift after irradiation is also dependent on the original colour saturation of the stones.

In case of rubies, there are some methods to remove their purplish tint and turn them to a brighter red colour which is achieved by the addition of a yellow hue such as low temperature heat treatment and Be heat treatment. For irradiation method, it is known that the yellow coloration after irradiation of corundum is related to defect structures (colour centres) and that they may be unstable to extensive exposure to daylight and/or thermal energy (Pisutha-Arnond et al., 2004). This is specifically the case when the colouration after being irradiated is unstable and fades back into the original colour.

Therefore, the authors have investigated a selection of irradiated rubies to better understand the effect of this treatment and to develop potential detection methods for gem testing laboratories. In the present study, selected rubies of purplish red colour from Myanmar, Mozambique, and Madagascar were investigated. Gamma and electron beam irradiation experiments on our ruby samples were carried out in a specialized facility in Thailand. All rubies were subjected to a colour stability test after being irradiated. The colour modification of the ruby samples was investigated by UV-Vis absorption spectra and colour photographs to compare their colour before and after irradiation and after the colour stability test.

Materials and Methods

Six untreated rubies were selected for the present study, consisting of rough and faceted samples. They are from three sources: Myanmar, Mozambique, and Madagascar. All samples were provided by the Gem Testing Laboratory of the Gem and Jewelry Institute of Thailand (Public Organization).

Photographs of the samples were taken in a standard light box with 5500K Fluorescence light bulbs. Colour stability

test of the rubies after irradiation was done using fiber optic lamp (halogen) at 15V and 150 W. Exposure time for testing was 6 hours.

Gamma and electron (e-beam) radiations were applied for ruby treatment at a dosage of 1,000 kGy. Gamma radiation was performed using six columns of cobalt-60 (⁶⁰Co) at an energy of 1.17 and 1.33 MeV. For electron beam irradiation we used a high-energy electron accelerator operated at 20 MeV with a power of 10 MW. The facility for both irradiations is located at The Thailand Institute of Nuclear Technology (Public Organization), Nakhon Nayok province. The UV-Vis absorption spectra for rubies before and after treatment were analyzed using a PerkinElmer LAMBDA 1050 spectrophotometer. The result of absorption intensity was reported in absorption coefficient (cm^{-1}) units.

Results of irradiation treatment

Colour modification by irradiation and colour stability test

Gamma radiation: Figure 2 shows the colour of rubies before and after irradiation, and also after colour stability testing. Gamma radiation produced a slight yellow tint in Mozambique ruby. This resulted in an orangey red colour of the sample. In addition, the blue colour banding disappeared. The colour of our Madagascar sample became slightly darker red after irradiation, whereas the ruby from Myanmar remained unchanged by the gamma-irradiation. After colour stability testing, the yellowish tint in the irradiated Mozambique ruby was removed and the sample turned to pinkish red, a distinctly brighter colour than before irradiation. In contrast to this, the ruby samples from Myanmar and Madagascar remained unchanged after colour stability testing.

Origin samples	Untreated	Irradiated (Gamma)	Colour stability tested
Myanmar	 5 mm	 5 mm	 5 mm
Mozambique	 5 mm	 5 mm	 5 mm
Madagascar	 5 mm	 5 mm	 5 mm

Figure 2: Colour modification of rubies after irradiation with gamma radiation and after colour stability test. Photos by W. Suwanmanee.

Electron radiation (e-beam): After electron beam irradiation, the additional ruby samples from Mozambique and Madagascar turned to a very slightly brighter red, whereas the ruby sample from Myanmar remained unchanged. All samples remained unchanged after being tested for colour stability (see in Figure 3.).










Origin samples	Untreated	Irradiated (Gamma)	Colour stability tested
Myanmar	 5 mm	 5 mm	 5 mm
Mozambique	 5 mm	 5 mm	 5 mm
Madagascar	 5 mm	 5 mm	 5 mm

Figure 3: Colour modification of rubies after irradiation with an electron beam and after colour stability test. Photos by W. Suwanmanee.

UV-Vis spectroscopy

The absorption spectrum of ruby is commonly dominated by two broad Cr^{3+} -related bands centered at about 411 and 558 nm and an additional series of small Cr^{3+} peaks at 693 nm (Schmetzer & Schwarz, 2004; Promwongnan & Sutthirat, 2019). An additional band at around 330 nm is due to the presence of Fe^{3+} - Fe^{3+} pairs (Promwongnan & Sutthirat, 2019).

The absorption spectra of the ruby sample from Mozambique (Figure 4) reveals the increase of the absorptivity in

the range of 300 – 600 nm after gamma-irradiation and a slight decrease after the stability testing. By subtracting the initial untreated UV-Vis absorption spectrum from the irradiated spectrum (Figure 5, black line) this increase in absorption after irradiation becomes even more evident (two broad bands between 300 – 600 nm) likely as a result of an activated colour centre (Pisutha-Arnond et al., 2004). However, these irradiation-induced bands were slightly reduced after being tested for color stability (Figure 5, red line).

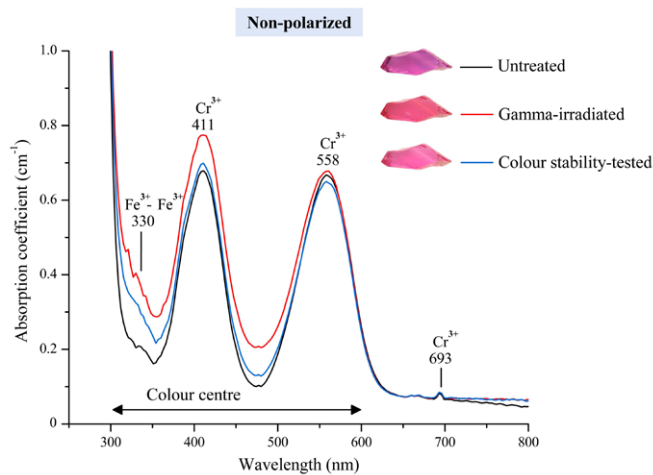


Figure 4: Comparison of the UV-Vis absorption spectra of the Mozambique ruby sample before treatment (black line), after being irradiated with gamma radiation (red line), and after colour stability testing (blue line).

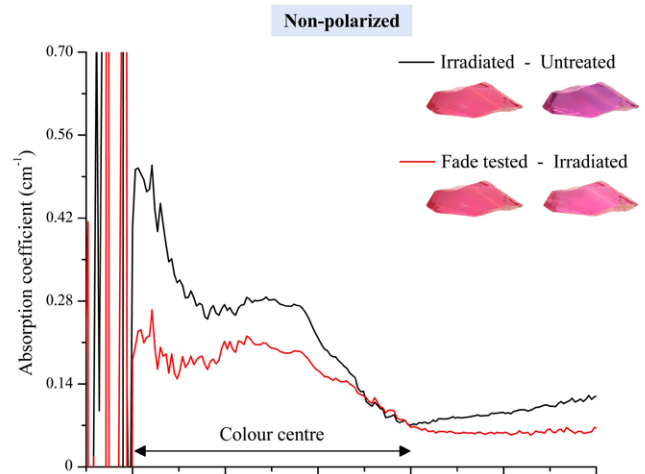


Figure 5: Resulting UV-Vis spectra after subtracting the initial untreated spectrum from the gamma-irradiated (black line), and the spectrum after colour stability test from the gamma-irradiated spectrum (red line).

Concluding remarks

The experimental results show that both gamma- and electron beam radiation may produce (a slight) yellowish colour hue in purplish red ruby, particularly in those from East-Africa (e.g., Mozambique and Madagascar). Our experiments have shown that gamma radiation can produce more pronounced yellowish colour hues than electron beam radiation. The slight yellow colour shift after irradiation results in a slight increase of absorption between 300 – 600 nm, caused by an activated defect structure (colour centres). By applying a colour stability test we were able to remove the yellowish hue partially in the irradiated ruby, specifically in the Mozambique ruby. But the colour in this sample did not fully revert to the original purplish red colour. As shown, the absorption spectrum may change slightly by this treatment. However, this slight spectral change can so far not be able to use safely as an indication that the ruby has been treated by irradiation. More experiments must be carried out in the near future to better understand irradiation treatments of rubies and its colour stability.

References

- Pisutha-Arnond, V., Hager, T., Wathanakul, P., and Atichart, W. 2004. Yellow and Brown Colouration in Beryllium-Treated Sapphires, *Journal of Gemmology*, 29 (2), 77-103.
- Pough, F.H. and Rogers, T.H. 1947. Experiments in x-ray irradiation of gemstones. *American Mineralogist*, 32 (1-2), 31–43.
- Promwongnan, S. and Sutthirat, C. 2019. An Update on Mineral Inclusions and Their Composition in Ruby from the Bo Rai Gem Field in Trat Province, Eastern Thailand, *Journal of Gemmology*, 36 (7), 634-645.
- Schmetzer, K. and Schwarz, D. 2004. The Causes of Colour in Untreated, Heat Treated and Diffusion Treated Orange and Pinkish-Orange Sapphires – A Review, *Journal of Gemmology*, 29 (3), 149-182.

Acknowledgements

This work was funded by the Gem and Jewelry Institute of Thailand (Public Organization) for fiscal budget in 2022 and was supported by Thailand Institute of Nuclear Technology (Public Organization) for irradiation treatment.

Low Temperature Heat Treatment of Burmese Ruby

E. Billie Hughes¹, Wim Vertriest²

¹ Lotus Gemology, Bangkok, Thailand, billie@lotusgemology.com

² GIA, Bangkok, Thailand

Detection of low-temperature heat treatment (below 1200°C) in ruby and sapphire can present challenges to gemologists, as alterations to the material are often subtle. In this study, the authors heated Burmese ruby samples from Mogok, Myanmar, at temperatures ranging from 600° to 1500°C. The samples were documented using macro-photography, photomicrography of inclusions, ultraviolet fluorescence imaging, and spectroscopic analysis (Raman, ultraviolet/visible/near-infrared, and infrared) to record any changes, with a focus on features that could help detect heat treatment.

A wide variety of solid inclusions, including calcite (Figure 1), mica, spinel, and zircon, were found in Mogok ruby. Many of those were found to be sensitive to heat treatment with regard to morphology and phase transition; their reactions varied depending on a number of factors such as size, distance from the surface, and species. Microscopic examination provided useful visual indications of heat treatment, even at lower temperatures (Figure 2).

Raman analysis of calcite and spinel inclusions (Figure 3) also proved valuable in providing complementary evidence of low-temperature heat treatment. Spinel inclusions in particular showed a widening of peak in the range of 405–420 cm^{-1} , which is known to occur when spinels are heated (Saeseaw, 2009).

Fluorescence images were also recorded before and after treatment (Figure 4).

The combination of these factors can assist gemologists in detecting low temperature heat treatment.



Figure 1: A pair of calcite crystals stands out above a cloud of undissolved rutile silk needles. Note the twinning planes in both crystals, a common feature for calcite. Photomicrograph by E. Billie Hughes; field of view 2 mm.

References:

- Saeseaw S., Wang W., Scarratt K., Emmett J.L., Douthit T.R., 2009. Distinguishing heated spinels from unheated natural spinels and from synthetic spinels: A short review of ongoing research. GIA Research News, <https://www.gia.edu/doc/distinguishing-heated-spinels-from-unheated-natural-spinels.pdf>, 13 pp.

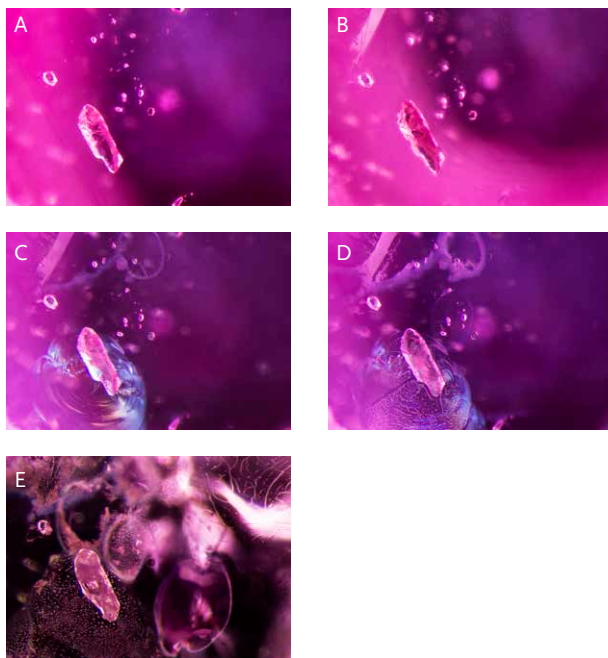


Figure 2.

A: (Unheated) An elongated mica crystal surrounded by several smaller crystals in sample 8.

B: (600°C) There is little noticeable change except at the top left, where a small fissure has formed.

C: (900°C) The scene shows obvious signs of heat alteration. In addition to the fissures seen earlier, glassy discoids appear around crystals in the background, and a shiny fissure is conspicuous around the biotite crystal in the foreground.

D: (1100°C) Some fissures have begun to heal; the glassy fissure around the biotite crystal has developed elongated channels, and the partially healed edges of the glassy discoid at the top of the frame have started to neck down and become wider.

E: (1500°C) The scene has changed dramatically; glassy discoids and partially healed fissures with a melted appearance are visible across the field of view, and the biotite crystal has developed an immobile gas bubble in its center. Images A and B were captured with darkfield illumination; diffused fiber-optic illumination has been added in C–E to reveal the fissures more clearly. Photomicrographs by E. Billie Hughes; field of view 1.5 mm.

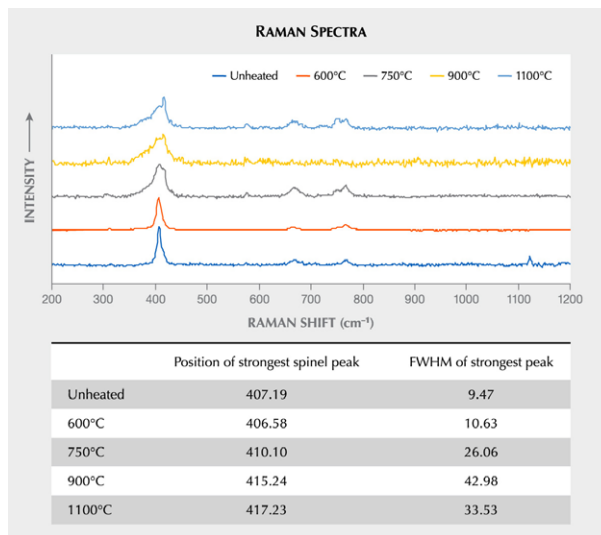


Figure 3. Raman spectra of a spinel inclusion in one of the heated ruby samples. After the first round of heating to 600°C, the spectrum remained consistent, but notable changes occurred after heating to 750°C. The peak between 405 and 420 cm^{-1} widened and shifted to a slightly higher wavenumber, a trend that continued with heating to higher temperatures. Spectra are offset vertically for clarity.

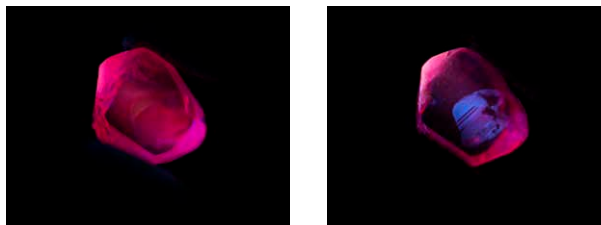


Figure 4.

A: Sample 46 displays a strong red short-wave fluorescence in its unheated state. Like the other samples tested, it did not display any change in appearance in short-wave UV illumination until after the last round of heating.

B: After heating to 1500°C, the ruby displays a clear, zoned chalky appearance in short-wave UV. Photos by E. Billie Hughes.

Milky appearance of Geuda sapphire from Sri Lanka

Bovon Ubolchay¹, Chakkaphan Sutthirat¹, Bhuwadol Wanthanachaisaeng², Gamini Zoysa³, Waratchanok Suwanmanee², Arūnas Kleišmantas⁴

¹ Department of Geology, Faculty of Science, Chulalongkorn University, Pathumwan, Bangkok 10330, Thailand

² The Gem and Jewelry Institute of Thailand (Public Organization), Bangrak, Bangkok, 10500, Thailand

³ Ceylon Gemmological Services (cgs@slt.net.lk), Colombo, Sri Lanka

⁴ Department of Geology and Mineralogy, Vilnius University, LT-03101 Vilnius, Lithuania

Keywords: Geuda sapphire, milky inclusion, Sri Lanka, UV-Vis

Introduction

Sri Lanka is famous for gems since several thousand years. Almost corundum varieties have been found in Sri Lanka including the rough of Geuda which has also given considerable attention to heat treatment (Soysa & Fernando, 1992).

Geuda is a whitish corundum, significantly founded in Sri Lanka, being a semi-transparent to semi-translucent stone with milky or silky appearance (Figure 1).

The appearance of Geuda sapphire is a translucent gemstone because of the tiny inclusions widely spreading throughout the stone. These inclusions appear as silky or tiny particles. The stone can be heated to improve transparency and to yield blue color (Schmetzer and Kiefert, 1990; Jaliya et al., 2020). Heat treatment usually affects milky and silky appearances as well as color modification, and even the internal appearance (including inclusions) of corundum.

Several researchers have previously described the technical heat treatment and cause of color in sapphire (e.g., Nassau 1981, Koivula 1987; Fritsch and Rossman, 1987; Schmetzer and Kiefert, 1990; Scarratt, 1999; Jaliya et al., 2020). Moreover, UV-Vis-NIR spectrophotometer is probably useful in the identification of sapphire, and it may also provide information on the geographic origin (Scarratt, 1999). In addition, the absorption spectra have been investigated for cause of blue color in sapphire; they display main broad absorption bands centred at around 570 nm (o-ray) and 730 nm (e-ray), responsible for Fe²⁺-Ti⁴⁺ intervalence charge transfer (IVCT) mechanism (Lehmann and Harder, 1970; Häger, 2001).

For the absorption spectrum, optical properties of particle inclusions, commonly found in Sri Lanka sapphire, have

been investigated. Mcneil and French (2000) studied various concentrations of TiO₂ particles on semi-transparent resin films. The absorption spectra showed the scattering of TiO₂ particles by the absorption edge below 400 nm. Moreover, Popov (2008) suggested that the TiO₂ nanoparticles can be used as the UV protectors to skin because the nano-sized TiO₂ spheres, ranged from 35-200 nm in diameter, can scatter the UV radiation (310 and 400 nm). According to the tiny inclusion in Geuda sapphire, the absorption edge might be found because of the scattering.

Therefore, the milky Geuda sapphires under this experiment were not only investigated regarding the color created by heat treatment but also the influence of tiny inclusions in absorption spectrum.

Materials And Methods

There were 10 rough samples of unheated Geuda sapphire from Sri Lanka in this study. The color of the samples was light-blue color with milky appearance. After sample preparation, cutting, and polishing both sides to be slab (without crystal orientation), they were showed clearly silk and cloud inclusions in all samples (Fig. 1). Electron Probe Micro-Analyzer (EPMA) JEOL model JXA-8100 was engaged for chemical analyses of major and trace element compositions of host sapphire samples. UV-Vis-NIR absorption spectra were measured by the VARIAN Cary 500 UV-VIS-NIR spectrophotometer with the wavelength range 175-3300 nm. Samples were heated by Linn electrical furnace (model HT 1800 Plus VAC Bottom Loader) at a temperature of 1650°C with 5 hours soaking time. The atmospheric condition in the chamber was controlled by pure N₂ gas feeding throughout the heating and cooling processes.

Results and Discussion

Physical properties:

The samples were typically semi-transparent to transparent appearance. Their RIs fall within 1.760–1.771 range, SG values are 3.90–4.00 with averaged birefringence of 0.008–0.010. All samples are inert fluorescence in both long-wave and short-wave UV radiation.

Inclusions of Geuda sapphire samples from Sri Lanka show a feature of milky appearance. In this study, the samples can be divided into two groups, based on inclusion appearance, i.e., silk and cloud. Silk inclusions appear intersecting of silk along the crystal structure. Cloud inclusions include minute particles dispersing throughout the sample. Both types of inclusions can be observed clearly under the gemological microscope which their sizes are less than 1 μm and disperse at a distance less than 1 μm (Fig. 2).

Absorption Spectra:

The absorption spectra of sapphire normally show the absorption bands of Fe^{3+} at 377, 388, and 450nm (Emmett, et al. 1993). Whereas the milky Geuda yields the absorption edge pattern in a range of 300 – 350nm. This absorption edge is probably caused by the amount and size of the inclusions (e.g., silk and cloud) in Geuda sapphire as previously reported at wavelength lower than 400 nm (Mcneil and French, 2000; Egerton, 2014).

After the heat treatment at 1650°C under a reducing atmosphere, Geuda sapphires turn whitish color to blue color. The absorption spectra show increasing band at around 560 nm, corresponding to the intervalence charge transfer in the form of $\text{Fe}^{2+} - \text{Ti}^{4+}$ (IVCT). However, the absorption edge is vanished away due to the dissolution of minute particles during heat treatment (Fig. 3).



Figure 1: Milky Geuda sapphire samples (1.78 ct and 1.01 ct)



Figure 2: Cloud inclusions containing minute particles (size of minute particles are less than 1 μm) that disperse at the

distance less than 1 μm between each other before heat treatment. Sample No. M02 (Left) and Sample No. M05 (Right)

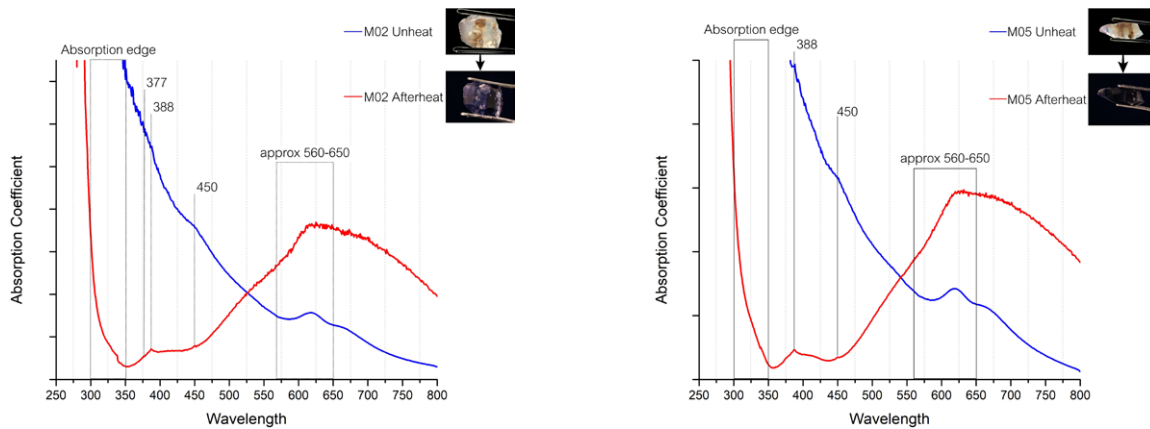


Figure 3: Absorption spectra of milky Geuda sapphire before (blue line) and after heat treatment (red line).

Conclusions

Geuda sapphire samples turn whitish color to blue color after heat treatment. The transparency gets better because of the disappearance of minute particles. The high absorbances in a range of 300 – 350 nm in unheated samples appear as the absorption edge which is caused by the high amount and minute particles within the Geuda sapphire. Regarding this evidence, this absorption edge is an indicator of the unheated sapphire.

References

- Emmett, J. L. and Douthit, T. R. (1993). Heat treating the sapphires of Rocks Creek, Montana. *Gems and Gemology*, 29(4): 250-272.
- Egerton, T.A. (2014). UV-absorption – The primary process in photocatalysis and some practical consequences. *Molecules*, 19: 18192 – 18214.
- Fritsch E. and Rossman, G. R. (1987). An update on color in gems. Part 1: introduction and colors caused by dispersed metal ions. *Gems and Gemology*, 23(3): 126 – 139.
- Häger, T. (2001). High temperature treatment of natural corundum. *Proceedings of the International Workshop on Material Characterization by Solid State Spectroscopy: April 4-10, 2001; Hanoi, Vietnam*, 24 – 37.
- Jaliya, R. G. C., Dharmaratne, P. G. R., and Wijesekara, K. B. (2020). Characterization of heat treated Geuda gemstones for different furnace conditions using FTIR, XRD and UV-Visible spectroscopy methods. *Solid Earth Science*. 5, 282-289.
- Mcneil, L. E., and French, R. H., (2000). Multiple scattering from rutile TiO₂ particles, *Acta Materialia*, 48: 4571–4576.
- Kröner, A., Cooray, P.G. and Vitanage, P.W. (1991). Lithotectonic subdivision of the Precambrian basement in Sri Lanka. In: Kröner, A. (ed.), Part I, Summary of Research of the German – Sri Lanka Consortium. Geological Survey Department, Lefkosia, 5–21.
- Koivula, J. I. (1987). Internal diffusion. *The Journal of Gemmology*, 20(7/8): 474-477.
- Lehmann, G. and Harder, H. (1970). Optical spectra of di- and trivalent iron in corundum. *American Mineralogist* 55: 98- 105.
- Nassau, K. (1981). Heat treating ruby and sapphire: Technical aspects. *Gems and Gemology*, 17: 121-131.
- Popov A. (2008). TiO₂ nanoparticles as UV protectors in skin. *University of Oulu*. 84.
- Scarratt, K. (1999). The Identification of Ruby and Sapphire. *Gems and Gemology*. 30: 82-83.
- Schmetzer, K. and Kiefert, L. (1990). Spectroscopic evidence for heat treatment of blue sapphires from Sri Lanka – additional data. *Journal of Gemmology*, Vol.22 (2), 80-82.
- Soysa, E. S. K. and Fernando, W. S., (1992). Field of classification of low value corundum in srilanka. *Journal of the National Science Foundation of Sri Lanka*. 20(1): 51-57.
- Sutthirat, S. P. a. C. (2019). An Update on Mineral Inclusions and Their Composition in Ruby from the Bo Rai Gem Field in Trat Province, Eastern Thailand. *The Journal of Gemmology*. 36(7): 634–645.

Explanation on Yellow, Green and Brown Coloration Series of Basalt Related Bangkokja Sapphires

Wiwat Wongkokua¹, Thanapong Lhuaamporn², Natthapong Monarumit¹, Phongsakorn Kajornboonsook¹ and Pornsawat Wathanakul¹

¹ Gem and Mineral Science Special Research Unit, Department of Physics and Department of Earth Sciences, Faculty of Science, Kasetsart University, Bangkok, Thailand

² Gem and Jewelry Institute of Thailand (Public Organization)
pwathanakul2@gmail.com

Keywords: Yellow sapphire, brown sapphire, green sapphire, Bangkokja, Chanthaburi, band model, UV-Vis-Nir absorption, FTIR

The basalt related Bangkokja sapphires, excluding the black star ones, commonly occur in three coloration series, i.e., the yellow, the green and the brown. Two representative samples of each colour series, altogether six, were selected from our Bangkokja sapphire collection (43 stones); those six

samples, i.e., light yellow and yellow, greenish yellow and green, and brownish yellow and brown represent the yellow, the green and the brown colour series, respectively. They have been studied to explain the true causes of their colour variations by using band models. Trace element chemistry, UV-Vis-NIR (both absorption and excitation), and FTIR spectra of the samples were recorded. Besides, their L*a*b* colour notations were measured using UV-Vis reflectance spectroscopy (Table 1).







Sample	Colour	Name	L*	a*	b*
	Light yellow	Bkj-11	91.87	-0.08	27.53
	Yellow	Bkj-21	85.20	0.30	37.56
	Greenish yellow	Bkj-25	92.23	-9.17	32.77
	Green	Bkj-32	59.35	-9.68	0.20
	Brownish yellow	Bkj-36	75.33	9.90	28.64
	Brown	Bkj-41	67.82	12.48	12.70

Table 1: Six out of forty-three of Bangkokja sapphire samples representing the yellow (Bkj-11 and 21), the green (Bkj-25 and 32) and the brown (Bkj-36 and 41) coloration series; showing the L*a*b* colour notations together with their visual colours.

The results confirm the pure yellow component is caused by Fe^{3+} with increasing intensity to the bright brown coloration so called the Mekong whisky colour, the most preferable yellow sapphires from Bangkok, Chanthaburi, Thailand, which also commands high pricing in the market among Thai people. This colour series shows UV-Vis absorptions at 377 nm, 388 nm and 450 nm similar to their polychromatic UV-Vis excitation spectra confirming that the samples are natural without beryllium heat treatment (Monarumit et al., 2020 and 2023). The more intense brown stones also show pronounced absorption at 450 nm which is also designated for the $\text{Fe}^{3+}/\text{Fe}^{3+}$ forbidden state (Häger, 2001). The tinted green samples, i.e., greenish yellow gradually ranges to green stones tend to have an increasing of Ti content. The three series have proven that the green is caused by gradually adding the blue component to the yellow which finally turns to blue with elevated Ti together with Fe content. Though this is rather commonly understandable, however, when the blue component has been added to the yellow, and the green (also blue-green till blue) varieties visually appear, the 580 nm and 710 nm absorptions present with a remarkably additional broad absorption at around 890 nm. Besides, their FTIR absorptions display the structural Ti-OH peak at 3309 cm^{-1} (Phlayrahan et al., 2018a, 2018b and 2019) while the greenish tint increases, finally the whole 3309 cm^{-1} series (3309 cm^{-1} , 3232 cm^{-1} and 3184 cm^{-1}) appears in the blue Bangkok stones. It is thus

revealed that the 580 nm, 710 nm and 890 nm absorptions are related to Ti. The increasing 890 nm absorption also normally indicates green/blue sapphires of basalt hosted known by most gem scientists (e.g., Palke et al., 2019). Hence, it is time to explain and understand, why there is no 3309 cm^{-1} absorption and its series in yellow/brown sapphires whereas those with blue tint do; this is because the Fe^{3+} and $\text{Fe}^{3+}/\text{Fe}^{3+}$ pairs provide balance substitution of Al^{3+} and 2Al^{3+} in the adjacent octahedral sites. Indeed, the $\text{Fe}^{3+}/\text{Ti}^{4+}$ pairs proposed by our previous work using the XANES technique (e.g., Wongrawang et al., 2016; Mogmued, et al., 2017), are responsible for the blue component which is increasingly added to Bangkok yellow sapphires resulting in greenish yellow and green stones. Therefore, an OH^- is required to balance the one-more excess positive charge of octahedral structural units which contain the $\text{Fe}^{3+}/\text{Ti}^{4+}$ pair ($7+$) instead of $\text{Fe}^{2+}/\text{Ti}^{4+}$ ($6+$) as the IVCT concept previously claimed and widely followed (e.g., Townsend, 1968; Nassau, 1978; Burns, 1981; Fritsch and Rossman, 1988).

The band models of yellow, green, and brown colour series of Bangkok sapphires have been proposed; the yellow component gradually ranges to the intense-brownish yellow to brown colorations due to Fe^{3+} and $\text{Fe}^{3+}/\text{Fe}^{3+}$ states in the yellow sapphire band gap (Figure 1a and c). Besides, the $\text{Fe}^{3+}/\text{Ti}^{4+}$ mixed acceptor states are additionally present in the green colour series (Figure 1b).

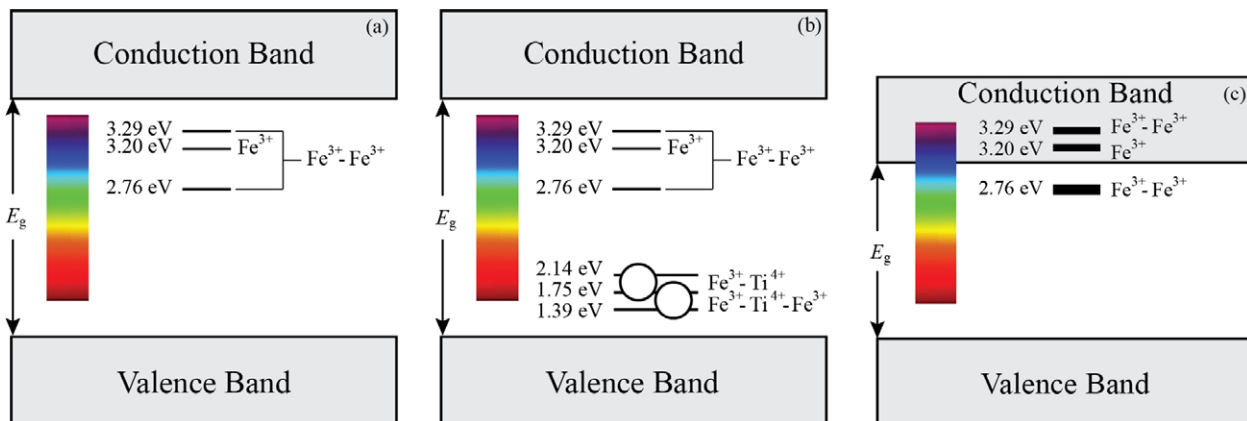


Figure 1: Band models showing (a) the stable defect centre of Fe^{3+} and $\text{Fe}^{3+}/\text{Fe}^{3+}$ states in yellow sapphire coloration series; (b) the Fe^{3+} and $\text{Fe}^{3+}/\text{Fe}^{3+}$ states and the $\text{Fe}^{3+}/\text{Ti}^{4+}$ mixed acceptor states in the energy gap of green sapphire series, and (c) the

Fe^{3+} and $\text{Fe}^{3+}/\text{Fe}^{3+}$ states with the very high density of states (thick bars) resulting in the intense brown colour series of Bangkok sapphires with the narrower energy band gap due to higher impurities in particular iron.

As the result of no-charge difference mentioned, the yellow as well as the brown sapphires never show the 3309 cm⁻¹ FTIR absorption (structural OH) unless the blue component which is caused by the Fe³⁺/Ti⁴⁺ mixed acceptor pair existing in the sapphire structure, resulting in the green coloration, and eventually the blue one. In the unheated stones, the molecular water would normally appear as a broad FTIR absorption at around 3400 cm⁻¹. The green coloration series of Bangkok sapphires is caused by addition of a blue component (Fe³⁺/Ti⁴⁺ pair) to the yellow. Hence, the OH⁻ is required only in greenish, green, and blue stones from Bangkok. This explanation can also be implied to yellow, green (till blue), and brown sapphires occurring elsewhere.

References

- Burns, R.G., 1981. Intervalence transitions in mixed valence minerals of iron and titanium, *Ann. Rev. Earth Planet. Sci.* 9: 345-83
- Fritsch, E., Rossman, G.R., 1988. An update on color in gems. Part 2: Colors involving multiple atoms and color centers. *Gems & Gemology*, 24, 3-15
- Häger, T., 2001. Proc. Int. Workshop on Material Characterization by Solid State Spectroscopy: The Minerals of Vietnam, 24-37
- Mogmued, J., Monarumit, N., Won-In, K., Satitkune, S., 2017. Spectroscopic properties for identifying sapphire samples from Ban Bo Kaew, Phrae Province, Thailand, *Journal of Physics Conference Series*, 901, 012075
- Monarumit, N., Lhuaamporn, T., Sakkaravej, S., Wathanakul, P., Wongkokua, W., 2020. The color center of beryllium-treated yellow sapphires, *Journal of Physics Communications*, 4, 105018
- Monarumit, N., Lhuaamporn, T., Wathanakul, P., Saiyasombat, C., Wongkokua, W., 2023. The acceptor-donor pair recombination of beryllium-treated sapphires, *Radiation Physics and Chemistry*, 206, 110756
- Nassau, K., 1978. The origins of colour in minerals, *The American Mineralogist*, 63, 219-229
- Palke, A.C., Saeseaw, S., Renfro, N.D., Sun, Z., McClure, S.F., 2019. Geographic origin determination of blue sapphire, *Gems & Gemology*, 55(4), 536-579
- Phlayrahan, A., Monarumit, N., Satitkune, S., Wathanakul, P., 2018a. Role of Ti content on the occurrence of the 3309 cm⁻¹ peak in FTIR absorption spectra of ruby samples. *Journal of Applied Spectroscopy*, 85, 385-390
- Phlayrahan, A., Monarumit, N., Boonmee, C., Satitkune, S., Wathanakul, P., 2018b. Fe oxidation state in heat-treated basaltic blue sapphire samples and its implication to the 3309 cm⁻¹-series peaks in infrared absorption spectra, *Journal of Physics: Conference Series*, 1144, 012057
- Phlayraharn, A., Monarumit, N., Lhuaamporn, T., Satitkune, S., Wathanakul, P., 2019. Spectroscopic investigation revealing the heating experiment of blue sapphire samples. *Journal of Applied Spectroscopy*, 86, 810-816
- Townsend, M.G., 1968. Visible charge transfer band in blue sapphire, *Solid State Communications*, 6, 81-83
- Wongrawang, P., Monarumit, N., Thammajak, N., Wathanakul, P., Wongkokua, W., 2016. Oxidation states of Fe and Ti in blue sapphire, *Materials Research Express*, 3, 026201

Acknowledgements

The Gem and Jewelry Institute of Thailand (GIT), Department of Physics and Department of Earth Sciences, Faculty of Science, Kasetsart University are thanked for the research facilities.

FTIR Fingerprinting: a case study on mineral inclusion identification by FTIR applied on rubies from marble-hosted deposits

Walter A. Balmer^{1,2}

¹ SSEF, Aeschengraben 26, 4051 Basel, Switzerland

² Collection Balmer LLC, Marktgasse 59, 3011 Bern, Switzerland; info@collectionbalmer.com

Keywords: FTIR fingerprinting, identification of mineral inclusions, higher-order phonon lines

Introduction

Fourier-Transform Infrared Spectrometry (FTIR) is a well-established analytical method in the field of gemmology (Suhner, 1979; Fritsch and Stockton, 1987; Smith, 1995; Beran and Rossman, 2006) and therefore used in many laboratories around the world. In this study which was part of a Ph.D. project (Balmer, 2011), FTIR fingerprinting was introduced as a comparative procedure in order to identify mineral inclusions by FTIR. The potential of such an approach was examined as a case study on rubies from marble-hosted deposits.

FTIR fingerprinting can be described as a procedure to compare FTIR signatures of known reference minerals with a sample spectrum in order to identify mineral phases which are present as inclusions in the host mineral. In corundum testing this approach is currently carried out on a routinely bases on a few aluminium- and iron-hydroxide phases such as diaspore, boehmite and goethite along with the minerals chlorite and kaolinite only.

One reason why FTIR fingerprinting has not yet been applied for a wider range of minerals may be the limited availability of reference spectra in the appropriate spectrum range. In order to avoid the strong absorption of the host-mineral itself and to allow identification of superimposed vibronic signals of mineral inclusions this range is between 1500 cm^{-1} and 5000 cm^{-1} (in the case of corundum). Typically, spectra from the RUFF reference database are limited to 4000 cm^{-1} and are often obtained by Attenuated Total Reflectance (ATR) showing a low signal to noise ratio (SNR) in the mentioned spectrum range.

Further, the strong absorption of the corundum limits observations to higher-order vibrations or phonon lines of potential mineral inclusions. This implies that the zero-phonon lines which typically would be considered diagnostic,

are not available. Further, the higher-order equivalents are per se lower in intensity, not as well-known nor well-referenced and therefore not been used systematically for mineral phase identification purposes in gemmology so far. Superimposed on the host-mineral's spectrum and in some cases even interfering with phonon lines of other mineral inclusions as well as atmospheric artefacts (e.g. water vapour) a vibronic overtone signal of a given mineral inclusion can easily be missed or misinterpreted.

Reference Material and Measurement Conditions

In the framework of this study, macroscopic reference mineral samples including the amphibole varieties actinolite and pargasite, the carbonate mineral dolomite, the aluminium-hydroxide diaspore, as well as tourmaline of a dravite-uvite composition were examined. The KBr reference samples on the other hand included the mineral phases calcite, the phyllosilicates chlorite, phlogopite, and muscovite, the iron-hydroxide goethite as well as the aluminium-hydroxide gibbsite.

Except from a simple cleaning procedure using a lint free cloth which was first moisturised by ethanol, the cut and polished macroscopic reference samples needed no further preparation. The sample materials for KBr pellets however had to be crushed and powdered using an agate mortar and pestle first. Then the powdered sample was mixed with KBr powder in the weight ratio of 1:100 to receive a sample with a total weight of 1g. Finally, the KBr pellet was pressed in a simple screw-press device.

The FTIR spectra in this study were collected by a Thermo Nicolet 6700 spectrometer at the premises of the Gem and Jewelry Institute of Thailand (GIT) in Bangkok. A beam condenser unit for data collection on cut and polished samples or a simple transmission sample holder for KBr pellets was applied respectively. The spectra were collected in absorbance between 1500 and 5000 cm^{-1} with increments of 1 cm^{-1} .

To improve the SNR as well as decreasing atmospheric noise, 124 measurements were accumulated for each sample. The obtained reference spectra were then compared with ruby spectra ($n=87$) from six different marble-hosted deposits.

Results and Discussion

During this study, it was possible to detect pargasite amphibole, tourmaline, and gibbsite as inclusions by FTIR fingerprinting in corundum (see Figure 1 & 2).

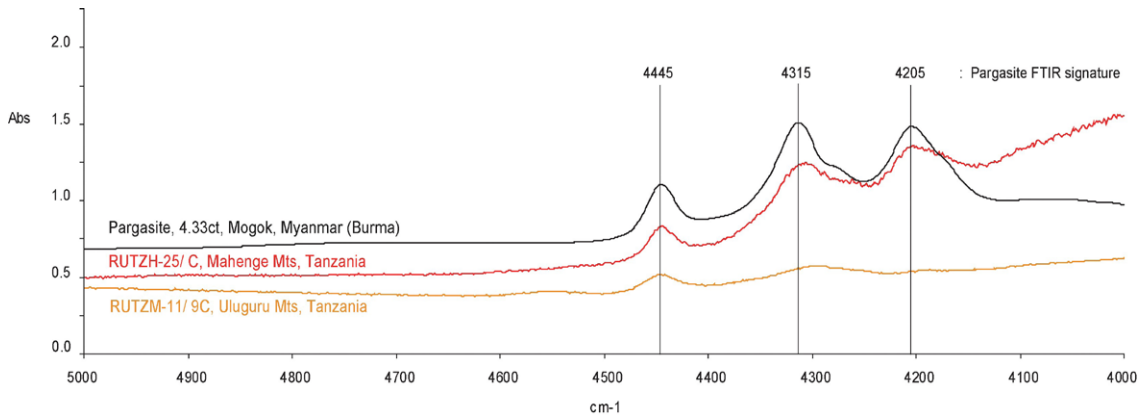


Figure 1: The comparison of a FTIR spectrum of a transparent 4.33ct pargasite amphibole reference sample from Mogok, Myanmar (Burma) with the weak but still detectable superimposed signature in a ruby from the Uluguru Mts,

Tanzania (RUTZM-11/ 9C) and the Mahenge Mts, Tanzania (RUTZH-25/ C) allowed the identification of pargasite amphibole to be present as a mineral inclusion in the examined ruby samples.

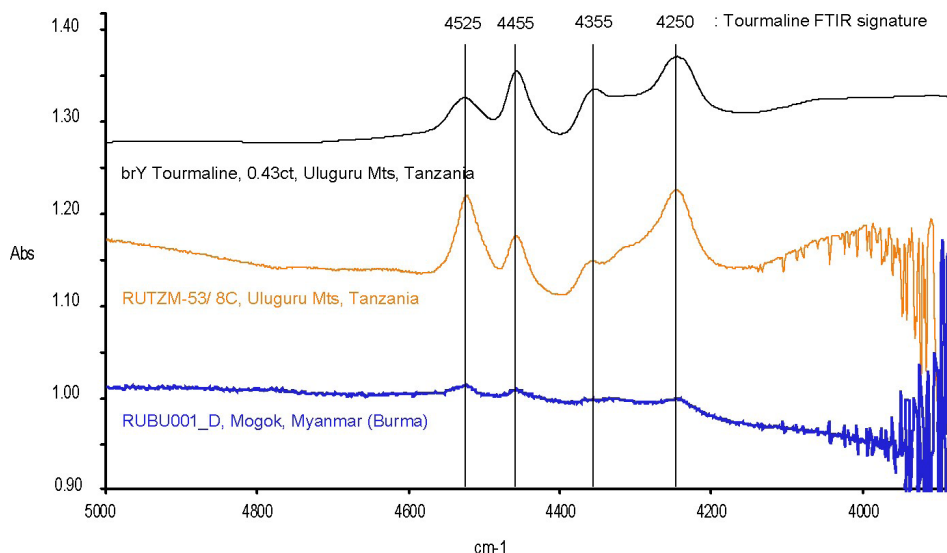


Figure 2: The FTIR reference spectrum of a 0.43 ct, cut, brownish-yellow, dravite-uvite tourmaline sample from the Uluguru Mts, Tanzania was compared with ruby spectra

recorded in this study. The comparison revealed the presence of tourmaline as an inclusion in the two ruby samples shown above.

The peaks in the range from 3200-3800 cm^{-1} have traditionally been attributed to kaolinite and chlorite group minerals in gemmology (Beran and Rossman, 2006). During the FTIR investigation in this study, however, it was recognised that these peaks might have been misinterpreted occasionally in the past. The reason for calling a long-standing interpretation into question is another phase which shows peaks in the same spectral range. In the examined water stretching vibration range gibbsite $[\text{Al}(\text{OH})_3]$, an aluminium-hydrox-

ide, shows specific peaks at 3375/3395, 3455, 3525, and 3620 cm^{-1} (Kloprogge et al., 2002; Balan et al., 2006). On the other hand, a chlorite KBr pellet sample investigated in this study (see Figure 3) as well as the spectra of chlorite group minerals published in the RRUFF spectra database lack the peaks at 3525 cm^{-1} and 3620 cm^{-1} . Additionally, the detection of gibbsite as a mineral inclusion implies that the examined corundum sample did not experience heat above 350°C (Kloprogge et al., 2002).

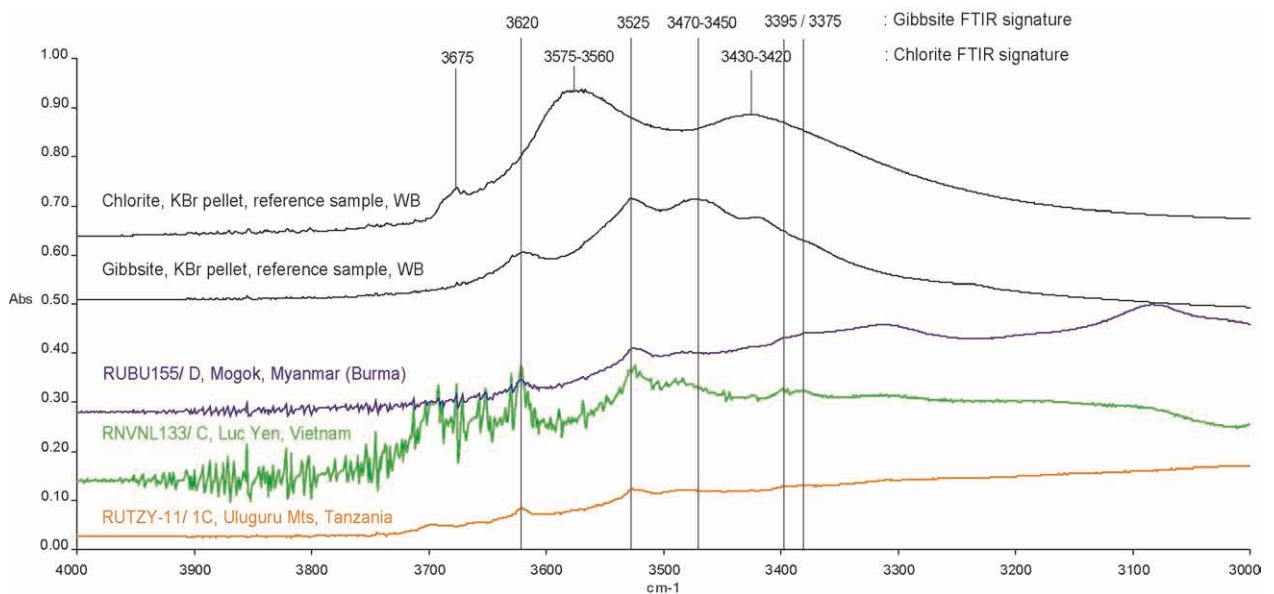


Figure 3: The comparison of two KBr pellet FTIR spectra obtained from a chlorite and gibbsite reference sample respectively, reveals clear differences in the main features of the FTIR signatures of these two minerals. Although the superimposed signal is not intensive in the spectra of the three

examined ruby samples, it is still possible to clearly determine the presence of gibbsite in all three spectra. The peaks not labelled in the spectra are caused by inclusions of kaolinite in sample RUTZY-11/ 1C, boehmite and calcite in RUBU155/ C respectively.

Conclusion

In this study, it was possible to show that careful FTIR spectrum investigations especially beyond the water stretching vibration range ($>3300\text{cm}^{-1}$) may reveal superimposed but diagnostically significant higher-order vibronic signals of various mineral inclusions. Compared with reference spectra in the appropriate spectrum range, the identification of such inclusions is made possible by FTIR fingerprinting. Therefore, high resolution reference spectra in the specific spectrum range including the most significant minerals known to occur as inclusions are key to an accurate spectrum interpretation by FTIR fingerprinting. Only if these pre-conditions are fulfilled and combined with the skills of an experienced FTIR operator the full information available in an FTIR spectrum can be extracted.

As an additional result of this study, the vibronic signatures of chlorite and gibbsite were characterised in the mentioned spectrum range, thus making the positive identification and separation between these two mineral phases possible by FTIR fingerprinting.

The identification of mineral inclusions by FTIR fingerprinting can be used as a valuable tool in excluding heat-treatment as a possibility, by indicating the presence of heat-sensitive mineral inclusions such as gibbsite, and in geographic origin determination. FTIR fingerprinting is also a viable alternative especially when access to more advanced analytic methods such as Raman spectrometry or LA-ICP-MS is limited. And as a non-destructive method FTIR fingerprinting can easily be included as an additional criterion in gem testing procedures in general and corundum testing in particular.

Finally, the results by FTIR fingerprinting published in this study are promising and encourage to further investigate FTIR spectra features beyond the range which is traditionally considered in gemmology. Even more so, because this study focused on rubies from marble-hosted deposits only. It is assumed that corundum from different deposit types as well as other host-minerals may reveal similar and additional features, which had not been discovered in this study yet.

References:

- Balan, E., et al., 2006. First-principle study of the OH-stretching modes of gibbsite, *American Mineralogist*, 91, 115-119.
- Balmer, W.A., 2011. Petrology, Geochemistry, and Gemmological Characteristics of Marble-Hosted Ruby Deposits of Morogoro and Mahenge, Tanzania, unpublished Ph.D. thesis, Chulalongkorn University, Bangkok Thailand, 185pp.
- Beran, A., Rossman, G.R., 2006. OH in naturally occurring corundum, *European Journal of Mineralogy*, 18(4), 441-447.
- Fritsch, E., Stockton, C.M., 1987. Infrared spectrometry in gem identification, *Gems & Gemology*, 23(1), 18-26.
- Kloprogge, J.T., Ruan, H., Ray L., Frost, 2002. Thermal decomposition of bauxite minerals: infrared emission spectroscopy of gibbsite, boehmite, and diaspor, *Journal of Material Science*, 37, 1121-1129.
- Smith, C.P., 1995. A contribution to understanding the infrared spectra of rubies from Mong Hsu, Myanmar, *Journal of Gemmology*, 24(5), 321-335.
- Suhner, B., 1979. Infrarot-Spektren in der Gemmologie. *Zeitschrift der Deutschen Gemmologischen Gesellschaft*, 28(2), 55-68.

Analysis of Myanmar golden-lipped cultured pearls using X-ray radiography, EDXRF, UV-Vis-NIR and Raman spectroscopy

Tay Thye Sun¹, Michael Krzemnicki^{2,3}, Gina Brombach², Thet Tin Nyunt⁴,
Myo Lwin⁴, Tay Zar Linn⁴, Loke Hui Ying¹

¹ Far East Gemmological Institute, 9 Perak Road, Singapore

² Swiss Gemmological Institute SSEF, Aeschengraben 26, 4051 Basel, Switzerland

³ Department of Environmental Sciences, Bernoullistrasse 36, 4056 Basel, Switzerland

⁴ Department of Geological Survey and Mineral Exploration, Ministry of Natural Resources and Environmental Conservation, Myanmar Gems Museum, Nay Pyi Taw, Myanmar.

tay@gem.com.sg

Keywords: Myanmar, cultured pearls, *Pinctada maxima*

Introduction

Myanmar golden-lipped pearl oysters (*Pinctada maxima*) are well-known to be found at the Myeik Archipelago - formerly also known as Mergui Archipelago - in the Andaman Sea in southern Myanmar (Tint Tun 1998; Strack 2006). One of the authors (TTS) visited there a pearl farm on February 2020 just before COVID-19 hit the world. The pearl farm is a joint venture between Myanmar Pearl Fishing & Culture Syndicate (government owned) and the South Sea Pearl Co. The farm is situated at Pa Lel Kyun (formerly known as Sir J. Malcolm island) about 70 nautical miles south-west of the city of Myeik (Tay et al, 2021). According to Myanmar Pearl Enterprise, about 1.3 million cultured pearls were produced that weighed 764,151 momme (about 2.8 t) in the two years period from 2019 to 2020 (Sze Man, 2018, 2019; Sto. Domingo, 2020).

The mollusc used for pearl cultivation is *Pinctada maxima*. From growing the spats either in the sea or the modern hatchery station, to eventually allowing the spat to grow to a size suitable for culturing (at sea) takes about 18 months. When the mollusc is about 12 cm in size, it is then implanted with a spherical bead nucleus of 4.5-7.0 mm size. It takes then another two years before the cultured pearl is harvested from the mollusc.

Figure 1: (a) Myanmar golden-lipped cultured pearls with *Pinctada maxima* shell (photo by Tay Thye Sun). (b) the colour of seven selected Myanmar cultured pearls ranges from yellow to light yellow and slightly cream, with their shape ranging from round to off rounded. In size these selected pearls range from 9 mm to 14 mm (photo by Michael S. Krzemnicki).



The author (TTS) bought seven cultured pearls from the pearl supplier at Myeik for further research. Their size ranges from 9 to 14 mm, and colour from yellow, light yellow to slightly cream. Besides basic gemmological methods such as binocular microscope, further analysis using x-ray radiography, UV-Vis-NIR reflectometry and EDXRF were applied to characterise these cultured pearls.

Gemmological investigation:

X-ray radiography of these seven samples confirms that they all are bead nucleated. Interestingly, the nacre overgrowth in these samples varies considerably in thickness from about 0.5 mm to about 3 mm with an average of about 2 mm (Fig.2). This may indicate that harvesting was done after different growth time in the mollusc (e.g. 1 to 3 years) apart from individual differences in nacre accumulation rates in individual molluscs. Chemical analyses with

EDXRF revealed a chemical composition typical for saltwater (cultured) pearls, consisting nearly entirely of CaCO_3 with only traces of Mn and Sr. All seven cultured pearl samples were examined in reflectivity mode using a UV-vis-NIR spectrophotometer. The reflectance spectra show an increasing reflectivity in the 330-450nm range (Fig.3), thus indicating that the yellow colour of these cultured pearls from *Pinctada maxima* is natural (Elen, 2001, Karampelas 2012). This was further confirmed using Raman spectroscopy (using a 514 nm argon laser) where small broad natural pigment-related Raman bands were commonly observed in *Pinctada maxima* apart from distinct peaks related to aragonite (nacre). In addition, X-ray micro-tomography was applied on all seven bead cultured pearls to further characterise their internal structure, specifically also to confirm that the spherical beads were cut from a (freshwater) shell showing parallel nacre layering.

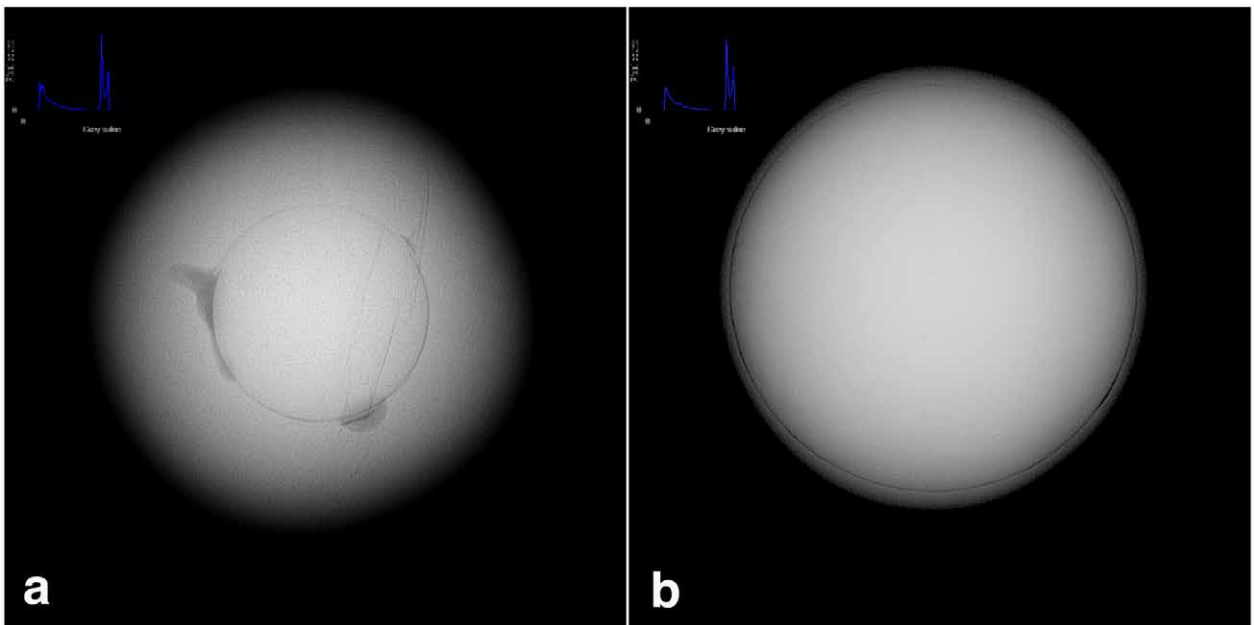


Fig.2. Radiographies of Myanmar golden lipped cultured pearls: (a) 3 mm thick nacreous layer, (b) 0.5 mm thick nacreous layer. (Radiography by Gina Brombach, SSEF).

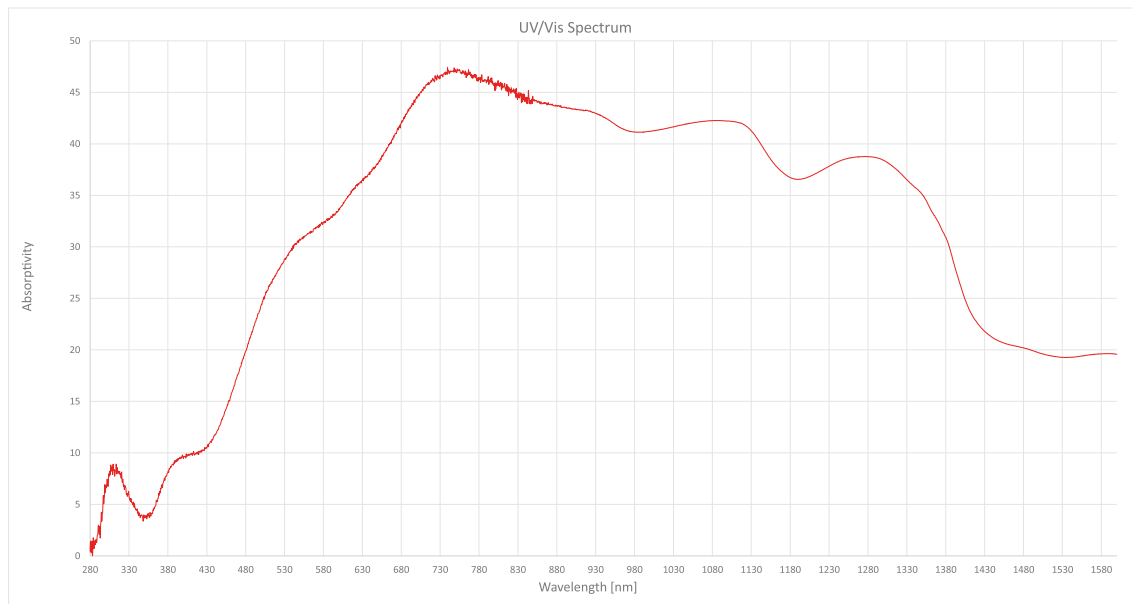


Fig.3. Reflectance spectrum of a Myanmar golden-lipped cultured pearl (*Pinctada maxima*) shows an increased absorption in the 330-450 nm range, an indication of natural colour (Spectrum by Gina Brombach, SSEF).

Conclusions

The Pa Lel Kyun (or “Pearl island”) in Myanmar has been producing golden-lipped cultured pearls since 1954. Seven cultured pearls were analysed and our findings using advanced instruments on a selection of this production confirm that these pearls are indeed “classic” bead-nucleated, saltwater cultured pearls, with a natural yellow colour.

References

- Bernardette Sto. Domingo, 2020. Myanmar eyes solid footing in global pearl market. Jewellery Net: Market Intelligence News, 3th February 2020. <http://www.jewellerynet.com/en/jnanews/features/23683>
- Elen S., 2001. Spectral reflectance and fluorescence characteristics of natural-color and heat-treated “golden” South Sea cultured pearls. *Gems & Gemology*, 37 (2), 114-123
- Karampelas S., 2012. Spectral characteristics of natural-color saltwater cultured pearls from *Pinctada maxima*. *Gems & Gemology*, 48 (3), 193-197. <http://dx.doi.org/10.5741/GEMS.48.3.193>.
- Strack, E., 2006. Pearl. Rühle-Diebener-Verlag, Germany, pp. 696
- Sze Man Young, 2018. Myanmar pearl dealer eyes Asia. *JNA*, 46.
- Sze Man Young, 2019. Myanmar finds footing in global pearl sector. *Pearl Report*, 36.
- Tay Thye Sun, Thet Tin Nyunt, Myo Lwin, Tay Zar Linn, 2021. Visit to a gold-lipped cultured pearl farm in Myanmar. *Journal Gemmology*, 37 (5), 463-464
- Tint Tun, 1998. Myanmar pearling: past, present and future. In: *SPC Pearl Oyster Information Bulletin*, 12, 3-7

Acknowledgements

Many thanks to travelling companion Mr Nyi Nyi Aung and also to Mr Win Thein (Assistant General Manager) and Mr Sai Aye Cho (marine biologist) and the staff of Myanmar Pearl Enterprise at Pa Lel Kyun.

DNA Fingerprinting and age dating of historic natural pearls: a combined approach

Laurent E. Cartier^{1,2}, Michael S. Krzemnicki^{1,5}, Bertalan Lendvay³,
Nadja Morf³, Joana B. Meyer⁴

¹ Swiss Gemmological Institute SSEF, Aeschengraben 26, 4051 Basel, Switzerland

² Institute of Earth Sciences, University of Lausanne, 1022 Chavannes-près-Renens, Switzerland

³ Institute of Forensic Medicine, University of Zürich, Winterthurerstrasse 190/52, 8057 Zürich, Switzerland

⁴ Swiss Federal Research Institute WSL, Zürcherstrasse 111, 8903 Birmensdorf, Switzerland

⁵ Department of Environmental Sciences, Bernoullistrasse 36, University Basel, Switzerland

laurent.cartier@ssef.ch

Keywords: Natural pearls, cultured pearls, DNA fingerprinting, 14C age dating

Abstract

Natural pearls are accidental formations in wild oysters. The lack of new supply in recent decades has meant that the trade is heavily dependent on old stocks of natural pearls, and that natural pearls of high quality can be considered rare. Auction results of natural pearls over the past two decades are a testament to this. As one of the world's oldest and most widely collected gems, pearls merit greater study. Research into species determination and radiocarbon age dating pearls is contributing to greater knowledge about the provenance of historic natural pearls. This paper presents some case studies of such recently tested samples and provides an outlook on combining age dating, DNA fingerprinting and more traditional methods for pearl analysis.

Introduction

DNA fingerprinting of pearls was first developed and published in 2013 using different types of pearls and oyster species (Meyer et al., 2013), and a more recent study of a similar methodological approach was published by Saruwatari et al. (2018). Since these publications, a wide-reaching global reference dataset of the most common natural and cultured pearl oyster species has been constituted by the University of Zürich and the Swiss Gemmological Institute SSEF. We will present this dataset, and demonstrate the approach used to assemble such a large collection and the limitations involved. Further, we present how radiocarbon age dating is used on real-world cases of pearls in a gemmological context (Krzemnicki and Hajdas, 2013, Krzemnicki et al., 2017).

Case Study 1: The Queen Mary Pearl

The Queen Mary Pearl was originally owned by Queen Mary (1867-1953), the wife of King George V of England (1865-1936). This significant pearl was subsequently passed down through generations within the royal family until it was eventually sold several years ago. It was recently resubmitted to our lab for testing (Figure 1), this was an opportunity to carry out additional DNA fingerprinting and age dating analysis. The findings of radiocarbon dating conducted at ETHZ have revealed an estimated historical age for the analysed pearl: the pearl is likely to have formed between 1707 and 1876 A.D. in coastal waters along the Pacific coast of Mesoamerica. Furthermore, the DNA analysis conducted has definitively identified the Queen Mary Pearl as belonging to the *Pinctada mazatlanica* species, commonly known as the Panama pearl oyster or La Paz pearl oyster. This particular species is found in the Pacific waters of Mesoamerica, ranging from Baja California (Mexico) to Ecuador and northern Peru.



Figure 1: The Queen Mary Pearl set as a pendant in a necklace. This pearl of 41 ct exhibits a delicate slightly grey colour and a very fine and smooth pearl lustre. Photo: L. Phan, SSEF.

Case study 2: Discovery of a new species for the pearl trade (*Pinctada persica*)

A natural pearl set containing 63 natural pearls was studied extensively (Figure 2). Sixty of the natural pearls were of saltwater origin, three were of freshwater origin. Three saltwater natural pearls were randomly selected and further age dating and DNA fingerprinting analysis was carried out. One of the pearls was conclusively identified as being from the *Pinctada radiata* species (Persian Gulf & Ceylon pearl oyster), a species that can produce pearls commonly called ‘Basra pearls’ in the trade. The other two sampled pearls were attributed to another species: *Pinctada persica* or *Pinctada margaritifera persica*, which is a rare member of the *Pinctada margaritifera* species complex. To our best understanding, this is the first report of pearls originating from *Pinctada persica*. Until now, this species has been exclusively documented in the Persian Gulf (Ranjbar et al., 2016). Based on our data, they probably formed between the 16th and 18th century A.D. with the highest probability of



Figure 2: A pearl jewellery set that consisted of 63 natural pearls, with 61 of them being strung on a thread and two additional loose natural pearls. Photo: L. Phan, SSEF.

formation having been in the 17th century (Figure 3). Mixing of pearls (different species, saltwater and freshwater) is not rare in historic natural pearl jewellery, as pearls were often collected and mixed together unknowingly.

Outlook:

This presentation will focus on these two case studies along with further recent case studies that highlight how a combined approach of age dating and DNA fingerprinting can be used in further documenting historical natural pearls. The ongoing research is also an opportunity to better understand pearl oyster genetics, as has been shown through the discovery of a previously unreported oyster species that has produced natural pearls for the trade.

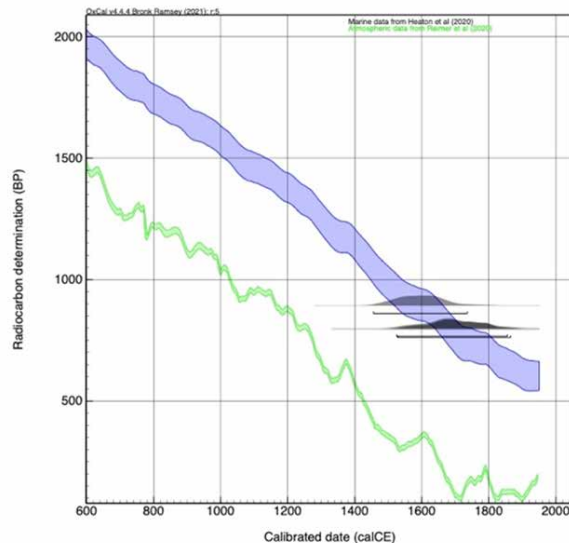


Figure 3: The three tested pearls show a similar historic age (calibrated date, calCE) ranging around the 17th century.

Figure: I. Hajdas, ETHZ.

References:

- Krzemnicki M. S., Hajdas I., 2013. Age Determination of Pearls: A New Approach for Pearl Testing and Identification, *Radiocarbon*, 55(2-3), 1801–1809.
- Krzemnicki M.S., Cartier L.E. and Hajdas, I., 2017. Radiocarbon age dating of 1,000-year-old pearls from the Cirebon shipwreck (Java, Indonesia). *Journal of Gemmology*, 35(8), pp.728-736.
- Meyer J.B., Cartier L.E., Pinto-Figueroa E.A., Krzemnicki M.S., Hänni H.A. and McDonald B.A., 2013. DNA fingerprinting of pearls to determine their origins. *PLoS ONE*, 8(10), article e75606, 11 pp., <http://dx.doi.org/10.1371/journal.pone.0075606>.
- Saruwatari K., Suzuki M., Zhou C., Kessrapong P. and Sturman N., 2018. DNA techniques applied to the identification of *Pinctada fucata* pearls from Uwajima, Ehime Prefecture, Japan. *Gems & Gemology*, 54(1), 40–50.

Nacreous Blister Pearl Discovered in Edible Oyster (*Crassostrea gigas*)

Sutas Singbamroong¹, Mohamed Karam¹, Nazar Ahmed¹, Nahla AlMuheiri¹, Thanong Leelawattanasuk², Bhuwadol Wanthanachaisaeng², Jirapit Jakkawanvibul²

¹ Dubai Central Laboratory (DCL), Dubai, United Arab Emirates, sssutas@dm.gov.ae

² The Gem and Jewelry Institute of Thailand (GIT), Bangkok, Thailand

A baroque pearl with a gray, nacreous appearance was discovered attached to the interior of an edible oyster while the author was enjoying a meal at home. The oyster had been purchased from a local seafood market in Dubai, United Arab Emirates. It was identified as a Pacific oyster (*Crassostrea gigas*) weighing 263.50 carats and measuring 10.9 x 5.9 x 3.0 cm. The pearl itself measured 18.1 x 11.7 x 10.6 mm (Figure 1) and was subsequently sent to the Dubai Central Laboratory for examination.



Figure 1: A grey nacreous blister pearl measuring 18.1 x 11.7 x 10.6 mm was found in an edible oyster (*Crassostrea gigas*)

Raman spectroscopy confirmed that both the shell and pearl were primarily composed of calcite, with distinct peaks in the spectrum observed at 280, 712, 1085, and 1437 cm^{-1} . Visual inspection of specific areas on the inner shell revealed patches of a mottled cellular structure that closely resembled the appearance of the pearl. Under fiber-optic light, the cellular structure within the oyster shell displayed a reflective colored sheen in certain orientations, resulting in an iridescent effect. This particular characteristic matched the surface appearance of the examined pearl (Figure 2).



Figure 2: A mottled cellular structure displayed a subtle reflective colored sheen on the surface of the pearl, resulting in an iridescent orient effect.

Chemical analysis conducted through energy-dispersive X-ray fluorescence (EDXRF) revealed low levels of manganese (Mn) in both the shell and pearl, consistent with the observed lack of luminescence during X-ray analysis. These findings confirmed the pearl's growth in a saltwater environment. Real-time microradiography (RTX) further illustrated the pearl's natural formation, displaying a growth arc structure mirroring the overall shape of the pearl, with a rounded core of slightly lower radio-opacity (Figure 3).



Figure 3: A growth arc structure mirroring the overall shape of the pearl, with a rounded core of slightly lower radio-opacity.

While previous literature mentions a few instances of oyster pearls, all recorded cases describe non-nacreous pearls (Scarratt et al., 2006; Zwaan and Groenenboom, 2014; Aslam et al., 2019; LeCroy and Homkrajae, 2020). Therefore, the discovery of this significant-sized nacreous pearl is especially noteworthy. Although oyster pearls are not highly sought-after in the global pearl market, they represent rare and captivating curiosities that provide valuable insights to the scientific community interested in pearls. This finding highlights the extremely uncommon occurrence of natural nacreous pearls produced by edible oysters.

References

- Aslam, S., Chan, M.W.H., Siddiqui, G., Kazmi, S.J.H., Shabbir, N. and Ozawa, T., 2019. A near-round natural pearl discovered in the edible oyster *Magallana bilineata*. *Gems & Gemology*, 55(3), 439-440.
- LeCroy, B. and Homkrajae, A., 2020. 15.53 ct pearl discovered in edible oyster from *Ostreidae* Family. *Gems & Gemology*, 56(3), 420-422.
- Scarratt, K., Pearce, C. and Johnson, P., 2006. A note on a pearl attached to the interior of *Crassostrea virginica* (Gmelin, 1791) (an edible oyster, common names, American or Eastern oyster). *Journal of Gemmology*, 30(1/2), 43-50.
- Zwaan, J.C., Groenenboom, P., 2014. Natural pearls from edible 'true oysters' in Zeeland, the Netherlands. *Journal of Gemmology*, 34(2), 150-155.

Baltic amber and its inclusions: an insight into the origin and nature of the trapped material

Costanzo A.¹, Bojarski B.², Kosior M.³, Klikowicz-Kosior A.³

¹ Earth and Ocean Sciences, School of Natural Sciences, University of Galway, Galway, Ireland;
alessandra.costanzo@universityofgalway.ie

² Faculty of Biology, Laboratory of Evolutionary Entomology and Museum of Amber Inclusions, Department of Invertebrate Zoology and Parasitology, University of Gdańsk, Gdańsk, Poland; blazej.bojarski@ug.edu.pl

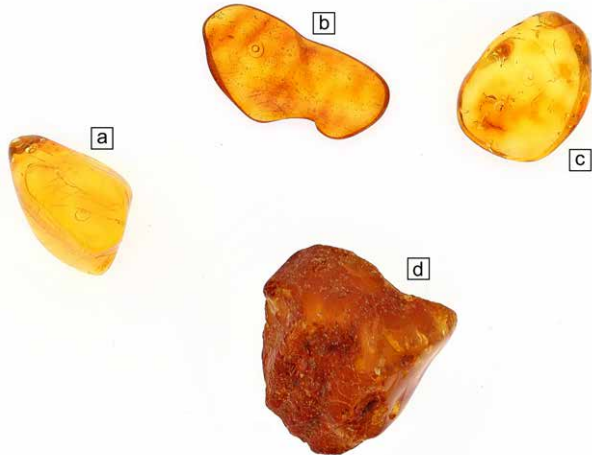
³ Amber Experts, Reduta Wysok 4, Gdańsk, Pomorskie, Poland; michal.kosior@gmail.com; akk@amberexperts.com

Keywords: Baltic amber, inclusions, paleobiology

Amber is a fossilised resin from ancient trees (coniferous and deciduous), which underwent the process of fossilisation in various epochs and depositional environments. Until the past decade, it was thought to be very rare, but new discoveries have shown that it is more abundant in terms of both geographical coverage and presence through time than was previously thought. (Seyfullah and Schmidt, 2015). For a long time, amber has been used as a source of paleobiological information as it frequently contains well preserved elements of past ecosystems (Antoine et al., 2006; Schmidt et al., 2006, 2010; Girard et al., 2009). Fossil inclusions in amber receive a great deal of attention in the study of paleoecosystems and evolutionary history (e.g. Briggs, 2018; Ross, 2021; Sadowski et al., 2021) and represent a critical window to the evolution of terrestrial environments across the Mesozoic–Cenozoic transition (e.g. Martínez-Delclòs et al., 2004; Penney, 2010; Sadowski et al., 2021). Fossils (also known as inclusions) in amber often have exquisite, three-dimensional preservation, retaining fine surface and structural details, and are frequently preserved at least roughly in a position that they would have had in life, and before much decay has set in (Seyfullah and Schmidt, 2015). ‘Exceptionally preserved’ fossils in amber may owe their high quality to the biocidal properties of resin as well as its role as a ‘conservation trap’ (Briggs, 2003). Resin can protect its inclusions from the physical and biological processes that ordinarily destroy non-biomineralized tissues in terrestrial environments (Jiang et al., 2022). Amber has also been a source for investigations into the potential preservation of ancient DNA (Cano et al., 1994; Greenblatt et al., 1999), with controversial results. Resin

does not just trap organisms but amber can also preserve vapour phases of various compositions and attempts have been made to analyse air and water bubbles contained in amber (Berner and Landis, 1988; Cerling, 1989) but the preservation of an original signal is still debated. They may represent ancient air trapped at the time the original resin was exuded from its host tree but may also contain modern air (Berner and Landis, 1987). Roedder (1984) also suggested that the trapped air might be mixed with volatile components of the amber.

In this study, we investigate inclusions in Baltic amber, Eocene in age. Numerous samples of raw (not processed) and non-raw (processed) material are used with the aim of investigating, through a multidisciplinary approach, the nature of the inclusions and determining their origin. The samples vary in size and weight (from 0.3 to 5 grams) and have all been selected according to their inclusion’s appearance (Fig.1). The inclusions consist of air bubbles, liquid and solid phases (e.g. marcasite) as well as spores. Previous studies (Jiang et al., 2022) demonstrate that resin and amber are not always closed systems. Fluids (e.g. sediment pore water, diagenetic fluid and ground water) at different burial stages have chances to interact with amber throughout its geological history and affect the preservation quality and morphological fidelity of its organic inclusions. There are indeed numerous problems with the preservation of original compositions in the amber matrix and therefore experiments related to man-made inclusions are also carried out. The processes used to prepare the samples, such as grinding and polishing, may force the entrapment of inclusions that have nothing in common to the original entrapment, therefore, post-processing water, impurities



or alteration materials need to be described and differentiated from the naturally entrapped inclusions. Data from light microscopy, scanning electron microscopy (SEM), energy-dispersive and wavelength-dispersive X-ray spectroscopy (EDX and WDX), X-ray micro-computed tomography (Micro-CT) and Raman spectroscopy will be presented.

Figure 1: Baltic amber (succinite) mined in South-East Poland (Lubartow region). (a,b,c) Polished pieces with visible two-phase liquid-gas inclusions and (d) rough amber piece darker in appearance but with obvious inclusions. Samples size: a) 0.31g; 14x9x9mm; b) 0.63g; 19x10x3mm; c) 0.70g; 15x11x7mm; d) 1.90g; 18x18x13mm.

References:

- Antoine, P.-O., De Franceschi, D., Flynn, J.J., Nel, A., Baby, P., Benammi, M., Calderón, Y., Espurt, N., Goswami, A., Salas-Gismondi, R., 2006. Amber from western Amazonia reveals Neotropical diversity during the middle Miocene. *Proceedings of the National Academy of Sciences* 103, 13595-13600.
- Berner, R.A., Landis, G.P., 1987. Chemical analysis of gaseous bubble inclusions in amber: the composition of ancient air? *American Journal of Science*, 287, 757-762.
- Berner, R.A., Landis, G.P., 1988. Gas-bubbles in fossil amber as possible indicators of the major gas-composition of ancient air. *Science* 239, 1406-1409.
- Briggs, D.E.G., 2003. The role of decay and mineralization in the preservation of soft-bodied fossils. *Annual Review of Earth and Planetary Sciences*, 31, 275-301.
- Briggs, D.E.G., 2018. Sampling the insects of the amber forest. *Proceedings of the National Academy of Sciences of the United States of America*, 115, 6525-6527.
- Cano, R.J., Borucki, M.K., Higbyschweitzer, M., Poinar, H.N., Poinar, G.O., Pollard, K.J., 1994. *Bacillus* DNA in fossil bees — an ancient symbiosis. *Applied and Environmental Microbiology* 60, 2164-2167.
- Cerling, T.E., 1989. Does the gas content of amber reveal the composition of paleoatmospheres. *Nature* 339, 695-696.
- Girard, V., Schmidt, A.R., Struwe, S., Perrichot, V., Breton, G., Néraudeau, D., 2009. Taphonomy and palaeoecology of mid-Cretaceous amber-preserved microorganisms from southwestern France. *Geodiversitas* 31, 153-162.
- Greenblatt, C., Davis, A., Clement, B., Kitts, C.L., Cox, T., Cano, R.J., 1999. Diversity of Microorganisms Isolated from Amber. *Microbial Ecology* 38, 58–68.
- Jiang, H., Tomaschek, F., Muscente, A.D., Niu, C., Nyunt, T.T., Fang, Y., Schmidt, U., Chen, J., Lönnartz, M., Mähler, B., Wappler, T., Jarzembowski, E.A., Szvedo, J., Zhang, H., Rust, J., Wang, B., 2022. Widespread mineralization of soft-bodied insects in Cretaceous amber. *Geobiology*, 20, 363-376.
- Roedder, E., 1984. Fluid Inclusions. *Reviews in Mineralogy*, Vol. 12, Mineralogical Society of America, 644 p.
- Ross, A.J., 2021. Supplement to the Burmese (Myanmar) amber checklist and bibliography, 2020. *Palaeoentomology*, 4(1), 57-76.
- Sadowski, E.-M., Schmidt, A.R., Seyfullah, L.J., Solórzano-Kraemer, M.M., Neumann, C., Perrichot, V., Hamann, C., Milke, R., Nascimbene, P.C., 2021. Conservation, preparation and imaging of diverse ambers and their inclusions. *Earth-Science Reviews*, 220, 103653.
- Schmidt, A.R., Ragazzi, E., Coppellotti, O., Roghi, G., 2006. A microworld in Triassic amber. *Nature* 444, 835.
- Schmidt, A.R., Perrichot, V., Svojtka, M., Anderson, K.B., Belete, K.H., Bussert, R., Dörfelt, H., Jancke, S., Mohr, B., Mohrmann, E., Nascimbene, P.C., Nel, A., Nel, P., Ragazzi, E., Roghi, G., Saupe, E.E., Schmidt, K., Schneider, H., Selden, P.A., Vávra, N., 2010. Cretaceous African life captured in amber. *Proceedings of the National Academy of Sciences*. 107, 7329-7334.
- Seyfullah, L.J., & Schmidt, A.R., 2015. Fossil focus: Stuck in time—life trapped in amber. *Palaeontology*, 5(12), 1-11.

Effects of weathering on FTIR spectra and origin traceability of archaeological amber: The case of the Han Tomb of Haihun Marquis, China

Yan Li¹, Minghan Peng², Yamei Wang^{1,3}

¹ Gemological Institute, China University of Geoscience, Wuhan 430074, China, yanli@cug.edu.cn

²Nanchang Relic Museum for Haihun Principality of Han Dynasty, Nanchang 330000, China

³Guangzhou Gem Testing Center of CUG, Guangzhou, 510000, China

Amber (fossil resin), known as the “capsule of time and space”, which is a complex biogenic polymer originated from ancient plants resin from different geological periods [1]. The archaeological amber artefacts inescapably undergone various degrees of weathering (typical irreversible oxidation) would change the appearance characteristics and internal compositions of amber [2], further resulting in alternations to the peak shape/position or signal noises in infrared spectra, which brings challenges in origin traceability of archaeological amber. This research [3] firstly reported a reference database of infrared fingerprint signatures of more than 113 pieces of different degrees of geological oxidised amber from Burma, Baltic region, and Fushun (China) to facilitate validation and further comparison with archaeological amber artefacts. Principal Component Analysis (PCA) and Linear Discriminant Analysis (LDA) were applied to discriminate infrared spectra data for dimensionality reduction, classification, and prediction. In this research, four cherished pieces of archaeological amber artefacts (No.1-No.4) excavated from the Haihun Marquis' Tomb of the Western Han Dynasty were investigated as a case study to source the archaeological amber. The external and internal features of them were observed using an optical microscopy. A non-destructive analysis (attenuated total

reflection Fourier-transform infrared spectroscopy [ATR-FTIR]) was performed on the archaeological amber artefacts (No.1-No.4), and different degrees of geological oxidised amber reference samples. Results from the infrared spectrum of archaeological amber artefact No.2 revealed peaks at 1226, 1149, 1035, and 974 cm^{-1} , which predominantly existed in the most Burmese amber. Archaeological amber artefacts (No.3 and No.4) displayed obvious oxidation characteristics (dark red colour, serious cracks), the FTIR peaks at 1050, 921, 553 and 476 cm^{-1} converged with that of the Burmese oxidised amber. However, the infrared spectrum of No.1 did not match well with the FTIR spectra characteristics of Baltic, Burmese and Fushun amber. PCA was further applied to reduce the dimension of spectra data, and the 15 principal component scores with high contribution were evaluated in LDA to obtain accurate classification results and prediction results. The prediction results indicated that four archaeological amber artefacts excavated from Haihun Marquis' Tomb were all from Burma based on the current existing detection and analysis techniques.

The archaeological amber artefacts witnessed the cultural exchange and mutual interaction on the Silk Road, and Burmese amber materials were delivered to China during the period of the Western Han Dynasty by road or via the Maritime Silk Road.

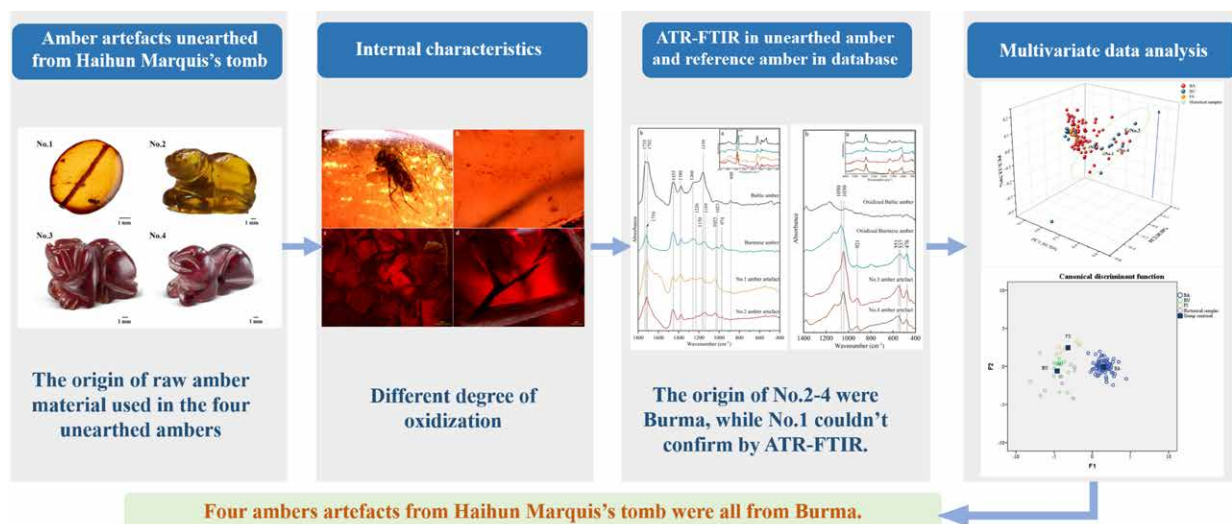


Figure. 1 The graphical abstract.

References:

- [1] Xiaopeng Su, Jing Yu, Zhaotong Shi, Yamei Wang*, Yan Li*, Headspace solid-phase microextraction comprehensive 2D gas chromatography-time of flight mass spectrometry (HS-SPME-GC × GC-TOFMS) for origin traceability of the genus *Hymenaea* resinites, *RSC Advances*, 2023, 13, 14150-14158
- [2] XingpingLi, YameiWang, GuanghaiShi, RenLu, Yan Li*. Evaluation of natural ageing responses on Burmese amber durability by FTIR spectroscopy with PLSR and ANN models. *Spectrochimica Acta Part A: Molecular and Biomolecular Spectroscopy*, 2023, 285: p. 121936.
- [3] Zhao T, Peng M, Yang M, Lu R, Wang Y*, Li Y*. Effects of weathering on FTIR spectra and origin traceability of archaeological amber: The case of the Han Tomb of Haihun Marquis, China. *Journal of Archaeological Science*, 2023, 153(105753).

Acknowledgements

This work has been funded by Hubei Gem & Jewelry Engineering Technology Center (No. CIGTXM-03-202104, CIGTXM-02-202001). The project was financially supported by the Fundamental Research Funds for National University, China University of Geosciences (Wuhan) (No. CUGDCJ202221).

Treated jadeite-jade: Unusually bright fancy colours

Supparat Promwongnan, Wilawan Atichat, Kannatee Fueangaksorn,
Visut Pisutha-Arnond, Thanong Leelawatanasuk

The Gem and Jewelry Institute of Thailand (Public Organization), ITF-Tower Building, Silom Road, Suriyawong, Bangrak,
Bangkok, 10500 Thailand; Corresponding author: awilawan@git.or.th



Figure 1: Six unusual bright fancy-coloured jade cabochons weighing between 7.63 and 95.70 ct were submitted to GIT-GTL for identification. Photo by C. Kamemakanon, samples with courtesy of Mr. Thamayuth Jenpichitkulchai

Introduction

Jadeite-jade is a precious ornamental stone that has been valued as the topmost decorative stone and has been used in jewelry, carvings, and other ornamental objects by many cultures throughout history, particularly in China and other parts of East Asia. The colour origin and treatment of jades are important factors that may impact the price of the stone. Natural untreated jadeite is called A-type in the Asian trade. The most common enhancement for jadeite-jade is polymer impregnation, classified as B-type, and dying, called C-type. Recently, the GIT-Gem Testing Laboratory (GIT-GTL) received six oval cabochons for identification which showed unusual bright fancy colours. Their striking fancy colour gave us immediately the impression that these samples were not common-coloured stones of

natural origin. Even though jadeite-jades of such colour had previously been seen in the market and mentioned by Mock and Hughes (2022), these samples were extraordinarily bright and colourful that needed an in-depth investigation.

Materials and methods

The studied six oval cabochons (Figure 1) possess unusual bright body colours as purple (FJBC001, 7.63 ct), purplish red (FJBC002, 83.42 ct), dark purplish red (FJBC003, 74.06 ct), blue-green (FJBC004, 76.25 ct), bluish green (FJBC005, 95.70 ct) and yellow (FJBC006, 68.22 ct). Such bright and fancy colours are not common for jades seen in the market. All samples were examined using standard gemological tools, and advanced equipment; a PerkinElmer Lambda 1050 UV-VIS-NIR spectrophotometer measured in UV-Vis (380-730 nm) range, a Thermo-Nicolet i550 FTIR spectrometer in the mid-IR (400-4900 cm^{-1}) and near-infrared (3700-6500 cm^{-1}) regions, a Renishaw inVia Raman spectrometer with a 532 nm Nd:YAG laser excitation and EDXRF Eagle III for chemical analysis.

Gemological Features

All the stones showed similar RI of 1.65-1.66 (spot reading) and SG of 3.26 -3.31 that are typical for jadeite. Furthermore, all samples exhibited strong bluish white reaction under LWUV and a weaker bluish white reaction under SWUV lamps. Such a fluorescent appearance is often found in polymer-impregnated jade.

Microscopic observations

Visually, these samples appeared to have even colour distribution and a smooth, polished surface texture. However, when observed under higher magnification, the purplish red sample (FJBC002) revealed distinctly large and small fractures and grain boundaries clearly filled with a material reaching the surface (Figure 2a). The yellow sample

(FJBC006) similarly showed a large open fracture filled with a material exhibiting a strong blue reaction under LWUV (Figure 2b). Thus, the filling material in all samples was likely a polymer as it showed strong blue fluorescence under LWUV. Using fiber-optic light, dyed-colour concentrations along fractures and grain boundaries were evident in almost all samples (see Figure 2c,d), but less obvious in the yellow sample.

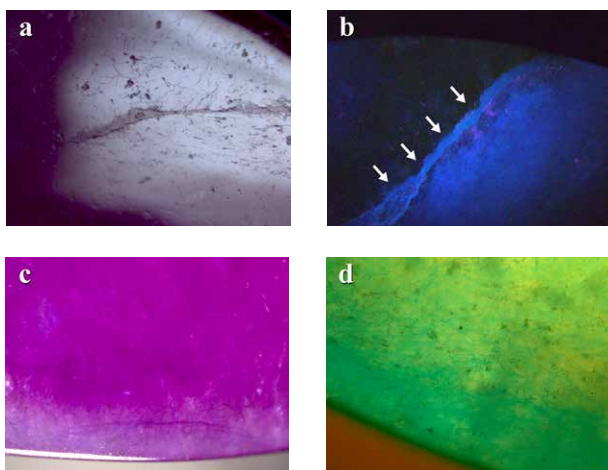


Figure 2: (a) Reflected light image of the purplish red sample (FJBC002) showing filling material (polymer) along large and small fractures and grain boundaries, field of view 3.5 mm; (b) LWUV fluorescence image of the yellow sample (FJBC006) showing a large open fracture filled with strong blue fluorescent material (polymer), field of view 7 mm; (c) and (d) Transmitted light images of the purple sample (FJBC001) and bluish green sample (FJBC005) respectively, showing colour concentrations along fractures and grain boundaries when using high magnification and fiber-optic light, field of view 4 mm. Photomicrographs by S. Promwongnan

Spectroscopic Features

Raman-spectroscopy

The identity of the stones was also confirmed by Raman spectroscopy. The Raman spectra of all samples showed dominant peaks at approximately 203, 370, 430, 522, 570, 695, 982, 1040 cm^{-1} (Raman shift) which perfectly match with the jadeite reference spectrum from the RRUFF database. The presence of polymer peaks was also detected around 2500-3000 cm^{-1} .

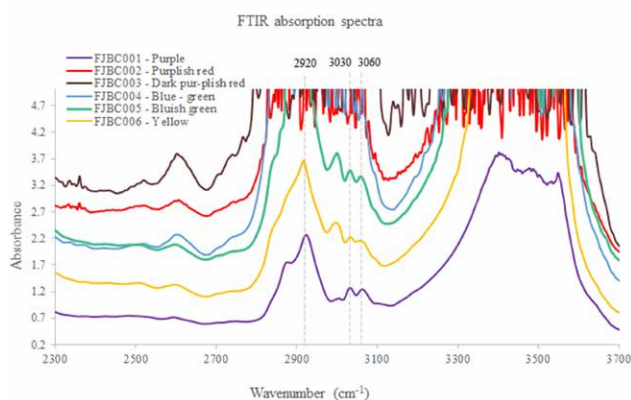


Figure 3: Mid-IR spectra of the treated jade samples reveal the characteristic absorption bands of polymer (phthalates) at approximately 2920, 3030 and 3060 cm^{-1} and jadeite-related absorption between 3400-3600 cm^{-1} .

Mid-Infrared Absorption Spectra

The mid-infrared spectra of the samples revealed characteristic absorption bands of polymers at approximately 2920, 3030 and 3060 cm^{-1} that match with a family of phthalates (Fritsch et al., 1992) (Figure 3). In the near-infrared spectra, all samples also showed additional bands of jadeite approximately 6200-5500 cm^{-1} and other features at 4050, 4530, 4612, 4665, 4880, 4970, and 5230 cm^{-1} that were identified as plastic (variety of organic polymer), which is likely a mixture of different polyacrylates (Hurwit, 1989).

Semi-quantitative chemical analyses

Semi-quantitative chemical analyses of all samples by EDXRF showed distinct concentrations of Na_2O (12.66-15.02%), Al_2O_3 (23.86-25.89%), SiO_2 (59.07-60.81%) with minor CaO (0.16-1.26%), and traces of V_2O_5 (0.01-0.14%), Cr_2O_3 (<0.01-0.06%), Fe_2O_3 (0.12-1.07%), TiO_2 (<0.01-

0.19%) and MnO (0.01-0.04%). These analyses are well in accordance with the expected composition of jadeite. Almost all samples contain relatively high iron contents.

UV-Visible Absorption Spectra

Nearly all samples showed a small absorption peak at 437 nm due to Fe³⁺. This peak is commonly found in jadeite of various colours (Koivula, 1982) and related to the relatively high iron contents of the investigated samples. The dyed purple sample (FJBC001, see Fig. 4a) displayed triple broad bands at about 540, 587 and 630 nm, likely related to the purple dye. The spectrum of this dyed sample is somewhat similar to a reference spectrum of a dyed and impregnated purplish jadeite (double broad bands near 562 and 602 nm, green line in Fig. 4a), but fairly different from the spectrum of a purple jadeite of natural colour (a large broad band near 572 nm due to Mn, red line in Fig. 4a) from our reference collection.

The spectra of the dyed samples of blue-green (FJBC004) and bluish green (FJBC005) colours (Figure 4b) exhibited quite similar absorption features, a small Fe³⁺ related peak at 437 nm and strong broad bands at about 620, 670 and 680 nm. These broad bands were probably caused by the blue-green dye. These absorption features are similar to a dyed green jadeite from our reference collection except the dyed green reference sample has also a strong absorption band in the blue-violet, thus shifting the transmission window to the green. The absorption features of the studied blue-green and bluish green samples, however, are quite different to green jadeite of natural colour (typical Cr³⁺ related bands at about 437, 655 nm and a sharp peak at 691 nm, yellow line in Fig. 4b). Our blue-green and bluish green dyed samples also show different absorption bands compared to dyed and impregnated blue jadeite (greenish blue line in Fig. 4b) and greenish blue jadeite of natural colour from our reference collection (red line in Fig. 4b).

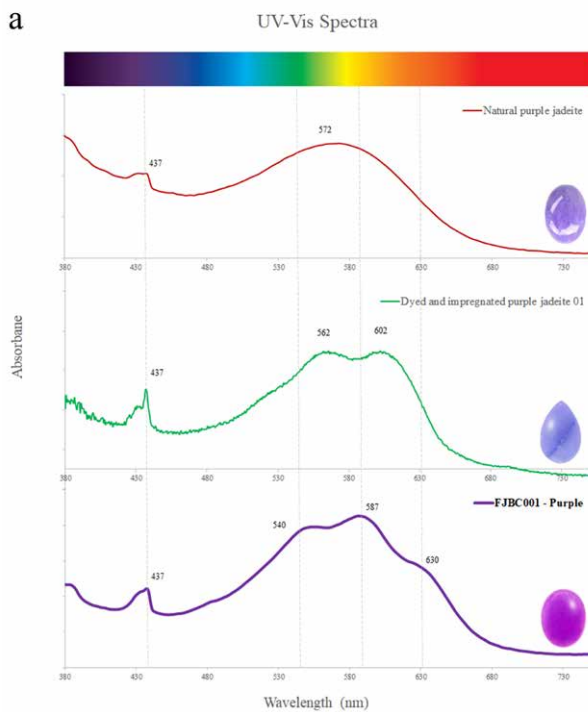


Fig 4a) Absorption spectrum of the dyed purple jadeite (FJBC001, bottom) compared to spectra of purple reference samples of dyed and natural colour.

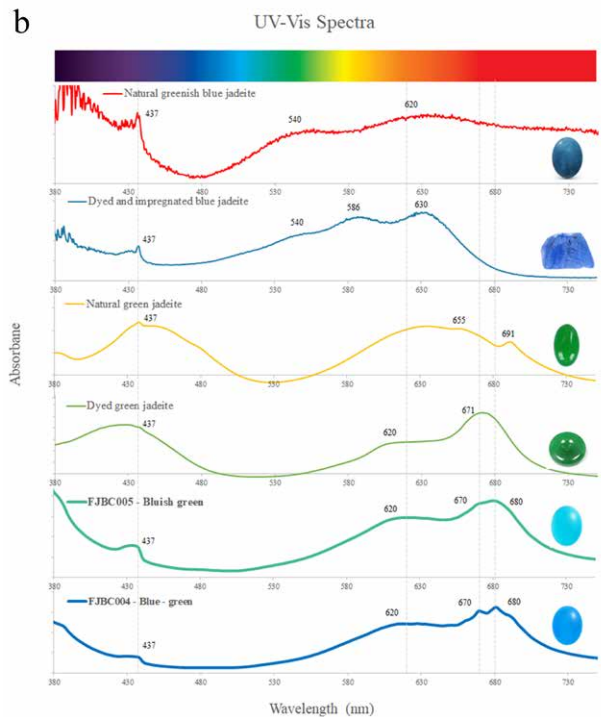


Fig 4b) Absorption spectrum of the dyed blue-green (FJBC004, blue line) and bluish-green jadeite (FJBC005, green line) compared to spectra of reference samples of dyed green, natural green colour, of dyed blue and natural blue-green colour.

The spectra of dyed samples of purplish red (FJBC002, red line in Fig. 5a) and dark purplish red (FJBC003, dark red line in Fig. 5a) colours display fairly similar absorption features, i.e. a small Fe³⁺ related peak at 437 nm and a strong broadband between 530 and 580 nm, probably caused by the red dye. The spectra of these two samples are however different from the spectrum of a dyed and impreg-

nated jadeite of brownish red colour from our reference collection (blue line in Fig. 5a). The spectrum of the dyed sample of yellow colour (FJBC006, yellow line in Fig. 5b) reveals a strong absorption band below ~480 nm towards the UV region, likely related to yellow dye, which matches somehow the spectrum of the dyed yellow sample of our reference collection.

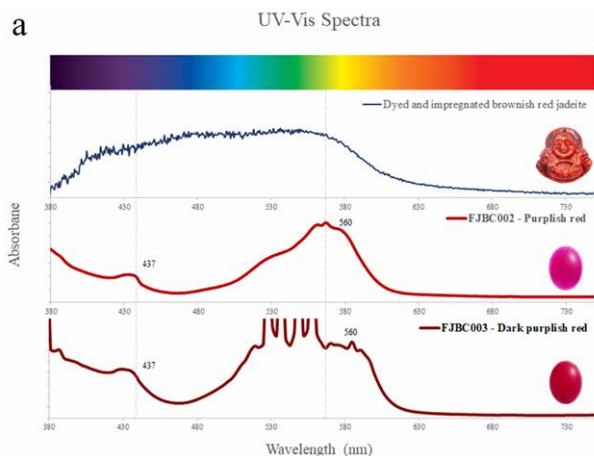


Fig 5a) Absorption spectrum of the dyed purplish red (FJBC002, middle) and dyed dark purplish red (FJBC003, bottom) jadeite samples compared to spectra of reference sample of the dyed and impregnated brownish red colour

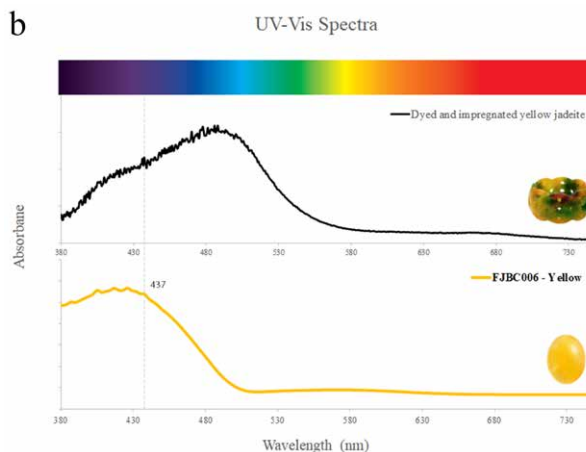


Fig 5b) Absorption spectrum of the dyed yellow (FJBC006, yellow line) compared to spectra of reference sample of dyed yellow colour.

Conclusion

Standards gem properties and the strong bluish white fluorescence reaction under LWUV clearly indicate that these samples are jadeite-jades that have been polymer-impregnated. High magnification revealed fluorescent polymer fissure filling and colour concentrations along fractures and grain boundaries strongly indicating a dye treatment. The identity of these samples as jadeite was also confirmed by Raman micro-spectroscopy. The presence of a polymer-impregnation was clearly detected by FTIR spectroscopy. The UV-Vis absorption spectra of all samples showed a small Fe³⁺-related peak at 437 nm and various broad absorption bands related to their specific colour and dye. The spectra showed some similarities with dyed samples from our reference collection, but were distinctly different from jadeite of natural colour (purple, green, green-blue) from our reference collection. Based on our analyses of these bright fancy colour stones, these samples are identified as dyed

and impregnated (B+C type) jadeite-jades of very unusual and bright “fancy” colours.

References

- Fritsch, E., Wu, S.T.T., Moses, T., McClure, S.F., Moon, M., 1992. Identification of bleached and polymer- impregnated jadeite. *Gems & Gemology*, 28(3), 176-187
- Hurwit, K., 1989. Gem trade lab notes: Impregnated jadeite jade. *Gems & Gemology*, 25(4), 239-240
- Koivula, J.I., 1982. Some observations on the treatment of lavender jadeite. *Gems & Gemology*, 18(1), 70-85
- Mock, D.W.K., Hughes, R.W., 2022, Jadeite jade and its identification, In *Jade: A Gemologist's Guide* by R.W. Hughes, RWH Publishing, Bangkok, 533pp.

Origin Identification Characteristics of High-quality Green Jadeite

Elizabeth Su

Gemsu Rona Jewellery (Shanghai) Co., Ltd, Shanghai, China,
esu_gems@yahoo.com

Introduction

Currently occurrences of jadeite mainly include Myanmar, Guatemala, Russia, Kazakhstan and Japan. Origin has a great impact on the price of high-quality green jadeite and at present Myanmar (Figure 2), and Guatemala (Figure 1) are the main producers.

This paper deals with the characterization of jadeite from these two occurrences by chemical composition, Raman spectra, infrared spectra and UV/Vis/NIR absorption spectra.

Results

The investigation results show that the contents of Na and Al are lower in the Guatemala green jadeite compared to Myanmar material, while Ca, Mg and Fe show higher concentrations because of the presence of an omphacite component (Figure1). Myanmar material is mainly composed of jadeite (Figure 2).

Differentiation can also be carried out by Raman and infrared spectroscopy as well as optical absorption spectra.

The Raman spectrum of green jadeite from Myanmar (Figure 3) is characterized by bands at 1036, 982, 696, 372, 325 and 308 cm^{-1} . Jadeite from Guatemala shows bands at 1022, 682 and 372 cm^{-1} and additionally bands of omphacite at 401 and 345 cm^{-1} .

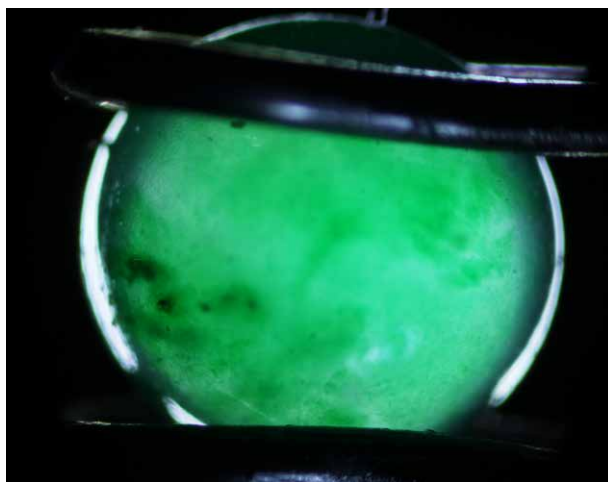


Figure 1: The black mineral (Omphacite) inclusions of Guatemala jadeite.

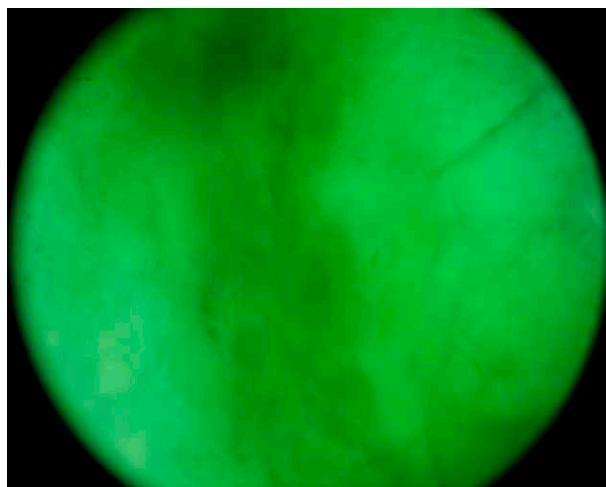


Figure 2: The structure of Myanmar jadeite under a microscope.

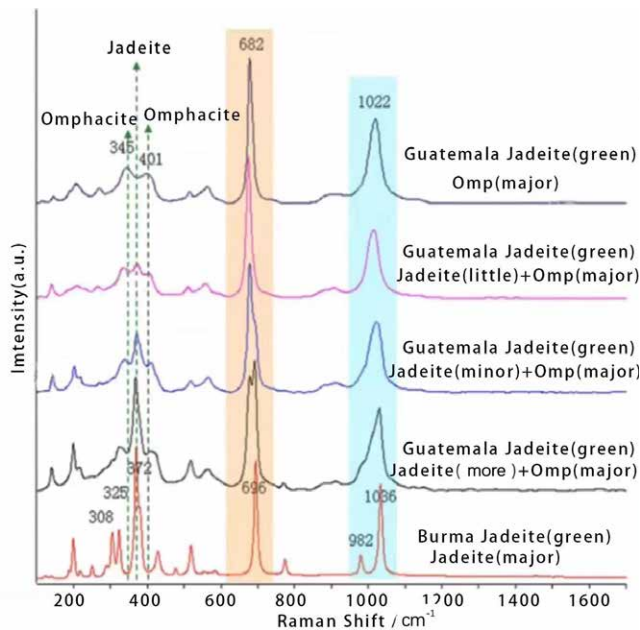


Figure 3. Typical Raman spectra of green Jadeites from Guatemala and Burma.

Conclusion

The results show that the origin of high-quality green jadeite can be effectively identified by the difference in jadeite composition and spectral characteristics.

References

- Quanli Chen, A., Zuwei Yin, S., Yuewen Bu, S., Zengqiu Zhong, S., 2012. Raman Spectroscopy Study on the Mineral Composition of the Guatemalan Jade, Spectroscopy and Spectral Analysis, 32(9),2447-2451
- Haoyu Xue, A., Tao Chen, S., Zhigang Li, S., 2020. Mineralogical comparison between omphacite-bearing jadeite from Guatemala and that from Myanmar, Acta Petrologica et Mineralogica, 39(4), 481-494
- Cocatto, A., Karampelas, S., Wörle, S., van Willigen, S. & Pétrequin, P., 2014. Gem quality and archeological green "jadeite jade" versus "omphacite jade". Journal of Raman Spectroscopy, 45 (11-12)

Acknowledgements

I thank Mr. Kai Zhang for supplying the Guatemala jadeite samples, Gemsu Rona Jewellery (Shanghai) Co., Ltd. for supplying the Burma jadeite samples, and Dr. Liu Xueliang from the Gemstone Testing Centre of ECUST obtained the origin determination and discussing the data for this paper.

Geographic Origin Determination of Fei Cui: A comparison of high-quality green Fei Cui from Myanmar, Guatemala, and Italy

Shang-I (Edward) Liu¹, Ka-Yi (Angela) Man²,
Montira Seneewong-Na-Ayutthaya³, Chanenkant Jakkawanvibul³

¹ The Gemmological Association of Hong Kong, Hong Kong, China; gemedward@hotmail.com

² Department of Applied Biology and Chemical Technology, The Hong Kong Polytechnic University,
Hong Kong, China; mankayi_plus2@yahoo.com.hk

³ The Gem and Jewelry Institute of Thailand (GIT), Bangkok, Thailand; smontira@git.or.th, jchanenkant@git.or.th

Keywords: Origin determination, Fei Cui, Jadeite jade, Omphacite jade

Fei Cui is a kind of jade that is defined as a granular to fibrous polycrystalline aggregate composed solely, or principally of any of the following or any combination of the following: jadeite, omphacite and kosmochlor (GAHK, 2016). For decades, Myanmar was the only source of “Imperial green” Fei Cui. Guatemala is another historical source of jade. Since 2021, “Imperial green” Fei Cui from Guatemala has been getting more popular in China, especially after a new mining area was discovered in Morales, Izabal Department in Guatemala. Besides, a small amount of high-quality Italian Fei Cui also appeared in the market in the past four years. To examine the possibility of origin determination on Fei Cui, a set of high-quality green Fei Cui from Myanmar, Guatemala, and Italy were collected and examined.



Figure 1: Top-quality green Fei Cui from Myanmar (left, Stanley Chu collection), one of the Guatemalan samples analysed in this study (right)

Conventional gemmological tests were carried out, including determination of specific gravity, refractive index, and microscopic observation. All samples' specific gravity and refractive index and thus are within the acceptable range (SG: 1.65-1.68; RI: 3.25-3.45) of Fei Cui Standards of the GAHK and the GIT (GAHK, 2016; GIT, 2022).

FTIR spectroscopy is the routine test in Fei Cui Standards for determining the identity and the treatments (GAHK, 2016; GIT, 2022). Based on the FTIR result, all samples were found to be Fei Cui and untreated. FTIR spectroscopy is also frequently used in research to examine the dominant clinopyroxene phase in this polycrystalline material (Ou-Yang et al., 2003; Liu et al., 2010; Franz et al., 2014; Zhang et al., 2022) and classify Fei Cui into three groups based on their main mineralogical constituent (GAHK, 2016). All investigated Italian samples are omphacite jade with an unusually shifted Si-O-Si asymmetric vibration peak at around 1100 cm⁻¹, which was also observed in Mn-bearing violet omphacite from Italy (Diella et al., 2021). Most of the Myanmar samples are classified as jadeite jade and a few samples are omphacite jade. In contrast, most of the Guatemalan samples are omphacite jade and a few samples are jadeite jade. Surprisingly, the dominant mineral phase in Guatemalan samples relates to the colour. We found that the top colour-graded samples are jadeite jade. A recent study on the mineralization stages also found that jadeite is the major mineral composition in green-coloured Guatemalan Fei Cui (Wang, 2022).

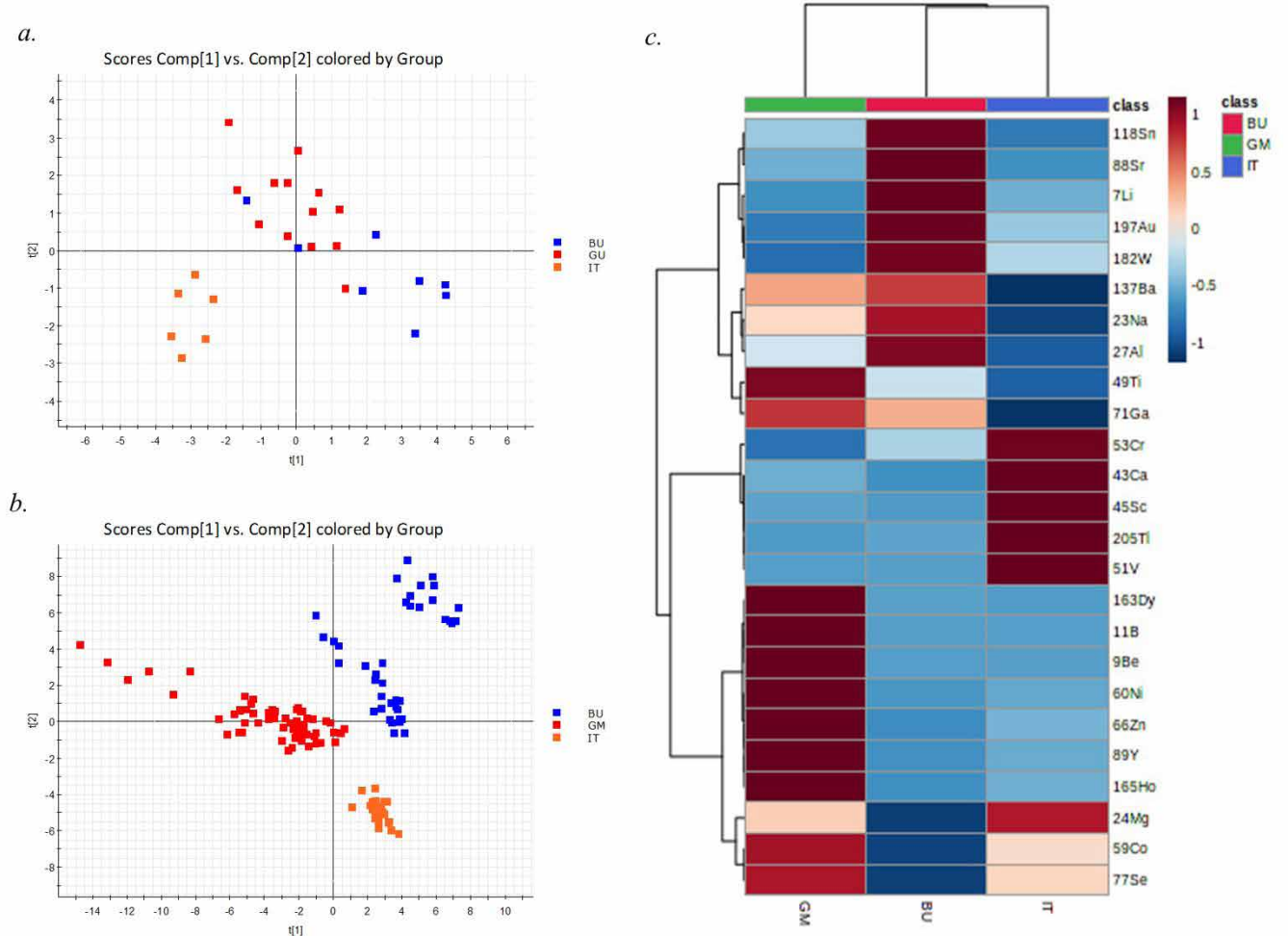


Figure 2: PCA score plot of (a) EDXRF and (b) LA-ICP-MS data of high-quality green Fei Cui from Myanmar (BU), Guatemala (GM) and Italy (IT) (c) Heatmap of LA-ICP-MS data

EDXRF and LA-ICP-MS were used to analyse the chemical composition in the samples. After statistical calculations, principal component analysis (PCA) was applied to investigate the classification power of two chemical analysis tools. EDXRF showed a confident differentiation power in the Fei Cui localities (Figure 2a). The Italian samples are separate from the other two localities. In contrast, an overlapping between Myanmar and Guatemala is observed in the PCA score plot. The differentiation power of EDXRF on separating Guatemala and Myanmar Fei Cui is 92% and 75% respectively. However, the mineral composition in the samples highly influences the EDXRF results. The PCA score plot of LA-ICP-MS (Figure 2b) displays a clear separation among three localities. The differentiation power of LA-ICP-MS is 100%. In the brief of the chemical difference, the Mg concentration in Burmese samples is the lowest due to the jadeite jade dominated. Italian samples showed the highest Cr content among the three localities, while the Guatemalan samples have the highest Fe abundance which aligns with the previous studies on Guatemalan jadeite jades (Liu, 2019; Zhang and Shi, 2022). Raman spectroscopy reflects the mineral component in the Fei Cui. (GIT, 2022) The Raman results are consistent with the FTIR and chemical analysis result from EDXRF.

Acknowledgements

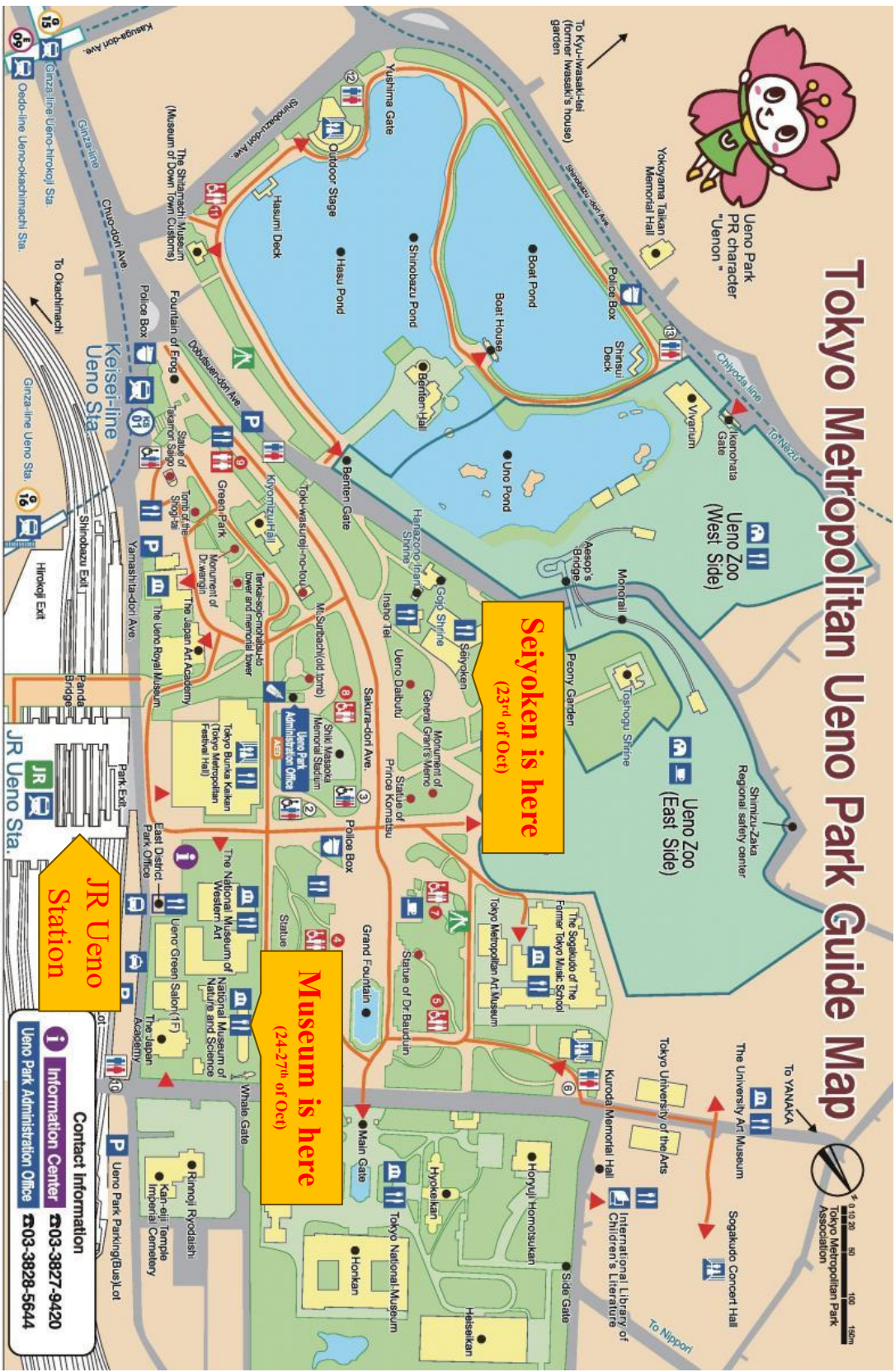
The authors are grateful to Tommy Kin-Wah Tsui, Chun-Kit Lau and Timothy Sheung-Yin Li of China Gems Laboratory Limited for providing FTIR spectroscopy and Raman spectroscopy.

References:

- Diella, V., Bocchio, R., Caucia, F., Marinoni, N., Langone, A., & Possenti, E. (2021). New insights for gem-quality Mn-bearing diopside-omphacite, violane variety, from Saint Marcel (Val D'Aosta, Italy): Its trace elements and spectroscopic characterization. *Minerals*, 11(2), 171.
- Franz, L., Sun, T. T., Hänni, H. A., De Capitani, C., Thanasuthipitak, T., Atichat, W. (2014). A comparative study of jadeite, omphacite and kosmochlor jades from Myanmar, and suggestions for a practical nomenclature. *Journal of Gemmology*, 34(3), 210-229.
- The Gemmological Association of Hong Kong (GAHK). (2016). Standard Methods for Testing Fei Cui for Hong Kong (HKSM/FCT-2016), GAHK. http://www.gahk.org/attachment/fc_std_eng.pdf
- The Gem and Jewelry Institute of Thailand (GIT). (2022). The Gem and Jewelry Institute of Thailand Standard-Testing of jade and Fei Cui (GIT 1013.1-2564), GIT.
- Liu, S.I., Peng, M.S., & Chen, H.C. (2010). A study of new high quality "imperial green" omphacite jade (Fei Cui) (in Chinese), *Acta Mineralogica Sinica*, 2010(suppl.), 26-27.
- Liu, S.I., Ouyang, C.M., & Ng, F.Y. (2015). The application of VPSEM-Raman coupled system in studying Fei Cui. *Proceedings of the 34th International Gemmological Conference IGC, Vilnius, Lithuania*, 76-79.
- Liu, S.I. (2019). Identification of Fei Cui and the interpretation of regional testing standard. *NGTC forum: Identification and Evaluation of Fei Cui, Hong Kong, China*.
- Ou-Yang, C. M., Qi, L. J., Lin, H. S., & Kwok, B. (2003). Recent studies on inky black omphacite jade, a new variety of pyroxene jade. *Journal of Gemmology*, 28(6), 337-344.
- Wang, L., Zhang, H., Liu, J., Wang, L., Ou-Yang, Q., Liu, D., Liu, W. (2022). Mineral component and genesis of high-grade green jadeite jade from Guatemala (in Chinese), *Journal of Gems & Gemmology*, 24(5), 11-30.
- Zhang, Y., & Shi, G. (2022). Origin of Blue-Water Jadeite Jades from Myanmar and Guatemala: Differentiation by Non-Destructive Spectroscopic Techniques. *Crystals*, 12(10), 1448.



Tokyo Metropolitan Ueno Park Guide Map



Seiyoken is here
(23rd of Oct)

Museum is here
(24-27th of Oct)

JR Ueno Station

- Legend**
- Art Museum / Museum
 - Police Box (Koban)
 - Station
 - Theater
 - Zoo
 - Parking lot
 - Bus Stop
 - Cafe
 - Restaurant
 - Library
 - Outdoor Stage
 - Fountain
 - Statue
 - Monument
 - Shrine
 - Vivarium
 - Mendai
 - Peony Garden
 - Shimizu-Zaka
 - Regional safety center
 - Ueno Zoo (East Side)
 - Ueno Zoo (West Side)
 - Seiyoken
 - General Gaiji's Memo
 - Monument of Prince Komatsu
 - Statue of Dr. Bandai
 - Tokyo Metropolitan Art Museum
 - The Sogakudo of The Former Tokyo Music School
 - Kuroda Memorial Hall
 - International Library of Children's Literature
 - Sogakudo Concert Hall
 - The University of the Arts
 - To YANAKA
 - To Nippori
 - JR Ueno Station
 - Ueno Park Administration Office
 - Contact Information
 - Accessible route (pathway with no steps)
 - Facility entrance
 - Accessible Toilet (with video guidance)
 - Toilet (with video guidance)
 - Nursing room
 - Playground
 - Travel stand
 - Cafe
 - Bus Stop
 - Parking lot
 - Zoo
 - Theater
 - Station
 - Police Box (Koban)
 - Art Museum / Museum

Contact Information
 Ueno Park Administration Office ☎03-3827-9420
 ☎03-3828-5644

RE:100 TOKYO
 2019. Published in Jan.

International Gemmological Conference

**Tokyo - Japan
October 2023**

www.igc-gemmology.org